

RICE UNIVERSITY

**One- and two-photon photoassociative  
spectroscopy of ultracold strontium**

by

**James Allen Aman**

A THESIS SUBMITTED  
IN PARTIAL FULFILLMENT OF THE  
REQUIREMENTS FOR THE DEGREE

**Doctor of Philosophy**

APPROVED, THESIS COMMITTEE:

---

Thomas C. Killian, Chair  
Professor of Physics and Astronomy

---

Randall G. Hulet  
Fayez Sarofim Professor of Physics and  
Astronomy

---

Kevin F. Kelly  
Associate Professor of Electrical and  
Computer Engineering

Houston, Texas

April, 2019

## ABSTRACT

One- and two-photon photoassociative spectroscopy of ultracold strontium

by

James Allen Aman

”Lorem ipsum dolor sit amet, consectetur adipiscing elit, sed do eiusmod tempor incididunt ut labore et dolore magna aliqua. Ut enim ad minim veniam, quis nostrud exercitation ullamco laboris nisi ut aliquip ex ea commodo consequat. Duis aute irure dolor in reprehenderit in voluptate velit esse cillum dolore eu fugiat nulla pariatur. Excepteur sint occaecat cupidatat non proident, sunt in culpa qui officia deserunt mollit anim id est laborum.”

## Acknowledgments

It is difficult to over state how much I have learned during my time in grad school. Not only pertaining to physics, engineering, and computer science but also about myself, my friends, and my communities.

I owe so much to Brian DeSalvo for being an inspiration. It was Brian who showed me my first Bose-Einstein condensate

I bugged him relentlessly as a naive undergraduate with so many questions.

# Contents

Abstract	ii
Acknowledgments	iii
List of Illustrations	vii
List of Tables	xi
<b>1 Introduction</b>	<b>1</b>
1.1 Few-body physics . . . . .	2
1.2 Halo molecules . . . . .	2
1.3 Properties of strontium . . . . .	5
1.4 Thesis Outline . . . . .	6
<b>2 The Neutral apparatus</b>	<b>8</b>
2.1 Experimental procedure . . . . .	8
2.1.1 Characteristic performance . . . . .	12
2.2 Vacuum system and atom source . . . . .	15
2.3 Laser systems . . . . .	24
2.3.1 Wideband cooling stage: 461 nm . . . . .	24
2.3.1.1 Overview . . . . .	24
2.3.1.2 922 nm master . . . . .	27
2.3.1.3 Zeeman subsystem . . . . .	31
2.3.1.4 MOT subsystem . . . . .	33
2.3.2 Narrowband cooling stage: 689 nm . . . . .	40
2.3.2.1 Overview . . . . .	40
2.3.2.2 689 nm Master . . . . .	43

2.3.2.3	Neutral red system . . . . .	44
2.3.3	Optical dipole trap: 1064 nm . . . . .	50
2.3.3.1	Modeling the potential . . . . .	52
2.3.3.2	Trap frequency calibration . . . . .	57
2.3.4	Optical toolbox . . . . .	62
2.3.4.1	Absorption imaging system . . . . .	62
2.3.4.2	Highly tunable 689 nm spectroscopy system . . . . .	67
2.3.4.3	Spin-manipulation laser with dynamic polarization control . . . . .	72
2.4	Apparatus interface . . . . .	75
2.4.1	Software . . . . .	75
2.4.2	Hardware control and measurement systems . . . . .	76
2.4.3	Ancillary laboratory systems . . . . .	79
2.4.3.1	Trim coils . . . . .	79
2.4.3.2	Zero crossing AC line trigger . . . . .	81
2.4.3.3	Pneumatic actuated mirror mounts . . . . .	84
<b>3</b>	<b>Photoassociation in ultracold gases</b>	<b>86</b>
3.1	Introduction . . . . .	86
3.2	Theory of trapped boson gases . . . . .	88
3.2.1	Extracting data from column densities . . . . .	90
3.3	Atomic collisions . . . . .	93
3.3.1	Single channel scattering near threshold . . . . .	94
3.4	Modeling of photoassociation lineshapes . . . . .	100
<b>4</b>	<b>High intensity PAS of a halo molecule</b>	<b>106</b>
4.1	Probing the ground state potential . . . . .	106
4.2	Experimental setup . . . . .	107
4.3	Modeling of the photoassociative loss . . . . .	114

4.3.1	Frequency dependence of the binding energy . . . . .	120
4.4	Multi-photon loss processes . . . . .	127
<b>5</b>	<b>Binding energy of the <math>^{86}\text{Sr}_2</math> halo molecule</b>	<b>131</b>
5.1	Modeling the PA spectra . . . . .	133
5.1.1	Consideration of the trap depth . . . . .	136
5.1.2	Fitting the thermally averaged spectra . . . . .	141
5.2	Determination of energy shifts . . . . .	145
5.2.1	AC Stark shift due to excitation lasers . . . . .	150
5.2.2	Density-dependent frequency shift . . . . .	151
5.2.3	AC Stark Shift due to Trapping Lasers . . . . .	153
5.3	Discussion of the halo binding energy . . . . .	155
<b>6</b>	<b>Progress towards studies of quantum magnetism</b>	<b>166</b>
6.1	Optical lattice trap: 532 nm . . . . .	166
6.2	Spin manipulation of $^{87}\text{Sr}$ . . . . .	183
6.3	Search for narrowline PA molecules using various spin mixtures . . . . .	185
<b>7</b>	<b>Conclusion</b>	<b>188</b>
<b>Bibliography</b>		<b>190</b>
<b>Appendices</b>		<b>203</b>
<b>A</b>	<b>Two-particle momentum probability distribution</b>	<b>204</b>
A.1	Standard form . . . . .	204
A.2	Truncated form . . . . .	205

# Illustrations

1.1 Example bound states . . . . .	3
1.2 Example halo state . . . . .	4
1.3 Partial energy level diagram of strontium . . . . .	7
2.1 Neutral apparatus vacuum system . . . . .	16
2.2 Source assembly - side view . . . . .	17
2.3 Source assembly - rear view . . . . .	17
2.4 2D collimator assembly . . . . .	18
2.5 Cryo tower assembly . . . . .	18
2.6 Typical fluorescence of Zeeman beam looking down 2D collimator . .	21
2.7 Atom oven and nozzle construction . . . . .	23
2.8 461 nm light generation system . . . . .	25
2.9 922 nm master optical schematic . . . . .	28
2.10 922 nm doubling cavity length stabilization feedback diagram . . .	29
2.11 922 nm frequency stabilization block diagram . . . . .	30
2.12 Zeeman subsystem optical schematic . . . . .	32
2.13 MOT subsystem optical schematic . . . . .	34
2.14 461 nm MOT schematic . . . . .	36
2.15 461 nm saturated absorption setup . . . . .	38
2.16 689 nm light generation system . . . . .	41
2.17 689 nm master system . . . . .	45
2.18 Neutral 689 nm trapping and cooling setup . . . . .	46

2.19	1064 nm optical dipole trap schematic . . . . .	51
2.20	Two-level avoided crossing . . . . .	53
2.21	Modeling an optical dipole potential . . . . .	56
2.22	Example center-of-mass oscillations . . . . .	58
2.23	Absorption imaging and blow away pulser optical schematic . . . . .	63
2.24	Timing diagram of PixelFly doubleshutter mode . . . . .	64
2.25	Comparison of background subtraction methods . . . . .	67
2.26	Optical schematic: 689 spectroscopy laser . . . . .	68
2.27	Infinite sample and holding timing diagram . . . . .	69
2.28	Characterization of the OPLL performance . . . . .	73
2.29	Zeroing residual magnetic fields . . . . .	80
2.30	Circuit diagram of the zero crossing AC line trigger . . . . .	82
2.31	Comparison of pulseblaster timing jitter . . . . .	83
2.32	Pneumatic actuators diagram . . . . .	85
3.1	Schematic of the photoassociation process . . . . .	87
3.2	Ballistic expansion of particles . . . . .	90
3.3	Examples of scattering state solutions . . . . .	95
3.4	Long range phase shift . . . . .	97
4.1	Strontium PAS potential . . . . .	108
4.2	Accessible halo resonance PAS processes . . . . .	110
4.3	Schematic of PAS light generation . . . . .	112
4.4	Histogram of PAS beam intensity variation . . . . .	114
4.5	Halo molecule spectroscopy . . . . .	116
4.6	Halo state resonances and susceptibilities, $\chi_{689}$ . . . . .	121
4.7	Comparison of a three-level model to experimental halo PAS . . . . .	123
4.8	Analytic approximation of the susceptibility . . . . .	125

4.9	Observation of higher order Raman processes . . . . .	128
4.10	Multi-photon Raman processes . . . . .	130
5.1	$^{86}\text{Sr}$ halo molecule wavefunction . . . . .	134
5.2	Surface plot of the trapping volume in single beam trap . . . . .	139
5.3	Relative collision energy distributions for various trap depths . . . . .	140
5.4	Comparison of lineshape fits at various $\epsilon_{\max}$ . . . . .	142
5.5	Variation of 1064 nm trap depth . . . . .	146
5.6	Variation of 689 nm excitation . . . . .	148
5.7	Fit of 689 nm AC Stark shift . . . . .	149
5.8	Measurement of halo state susceptibility, $\chi_{1064}$ . . . . .	154
5.9	Determination of 86 scattering length . . . . .	157
5.10	Comparison of $C_6$ coefficient estimates . . . . .	158
5.11	$^{86}\text{Sr}$ collision wavefunction . . . . .	160
5.12	Estimation of scattering lengths via mass scaling . . . . .	161
6.1	1D band structure as a function of lattice depth . . . . .	169
6.2	Lattice optical schematic . . . . .	172
6.3	Lattice Arm A profile . . . . .	173
6.4	Lattice Arm B profile . . . . .	173
6.5	Lattice Arm C profile . . . . .	174
6.6	Center-of-mass amplitude suppression when overlapping traps . . . .	176
6.7	Observation of breathing mode oscillation . . . . .	177
6.8	Evolution of plane wave population using Kapitza-Dirac . . . . .	180
6.9	Oscillation period between $n = 0 \rightarrow n = 2$ band at $q = 0$ . . . . .	180
6.10	Lattice depth calibration . . . . .	181
6.11	Characterization of heating in the optical lattice . . . . .	184
6.12	$^{87}\text{Sr}$ $^1S_0 \rightarrow ^3P_1$ hyperfine structure . . . . .	186

A.1	2D Surface plot of the relative collision likelihood . . . . .	209
A.2	Behavior of $G(\epsilon, \eta)$ vs. collision energy . . . . .	209
A.3	Behavior of $G(\epsilon, \eta)$ vs. $\eta$ . . . . .	210

## Tables

2.1	Sample trapping performance of $^{84}\text{Sr}$ . . . . .	13
2.2	Sample trapping performance of $^{86}\text{Sr}$ . . . . .	13
2.3	Sample trapping performance of $^{88}\text{Sr}$ . . . . .	14
2.4	Example trapping performance of $^{87}\text{Sr}$ . . . . .	14
2.5	461 nm system AOM details . . . . .	26
2.6	689 nm system AOM details . . . . .	42
2.7	Arbitrary waveform generation details . . . . .	77
6.1	Lattice optics details . . . . .	171

# Chapter 1

## Introduction

The ability to engineer and manipulate quantum states lies at the heart of modern atomic physics experiments using ultracold gases [14, 52, 61? ? ? ]. Two important tools for this pursuit are Feshbach resonances [17, 50] and optical lattices [? ]. This proposal will detail our recent work building and characterizing a three-dimension optical lattice for use with ultracold and quantum degenerate gases of neutral strontium. Furthermore, we will present the first experiment we hope to pursue with the optical lattice; the creation of Feshbach molecules using an optical Feshbach resonance. We will also briefly discuss other future plans such as the production of highly excited ground state  $\text{Sr}_2$  dimers through adiabatic internal state transfer.

Should probably mention somewhere that this is long-range PA, in contrast to short-range stuff being explored now.

Julienne form of the corss section 6.16 in CM. Discuss how important the phase space density is, the timescale for interactions, and the complex PA favors physicist molecules

PA can come in many forms (in a lattice, in a bulk gas, via dissociating molecules) Experimentally we observe PA by looking for trap loss [doublon paper](#). There are multiple flavors of PAS. Can do one-photon or two-photon. study of simplest molecules

[1]

## 1.1 Few-body physics

field of photoassociation in ultracold gases, wherein studies of molecular structure have revealed the most accurate descriptions of atomic interactions and have become a fundamental probe of the ultracold toolbox [42].

Pioneering work done in the early 90's used PA to interrogate the structure of interatomic potentials to deduce the scattering lengths between atoms.

a photoassociation experiment can be used to map the square of the scattering wave function in the ground electronic state at the Condon points corresponding to the different excited bound levels. [11]

rabi oscillations between atomic and molecular condensates (cite ours and the lattice experiment that followed)

short-range PA This work is focused on long-range PA but in recent years groups have also developed short-range PA techniques for the creation of rovibrational ground state molecules. These techniques rely heavily on favorable overlap integrals between molecular wavefunctions and typically searching for favorable intermediate states is a pain (that is why our large FCF might be useful)

Most of what we know about quantum mechanics comes from either scattering experiments or spectroscopy.

## 1.2 Halo molecules

Mostly studied in helium

Comes from bound state of the dirac potential. Unsure how much detail I want right here

Check out CM Juleinne pg 229. He has a ref

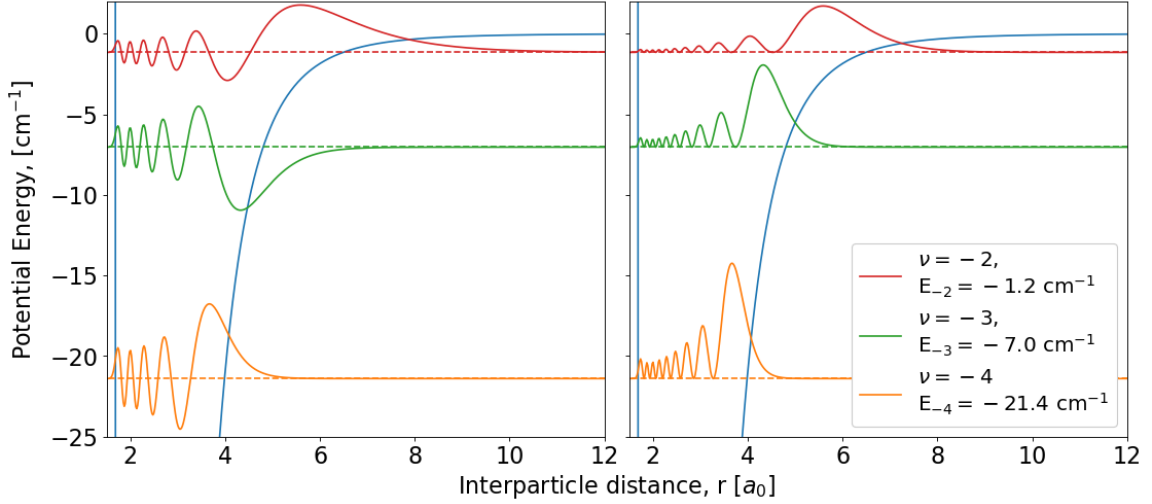


Figure 1.1 : Example bound states

Understanding the potential is hard weakly bound dimers probe the long range part of potential halo dimers especially are

Weakly bound ground-state dimers are of great interest in ultracold atomic and molecular physics.

In the extreme case of a scattering resonance, the least-bound state represents an example of a quantum halo system [40] with spatial extent well into the classically forbidden region.

Halo molecules show universality, meaning that molecular properties such as size and binding energy can be parameterized by a single quantity, the *s*-wave scattering length  $a$ , independent of other details of the atom-pair interaction [12? ].

For potentials that asymptote to a van-der-Waals form, an additional parameter, the van der Waals length  $l_{\text{vdW}}$ , can be introduced for a more accurate description.

Efimov trimers also exist in systems near a scattering resonance, influencing dimer and atomic scattering properties and introducing additional universal phenomena

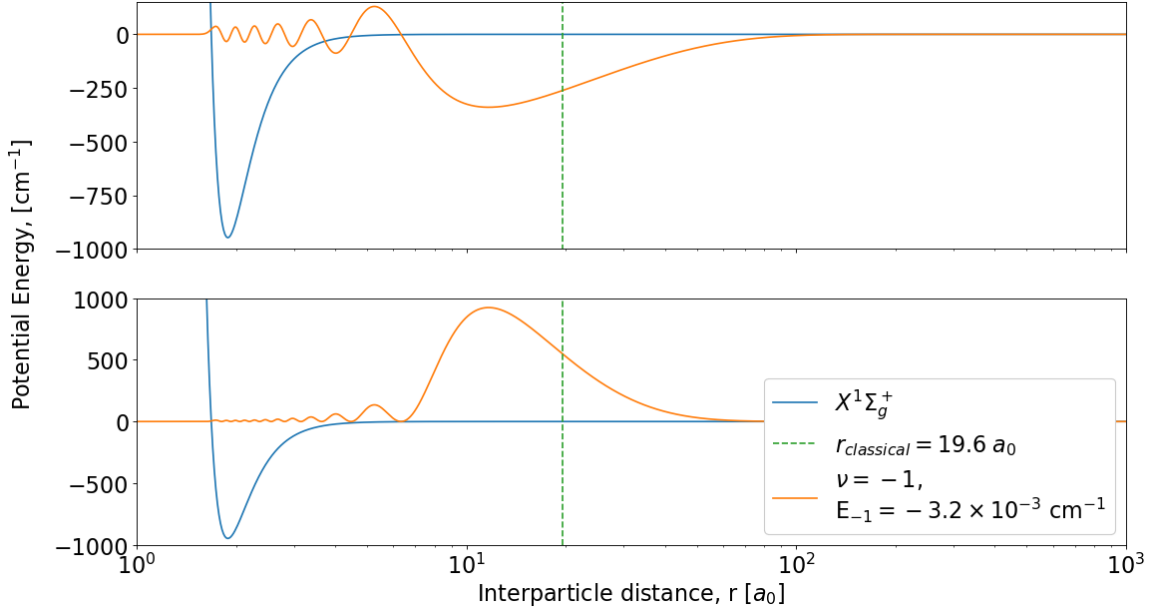


Figure 1.2 : Example halo state

[13, 68].

Ultracold halo molecules are often associated with magnetic Feshbach resonances [? ], for which the scattering state and a bound molecular state can be brought near resonance by tuning a magnetic field.

This is a naturally occurring halo molecule, meaning it exists in the absence of tuning with a magnetic Feshbach resonance. A well-known example of a naturally occurring halo molecule is the  ${}^4\text{He}_2$  dimer [55, 75? ]. Moreover, the least-bound vibrational level of the ground state of  ${}^{40}\text{Ca}_2$ , which was recently studied using similar methods [71], is similarly related to this regime.

There are important differences between halo molecules associated with magnetic Feshbach resonances and the naturally occurring halo molecule in  ${}^{86}\text{Sr}$ . With magnetic Feshbach resonances, the relevant scattering and bound molecular states lie on

different molecular potentials, and single-photon magnetic-dipole transitions can be used to measure molecular binding energies with RF or microwave spectroscopy [18? ? ]. Typically, this is done by first forming molecules through magneto-association and then driving bound-free or bound-bound transitions converting the halo molecule into a different state. Other methods include spectroscopy with an oscillating magnetic field [? ], a modulated optically controlled Feshbach resonance [21], and Ramsey-type measurements of atom-molecule oscillation frequencies [22]. It is also possible to efficiently populate halo states with a magnetic-field sweep [30] or evaporative cooling [41] near a magnetic Feshbach resonance [? ]. These are powerful techniques for manipulating quantum gases of alkali metals and other open-shell atoms, for which there are many magnetic Feshbach resonances. Strontium, however, due to its closed-shell electronic structure, lacks magnetic Feshbach resonances in the electronic ground state.

### 1.3 Properties of strontium

Therefore, photoassociation relative to the narrow 1S0 to 3P1 transition in Sr can be performed with precisions on the order of kHz. Previous narrow line photoassociation spectroscopy (PAS) has been performed in 88Sr [40, 43], 86Sr [177], and in 84Sr [50]. In addition, two-color photoassociation of the 1S0 to 3P1 line in 88Sr was used to measure the scattering lengths of all the strontium isotopes [42] and several subradiant 1g states have been probed in 88Sr [178]. The ground [96, 179] and excited [180] state molecular potentials have also been explored by Fourier transform spectroscopy. In addition to probing the shapes of the molecular potentials, photoassociation efforts are motivated by interest in creating ground-state molecules. Ground state molecules have been proposed as a platform for precision measurements, for example to study

deviations of the proton-electron mass ratio [181, 182], and/or the fine structure constant [183]. The production of ground state molecules has been demonstrated by decay from excited- molecular states in  $^{88}\text{Sr}$  [51] and by using stimulated Raman adiabatic passage (STIRAP) in  $^{84}\text{Sr}$  [50,52,184]. In particular, the technique in [184] may offer a path towards creating a molecular BEC. 173, 180

The experiments in this proposal will be realized using an ultracold gas of atomic strontium. Fig. ?? shows all of the stable isotopes of strontium, their natural abundance, as well as their inter-particle scattering lengths. The isotopic differences in strontium have important implications for their use in certain experiments. For example, none of the bosonic isotopes of strontium ( $^{88}\text{Sr}$ ,  $^{86}\text{Sr}$ , or  $^{84}\text{Sr}$ ) display hyperfine structure since they have no nuclear spin,  $\mathbf{I} = 0$ . However, the fermionic isotope  $^{87}\text{Sr}$  has a large nuclear spin,  $\mathbf{I} = 9/2$ , which makes it an ideal candidate for exploring exotic phases of quantum magnetism [6, 16? ]. In the studies presented in this proposal, we are sensitive to the isotopic shifts of the bosonic photoassociation lines along the  $^1S_0 \rightarrow ^3P_1$  transition as well as the various interspecies scattering lengths.

## 1.4 Thesis Outline

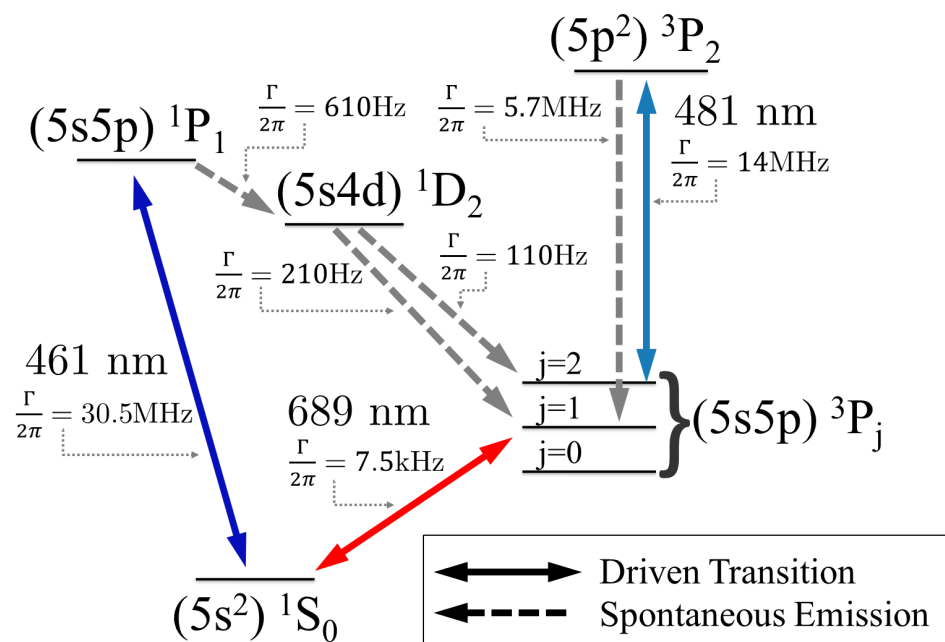


Figure 1.3 : Partial energy level diagram of strontium

Shown are the relevant transitions and decay rates utilized to perform laser cooling and spectroscopy.

## Chapter 2

### The Neutral apparatus

The Neutral apparatus has been one of the pioneering experiments for the trapping, cooling, and creation of quantum degenerate gases of neutral strontium BEC refs. As such, there is a plethora of previous theses and publications that explain how to achieve these goals. refs. In particular, we refer the reader to the PhD theses of previous Killian lab students: Francisco Camargo, Brian DeSalvo, Mi Yan, Pascal Mickelson, Natali Martinez de Escobar, and Sarah Nagel. Additionally, the PhD work of Simon Stellmer [77] and review of strontium quantum degenerate gases are also highly recommended reading [78].

Building upon this previous work, this chapter will forego an extensive review of the laser cooling techniques for strontium. Instead, we will focus on the systems and processes that are crucial to the operation of the experiment with an emphasis on technical findings and recent changes.

We will begin with a brief overview of our trapping procedure in order to contextualize the remaining sections focusing on the hardware including the vacuum system, various laser systems, and experimental control software, hardware, and electronics.

#### 2.1 Experimental procedure

Experiments begin by cooling and trapping atomic strontium utilizing well-established atomic physics techniques [8, 25, 35, 38, 47, 54, 57, 65, 67, 79, 80, 84]. Fig. 1.3 shows

the simplified energy level diagram employed in our cooling process. The majority of cooling is done using 461 nm light acting on the strong  $5s^2 \ ^1S_0 \rightarrow 5s5p \ ^1P_1$  transition. The excited state lifetime of 5 ns ( $\Gamma = 1.9 \times 10^8 \text{ s}^{-1}$ ) and large energy separation between the states results in a hefty saturation intensity of  $40.5 \text{ mW/cm}^2$  for this transition. Therefore laser powers on the order of 100 mW are necessary to produce large optical forces and rapid cooling rates. Once cooled, we typically obtain bulk samples in an optical dipole trap containing on the order of  $10^6$  atoms at temperatures  $< 1\mu\text{K}$  and densities between  $10^{12} - 10^{15} \text{ cm}^{-3}$  depending upon the isotope.

The procedure outlined below is generally followed for trapping all isotopes of strontium with the major difference being timescales and laser frequencies. Trapping of the bosonic isotopes of strontium is nearly identical across isotopes while fermionic  $^{87}\text{Sr}$  presents a greater challenge due to its high nuclear spin,  $I = 9/2$ . For a thorough and detailed discussion of the relevant physics of trapping  $^{87}\text{Sr}$ , we refer the interested reader to the fermion portion of section 2.7.3 in the PhD thesis of Simon Stellmer [77] and section 2.2.1 of Pascal Mikelson's PhD thesis [64].

The trapping process begins with heating solid strontium in an oven to approximately 400 °C. The resulting strontium vapor escapes through collimating tubes to produce a partially collimated beam with a mean velocity of  $\sim 450 \text{ m/s}$  [60]. To aid in collimation, the atoms undergo a stage of transverse two dimensional optical molasses. We typically observe a  $7\times$  improvement in trapped atom number with the 2D collimator versus without.

Upon entering the magnetic field of the Zeeman slower, the highest velocity atoms begin to scatter photons from the Zeeman beam, which is red detuned from the  $^1S_0 \rightarrow ^3P_1$  transition by  $\sim 16\times$  the natural linewidth. Large detunings help to eliminate unwanted photon scattering from the Zeeman beam once atoms have been

sufficiently cooled and are accumulating in the MOT fields of the science chamber. After reducing the atoms velocity down to  $\sim 30$  m/s, the atoms exit the Zeeman slower, pass through a minimum in the magnetic field\*, and begin scattering photons in a 461 nm magneto-optical trap (MOT) also using the  $^1S_0 \rightarrow ^1P_1$  transition. Typically the MOT operates at a detuning of approximately  $-3\Gamma/2 \approx -45$  MHz, however, the optimal trapping frequency is slightly varied for each isotope using a tunable saturated absorption spectroscopy setup, described in Sec. 2.3.1.4.

The broad dipole allowed  $^1S_0 \rightarrow ^1P_1$  transition used for the MOT is not completely closed as shown in Fig. 1.3. The leak to the  $^3P_2$  state results in population of magnetically trappable low-field seeking  $m_j$  states. These atoms are trapped by the anti-Helmholtz field of the MOT and are dark to the 461 nm light natali refs [78, 79, 80, 65]. This allows us to take advantage of the long lifetime of the metastable  $^3P_2$  state and accumulate a large number of atoms which can then be repumped back down to the  $^1S_0$  ground state. The lifetime of the magnetic trap is typically limited by background pressure ( $\sim 15$  - 25s) and therefore the maximum number of atoms which can be held by the magnetic trap is much greater than in the MOT. On average, an atom will fall into the  $^3P_2$  state after scattering  $\approx 5 \times 10^4$  photons from the  $^1S_0 \rightarrow ^1P_1$  transition [23]. However, only 2 out of 5 of the magnetic sub-levels are trappable.

Repumping from the  $^3P_2$  state is achieved via a 481 nm transition along the

---

\*While the functioning of a Zeeman slower only relies on the magnitude of the B-field, the anti-Helmholtz MOT field and the decaying field outside of the Zeeman slower may lead to a local maximum or zero near the interface of the Zeeman and science chamber dependent on the orientation of the Zeeman B-field. The configuration used produces a zero, which gives 2 $\times$  more trapped atoms compared to the other possible configuration.

$(5s5p)^3P_2 \rightarrow (5p^2)^3P2$  transition for approximately 50ms. During the repumping exposure we continue to illuminate the cloud with 461 nm light but reduce the light intensity by an order of magnitude. We refer to this stage as the "cold" blue MOT and find that reduction of the intensity, while maintaining consistent laser detuning, significantly increases the transfer efficiency into the red MOT stage. <sup>†</sup>

Once the atoms have been returned to the ground state, we begin a second MOT stage using the narrow intercombination transition  $^1S_0 \rightarrow ^3P_1$  to cool below 1 mK. The  $(5s5p)^3P_1$  state has a reasonably long lifetime of  $21\ \mu s$  ( $\Gamma = 4.7 \times 10^3\ s^{-1}$ ). Thus the narrow line MOT operates in a different regime compared to typical dipole allowed MOTs. We replicate the behavior of a broad transition by frequency modulating the 689 nm light using voltage controlled RF sources coupled to the light via an acousto-optic modulator (AOM) during the initial stages of cooling. Additionally, the overall laser detuning, amplitude of modulation, and laser intensity begin at large values in order to trap the initially hotter atoms from the blue MOT stage. As cooling with the 689 nm light becomes increasingly effective, we dynamically vary these three parameters along with the magnetic field gradient in order to efficiently cool and compress the entire sample. Ultimately, the red MOT is reduced to single frequency operation near resonance at extremely low laser intensity to achieve final temperatures between  $1 - 2\ \mu K$  after 400 ms of cooling.

During the last 50 - 100 ms of the 689 MOT (typically during single frequency operation) we additionally overlap and load the high intensity 1064 nm optical dipole trap (ODT). The red MOT can then cool atoms into the typically  $10\ \mu K$  deep ODT

---

<sup>†</sup>We have explored ramping the laser intensity closer to atomic resonance as we expected reduced intensity at farther red-detuning to result in a weakened trapping force. However, we did not find any improvement with the added complexity of varying the blue laser frequency during this stage.

with transfer efficiencies as high as 75%. After loading, we subsequently extinguish the red MOT and allow a period ( $\sim$ 10 - 100 ms) of free evaporation for the sample to equilibrate in the ODT before beginning forced evaporative cooling to produce the final sample of ultracold or quantum degenerate gas.

The end of the evaporation typically marks the beginning of the experimental phase and the divergence of the protocol into the specific procedures necessary. These may include ramping or pulsing on lattice beams, exciting a collective mode, probing the gas with PAS laser, shelving, etc. After completing the experimental phase, we measure the cloud characteristics via absorption imaging along the  $^1S_0 \rightarrow ^1P_1$  transition. Typically absorption imaging follows a time-of-flight to measure both the atom number and temperature at the time of release. However, this is not strictly necessary and certain experiments may result in low atomic densities which are not amenable to a time-of-flight diagnostic due to their low optical depth.

### 2.1.1 Characteristic performance

Tables 2.1-2.4 outline sample trapping performance at various stages of the cooling procedure for each isotope. Note, that while we have recently demonstrated the ability to dual trap 84 and 87, full characterization and optimization of this process is currently the subject of investigation.

Date	Load Time [s]	Magnetic trap	BB Red MOT		SF Red MOT		ODT	
		Num. ( $\times 10^6$ )	Num. ( $\times 10^6$ )	Temp. [ $\mu\text{K}$ ]	Num. ( $\times 10^6$ )	Temp. [ $\mu\text{K}$ ]	Num. ( $\times 10^6$ )	Temp. [ $\mu\text{K}$ ]
1/18/16	5	–	–	–	3.5	1.7	2	1.4
	15	–	–	–	6	1.7	4.3	1.4
8/11/16	5	–	–	–	3.2	2.1	1.4	2.1
	15	–	–	–	7.6	2.1	3.3	1.9
3/15/18	5	–	2.2	4.5	2.2	1.8	1.6	1.5
	15	–	4	4.2	3.8	1.8	2.6	1.5
5/23/18	5	5.8	3.1	5.8	2.6	2.2	1.3	1.6
	15	13.3	5.5	8	4.5	2.3	2.3	1.6
8/3/18	5	–	3.3	5.1	2.8	1.7	–	–
	15	–	5.8	5.2	5.2	1.9	–	–

Table 2.1 : Sample trapping performance of  $^{84}\text{Sr}$ 

Each column shows the number of atoms and measured temperatures from time-of-flight (not applicable for the magnetic trap). The abbreviated column labels refer to the broadband (BB) and single frequency (SF) Red MOTs and ODT is the optical dipole trap.

Date	Load Time [s]	Magnetic trap	BB Red MOT		SF Red MOT		ODT	
		( $\times 10^6$ )	Num. ( $\times 10^6$ )	Temp. [ $\mu\text{K}$ ]	Num. ( $\times 10^6$ )	Temp. [ $\mu\text{K}$ ]	Num. ( $\times 10^6$ )	Temp. [ $\mu\text{K}$ ]
11/29/16	1	–	–	–	9.5	2	7.4	1.7
	3	–	–	–	23	2.5	15	2
1/20/17	1	–	–	–	5	1.7	4	1.6
	3	–	–	–	9.1	2	7.7	1.7
3/30/17	1	–	–	–	6.6	2	5	1.7
	3	–	–	–	12.8	2.7	9	1.9
11/15/18	1	7.9	9.7	4.7	7.3	3.4	6.1	3.5
	3	24	21.5	5.1	14.4	3.5	11.4	3.7

Table 2.2 : Sample trapping performance of  $^{86}\text{Sr}$

Date	Load Time [s]	Magnetic trap ( $\times 10^6$ )	BB Red MOT		SF Red MOT		ODT	
			Num. ( $\times 10^6$ )	Temp. [ $\mu\text{K}$ ]	Num. ( $\times 10^6$ )	Temp. [ $\mu\text{K}$ ]	Num. ( $\times 10^6$ )	Temp. [ $\mu\text{K}$ ]
6/14/17	0.5	–	–	–	3.2	1.6	–	–
	1.5	–	–	–	5	1.6	–	–
2/1/18	0.5	–	–	–	10	2.1	5	1.4
	1.5	–	–	–	19	2.2	6.5	1.4
2/12/18	0.5	25	–	–	–	–	–	–
	1.5	54.1	–	–	–	–	–	–

Table 2.3 : Sample trapping performance of  $^{88}\text{Sr}$ 

Date	Load Time [s]	Magnetic trap ( $\times 10^6$ )	BB Red MOT		SF Red MOT		ODT	
			Num. ( $\times 10^6$ )	Temp. [ $\mu\text{K}$ ]	Num. ( $\times 10^6$ )	Temp. [ $\mu\text{K}$ ]	Num. ( $\times 10^6$ )	Temp. [ $\mu\text{K}$ ]
8/15/17	5	–	–	–	0.7	3	0.22	1.7
	15	–	–	–	1.6	2.6	0.5	1.7
9/8/17	5	–	–	–	1	1.8	0.6	1.6
	15	–	–	–	1.8	1.6	1	1.4
	40	–	–	–	1.8	1.6	1.5	1.4
5/1/18	5	8	5.5	8.4	1.8	1.1	1.5	1.1
	15	17	10	11	2.6	1.2	2.2	1.2
12/13/18	5	15	10.3	8.1	2.65	2.3	1.8	2
	15	31	18.7	8.5	4	2.2	2.6	2.1
2/26/19	5	13	8.5	9.9	1.7	1.9	1.25	1.6
	15	21	12	12	2.5	2	–	–

Table 2.4 : Example trapping performance of  $^{87}\text{Sr}$

## 2.2 Vacuum system and atom source

### Overview

The Neutral apparatus is built around a custom stainless steel chamber positioned above the table to facilitate optical access. Typical pressures are in the ultrahigh vacuum regime,  $< 1 \times 10^{-10}$  torr. Details on the original construction can be found in Refs. [58, 64]. The master's of Francisco Camargo [15] outlines the construction of the similar Rydberg apparatus. This more recent apparatus has benefited from the many lessons learned during the early life of the Neutral experiment.

Figure 2.1 shows a complete overview of the assemblies that form the Neutral vacuum system. Figures 2.2 - 2.5 show various views of the atom source, 2D collimator, and cryo tower assemblies. Note the red markers and green arrows denote the positions of heater bands and thermo-couples respectively. For more information please see App. ??.

From right to left, the system starts with an oven source based around a custom nozzle design that uses a rod heater to vaporize elemental strontium. Next, there is a 6-way tee used for the optical molasses step that we refer to as the 2D collimator. From here atoms pass through a narrow differential pumping tube and into the entry port of the Zeeman slower where a majority of the laser cooling takes places as atoms traverse the one dimensional cooling stage. Following the Zeeman slower, atoms enter the science chamber where a plethora of lasers are used to manipulate and probe their behavior. Chief among these laser systems are the MOT beams and high intensity far off-resonant optical dipole traps used for the final stage of confinement. Lastly, the body of the science chamber is supported by the cryo tower which houses a titanium sublimation cartridge (model: Varian 916-0061 series) and is the entry point for the

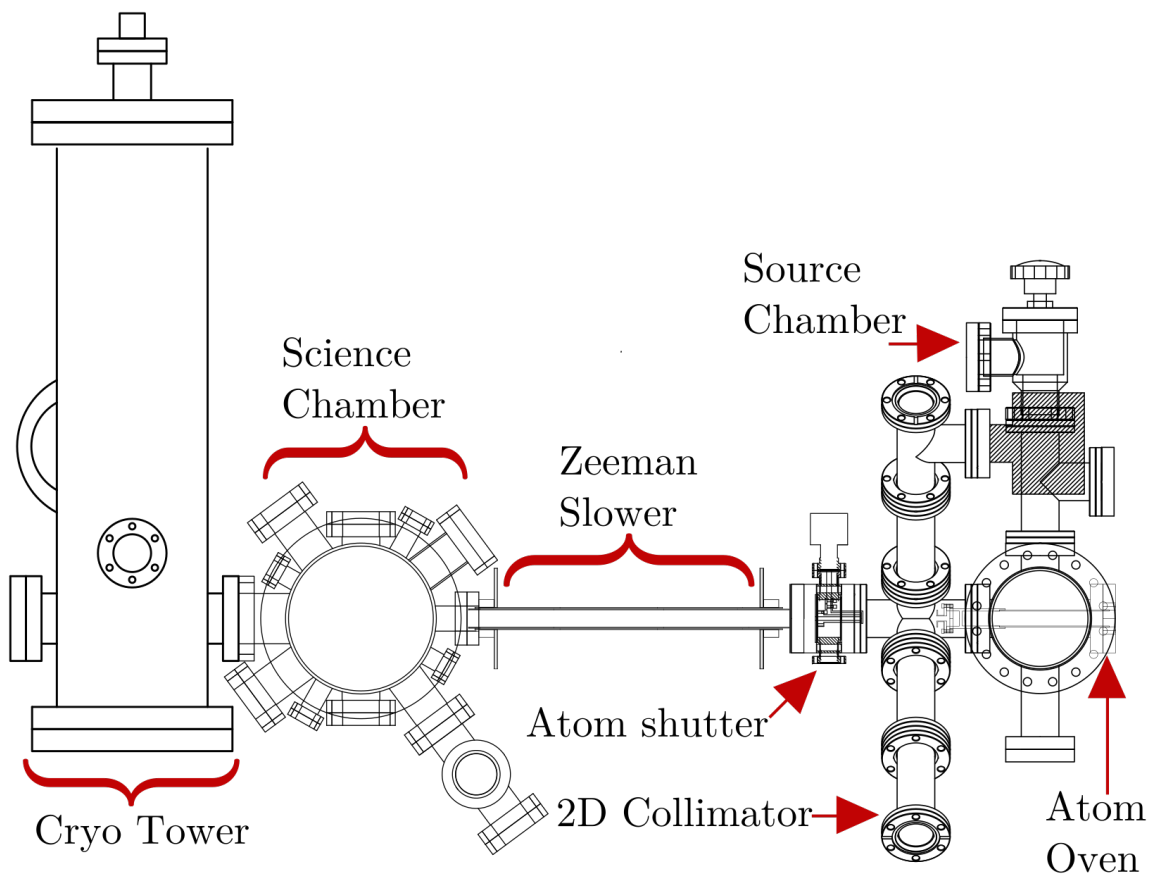


Figure 2.1 : Neutral apparatus vacuum system

Some components are rotated to provide easier identification.

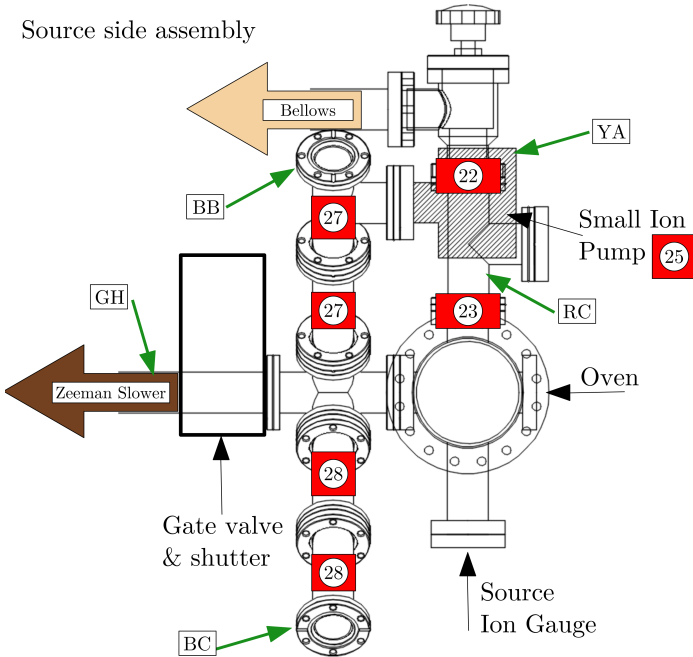


Figure 2.2 : Source assembly - side view

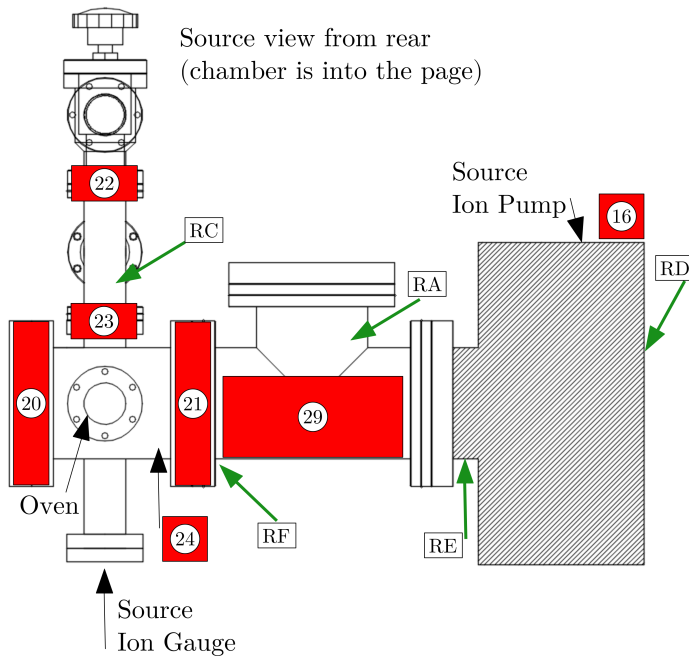


Figure 2.3 : Source assembly - rear view

2D Collimator view from rear  
(source is out of page and chamber is into page)

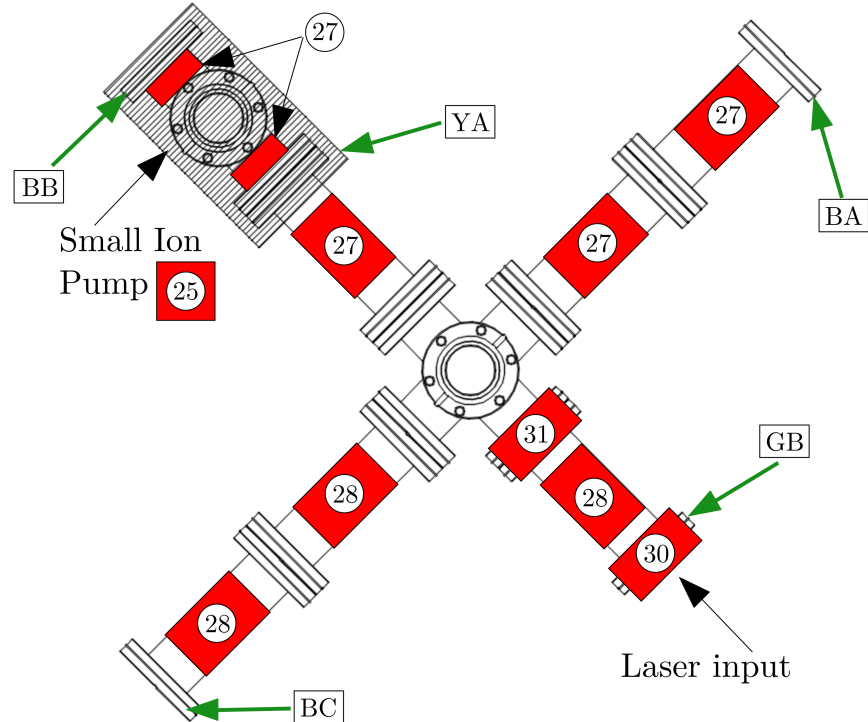


Figure 2.4 : 2D collimator assembly

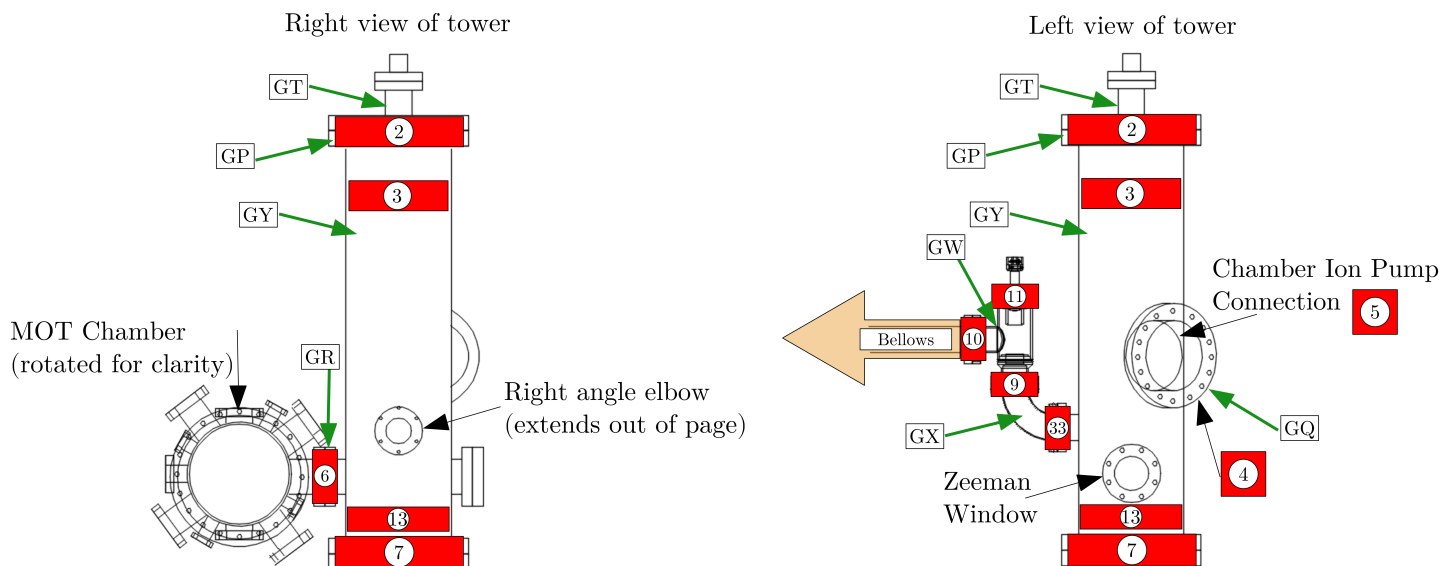


Figure 2.5 : Cryo tower assembly

Zeeman laser. It is worth explicitly noting that this Zeeman window is necessarily directly opposite the atomic source and therefore is subject to a flux of hot atomic strontium which will eventually coat the vacuum side. A brief note on a possible solution to this problem is explored at the end of this section.

While the source and science chamber have remained largely unchanged since the publication of Natali de Escobar's thesis, several key improvements and events have occurred over the last few years\*. The original drawings of these components can be found in App. A.10 of [58] along with detailed information on the window coatings.

### Recent changes

**Addition of platform:** While exploring routes to produce quantum degenerate gases of strontium, it was determined that different geometries of traps were necessary to achieve efficient forced evaporation. The task of redesigning the optical dipole traps was undertaken by Ying Huang and is detailed in her master's thesis [36]. As part of this project, a raised platform was designed and built around the chamber to facilitate beam shaping and launching of the ODT laser. Details of the platform are available in the main apparatus CAD drawing.

The raised platform has become the primary method for directing lasers into the chamber including the 1064 nm bulk optical dipole trap and the 532 nm optical lattice, both of which are outlined below. During installation of the free space optical lattice we observed heating and hypothesized that relative movement of the platform and

---

\*As of April 2019, the most up to date CAD drawing for the Neutral apparatus is located at KillianDrobo:\Neutral\Laboratory Systems\Vacuum Chamber\Neutral Chamber\2017.12.26\_strontiumvacuum35\_latticetable.dwg. Additionally, please consult the README file located in this folder for further information.

chamber may be a cause. Supporting struts were then added beneath the chamber in an attempt to secure it to the platform around 2016. However, the extreme sensitivity of cold atoms and occasional observation of shot to shot fluctuations persisted.

We observed increased stability with the addition of a partial cover over the platform optics for the optical dipole and lattice traps. Initially meant as an optical safety measure for enclosing the high power beams, the cover led to a marked decrease in shot to shot fluctuations of the cloud position after a time of flight. With further testing we were able to attribute the increased stability to a mitigation of air currents caused by close proximity of the platform optics to the ventilation system meant to reduce dust accumulation inside the experimental enclosure.

**Running out of strontium:** In the winter of 2017 the neutral apparatus had been under vacuum for  $\sim$ 8 years when abruptly we were no longer able to trap a significant number of atoms <sup>†</sup>. After extensive testing, we hypothesized that we had run out of elemental strontium within the atomic source. This led us to break vacuum, reload strontium, and perform a light bakeout procedure to reestablish the requisite ultrahigh vacuum for experiments. Details of this bakeout procedure can be found in App. ???. Through this process we confirmed our hypothesis that lack of strontium was the cause of the issue. Figure 2.6 shows the atom beam fluorescence after refilling the oven. This image was taken while using the Zeeman laser to cause photon scattering and looking down the 2D collimator. Prior to this event the Neutral apparatus enjoyed lifetimes of approximately 25 s as measured by background lifetimes measurements within the IR optical dipole trap. Approximately a year after restoring

---

<sup>†</sup>It is was expected any trapping loss due to low strontium would be gradual and we were not able to determine the cause of the sudden behavior.

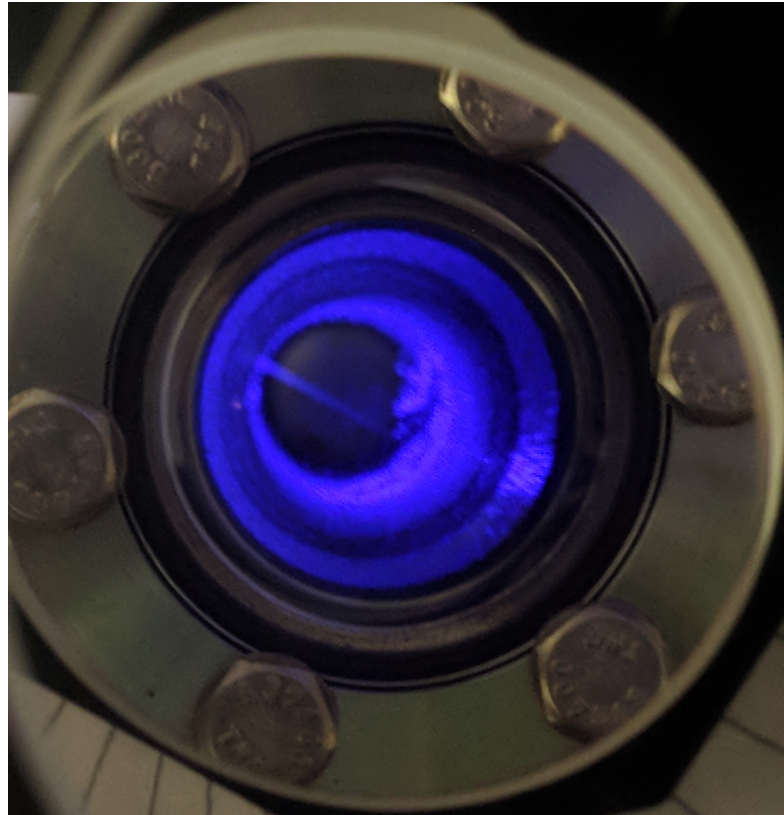


Figure 2.6 : Typical fluorescence of Zeeman beam looking down 2D collimator  
This view is found using a 2 in mirror aligned along the path of the first pass of the 2D collimator and looking down the collimator tube. While looking at this angle, we are able to see the Zeeman beam move across the atom column when moving the last turning mirror. Reduction in this fluorescence signal from that shown was the primary indicator of lack of strontium in the source.

vacuum we have measured lifetimes on the order of 15s. Details of the nozzle design can also be found in App. ?? along with potential future upgrades.

Finally, after removing the atom oven to replace strontium, we placed a temporary viewport to facilitate alignment of the Zeeman beam through the length of the vacuum system. While aligning we observed an unexpected partial occlusion of the Zeeman beam and upon further investigation learned that the differential pumping tube is noticeably not parallel to the atom trajectory. We were not able to determine the severity of the misalignment since the tube is not easily accessible and replacement is problematic as the tube is attached to a copper gasket held between flanges connecting the atom source chamber and the 6-way tee of the 2D collimator. The main readily measurable symptom is the occlusion of the Zeeman beam, which with an input power of  $\sim 120$  mW before expansion optics and entering the chamber, only measures  $\sim 60$  mW of transmitted power through the length of the vacuum system. However, full repair of the tube would necessitate a drastic and practically infeasible deconstruction of the vacuum system.

### Clarifications from Natali de Escobar's thesis

**HV version 1 & 2:** As a point of clarification, Natali de Escobar's thesis[58] presents two versions of the HV chamber in figures A.42 - A.47 while referencing that the original construction proceeded with version 1. However, version 2 (the cryo tower) was installed around 2011 and is currently in use. Version 2 is shown in Fig. 2.5 and details are available in the apparatus CAD drawing.

**Collimating array in nozzle:** Natali de Escobar's thesis refers to the installation of an improved nozzle design incorporating an array of collimating tubes con-

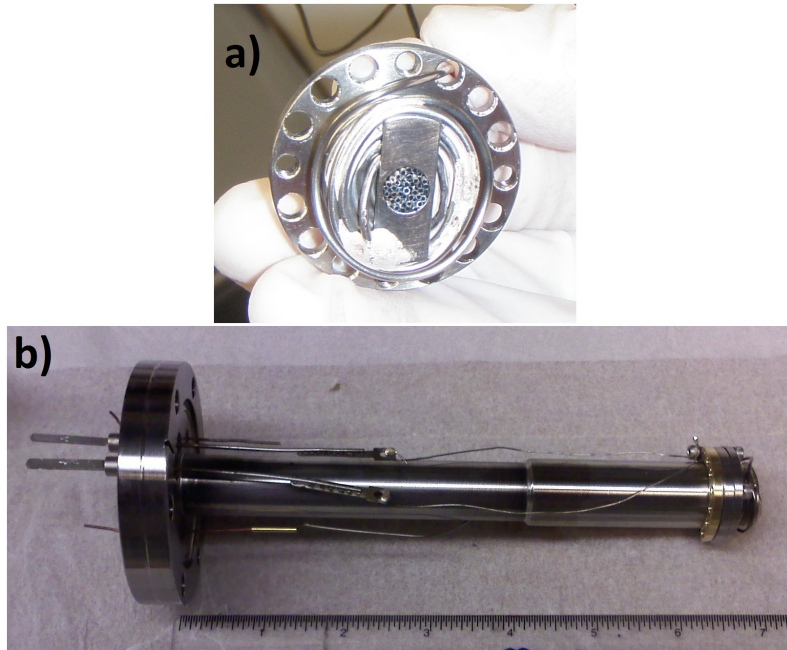


Figure 2.7 : Atom oven and nozzle construction

- a) The nozzle through which vaporized strontium enters the experiment. Here we see the array of collimating tubes behind which solid strontium is packed. b) The complete oven construction which houses the cartridge heater and the nozzle at the tip.

structed from  $2\mu\text{m}$  hypodermic needles. Modeling and construction of this design was done by Anton Mazurenko, [60], with the goal of improving the angular discrimination of the oven assembly to produce a better collimated beam of atoms. Figure 2.7 shows the improved nozzle design <sup>‡</sup>. The original assembly of this oven also incorporated a heat shield that would insert over the construction shown in Fig. 2.7b but this shield is not currently installed on the source oven.

---

<sup>‡</sup>For reference, this nozzle design is labeled "new nozzle summer 2010" in the apparatus CAD file to distinguish it from the other nozzle drawings also present.

## 2.3 Laser systems

The heart of any atomic physics experiment is the laser systems which form the basis for laser cooling and various probes. Our lab has transitioned to primarily using diode laser system and relies heavily upon the use of injection locked master - slave setups.

**ref** Below we will outline the specifics of our light generation setups.

### 2.3.1 Wideband cooling stage: 461 nm

#### 2.3.1.1 Overview

As discussed in the experimental overview, the majority of our laser cooling is done using 461 nm light. We generate and control these photons by amplifying and frequency doubling 922 nm light from a master ECDL diode laser. Fig. 2.8 shows an overview of how we generate and use the 461 nm light. We will explore each of these sections in detail below, with emphasis on the MOT subsystem since it is the basis for many different components of the overall 461 generation.

In conjunction with the block diagram, Table 2.5 shows the details of the frequency shifts and AOM details. The position of these AOMs is represented by the numbered grey squares, while the labeled red squares define the system frequencies at various points along the system. The primary frequency relations for trapping and imaging are schematically represented in the lower portion of Fig. 2.8 and are determined via Eq. 2.1. Table 2.5 defines the shift variables used in these equations.

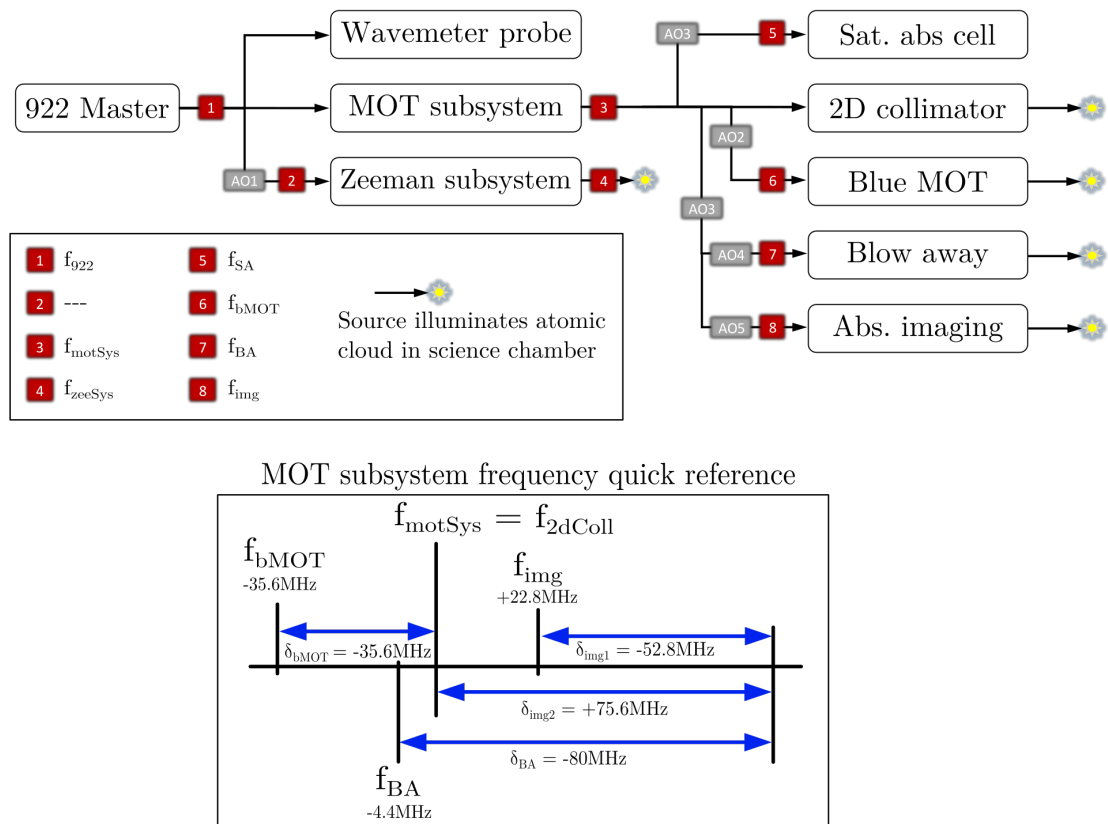


Figure 2.8 : 461 nm light generation system

Top - Block schematic showing the relations of the various systems, AOMs, and frequencies used to lock the system for 461 nm trapping and spectroscopy. Sat. abs. refers to the saturated absorption cell and abs. imaging refers to the absorption imaging system. See Table 2.5 for information on the AOMs. Bottom - Relative frequencies of the MOT subsystem at various stages of the 461 system. Frequencies are quoted with respect to  $f_{\text{motSys}}$  which in turn is controlled via the tunable saturated absorption cell to address different isotopes.

Label	Ind.	System	Shift variable	Nominal Freq. [MHz]	Freq. Source	Freq. control	AOM Model
Zeeman	AO1	922 master	$\delta_{\text{zeeman}}$	-252.4	Mini Circuits ZOS-300	Static voltage	Crystal Tech. 3200-1113
Blue MOT	AO2	MOT	$\delta_{\text{MOT}}$	-35.5	Mini Circuits ZOS-50	Static voltage	IntraAction AOM-402A1
Image 2	AO3	Abs. imaging & Blow away	$\delta_{\text{mrg2}}$	+75.6	Mini Circuits ZOS-75+	Static voltage	IntraAction ATM-1001A1
Image 1	AO4	Abs. imaging	$\delta_{\text{mrg1}}$	-52.8	Mini Circuits ZOS-150	Static voltage	IntraAction AOM-602A1
Blow away pulser	AO5	Blow away	$\delta_{B_A}$	-80	IntraAction ME-S01T7	Internal synth.	IntraAction ATM-802DA1
Sat. abs. shifter	AO6	Sat. abs	$\delta_{S_A}$	+317.3	Mini Circuits ZOS-400+	Static voltage	Crystal Tech. 3200-141

Table 2.5 : 461 nm system AOM details

Ind. column labels the AOMs as shown in Fig.2.8. The sign of the nominal frequency indicates the AOM order used.

$$\begin{aligned}
f_{\text{motSys}} &= 2f_{922} & f_{\text{zeeSys}} &= 2(f_{922} + \delta_{\text{zeeman}}) \\
f_{\text{2dColl}} &= f_{\text{motSys}} & f_{\text{bMOT}} &= f_{\text{motSys}} + \delta_{\text{bMOT}} \\
f_{\text{img}} &= f_{\text{motSys}} + \delta_{\text{img2}} + \delta_{\text{img1}} & f_{\text{SA}} &= f_{\text{motSys}} + \delta_{\text{SA}} \\
f_{\text{BA}} &= f_{\text{motSys}} + \delta_{\text{img2}} + \delta_{\text{BA}}
\end{aligned} \tag{2.1}$$

Overall frequency control,  $f_{922}$ , is determined via the magnetically tunable saturated absorption cell. The use of magnetic tunability to control the 461 nm light frequency is well documented in section 2.2.1 of Natali de Escobar's thesis [58] and section 2.1.1 of Pascal Mikelson's thesis [64]. A more recent undergraduate project also explored optimizations of this scheme for the Rydberg apparatus [63].

### 2.3.1.2 922 nm master

The master 922 laser is derived from a Sacher Lynx 922 nm IR diode laser in a Littrow ECDL configuration. Fig. 2.9, shows a simplified optical schematic of the master setup.

Starting at the master output, the beam is shaped and sent through two optical isolators before it is coupled into an optical fiber. The fiber output immediately goes through an AOM which detunes the diffracted order by approximately 250 MHz. The diffracted and zeroth order are then separated with the unshifted beam sent towards the MOT generation subsystem and the shifted light towards the Zeeman subsystem. We find it necessary to include dual isolators in front of the master laser and have found that inadequate alignment of these isolators can lead to significant instability in the frequency of the master, which in turn may lead the doubling cavities to be unable to maintain a lock.

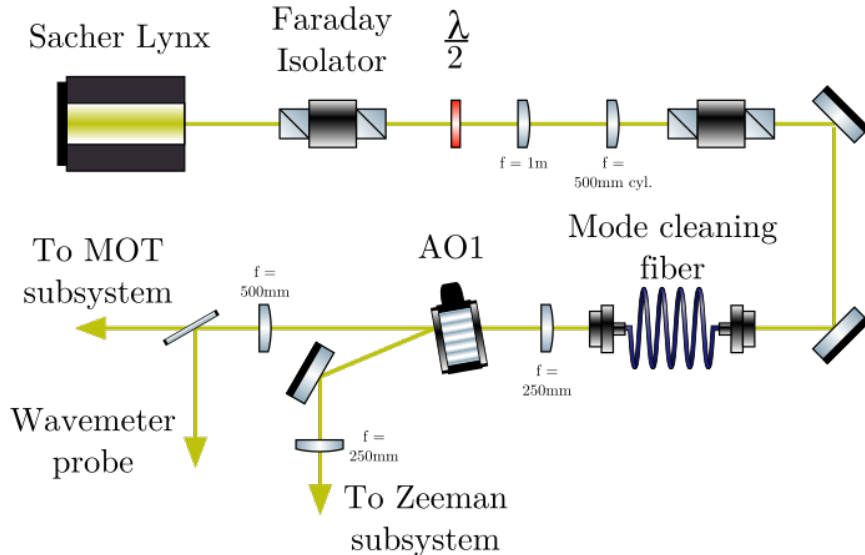


Figure 2.9 : 922 nm master optical schematic

Fig. 2.10 shows a simplified schematic of the negative feedback path for stabilizing the length of the doubling cavities. Light out of the 922 master has sidebands added via a high bandwidth AC coupled current modulation directly to the laser diode \*. The doubling cavities of the MOT and Zeeman subsystems are length stabilized via these sidebands using the Pound-Drever-Hall (PDH) technique refs. Currently, the reference oscillator RF source is a PTS 160 from Programmed Test Sources with an output power of 12 dbm and frequency of 39.55 MHz. This RF is sent to a 3-way power splitter which sends roughly a third of the power ( $\sim 4\text{ dbm}$ ) to each of the MOT and Zeeman PDH mixers for demodulation. The remaining third is attenuated by 3db before coupling directly to the laser diode.

---

\*This direct coupling means the RF must be turned on prior to enabling the DC current. Conversely, the DC current should be disabled before turning off the RF source. Failure to follow this order may result in destruction of the laser diode.

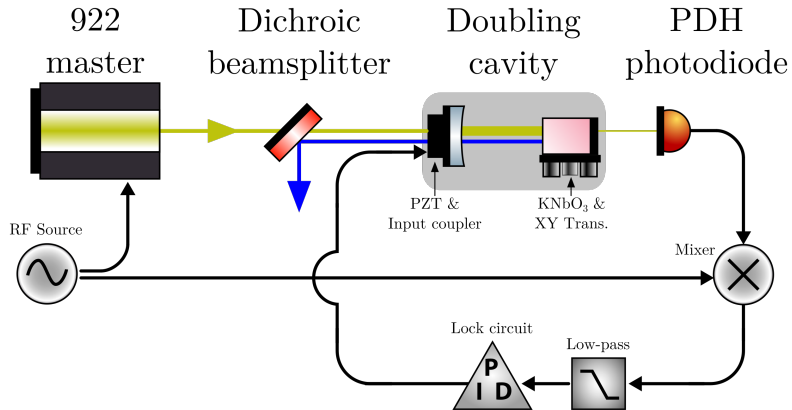


Figure 2.10 : 922 nm doubling cavity length stabilization feedback diagram

Once 461 nm light is available, we stabilize the frequency of the 922 nm master using light from the MOT subsystem to interrogate a strontium heat pipe via frequency modulated Doppler-free saturated absorption from which an error signal of the  $^1S_0 \rightarrow ^1P_1$  transition is derived. As shown in Fig. 2.11, this error signal is sent into a homemade integrator circuit with a fast feedback path controlling the 922 nm diode current and a super low-bandwidth<sup>†</sup> path controlling for long term frequency drifts via the ECDL's internal PZT. We found that addition of this super low-bandwidth lock has significantly improved the continuous lock time of the 461 system. When enabled, the experiment may stay locked for upwards of 24 hours at a time. Additional details on the original construction of the 922 nm system can be found in App. A.8 of Natali de Escobar's thesis [58].

---

<sup>†</sup>This super low-bandwidth lock is based on an Arduino PID controller with a long time constant and was built by Josh Hill. We refer the interested reader to Josh's forthcoming thesis for details of this general purpose slow lock.

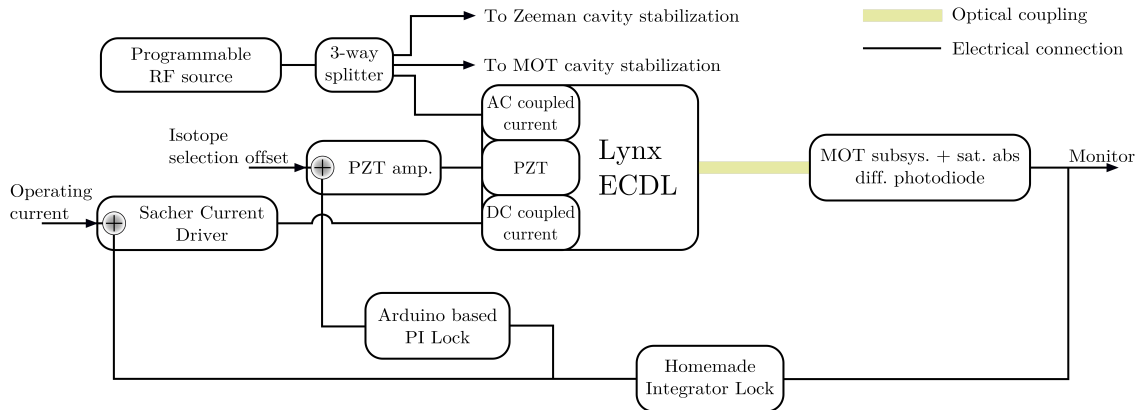


Figure 2.11 : 922 nm frequency stabilization block diagram

Multiple feedback paths allow for controlling the 922 master across disparate timescales. Note that the generation of the error signal used in the feedback is optically connected to the 922 master via the MOT subsystem and saturated absorption cell discussed in Sec. 2.3.1.4.

### Historical notes and tips for usage

**PZT driver and replacement:** The PZT driver provided by Sacher has become problematic over the last few years. When varying the voltage we would occasionally hear a "clicking" noise from the Lynx laser as if the voltage was abruptly changing. We began using a Thorlabs analog PZT driver (model: MDT694A) and no longer observe this behavior<sup>‡</sup>.

In early 2017, we found that the Lynx PZT was no longer responding to applied voltage. We believe this was caused by the aforementioned "clicking" issue and was

---

<sup>‡</sup>We attempted to use the newer Thorlabs MDT694B which incorporates a digital potentiometer instead of the analog pot of the "A" model. However, we found the resolution of the digitization caused the laser frequency to jump and we were unable to maintain the frequency lock.

the motivation for changing PZT drivers. Details and pictures of the PZT replacement are available in App. ??.

**Sacher temperature setpoint:** Care must be taken when attempting to change the set temperature of the laser diode as the internal potentiometer does not maintain full contact such that when attempting to turn it ever so slightly, the set point temperature may jump from  $\sim 16$  °C to 11 °C . Worse yet, we have observed that after changing the temperature there is a settling time during which the temperature setpoint may change while not be monitored. For these reasons we generally avoid touching this control as the present setpoint of 16.1 °C is adequate and no major improvements have been found when changing this temperature.

**Daily alignment:** The input coupler for the 922 cleanup fiber is not a reliable mount and tends to drift significantly from day-to-day. Therefore, we find it necessary to regularly peak up the alignment into this fiber and typically achieve a coupling efficiency of  $\sim 51\%$  through the 922 mode cleaning fiber.

### 2.3.1.3 Zeeman subsystem

The Zeeman subsystem is a dedicated TA + doubling cavity for 461 nm light exclusively used for the one-dimensional Zeeman cooling stage. The original construction details are available in App A.8 of Natali de Escobar's thesis [58]. Figure 2.12 shows a simplified optical schematic of this system. Light from the 922 master ( $\sim 20$  mW) is shaped and coupled into a tapered amplifier to produce nearly 300 mW of 922 nm light. After being shaped further and passed through dual isolators, the light is then coupled into the homemade doubling cavity where a potassium niobate crystal is held within an optical resonance cavity to produce the 461 nm light. For approximately

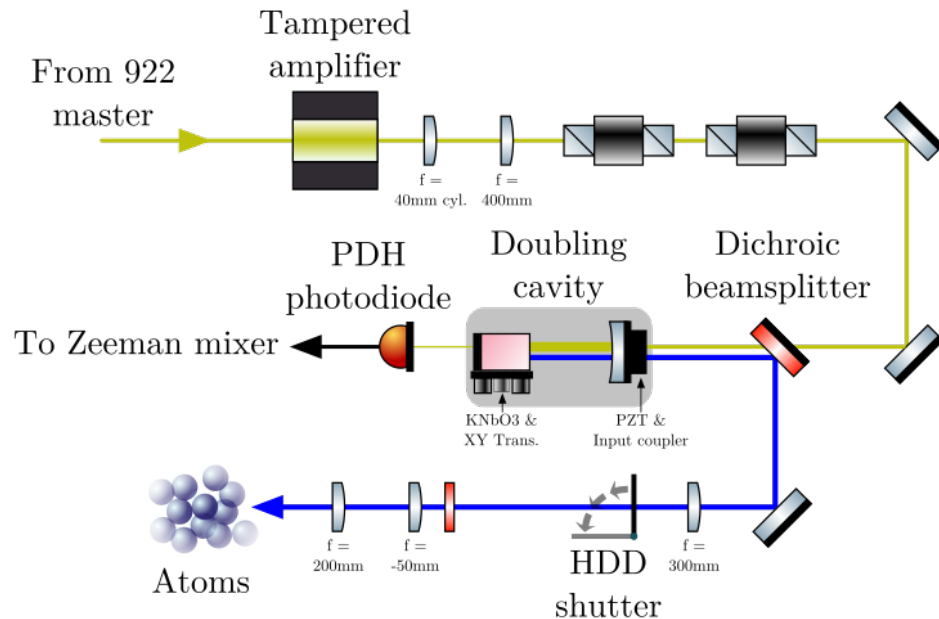


Figure 2.12 : Zeeman subsystem optical schematic

300 mW into the cavity we are able to produce  $\sim$ 125 mW of 461 nm light. This light is sent through a final beam expander and into the chamber where we have designed the system to focus the Zeeman beam just at the tip of the atom nozzle to maximize the spatial and temporal interaction between hot atoms and the Zeeman beam.

### Historical notes and tips for usage

**Mode instability:** Doubling cavities at short wavelengths are known to be mercurial [aaron refs](#) so stabilizing them can be difficult. We find that this cavity tends to become stable with  $\sim$ 300 mW of input power but increasing the power results in an initial cavity lock producing more 461 nm light but which quickly mode releases into a lower power mode. While we have seen cavity output powers of up to 150+ mW, these are not stable modes. Additionally, the locking circuit contains an auto re-

lock feature that can occasionally result in locking to a lower power mode, usually around  $\sim 80$  mW. We have found that power cycling the TA current driver is the least intrusive and quickest method to reattain the 125 mW output. If cycling does not work, then the TA current output may need to be adjusted or the cavity alignment tweaked.

#### 2.3.1.4 MOT subsystem

The MOT path generates light used for a multitude of processes as shown in Fig. 2.8. Here we detail the systems required for laser cooling and trapping, leaving the details of the blow away pulser and absorption imaging to be discussed in Sec. 2.3.4. Furthermore, we begin our discussion with a focus on the light generation of the MOT subsystem and next we will explore the child setups derived from this subsystem.

Fig. 2.13 shows a simplified optical schematic of the MOT subsystem which is modeled after the Zeeman setup described previously. Light from the 922 nm is shaped, amplified, and coupled into the doubling cavity where the same feedback mechanism shown in Fig. 2.10 is used to stabilize the cavity length. Since the MOT system is situated close to the experimental chamber, a "black-house" wall and shroud were constructed to minimize stray reflections (not shown in figure). This enclosure was placed around the MOT subsystem to mitigate stray 461 nm light which can significantly hinder the achievement of quantum degenerate strontium gases<sup>§</sup>. Part of this enclosure is a fast ( $\sim 2$  ms) shutter (model: Uniblitz CS45) used to block the 461 nm light during the red MOT and evaporation stages. Additional hard drive (HDD) shutters are also placed along the MOT path behind the black-house shutter

---

<sup>§</sup>Even stray reflected light off the glossy ceiling of the experimental enclosure has been found to cause atom heating!

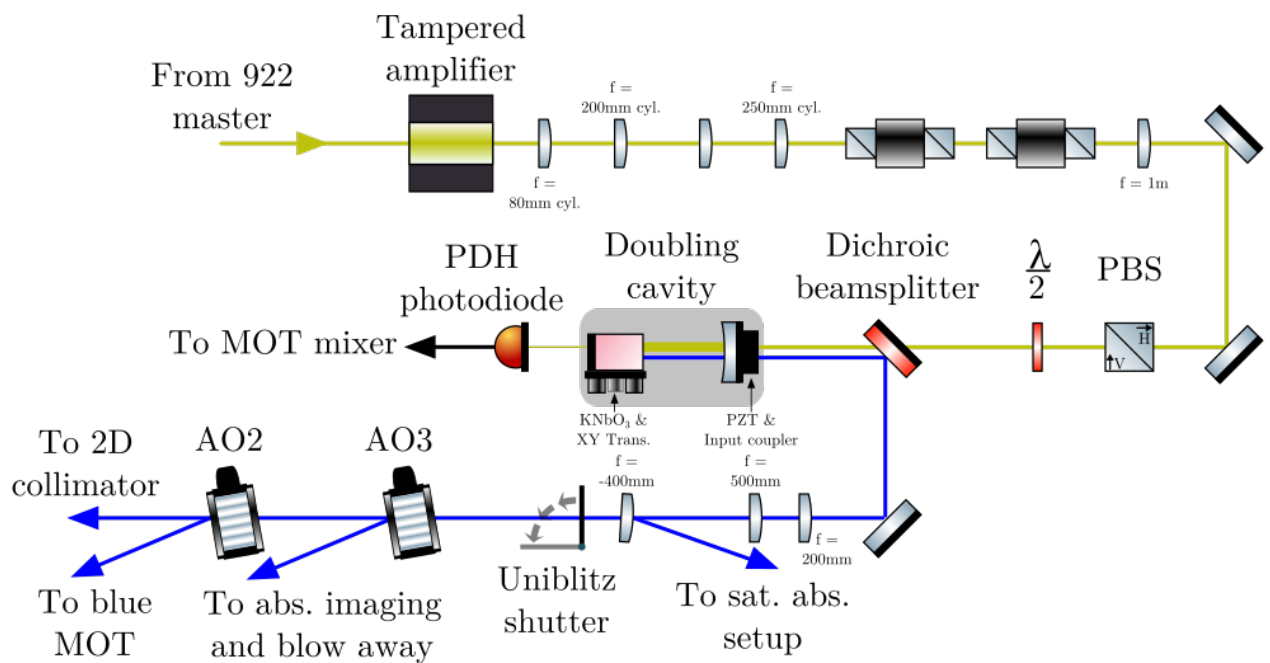


Figure 2.13 : MOT subsystem optical schematic

Note the sharing of power between the 2D collimator and blue MOT paths. While the blue MOT is power stabilized as shown in Fig. 2.14 the 2D collimator utilizes the remaining laser power.

as leakage light through the blue MOT AOM (AO2) was seen to cause additional heating when utilizing the blow away pulser.

One concern we face with this MOT setup is the coupling of power between the various paths. Typically we do not operate the imaging & blow away pulser while trapping so all available power from the doubling cavity is available for these processes. However, the 2D collimator and 461 nm MOT operate concurrently during the first stages of trapping, thus the available laser power must be split between these two systems.

## 461 nm MOT

Fig. 2.14 gives an overview of the 461 nm MOT optics<sup>¶</sup>. Separation of the laser beams is performed on the table level where custom dichroics are used to combine the 461 and 689 MOT paths. Following the dichroics, the MOT beams are directed up to the platform layer via periscopes and subsequently pass through dual wavelength waveplates which retard 461 nm light by three-quarters of a period and 689 nm by one-quarter. This setup allows us to maintain well defined polarization along the MOT paths.

## Saturated absorption

The saturated absorption cell is used to interrogate the  $^1S_0 \rightarrow ^1P_1$  transition to lock the frequency of the 922 master. App. ?? outlines a brief derivation for determining the lock point when a constant offset is added to the laser frequency, as is the case here. As outlined in the derivation, by utilizing the Zeeman tunability of magnetic

---

<sup>¶</sup>The MOT arms are labeled as they are organized on the table, where Arm B is closest to the "computer side" of the table.

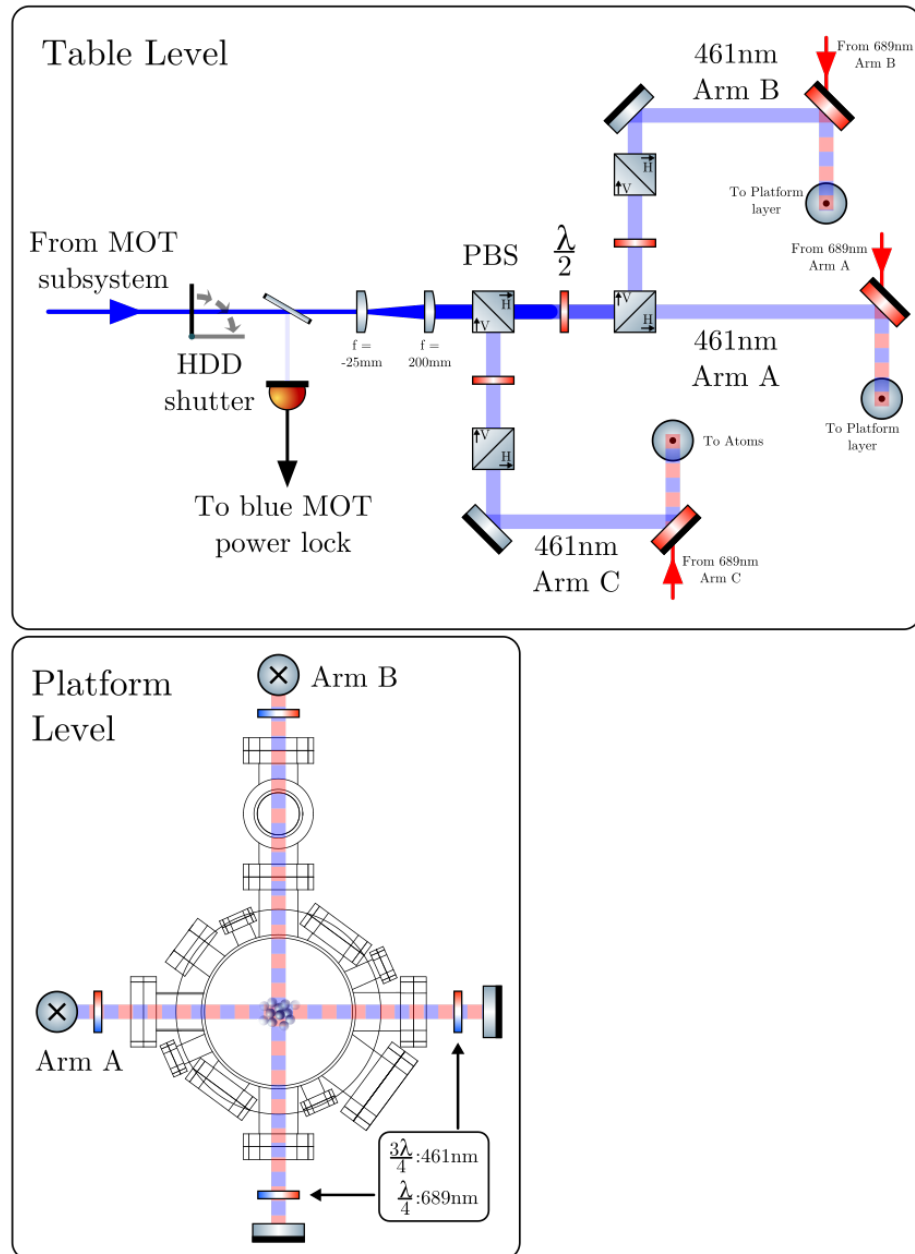


Figure 2.14 : 461 nm MOT schematic

Typical MOT setup with an additional HDD shutter to mitigate light leakage from AO2. Transparency of the laser beams represents the intensity. Note the 461 nm and 689 nm light follow the same path through the science chamber. Custom waveplates acting on both wavelengths are used to provide the appropriate polarization.

sublevels, we can shift the resonance frequency of the atoms in the heat pipe. Thus, by interrogating and locking to the transition frequency of the most abundant isotope,  $^{88}\text{Sr}$ , we can shift its resonance to cover the isotope shifts of the other strontium isotopes. This provides a simple method for trapping various isotopes and mixtures of strontium.

A detailed walkthrough of the construction and relevant physics of a blue saturated absorption cell can be found in the undergraduate report of Michael Viray [63]. Additionally, the original construction of the Neutral cell is covered in section 2.2.1 of Natali de Escobar's thesis. Fig. 2.15 shows the optical setup used to generate the error signal and reference traces of Doppler bowl and frequency lock error signal. This error signal is generated by frequency modulating the magnetic field of the cell and performing Doppler-free saturated absorption.

### **Historical notes and tips for usage**

**Daily alignment of MOT TA:** The simplified optical schematic of the MOT subsystem in Fig. 2.13, does not reflect the approximately two meter lever arm which is present between the Zeeman split AOM and the input to the MOT TA due to the relative positions of the cavities. We have found this requires us to peak up the alignment of the 922 master beam into the MOT TA on a daily basis and is hypothesized to be the cause of large long time power variations ( $\sim 15\%$ ) on the output power of the MOT cavity which we observe throughout the course of the day. Typically with an input power of  $\sim 300$  mW of 922 nm light we get between 100 - 115 mW out on a daily basis.

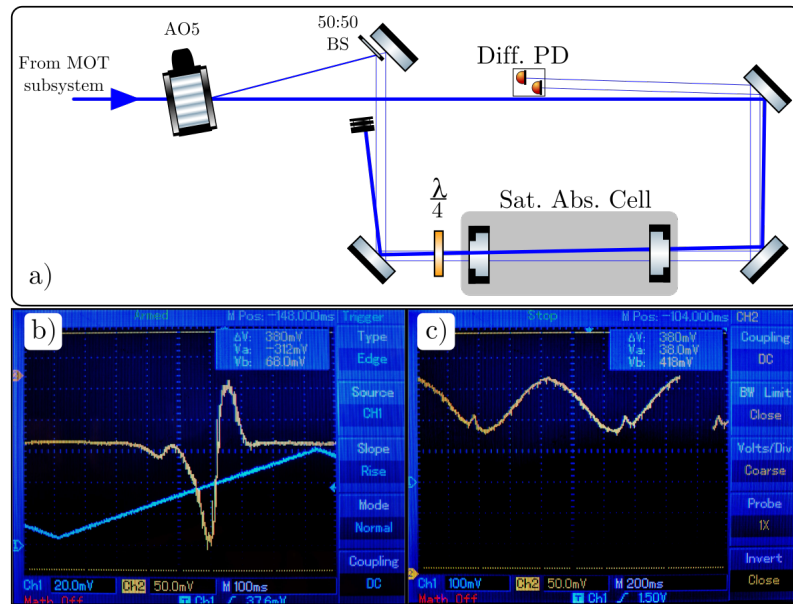


Figure 2.15 : 461 nm saturated absorption setup

a) Optical setup for frequency locking the 922 nm master. b) Example error signal. The cause of the asymmetry is unknown but occurs around approximately  $\pm 1.7\text{A}$  drive. The offset seen here can be nulled by balancing the amplification applied to the differential photodiode inputs. c) Example of the Doppler bowl where the Lamb dip can be seen. Note that the Lamb dip interacts with a specific velocity class determined by  $\delta_{SA}$ .

**Note on changing isotopes:** While the basic setup of the saturated absorption cell has not changed over the many years, we have recently moved away from the original current source based on a home built high-current FET amplifier to a Bi-polar current source (BOP) (model: Kepco BOP-20-10DL). This change allows for more expansive coverage of the  $^1S_0 \rightarrow ^1P_1$  isotopes shifts. The previous current source limited our dual trapping capability to 87+88, and required an AOM to be tweaked and the saturated absorption cell to be realigned for trapping 84 and 86. Using the BOP, we can now easily shift the transition frequency over  $\sim 200$  MHz which allows us to span the range between 84 and 87 within a single experimental cycle. Given the geometry of our solenoid, large currents are required to apply such large Zeeman shifts. We have observed that these large currents increase the heat load on the cell, which can lead to a reduction in the error signal. We mitigate this additional heating by varying the heater current to maintain approximately 50% absorption of the pump beam. As we expect, the timescale for these effects are minutes, so short term variations (i.e. when doing spectroscopy) do not cause significant heating when the duty cycle is kept low.

Due to the heating from the Zeeman coil, we chose to balance the currents needed to trap 84 and 87 by "centering" the pump-probe beams frequency such that the magnitude of the currents needed for both isotopes is similar, but with 84 requiring a (+) current and 87 a (-) current. However, trapping of 88 still requires the realignment of the saturated absorption cell pump-probe beams as this shift is just beyond the capabilities of the current drive. Care should be taken when adjusting this alignment as the paths are highly coupled as can be seen in Fig. 2.15a.

### 2.3.2 Narrowband cooling stage: 689 nm

#### 2.3.2.1 Overview

Arguably the most important transition for strontium is the  $^1S_0 \rightarrow ^3P_1$  intercombination line transition at 689 nm. In addition to cooling and trapping, most experiments performed in our lab utilize this transition as the primary spectroscopic probe owing to the long lifetime of the excited states. This allows for high precision measurements and large detunings using conventional techniques. This section describes the generation and trapping setups in use on the Neutral apparatus. The primary spectroscopy probe system and spin manipulation setup are outlined in section 2.3.4.

Recently, the 689 nm generation system has seen significant growth and undergone a complete restructuring. For notes on the original Neutral setup refer to App A.3 & A.4 in Natali de Escobar's thesis. Most notably, the master laser system is now shared between multiple laboratories including the Rydberg apparatus, the Dunning lab, and the Neutral apparatus. This setup has required a modular approach to the master 689 nm system to ensure independence of the various lab activities.

Fig. 2.16 shows a block diagram outlining the relationships between the master laser setup and various Neutral systems which utilize this stable light source. In conjunction with the block diagram, Table 2.6 details the frequency shifts and AOMs in use. The block diagram denotes the position of AOMs by the grey squares and the red squares denote system frequencies determined by the various shifts. Lastly, the frequency axis beneath the block diagram illustrates the relative frequencies at various points of the complete red system specified with respect to the  $^{88}\text{Sr} \ ^1S_0 \rightarrow ^3P_1$  transition and shown along with the isotope shifts of the same transition.

The versatility of the 689 nm transition is apparent from Fig. 2.16 but comes at

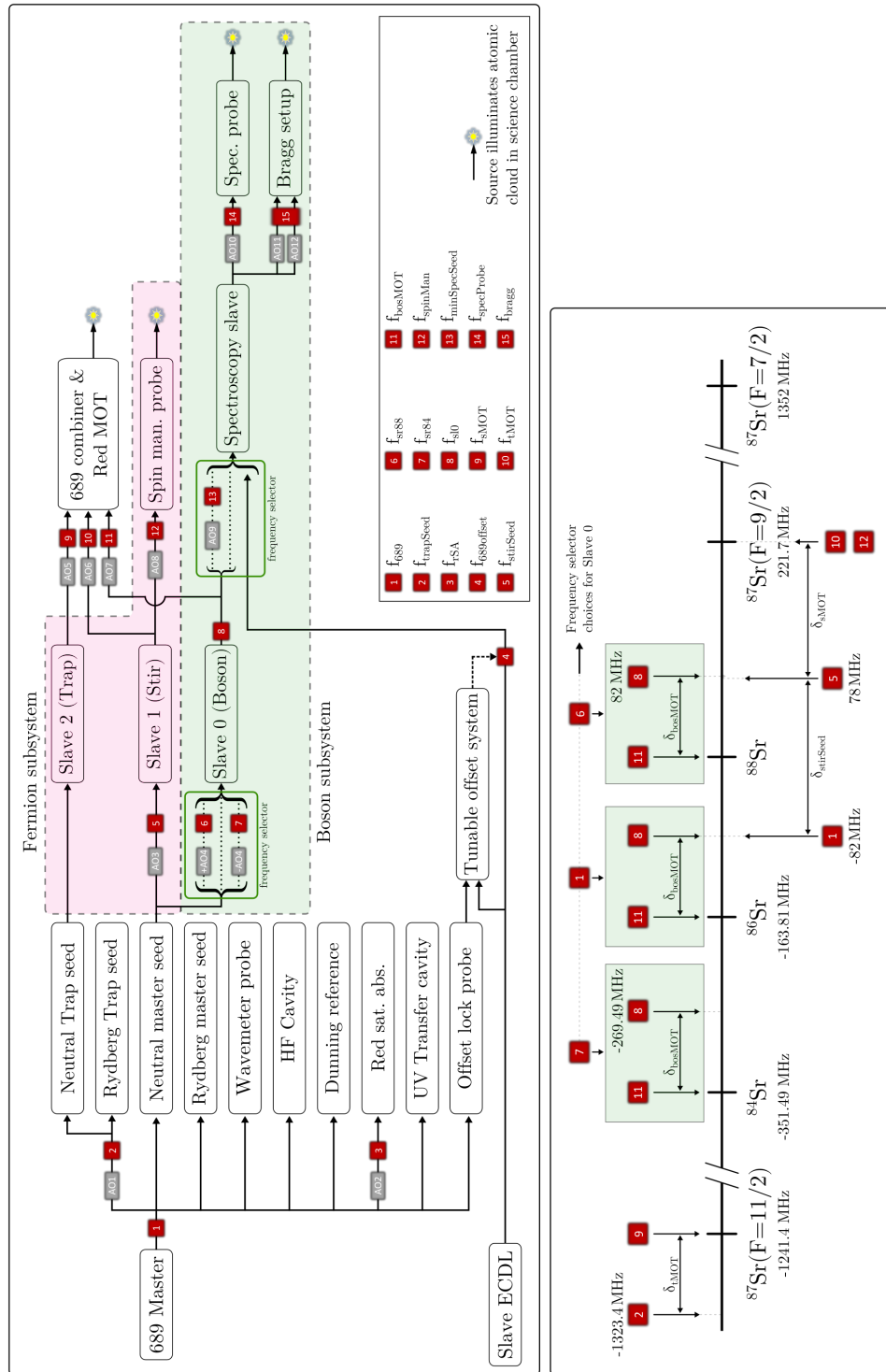


Figure 2.16 : 689 nm light generation system

Top - Block diagram showing various systems, AOMs, and the frequencies of red system. Table 2.6 gives further details on the AOMs. Bottom - Relevant isotopic shifts and system frequencies given relative to  $^{88}\text{Sr}$  intercombination transition.

Label	Ind.	Shift variable	Nominal Freq. [MHz]	Freq. Source	AOM Model
Trap Seed	AO1	$\delta_{trapSeed}$	-1241.44	Novasource G6	Brimrose TEF-1300-200-550
Red Sat. Abs.	AO2	$\delta_{rSA}$	+164±0.5	Novatech 409B (Dithered)	IntraAction ATM-1643DA1
Stir Seed	AO3	$\delta_{stirSeed}$	+160	Novatech 409B	IntraAction ATM-1602DA1
Boson isotope Selector	AO4	$\delta_{isoSel}$	+164 or -187.49	Novatech 409B	IntraAction ATM-2001A2
Trap MOT	AO5	$\delta_{tMOT}$	+82	Trap VCO / Novatech 409B	IntraAction ATM-852DA2
Stir MOT	AO6	$\delta_{sMOT}$	+143.7	Stir VCO / Novatech 409B	IntraAction ATM-1402DA1
Boson MOT	AO7	$\delta_{bosMOT}$	-82	Boson VCO / Novatech 409B	Isomet 1205C-2
Spin man. probe	AO8	$\delta_{spinProbe}$	-144±2	Novatech 409B	IntraAction ATM-1402DA1
Spec. slave seed	AO9	$\delta_{specSeed}$	-40	Novatech 409B	IntraAction AOM-402A1
Spec. probe	AO10	$\delta_{specProbe}$	-82±20	Novatech 409B	IntraAction ATM-902DA1
Bragg #1	AO11	$\delta_{bragg1}$	90±20	Novatech 409B	Crystal Tech. 3110-125
Bragg #2	AO12	$\delta_{bragg2}$		Novatech 409B	Crystal Tech. 3110-125

Table 2.6 : 689 nm system AOM details

Ind. labels the AOMs as shown in Fig. 2.16. The sign of the nominal freq. indicates the AOM order. The MOT AOMs are shown with two freq. sources which are used during the broadband red MOT and single frequency red MOT respectively.

the cost of increased complexity. Unlike the blue system, where the overall system frequency was determined by varying the master laser frequency, the red master is locked at a fixed frequency relative to the  $^{88}\text{Sr}$   $^1S_0 \rightarrow ^3P_1$  transition. Nearly all frequency shifts are accomplished using AOMs driven with digital synthesizers such that each subsequent system derived from the master laser inherits the frequency stability and narrow linewidth of the master.

Fig. 2.16 also highlights the boson and fermion subsystems. These setups allow the Neutral apparatus to simultaneously trap and cool mixtures of a single bosonic isotope and fermionic strontium-87. The isotope selector AOM (A04) determines which bosonic isotope this system can trap. We denote the different frequencies available to injection lock slave 0 through the "frequency selector" box in the top part of the above figure. From each choice of input frequency, the output of slave 0 is also shown relative to other laser trapping frequencies and the isotope shifts of the  $^1S_0 \rightarrow ^3P_1$  transitions.

### 2.3.2.2 689 nm Master

Our master 689 nm source is a Toptica DL-pro. This is a Littrow configuration ECDL which outputs  $\sim 30$  mW of usable 689 nm light past its internal optical isolator. Fig. 2.17a shows how this power is distributed amongst the various subsystems and directed towards each laboratory. From the figure we see that the gigahertz AOM (AO1 is the first optic the light passes through since this AOM has a diffraction efficiency around  $\sim 20\%$ . The  $\sim 6$  mW of shifted light is then split between the Neutral and Rydberg experiments where it is used to injection lock a dedicated slave diode used for the trapping MOT light needed for strontium-87.

Following the GHz AOM, a series of waveplates and PBS cubes are used to ap-

portion light to various fiber paths and laboratories. A beam sampler along the path directs light into a mode-cleaning fiber that outputs to the high-finesse cavity system and the remaining power ( $\sim 2 \text{ mW}$ ) is sent to a long heat pipe in order to interrogate the intercombination line transition.

The moderate finesse cavity is used to narrow the laser linewidth using the Pound-Drever-Hall (PDH) technique. The cavity length is varied with a PZT to lock the laser laser frequency to the atomic transition via saturated absorption, as illustrated in Fig. 2.17b. The atomic error signal is generated using standard frequency modulated Doppler-free saturated absorption where frequency modulation is performed via fast switching ( $\sim 11 \text{ kHz}$ ) of the RF drive frequency applied to AO2. The narrowing cavity is discussed in detail [section?](#) in Natali de Escobar's thesis and has remained unchanged since her publication<sup>||</sup>.

### 2.3.2.3 Neutral red system

The Neutral 689 nm system is composed of four slave diodes, which may be designated into the Boson and Fermion subssytems as illustrated in Fig. 2.18. Light from the 689 master system is transported to the Neutral apparatus via the master seed and trap seed fibers. These fiber outputs provide approximately 3 mW and 1 mW for the master and trap respectively. This light is used to seed slaves 0-2, with spectroscopy slave (or slave 3) injection locked from the slave 0 output. Each of the three MOT systems integrates an independent AOM which is used to provide dynamic intensity control and frequency offset & dithering during the 689 nm trapping and cooling stage. The gross detuning of these AOM's is fixed and specified in Table 2.6.

---

<sup>||</sup>As of April 2019, a ultra-low expansion cavity system is being implemented and tested to replace our homemade HF cavity.

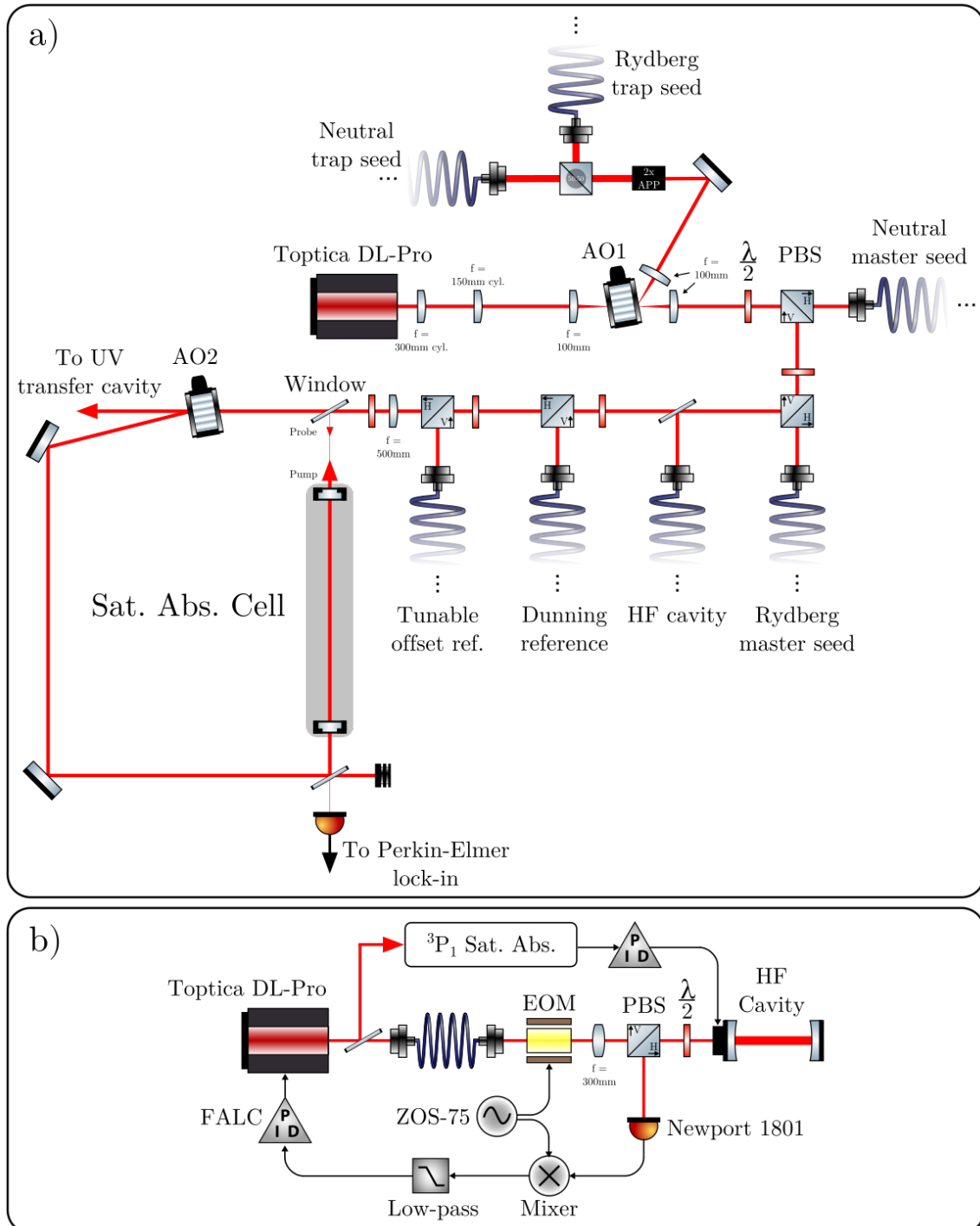


Figure 2.17 : 689 nm master system

- a) A simplified optical schematic showing the distribution of light as outlined in Fig. 2.16. b) Frequency stabilization scheme for the 689 nm master.

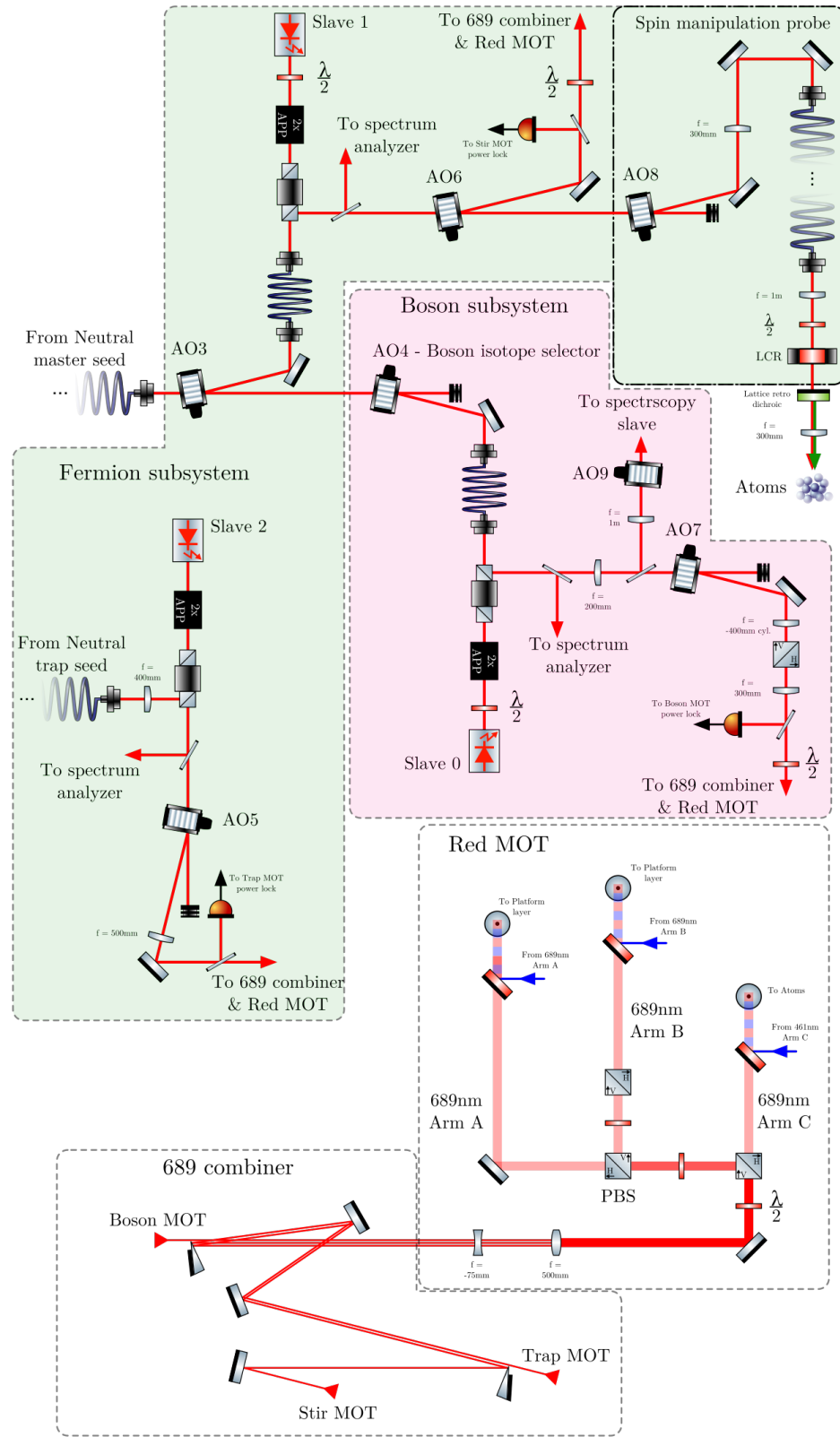


Figure 2.18 : Neutral 689 nm trapping and cooling setup

**Fermion subsystem:** Fig. 2.18 highlights the Fermion subsystem in green and is dedicated to the  $^{87}\text{Sr}$  isotope. This allows the seed laser frequencies to remain fixed as shown on the frequency axis given in Fig. 2.16.

As discussed in Sec. 2.1, trapping strontium-87 requires us to address two hyperfine transitions, which we label the trap, operating along  $^1S_0(F = 9/2) \rightarrow ^3P_1(F = 11/2)$ , and the stir, operating along  $^1S_0(F = 9/2) \rightarrow ^3P_1(F' = 9/2)$ . Due to the change in spin between the singlet and triplet series, there is a mismatch in the Zeeman shifts of the  $^1S_0$  and  $^3P_1$  states, which results in anti-trapped edge states causing atoms to be expelled from the MOT laser acting on the trapping transition. The complication can be overcome by adding an additional stir laser to randomize the  $m_F$  populations in the  $^1S_0$  ground state.

We generate these trapping and cooling photons using independent laser diodes, slave 1 and 2 for the stir and trap respectively, seeded with appropriately shifted light from the master laser. Light from slave 2 is used exclusively for the trap MOT while slave 1 is used for the stir MOT and spin manipulation probe, both of which operate along the ( $F = 9/2 \rightarrow F = 9/2$ ) transition.

**Boson subsystem:** Fig. 2.18 highlights the Boson subsystem in red. This setup enables the Neutral apparatus to individually trap each of the three bosonic isotopes of strontium. Additionally, this setup incorporates a spectroscopy probe that also features several choices for the input seed frequency. This system is detailed in Sec. 2.3.4.

Changing the bosonic isotope of interest is accomplished via switching the RF drive to the boson isotope selector AOM (AO4) and realigning through the mode-cleaning fiber to injection lock slave 0. This process has proven to be a fast and robust means for switching between various isotopes without the need for dedicated

diode systems for each isotope. Accounting for the boson MOT AOM (AO7) frequency, Table 2.6 gives the necessary drive frequencies for trapping strontium-88 and strontium-84. Strontium-86 is attainable by removing the drive frequency from the AOM such that slave 0 follows the 689 master frequency. Therefore, relative to the  $^{88}\text{Sr } ^1S_0 \rightarrow ^3P_1$  transition, the input frequencies for slave 0 are [ $^{84}\text{Sr} \rightarrow -269.49\text{ MHz}$ ,  $^{86}\text{Sr} \rightarrow -82\text{ MHz}$ ,  $^{88}\text{Sr} \rightarrow +82\text{ MHz}$ ]. These details are represented schematically on the frequency axis of Fig. 2.16.

**689 combiner & MOT:** Finally, Fig. 2.18 also illustrates the 689 combiner & red MOT paths. The 689 combiner is a series of D-type mirrors for combining the boson, stir, and trap MOT beams such that these three light sources co-propagate onto the atoms. We find that long path lengths ensure acceptable alignment along the entire path length with the only major drawback that the individual arm powers are not independently controllable for each of the three MOT beams.

As outlined in Fig. 2.14 and Sec. 2.3.1.4, the red MOT and blue MOT share the same path through the science chamber by utilizing beam combining dichroics and custom dual-wavelength waveplates.

### Historical notes and tips for usage

**Fiber usage for injection locking:** Optical fibers provide several key advantages when used to injection lock slaves. The foremost being a cleaner  $\text{TEM}_{00}$  output mode that can be easily mode-matched to the slave. Additionally, fibers provide a quick and effective means for ensuring optimal alignment of the injection locking light by coupling the rejected light from the slave diode "backwards" through the fiber. Although rejected light is typically minimized when setting up a slave diode,

by temporarily placing a waveplate before the isolator you can scramble the input polarization and increase the rejected power to facilitate alignment through the fiber. This process generally results in a quite robust alignment of the fiber output and the laser diode and is much faster than the free space method of coupling over a long distance. This alignment advantage along with improved mode matching has allowed us to injection lock a slave diode with as little as  $300\ \mu\text{W}$  while producing up to  $\sim 30\ \text{mW}$  of output power.

### 2.3.3 Optical dipole trap: 1064 nm

The ground state of strontium is a spinless  $J = 0$  state. Therefore, magnetic traps, which are common to alkali experiments, cannot be used for trapping the strontium ground state. Instead, we utilize optical dipole traps (ODT), which rely on the AC stark shift for trapping atoms.

The isotopes of strontium display a wide range of thermalization behavior due to their variation in scattering lengths. These differences in thermalization make it difficult to use a single ODT geometry for efficient trapping and evaporation of strontium. For this reason, the Neutral apparatus underwent a significant redesign of our ODT system as outlined in Ying Huang's thesis<sup>ref</sup>.

The experiments presented in chapter 5 of this thesis have relied on the trap configuration we call the independent arm ODT. Fig. 2.19 shows a simplified optical layout of this configuration which is composed of two 1064 nm beams labeled the loading and sheet traps which are controlled by independent AOMs. At the atoms, the approximate spot size of the loading trap is  $300 \mu\text{m} \times 60 \mu\text{m}$  and the sheet trap is  $400 \mu\text{m} \times 40 \mu\text{m}$ . Both beams have the short axis parallel to gravity to produce an oblate spheroid trapping volume which is useful for maintaining low density strontium-86 gases which reduces three-body recombination.

As shown in the figure, the two AOMs for the ODT are placed sequentially to better utilize the available 18W from the IPG. We typically load into a  $10 \mu\text{K}$  deep trap from the red MOT which requires  $\sim 4 \text{ W}$  in the loading trap and  $\sim 3 \text{ W}$  in the sheet trap. Once transferred into the ODT, we perform forced evaporation following a power law trajectory <sup>ohara</sup>, where the timescale for evaporation is isotope dependent. For our experiments with strontium-86, the evaporation timescales were on the order of 1-2 seconds for achieving sample temperatures near 100-200 nK and densities as

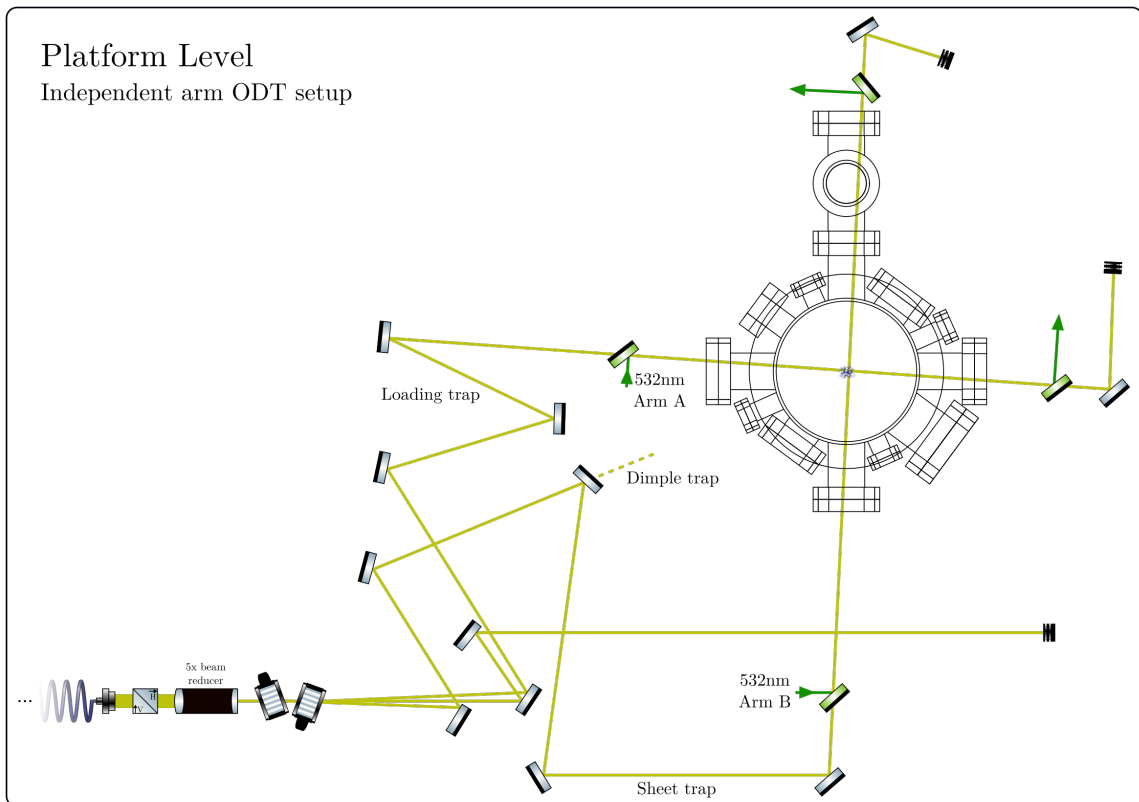


Figure 2.19 : 1064 nm optical dipole trap schematic

Paths for the loading and sheet traps are shown as they are realized on the apparatus. Also shown is the dimple trap path which is an optional configuration of the sheet trap [36].

high as  $10^{12} \text{ cm}^{-3}$ .

### 2.3.3.1 Modeling the potential

Optical dipole traps result from the AC stark shift present whenever an atom interacts with a light field [32]. In the simple two-level dressed atom model, the AC stark shift can be viewed as a mixing of the bare atomic states by the light field ref. Fig. 2.20 shows a schematic avoided crossing of a two level system near resonance. Here the separation between states is defined as  $\Omega$ , or the Rabi frequency given by

$$\Omega = \frac{1}{\tau} \sqrt{\frac{I}{2I_{sat}}} \quad (2.2)$$

where  $\tau$  is the lifetime of the excited state,  $I_{sat}$  is the saturation intensity of the transition, and  $I$  is the applied intensity. Using this we can understand the origin of the potential which provides the trapping force in ODTs.

Considering an atom in the ground state,  $|1\rangle$ , a light field with red detuning,  $\Delta < 0$ , and the intensity dependence of Eq. 2.2. We see that at low intensity,  $\Omega^{\text{low}}$ , the energy of state  $|1\rangle$ ,  $E^{\text{low}}$ , is nearly unchanged from the non-interacting case. However, as intensity is increased,  $\Omega^{\text{high}}$ , the energy of state  $|1\rangle$  decreases. Thus, atoms in  $|1\rangle$  will experience a force,  $F(\mathbf{r}) = -\nabla U(\mathbf{r})$ , directed towards higher intensity regions when there is a spatial dependence of the potential energy.

With respect to the detuning,  $\Delta$ , from resonance, the potential energy of the atom scales as

$$U(r) \propto \frac{\Gamma}{\Delta} I(r) \quad (2.3)$$

where,  $\Gamma$  is the natural linewidth of the transition determined by it's spontaneous decay lifetime, and  $I(r)$  is the spatial dependence of the light intensity. Optical dipole traps are also characterized by their off-resonant scattering rate. This rate is

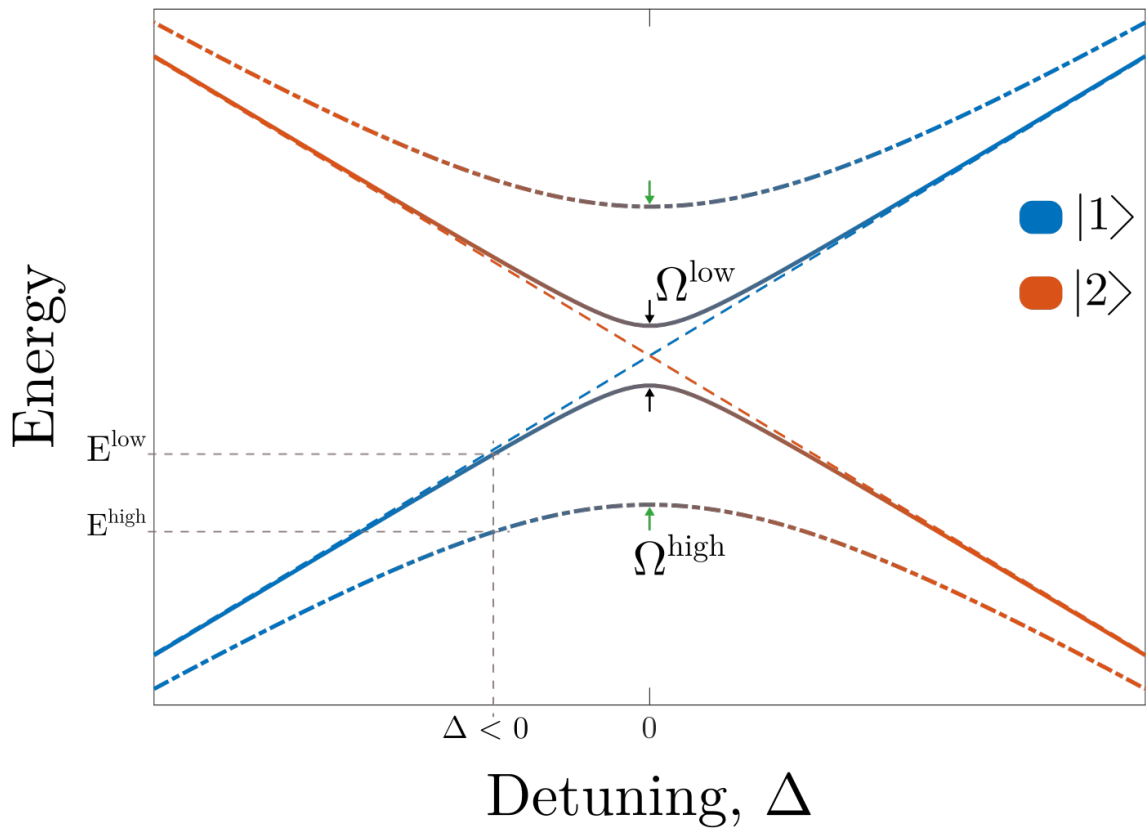


Figure 2.20 : Two-level avoided crossing

In the dressed atom model, coupling between the bare atomic states  $|1\rangle$  and  $|2\rangle$  results in an avoided crossing where the energy gap is determined by the coupling strength  $\Omega$ . The no coupling case is given by the dashed lines, while weak coupling is shown by the solid line, and strong coupling by the dash dotted line.

proportional to

$$\Gamma(r) \propto \left(\frac{\Gamma}{\Delta}\right)^2 I(r) \quad (2.4)$$

Comparing Eqs. 2.3 & 2.4, we find a favorable scaling for far off-resonant optical traps since the potential energy varies as  $1/\Delta$  and the scattering rate varies as  $1/\Delta^2$ .

The spatial dependence of  $U(\mathbf{r})$  derives from the TEM<sub>00</sub> gaussian intensity profile of the incident lasers given by

$$I(r, z) = \frac{2P}{\pi w(z)^2} \exp\left(\frac{-2r^2}{w(z)^2}\right) \quad (2.5)$$

where  $z$  is oriented along the beam propagation axis and  $r$  is transverse to this axis. Additionally,  $P$  is the incident laser power,  $w_0$  is the waist radius at  $z = 0$ , and the axial profile  $w(z)$  is given by

$$w(z) = w_0 \sqrt{1 + \left(\frac{z\lambda}{\pi w_0^2}\right)^2} \quad (2.6)$$

where  $\lambda$  is the laser wavelength.

Combining Eqs. 2.3 & 2.5 we find the three dimensional potential generated by two orthogonal lasers to be

$$U(x, y, z) = mgz + \frac{\alpha(\lambda)}{2\epsilon_0 c} \frac{2}{\pi} \left[ \frac{P_1}{w_1^y(x) w_1^z(x)} \exp\left(\frac{-2(y^2 + z^2)}{[w_1^y(x)]^2 [w_1^z(x)]^2}\right) + \frac{P_2}{w_2^x(y) w_2^z(y)} \exp\left(\frac{-2(x^2 + z^2)}{[w_2^x(y)]^2 [w_2^z(y)]^2}\right) \right] \quad (2.7)$$

where  $mgz$  accounts for the influence of gravity on the atoms of mass  $m$ , labels 1, 2 specify the two intersecting laser, i.e. the load and sheet traps as illustrated in Fig. 2.19,  $\alpha(\lambda)$  is the AC polarizability of the ground state at a given wavelength,  $\epsilon_0$  is the vacuum permittivity, and  $c$  is the speed of light. This polarizability encapsulates the natural linewidth, detuning, and resonant behavior of the light field interaction with the bare atomic states [32]. Sec. 2.3.1 and App. A of Pascal Mikelson's PhD thesis

[64] outlines a calculation of the AC polarizability, which at 1064 nm is  $\frac{\alpha(\lambda=1064 \text{ nm})}{2\epsilon_0 c} = -10.9 \text{ Hz}/(\text{W/cm}^2) = -5.23 \times 10^{-8} \mu\text{K}/(\text{W/cm}^2)$ \*. Furthermore,  $w_{(1,2)}^{(x,y,z)}$  generalizes Eqs. 2.5 and 2.6 for astigmatic laser profiles whereby the waist position and size are not common to both beam axes as assumed in these simple equations†.

The effects of gravity are a significant limiting factor for ultracold atoms as it is the dominant force that must be counteracted by the optical dipole trap. Fig. 2.21a shows the effects of gravity considering a simple one-dimensional gaussian potential,  $U(z) = mgz + A \exp\left(\frac{-z^2}{2\sigma^2}\right)$ . Here we've chosen a general form of the gaussian for illustrative purposes. In the figure, we define the trap depth as the difference between the trap minimum and the lowest saddle point. Additionally, by making a harmonic approximation, shown by the dashed line, we can Taylor expand Eq. 2.7 and determine the expected trap frequencies. Fig. 2.21b illustrates a realistic three-dimensional profile of an optical trap. Analyzing the 3D profiles, we find that the saddle points may not be along the  $X = 0$  line and therefore we must consider the full trap profile when determining the trap depth. This is particularly important for shallow traps (low power) where the trap depth is more likely to be defined by a saddle point along a non-trivial trajectory. This realization has important repercussion for our analysis of the halo binding energy described in Ch. 4.

---

\*Units here are convenient lab units for quick calculation of trap parameters. Polarizability of  ${}^1S_0$  in atomic units is  $\alpha = 232.857 \text{ au}$ .

†Eq. 2.7 is given assuming a coordinate system where one beam propagates along  $X$ , another along  $Y$ , and  $Z$  is parallel to gravity.

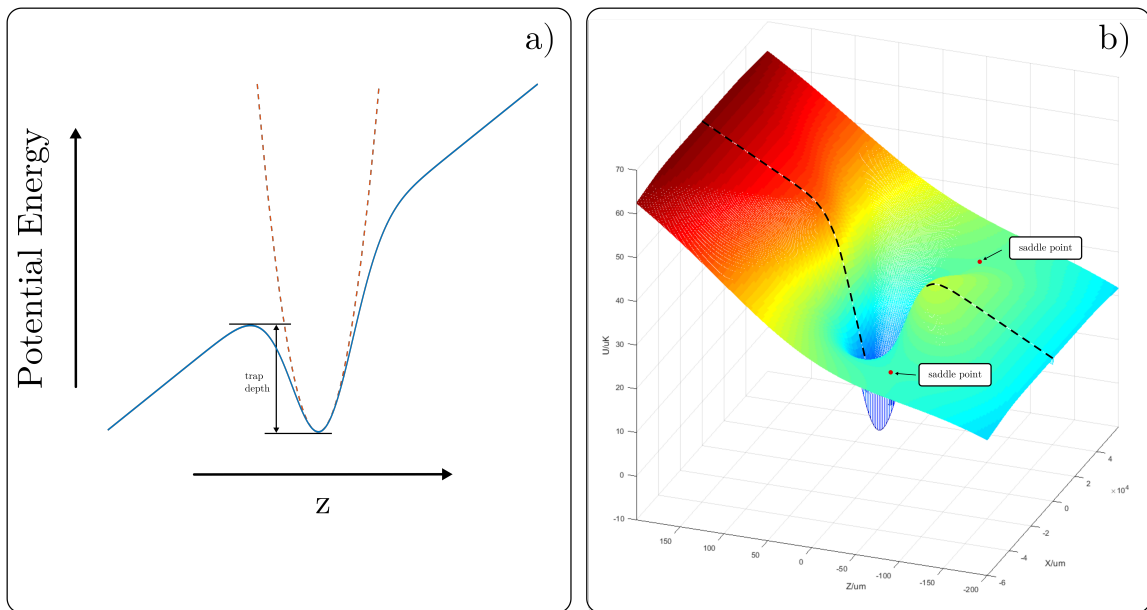


Figure 2.21 : Modeling an optical dipole potential

a) A one-dimensional view along the trap axis parallel to gravity. The trap depth is defined between the trap minimum and the nearest saddle point. Also shown is the harmonic approximation used for defining trap frequencies. b) A pseudo-color volumetric plot of a three-dimensional potential. Here we see a saddle point similar to the 1D case along  $X = 0$  but there is also a lower saddle point indicated by the black arrows.

### 2.3.3.2 Trap frequency calibration

Measurement of the trap frequencies provides the link between our theoretical models and the experimental realization of the optical dipole trap. Previously, these measurements were performed by parametric heating via intensity modulation of the optical dipole trap [cite Ying thesis](#). This process causes atom loss via resonant heating when the modulation frequency matches a trap oscillation frequency. While convenient and simple, parametric heating can lead to a complicated spectrum to decipher since the heating process does not discriminate directional information and causes coupling of higher harmonics of the trap frequencies.

Recently, we have found excitation of center-of-mass (COM) oscillations to be a robust mechanism for measuring trap frequencies. Fig. 2.22 shows an example of trap frequency measurements taken via center-of-mass oscillations. This example illustrates the long-lived nature of these collective modes which can extend for hundreds of milliseconds. Furthermore, the frequency discrimination provides an unambiguous estimate of the underlying trap frequency.

Exciting vertical trap frequencies, along  $Z$ , is a straightforward process whereby we excite oscillations by quickly extinguishing one arm of the optical dipole trap for 1-2 ms before turning it back on and allowing the cloud to evolve in time. We measure the trap frequency by varying this evolution time subsequently performing a standard time-of-flight absorption imaging step<sup>‡</sup>.

Exciting oscillations along the horizontal directions, is a bit more challenging. We have developed two mechanisms for exciting these modes which we call the kicking

---

<sup>‡</sup>On a technical note, we find that this rapid on-off of the beams results in a brief overshoot of the power locks due to the reacquisition. However, the power lock equilibrium is restored after a few milliseconds and therefore we evolve for a time long compared to this perturbative behavior.

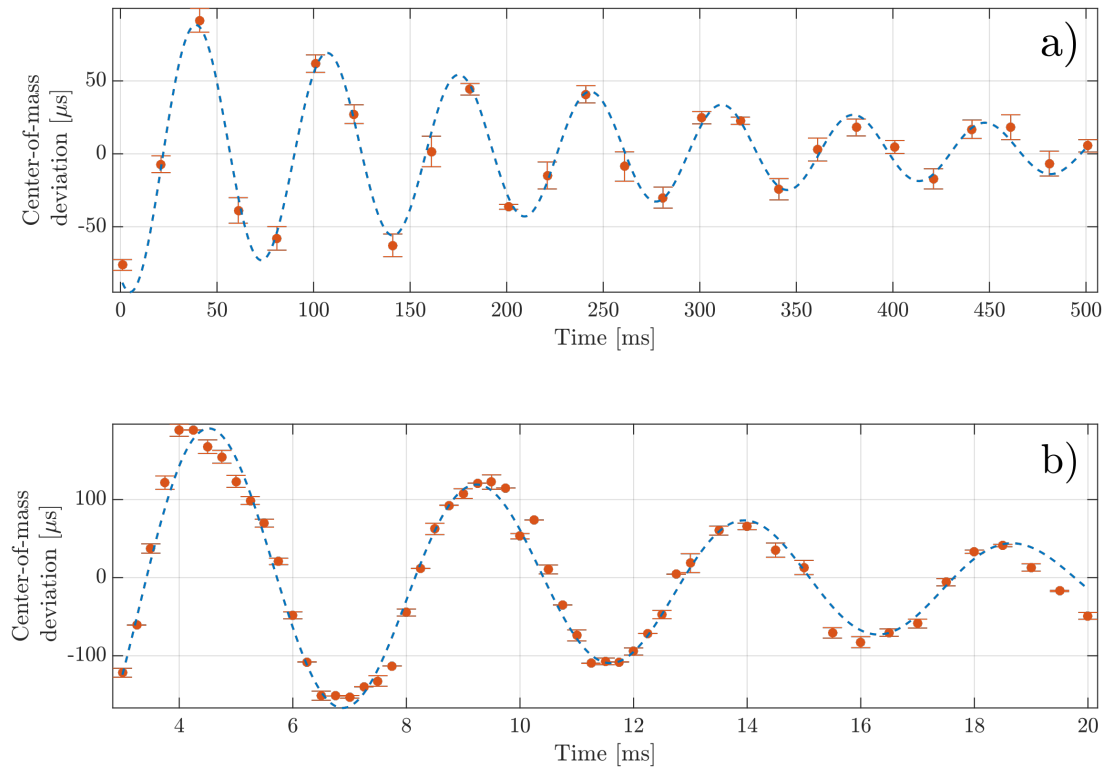


Figure 2.22 : Example center-of-mass oscillations

These measurements were taken in the independent arm ODT with strontium-84. This isotope has a scattering length  $a = 124 a_0$  leading to slow decay of the oscillations.

a) Horizontal trap frequency of  $\sim 13$  Hz extending over 500 ms. This mode was excited via the kicking method. b) Vertical trap frequency of  $\sim 220$  Hz. This mode was excited by momentarily pulsing one of the ODT beams off. Further details are given in the text.

method and the pulling method. The following sections provide further detail<sup>§</sup>.

**Kicking method:** The kicking method has been primarily used for measuring the trap frequencies of the independent arm ODT. In this configuration the two ODT beams intersect in a horizontal plane parallel to the optical table and orthogonal to one another. Excitation of the center-of-mass oscillation occurs via an abrupt step of the AOM drive frequency. This changes the deflection angle of the IR beam out of the AOM which, in turn, "kicks" the cloud. Briefly, the kicking procedure is

- I. During the ODT loading phase, load into a trap with one beam offset
  - A. In our current configuration, an offset of the AOM frequency by  $\approx 1$  MHz results in a reasonable excitation amplitude.
- II. Once the red MOT is extinguished and ODT loading is complete, evaporate down to the trap or intensities of interest in the offset trap.
  - A. It is useful to follow the evaporation trajectory for the experiment at hand. This allows adequate modeling of the experimental potential and evaluation of the trap depth at various points of interest.
- III. After evaporation, let the atoms equilibrate for  $\approx 250$  ms then suddenly switch the frequency of the trap and hold for a variable evolution time before releasing and imaging.
  - A. This offset will excite oscillations along the opposite beam and measure the confinement due to the beam being shifted.

---

<sup>§</sup>Note that timescales specified below are given with strontium-84 as the example. This isotope has favorable scattering properties and is typically our prototyping isotope for new techniques.

**Pulling method:** With the recent addition of the high power 532 nm for the optical lattice, we have explored an alternative method of inducing a center-of-mass oscillation. This method uses a single pass of vertically propagating green light (Arm C) to pull the atoms out of equilibrium to excite an oscillation. Details of the 532 nm setup are given below in 6.1.

The pulling method has become our preferred method of trap frequency measurement, as it does not require us to change any AOM frequency sources unlike the kicking method<sup>¶</sup>. Additionally, the pulling method can be applied to traps where the 1064 nm light is recycled whereas previously our only recourse in this configuration was to measure trap frequencies via intensity modulation. Briefly, the pulling procedure is

- I. Using an unmodified ODT, load and evaporate down to the trap of interest.
  - A. While evaporating, apply slightly mis-aligned lattice Arm C light to the atoms.
  
- II. After evaporation, ramp up Arm C to high power over 250 ms then allow the atoms to equilibrate for another 250 ms in the combined two beam IR, one beam 532 ODT.
  - A. The final power of the 532 nm beam when enabled should be adjusted to provide an adequate force without collapsing the IR ODT.

---

<sup>¶</sup>The loading trap uses a VCO so changing the voltage source is enough. However, the sheet/dimple is run from a IntraAction driver with a fixed digital synthesizer as the input. For kicking with the sheet, we temporarily replace the synth with a VCO, but be careful as this will also change the gain of the power lock circuit (Synth outputs  $\approx$ 0 dbm but VCO outputs  $\approx$ 10 dbm)

III. Diabatically extinguish the 532 nm beam and hold in the optical dipole trap for varying evolution times before releasing and performing time-of-flight imaging.

The controlled mis-alignment of the 532 nm Arm C beam is facilitated by an absolute positioning mirror (model: Newport Conex-AG-M100D). This mirror provides a computer controllable interface for reproducibly changing the Arm C beam alignment and exciting center-of-mass oscillations along each of the IR beam directions.

### **Historical notes and tips for usage**

**IPG failure:** In the fall of 2018, the IPG YLR-20-LR, which had been in use for about a decade, died due to a thermal issue that caused the internal fiber amplifier to overheat and burn. As of April 2019, this laser is being replaced by an IPG YLR-50-1064-LR which is a diode pumped, multi-mode, linearly polarized Ytterbium fiber laser with a maximum power output of 50 W. This system is being installed by Josh Hil, who is also reconstructing some elements of the paths reported in Ying Huang's thesis.

### 2.3.4 Optical toolbox

#### 2.3.4.1 Absorption imaging system

Absorption imaging is a destructive measurement process that is predicated on measuring the spatially dependent attenuation of laser light after passing through an atomic cloud. In this section we will discuss the technical details of the Neutral absorption system and postpone the theoretical description of the process to Sec. 3.2.1. Additionally, we will reserve the discussion of image processing for App. ?? which details software used to analyze the images and extract physical measurements.

Fig. 2.23 shows a simplified schematic of the absorption imaging system. Light is derived from the MOT path subsystem and guided to the atom chamber via freespace propagation. After passing through the atoms, an imaging system shapes and focuses the image onto a Cooke PixelFly CCD camera. The PixelFly is a 12 bit 1280x1024 CCD with a pixel size of  $6\ \mu\text{m}$ . The imaging relay system shown after the atomic sample was developed by Mi Yan and is outlined in detail in App. A of his PhD thesis [91]. Much of the imaging sequence is a standard procedure, however, day to day operation may be affected by system performance.

When taking images, we measure the optical depth to extract the properties of the atomic cloud, the physics of which is discussed in Sec. 3.2.1. For now, we will take as a given that each experimental sequence acquires one image with the atoms in frame and another background image without the atoms. In the ideal scenario these two images would be identical except in the region of the atom cloud and thus information about the cloud could be inferred using Beer's law [ref](#). Practically, we must wait for the atoms to exit the frame before taking a background image. This introduce a time delay between the consecutive images, which we seek to minimize. For this reason we

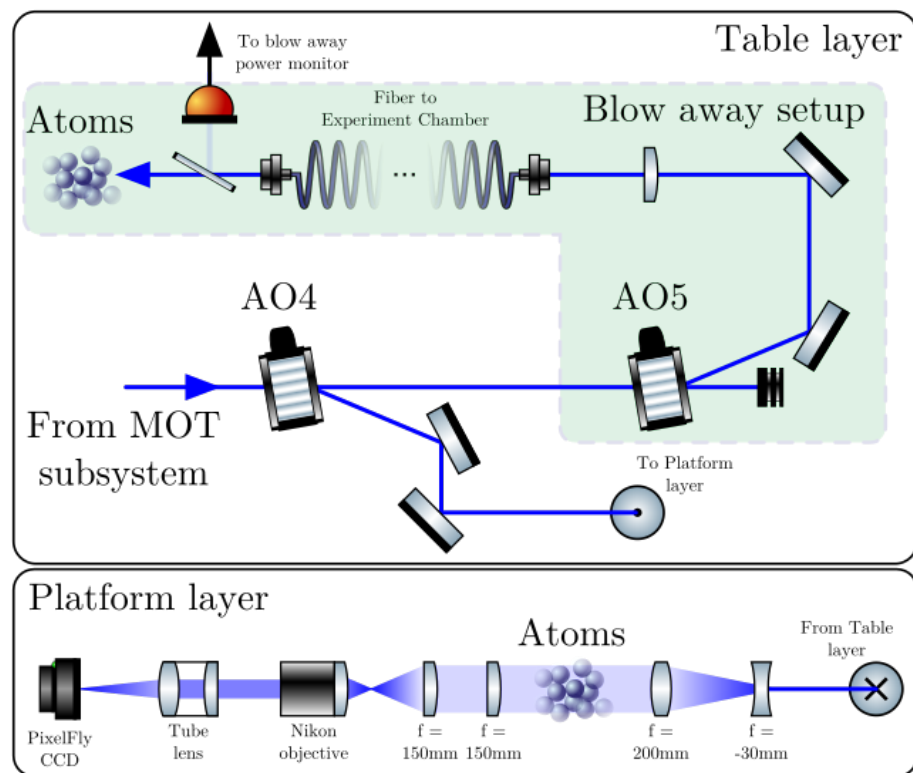


Figure 2.23 : Absorption imaging and blow away pulser optical schematic

Details on the construction and characterization of the blow away setup are available in Josh Hill's masters thesis [ref.](#)

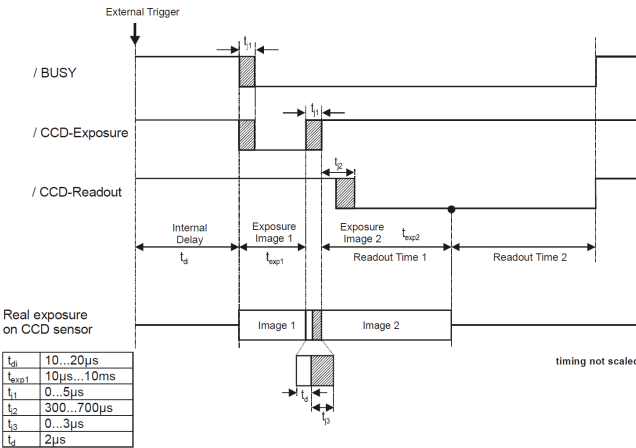


Figure 2.24 : Timing diagram of PixelFly doubleshutter mode

$t_j$  refers to timing jitter inherent to the camera. In this scheme the first exposure can be controlled via the external trigger but the second image exposure is fixed to the readout time of the first image.

utilize a special feature of the PixelFly called "double-shutter" mode. This particular imaging mode of the camera utilizes a second hidden set of pixels that are interleaved with the active pixels of the CCD. Typically the acquisition time between consecutive images taken with a CCD is limited by the analog-to-digital conversion time needed to readout the image from the pixels into the camera's memory. However, because of the PixelFly's set of hidden pixels, after the first image is taken, it is simply shifted one row down from the active pixels into the hidden area. Once shifted down, the active pixels are free to be exposed again. With this process, the time between images is reduced to 5 $\mu$ s. Fig. 2.24 shows a full overview of this process. The drawback of this scheme is that for exposure times less than the readout time of an image, the second image is forced to have a minimum exposure of the readout time. This presents a challenge as our exposure time is about four orders of magnitude faster than the

readout time. To overcome this, we rely on the fast response of the imaging system AOMs, a high extinction ratio of the 461 nm photons, and a narrow line filter centered at 461 nm attached directly to front of the CCD. Fig. 2.23 shows two AOM's along the imaging path before the atoms. We found two AOM's necessary to attenuate leakage light along the path to acceptable levels while maintaining fast response times that a physical shutter cannot replicate.

Great care is taken to reduce the time between images since the laser intensity and frequency might drift between the atom and background images. Variations in intensity have straightforward implications for errors in measuring the optical depth since the characterization of the atomic number density assumes the only difference between the images is due to the presence of scattering particles and does not account for fluctuating photon number.

A more insidious source of error is variation of the optical frequency. Coherent, frequency stabilized radiation is used to illuminate the atom cloud so that we may control the optical absorption cross section and accurately model the atomic number density. However, this laser light is passed through many optical components on its path to the atoms and ultimately the imaging camera. Small reflections along this path result in a multitude of interferometers that cause small scale spatial intensity variation across the beam. Exacerbating this problem are short time frequency drifts that may occur between the atom and background images that result in slightly different fringe patterns in the atom and background images. Fringe patterns are a well known nuisance in experimental AMO images and it has become routine to use linear algebra techniques (PCA, ICA, etc.) to create a composite background image for each atom image during analysis in order to create a higher quality image of the optical depth [76]. A brief discussion of the principal component analysis (PCA)

algorithm employed by the Neutral analysis routine is outlined below.

Briefly, the PCA approach is as follows:

- I. Find a basis set of background images from a large set of raw background images.
- II. For a single atom image, construct an initial guess at a composite background image using coefficients to weight each basis image resulting in a superposition of the basis images.
- III. Segment the atom image into multiple regions by separating out the region of interest that includes the atom cloud.
- IV. Comparing regions of the composite background and the region excluding the atom cloud, perform a least-squares minimization by varying the weighting coefficients of the composite background.
- V. Once a suitable composite background has been found, calculate the optical depth using the region including the atom cloud and the corresponding region of the minimized composite background image.

This procedure is repeated for each atom image using a static background basis set that is computed for each scan. Fig. 2.25 shows an example of this technique with a background set of 20 other images (not shown). While PCA does not completely eliminate the visible fringe patterns, there is a noticeable reduction of the fringes in the PCA image versus the partner-in-time method.

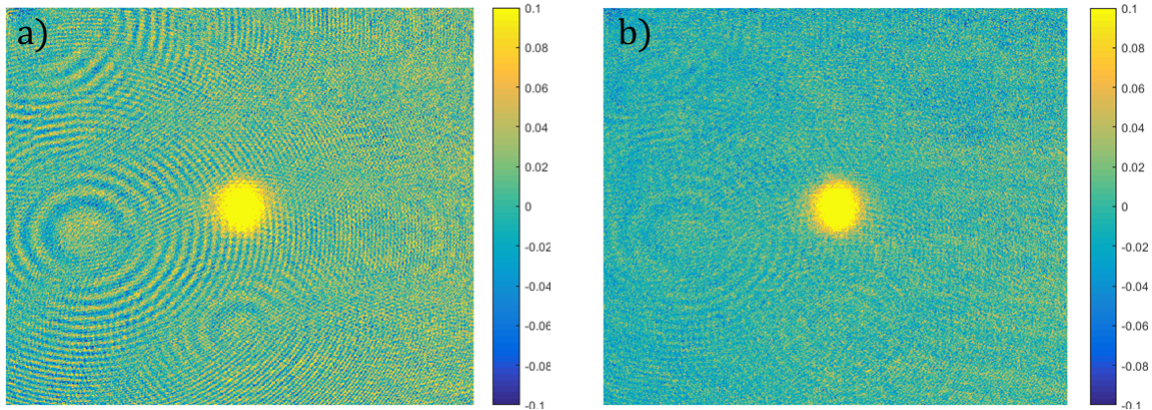


Figure 2.25 : Comparison of background subtraction methods

Background subtraction on the same image performed using two different methods and plotted on the same color scale. a) The partner-in-time background to the atom image is used. b) A composite background image formed via PCA is used.

### 2.3.4.2 Highly tunable 689 nm spectroscopy system

The spectroscopy laser is derived from a dedicated slave diode and is our primary 689 nm probe for bosonic isotopes, with the spin manipulation laser described below being used for fermions. This laser system is used for general intercombination line spectroscopy, photoassociation, Bragg scattering, and Rabi oscillation measurements.

Fig. 2.26 shows a simplified optical diagram. We found it necessary to increase the isolation out of the laser as the injection lock became unstable when coupling into fiber due to back reflections. We typically get  $\sim 25$  mW of usable power past the second isolator. As this is our primary spectroscopy laser, its optical setup tends to be in flux but a couple of noteworthy innovations have been implemented in recent years. These include the development of an infinite sample and hold for intensity stabilization, a versatile injection locking scheme, and a shallow angle Bragg scattering setup which

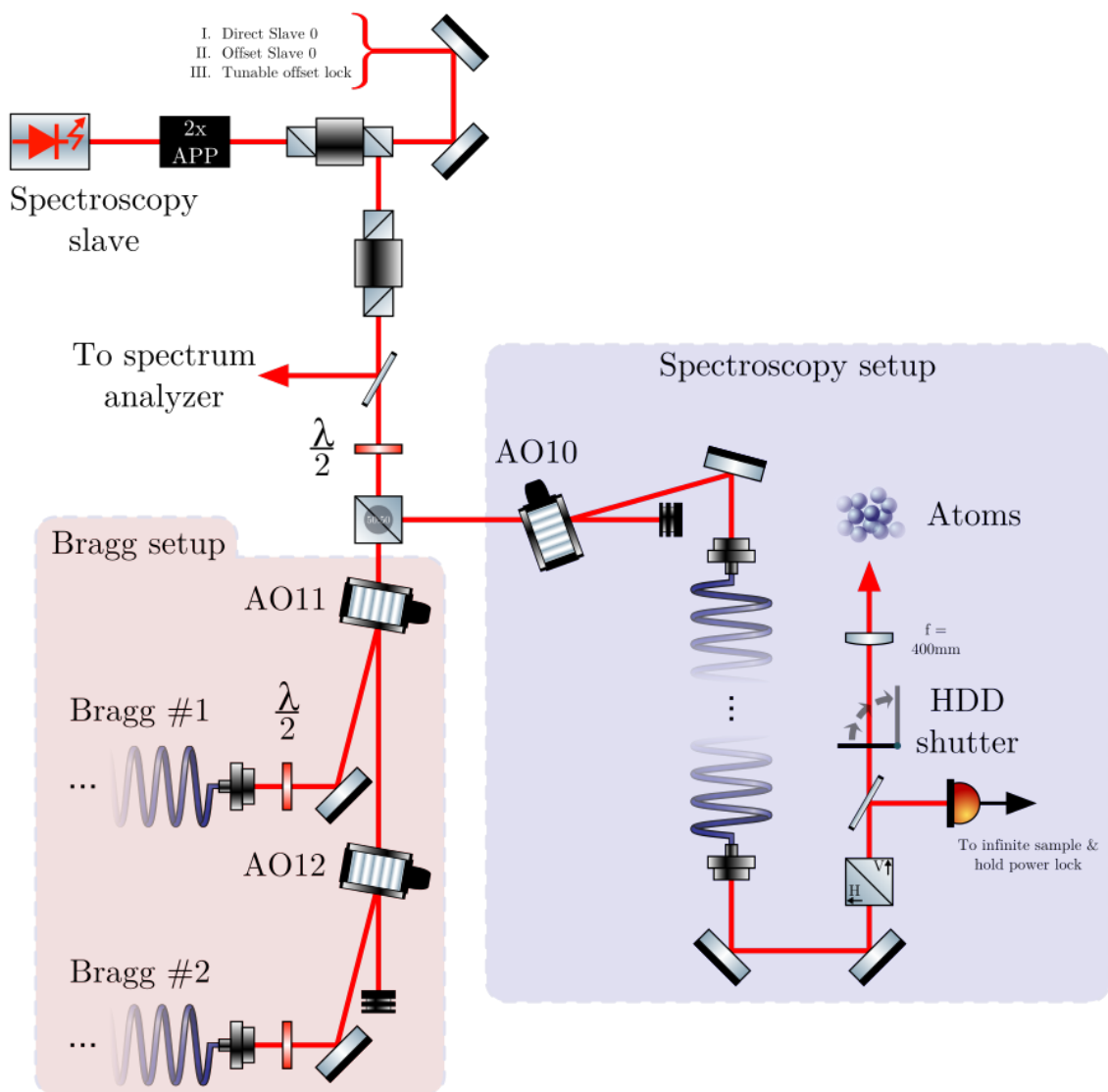


Figure 2.26 : Optical schematic: 689 spectroscopy laser

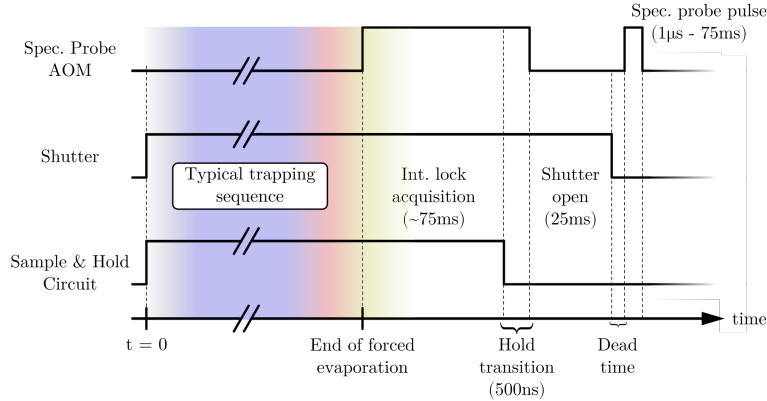


Figure 2.27 : Infinite sample and holding timing diagram

The HDD shutter in use has a full open time of  $\sim 15\text{ ms}$  and the acquisition time of the sample and hold chip is on the order of  $\sim 500\text{ ns}$ .

are discussed below.

**Infinite sample and hold:** The infinite sample and hold (ISH) circuit is used in conjunction with an intensity stabilization lock circuit and was built to allow for intensity stabilized pulses on timescales much faster than the acquisition time of the intensity lock circuitry, typically  $\sim 70\text{ ms}$ . This circuit was developed and built by Josh Hill and is based on the LTC1417 which is a low power 14-bit 400 kS/s ADC.

The ISH is currently placed on our spectroscopy probe and is situated between the intensity stabilization lock circuit and RF voltage controlled attenuator. This allows the ISH to passively sample the control voltage from the lock circuit. In sample mode the ISH output follows the input from the lock circuit. When the ISH is transitioned into hold mode, it begins ignoring changes on its input and outputs the last voltage that was sampled before the transition. A timing diagram of the infinite sample and hold usage is outlined in Fig. 2.27. Following our typical preparation sequence we place

the ISH in sample mode and enable the spectroscopy probe with the HDD shutter blocking the beam. This allows the lock circuit time needed to acquire and stabilize the feedback voltage required to maintain the present intensity setpoint. Following lock acquisition, we transition the ISH into hold mode, open the shutter, and pulse the RF onto the spectroscopy AOM (AO10) via a fast RF switch, where the RF amplitude is attenuated via a voltage controlled attenuator and the voltage input is the fixed output value from the ISH. This momentary transition to open-loop operation of the intensity stabilization circuit does suffer from slow long term fluctuations shot to shot, but provides a marked improvement on the intensity reproducibility without placing restrictions on the minimum pulse time required. Furthermore, by monitoring and recording the slowly varying intensity fluctuations, we can model any error introduced by the reduced intensity variation.

**Versatile injection locking scheme:** This scheme allows us to change the seed laser frequency via three different methods outlined below.

I. Directly following slave 0

A. A small amount of light from slave 0 is coupled directly into the rejected port of the spectroscopy slave isolator, resulting in the frequency of spectroscopy slave following slave 0. Fig. 2.18 shows the position of this pick-off before the boson red MOT AOM. Recalling that slave 0 is always positioned +82 MHz of the bosonic isotope of interest, the direct method will position the frequency of the spectroscopy slave to also be +82 MHz.

II. Slave 0 minus 40 MHz

A. The light sent from slave 0 is shifted down 40 MHz by the spectroscopy

offset AOM. This positions the spectroscopy slave frequency at +42 MHz of the intercombination line of interest.

### III. Programmable offset

A. In 2018 we re-purposed the original homemade 689 master ECDL described in Natali de Escobar’s thesis as a slave ECDL and directed light from this setup as a tertiary method for tuning the frequency of the spectroscopy slave.

There are several things to note concerning the above descriptions. First, the ”of interest” designation specifically refers to the variability of the laser frequency of slave 0, which is dependent on the configuration of the isotope selector AOM. Second, switching between case I and II is surprisingly trivial given the realized setup on the table. In practice, a flipper mirror and clever optical path alignment allow us to switch between these two injection methods in a matter of seconds and has demonstrated remarkable stability. Finally, while the programmable offset is the most versatile of the presented schemes, it also has the greatest frequency uncertainty and is fundamentally a different approach that we are still in the process of exploring.

The slave ECDL, beatnote generation, and phase locked loop (PLL) integrated circuit was a project begun by a visiting student and later completed by Josh Hill. It is based on the 2009 work of Appel et. al. [94] which outlines a versatile optical phase locked loop with a claimed frequency range of sub-MHz to 7 GHz.

As a brief reminder, phase locking is a feedback scheme which seeks to maintain the a fixed and phase relationship frequency between two sources. This process is heavily used in the telecommunications industry and analog phase locking is a common technique in atomic physics laboratories as well. In atomic physics, the general

idea is to generate a beatnote by interfering two single frequency lasers on a high bandwidth photodiode. From this optical beatnote we observe the difference frequency of the two lasers as the summing frequency is well outside the bandwidth of photodiodes. The difference frequency can then be further interfered against an RF reference frequency and low-passed to generate an error signal that can be used to stabilize the difference frequency against the RF reference.

The versatile OPLL is a digital realization of this approach which, we have used to lock the relative frequency difference between the Toptica master and slave ECDL from approximately 1 MHz to 1.2 GHz. The upper limited is currently bandwidth limited by our AC coupled photodiode and not by the OPLL circuitry. Fig. 2.28a shows an example of the optical beatnote monitored via an RF spectrum analyzer. Notably, while we do observe suppression of frequency components around the set point which is characteristic of locking, we also see resonant peaking instead of a single narrow frequency peak as expected. Further investigations showed that the individual frequencies were fairly narrow as shown in Fig. 2.28b where we observed atom loss on the  $F = 9/2 \rightarrow F' = 11/2$  transition with linewidths on the order of 60 kHz.

Finally, we note that this system has also been used to perform Bragg spectroscopy as reported in the PhD thesis of Brian DeSalvo [ref](#). Detailed drawings of the optical setup used for shallow angle Bragg scattering can be found in App. ??.

#### 2.3.4.3 Spin-manipulation laser with dynamic polarization control

Fermionic strontium-87 has become of particular interest for experiments studying quantum magnetism in a highly degenerate SU(N) system. Key to these studies is the creation and manipulation of arbitrary spin mixtures. We have recently implemented

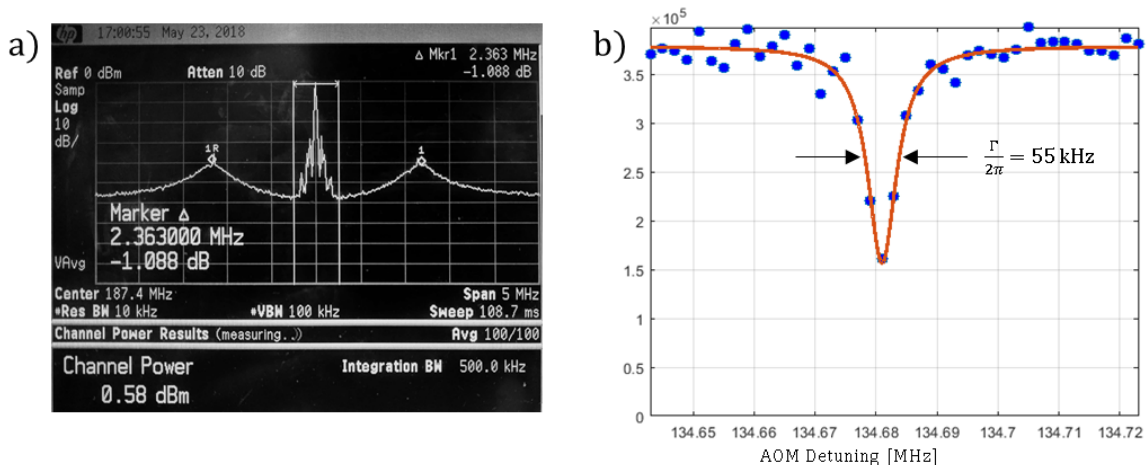


Figure 2.28 : Characterization of the OPLL performance

a) RF spectrum of the optical beatnote when the OPLL is engaged. Resonant peaking can be seen in the 500 kHz band around the center frequency. b) Atom loss spectrum which shows that the central peak is narrow. Differences between the AOM detuning shown and the center frequency of the OPLL are due to various AOM shifts between components.

a spin manipulation laser probe (spin-man) acting on the  $F = 9/2 \rightarrow F' = 9/2$  hyperfine transition of the intercombination line for the purpose of creating well defined spin mixtures. Preliminary investigations using this system are reported in Ch. 6.

Fig. 2.18 illustrates the optical schematic of the spin-manipulation system which is derived from slave 1 and is related to the stir MOT system. The original construction of the output optics is outlined in Ch. 5 of Josh Hill's masters work [34] and is part of the layered optical systems added to the top of the optical chamber in 2017.

A key component of this layered system is the liquid crystal retarder (model: MeadowLark Optics LV-300 LCR), which allows us to dynamically control the polarization incident on the atoms. Additionally, a configurable high precision RF system for dynamically changing the spin-manipulation laser frequency allows us to perform optical pumping in a magnetic field by addressing each Zeeman transition independently. In concert, these devices allow us to, for instance, polarize to the  $^1S_0 (F = 9/2, m_F = 9/2)$  using  $\sigma+$  and once polarized use the LCR to rotate the light polarization to  $\sigma-$  and probe the polarized ground state along the  $^1S_0 (F = 9/2, m_F = 9/2) \rightarrow ^3P_1 (F' = 9/2, m_F = 7/2)$ . Details of these experiments and further characterization of this system are presented in Ch. 6.

The RF tunability for optical pumping is based on the "table mode" feature of the Novatech 409B digital synthesizers which can be externally triggered to progress through a table of configured frequencies.

## 2.4 Apparatus interface

The Neutral apparatus interfaces to our digital infrastructure via specialized hardware implementations and custom written software. Over the last seven years nearly all of this digital infrastructure has been refactored, upgraded, or replaced. Therefore, the following sections will briefly outline these new constructs, providing references to code repositories when possible. However, detailed discussions on the usage of this infrastructure will be relegated to their respective appendices.

### 2.4.1 Software

The primary control software is a custom built Labview application based on a synchronous state machine\*[ref](#). The Neutral implementation of this software is called neuKLEIN (Neutral Killian Lab Experimental Interface) and is based on a major overhaul, by Joe Whalen, of the original control software. A detailed overview of the capabilities, limitations, and instructions for use of neuKLEIN is available in App. ??.

In short, an experimental sequence begins with serially programming each voltage output device. The pulseblasters are programmed last and are triggered via the global experimental trigger discussed in 2.4.3.2 below. Once all devices are ready the pulseblasters become the global clock and the neuKLEIN software begins polling the PixelFly camera waiting for a new image. Once an image is received various experimental parameters are recorded into text files and saved to disk. This process continues within the primary WHILE loop of the state machine and steps through the predetermined experimental settings array. Primary exit conditions for the loop

---

\*Currently this project can be found at <https://github.com/KillianRice/neuKlein>

are encountering an error, conclusion of the settings array, or manual abortion.

Once the files are written to disk, we perform image analysis using a custom Matlab<sup>TM</sup> routine imaginatively named Neutral imagefit routine<sup>†</sup>. An in-depth discussion on the usage, extensibility, limitations, and feature improvements is available in App. ??.

#### 2.4.2 Hardware control and measurement systems

The hardware control system is composed of several primary components including the experimental clock, voltage output devices, and measurement instruments. We use a series of National Instruments<sup>TM</sup> data acquisition cards (NI-DAQs) and a re-configurable FPGA for generating output voltages. The experimental clock is based on a pair of SpinCore PulseBlaster TTL generators and a Cooke PixelFly camera is used for collecting absorption images. We also have access to a PicoScope 5000 digital oscilloscope for high resolution signal monitoring and recording. Typically this is used for recording experiment specific photodiode signals for later analysis.

Table 2.7 gives the models of the NI-DAQ cards and additional details such as the resolution, the shared FIFO (first-in, first out) buffer sizes, and the maximum sample rates as a function of the number of channels in use. Though these cards are known as acquisition cards, we instead rely heavily on the arbitrary waveform generation capabilities for dynamically generating analog output voltages. Furthermore, we do not stream data to cards during the experimental sequence but use only the on-board FIFO buffer for storing the arbitrary waveform.

Importantly, the finite buffer size and maximum sample rate define two extremes for time-based waveform generation due to the discretization of the waveform. For

---

<sup>†</sup>Currently this project can be found at [https://github.com/KillianRice/neutral\\_imagefit\\_routine](https://github.com/KillianRice/neutral_imagefit_routine)

Model	Resolution		FIFO buffer Size	Max sample rate	
	Bit depth	Voltage [mV]		Channels used	Rate [kS/s]
6713	12	5	16,384	1 - 5	1,000
				6	952
				7	833
				8	740
6221	16	0.03	8,191	1	833
				2	740
6229	16	0.03	8,191	1	833
				2	740
				3	666
				4	625
6733	16	0.03	16,384	1 - 5	1,000
				6	952
				7	869
				8	769

Table 2.7 : Arbitrary waveform generation details

All cards specified are the PCI model and interface with the experiment control computer directly through the motherboard or via a PCI expansion bin (model: StarTech PEX2PCIE4L). Sample rates are given in kilosample per second (kS/s) and are the same across all enabled channels. The FIFO buffer stores the individual waveform points and is also shared amongst all enabled channels. Full voltage output range is  $\pm 10\text{ V}$ .

short times, the maximum sample rate sets the minimum possible time step between two points on the voltage output. At long times, a fixed number of points between the start and end points may lead to unacceptably large voltage steps between two points on the voltage output. Balancing these two tradeoffs is essential and is the primary driver for the plethora of various cards so that we may dedicate their finite resources to specific tasks.

While arbitrary waveform generation is useful for dynamically varying voltages during an experimental sequence, there are a number of applications where a static voltage is needed or smoothly varying between two or more voltages is not required. Until recently, the NI-6713 was our only source of experimentally controlled static voltages (in contrast to a static voltage from a supply) and switching between driving voltages was done via a bank of standalone fast analog IC switches (primarily the ADG419). Fast switching of the set point voltage has traditionally been how we control a number of systems through their feedback circuitry. For example, the 922 nm frequency is jumped from the optimal trapping frequency to the optimal imaging frequency at the end of the experimental sequence via the saturated absorption cell solenoid current. The change in magnetic field shifts the resonance frequency of the loss feature and the 922 nm frequency lock responds by varying the master laser frequency to restore the resonance condition. However, the NI-6713 + switch bank limited the number of controlled static voltages to eight and the simple standalone switches were insufficient for applying application logic or dynamically choosing driving voltages<sup>‡</sup>.

These shortcomings led us to develop a real-time based NI-FPGA for the develop-

---

<sup>‡</sup>An example of this application logic might be any set point that could be controlled via boolean logic conditioning.

ment of custom reconfigurable logic and static voltage output. This system is based on a NI cRIO-9063 with integrated Artix-7 FPGA, a NI-9403 32ch TTL input/output (I/O) module, and a NI-9264 16ch analog output module. The cRIO device manages the control layer of the system, hosts the embedded operating system and allows us to easily develop, compile, and deploy our custom control logic to the FPGA via Labview. The FPGA (field programmable gate array) executes the user-defined logic on a user-defined loop-time (minimum 50  $\mu$ s.) with the 32 TTL I/O channels and 16 analog output available for reading and writing each cycle. We typically do not use the output functionality of the TTL channels and instead opt for 32 input channels which can be dynamically assigned to control the 16 analog outputs. These analog outputs may be conditioned as static, simple switched, cascading switched, or simple boolean controlled outputs all configurable via software. Additional features include logic inputs which can be shared to multiple outputs and simple waveform generation such as linear ramps.

### **2.4.3 Ancillary laboratory systems**

#### **2.4.3.1 Trim coils**

The trim coils are a cubic, 11.5" cage with current coils providing B-field in a Helmholtz configuration. These coils are used to trim out static residual magnetic fields and to apply dynamic and well controlled bias magnetic fields. We commonly use the coils along the Z-direction to apply bias magnetic fields during spectroscopy as shown in Fig. 2.29a.

The narrow linewidth of the  $^3P_1$  states provide a very sensitive probe for precisely zeroing the residual magnetic field. We determine the required bias fields by performing loss spectroscopy with unpolarized light along the  $^1S_0 \rightarrow ^3P_1$  transition using a

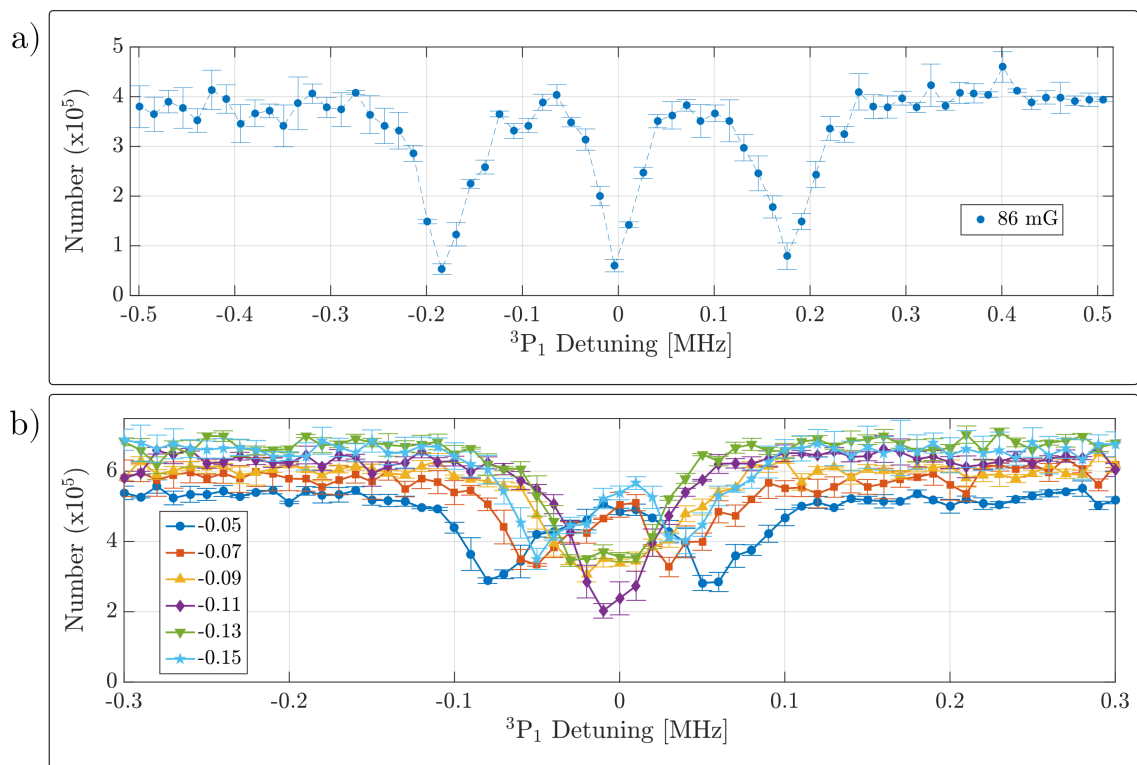


Figure 2.29 : Zeroing residual magnetic fields

Loss spectroscopy in various bias fields. a) Example of resolved Zeeman splitting of the  ${}^3P_1$  magnetic sub-levels. b) Typical B field variation for determining the zero field position. The applied bias is increased for each subsequent scan and a clear zero crossing is observed. The legend has been left in arbitrary lab units to emphasize the B-field zero crossing which occurs around -0.11.

bosonic isotope. Next we fit the  $m_j = \pm 1$  spectral features to a loss line-shape (either gaussian or lorentzian) and plot the line center as a function of applied magnetic field along each dimension. Fig. 2.29b shows an example of the change in Zeeman splitting of the  $m_j$  levels using strontium-84. Finally, we perform a linear fit to the line center variation and extract the intercept which nulls the residual field and the slope which calibrates our applicable field strength per ampere. We have found these calibrations to be  $[\delta B_z = 0.985, \delta B_y = 0.982, \delta B_z = 0.987] \text{ G/A}^{\frac{1}{2}}$ .

#### 2.4.3.2 Zero crossing AC line trigger

Fig. 2.30 shows the circuit used to start the Neutral experimental sequence. It is based on deriving a TTL pulse at the positive-going zero crossing of the 60 Hz building line. Manual triggering is essential since we do not share the same clock source between the two independent pulseblasters (PB0 & PB1). Instead relying on their relative precision and low timing jitter to maintain experimental synchronicity when triggered from a shared source.

Fig. 2.31 shows a comparison of the timing uncertainty when a short 200 ns pulse is output from both pulseblasters and the oscilloscope is triggered from the zero crossing of the AC line. While this measurement does not reveal the cause of the relative instability between the three sources (PB0, PB1, or AC line), we do observe a relative instability of  $\sim 1 \mu\text{s}$ . For most use cases with ultracold matter, this timing uncertainty is entirely reasonable and presents no practical limitation. However, this behavior does preclude the usage of cross-triggers between the pulseblasters when

---

<sup>§</sup>Further details available in Onenote under Research Projects → Routine Studies → B-field zeroing → Zeroing summary

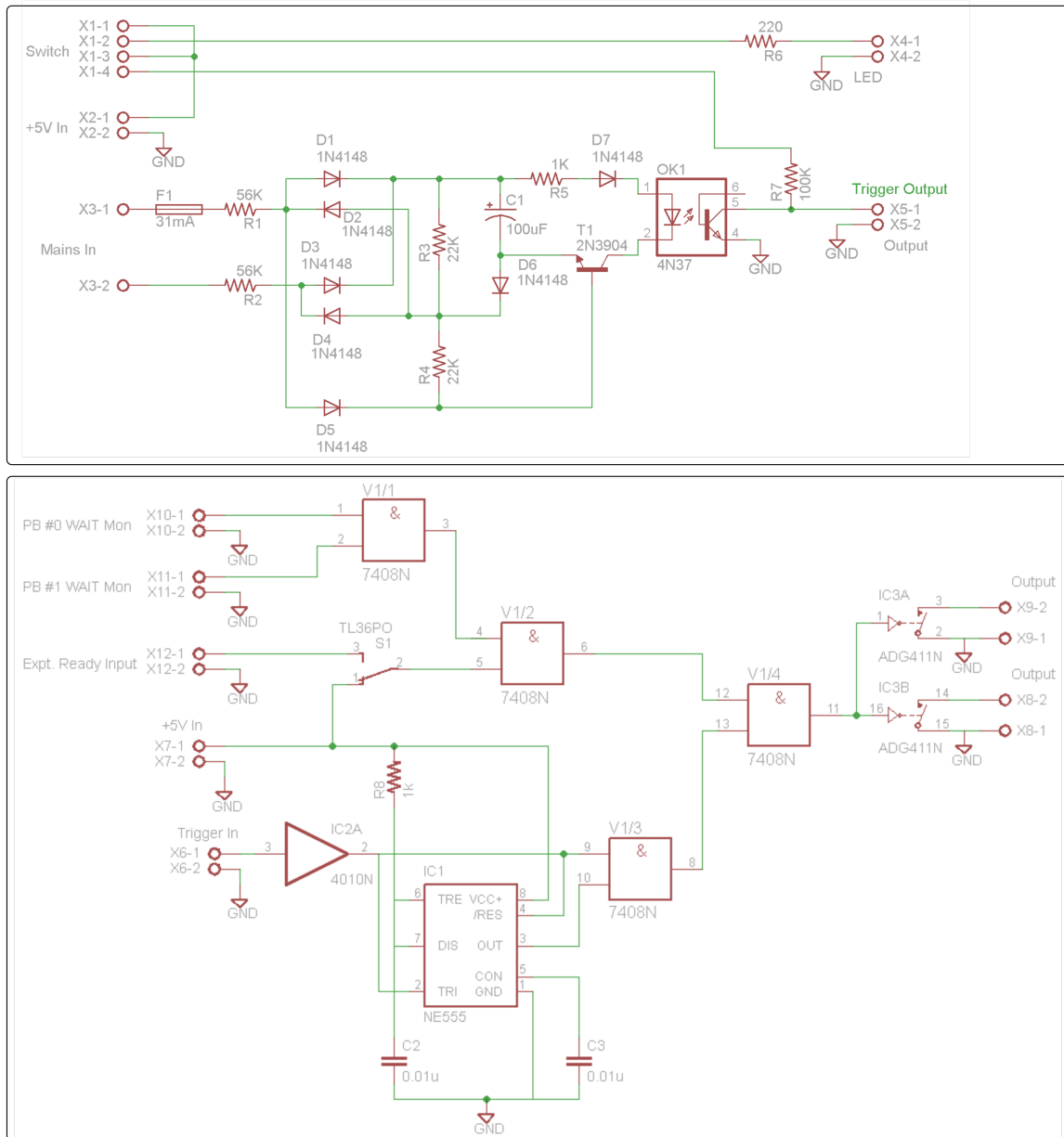


Figure 2.30 : Circuit diagram of the zero crossing AC line trigger

Top - 120 Hz square wave pulser which generates a short pulse on the 60 Hz zero crossing. Bottom - Synchronizer circuit between both pulseblasters, an optional experiment-ready trigger (which ensures the atom shutter is open), and the AC zero-crossing trigger. Trigger input is from the top circuit and is used with the 555 timer in a one-shot configuration. This ensures only every other pulse from the AC trigger produces a TTL high output past the AND gate V1/3.

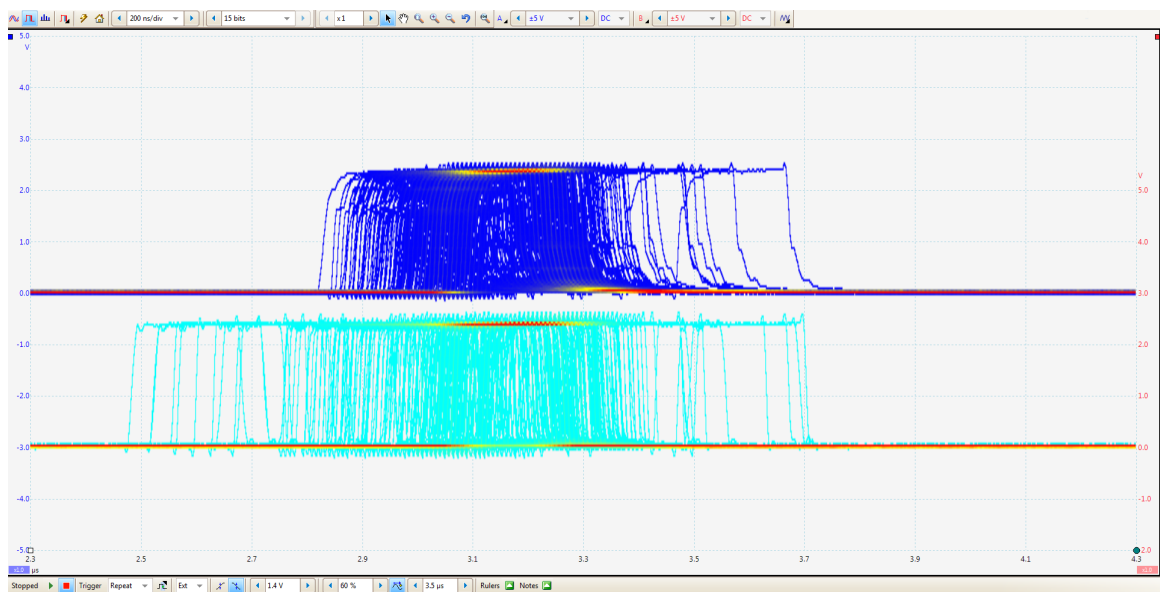


Figure 2.31 : Comparison of pulseblaster timing jitter

A persistent oscilloscope trace showing repeated measurements of a 200 ns logic pulse from each pulseblaster. The upper signal is PB0 and the lower is PB1. The scope is externally triggered by the zero crossing AC line trigger.

performing experiments with the optical lattice<sup>¶</sup>. This timing difference results in a consideration of the discrete timing discussed in Sec. 6.1 whereby, dependent on the dynamics under investigation, even small timing difference can lead to significant variation in the observed phenomena. We mitigate this effect by taking care to trigger all related processes from the same pulseblaster where the timing jitter is reduced to 50 ns.

We choose to trigger off the building wide 60 Hz line in order to maintain a fixed phase relationship from shot to shot. This is thought to act as a common-mode rejection of electrical noise that could couple into our measurements via intensity or frequency noise. Although, we have not rigorously evaluated this hypothesis and no significant change was observed when changing the global experimental trigger.

Finally, the additional logic gates ensure that the pulseblasters trigger at the same time since they are programmed serially by the neuKLEIN software. This process is enabled by a WAIT signal that each pulseblaster outputs when in this state, which is used to ensure proper initialization of the system before starting an experimental sequence.

#### 2.4.3.3 Pneumatic actuated mirror mounts

The lattice arms in the plane of the atoms (A & B) are combined and separated along the 1064 nm ODT path using harmonic beamsplitters as shown in Fig. 6.2. Alignment of the vertical propagating beam presents a challenge as the optical access into the chamber is limited and position of the MOT beams require waveplates along the vertical axis. This places prohibitive constraints on the availability of passive optical

---

<sup>¶</sup>Cross-triggers are defined as the mixing of timing signals between the two pulseblasters. For instance, using PB0 to trigger the turn on of lattice arm A and PB1 to trigger arm B.

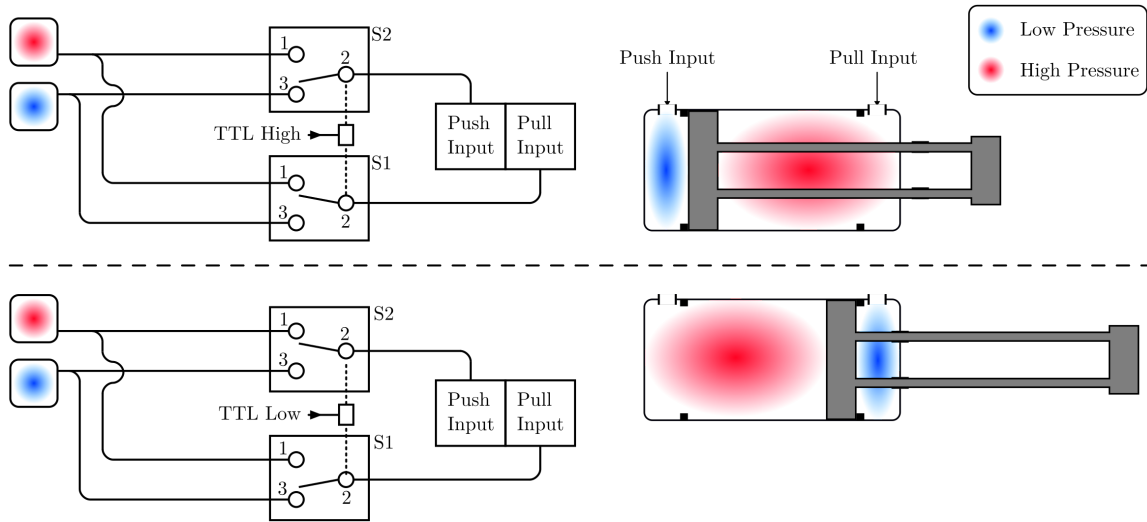


Figure 2.32 : Pneumatic actuators diagram

Example schematic for a single actuator. Three actuators are used on the apparatus to move several components simultaneously. Not shown is the 4-way cross which splits the output from each valve (S1 and S2) to each actuator.

components that might combine the MOT and lattice traps along the vertical path. To overcome this, we employ pneumatic valves and actuators to move the waveplates and requisite MOT mirrors out of the path before turning on the 532 nm light.

Fig. 2.32 shows the flow diagram for switches S1 and S2 for this system where the default position is the lower figure with the actuators extended. As one might expect, this abrupt movement does impart vibrations into to the table which we dampen by slowing the movement and cushioning the stops. In practice we find that the system is fairly robust against these small "kicks" ||.

---

|| Although occasionally the air pressure must be adjusted if the lasers are behaving erratically.

## Chapter 3

### Photoassociation in ultracold gases

#### 3.1 Introduction

Photoassociation is the process by which colliding atoms, illuminated by resonant laser light, absorb photons and associate to form a bound molecule. Shown in Fig. 3.1a, one-photon photoassociation results in the creation of an excited weakly-bound molecular state when the laser frequency is appropriately tuned. Photoassociation is primarily concerned with long-range weakly bound molecules since the excitation rate to these states depends on the overlap of the initial scattering state and the bound state. Fig. a shows that primary interparticle spacing which contributes to the overlap integral is situated around the classical turning point of the molecule, this point is known as the Condon point,  $R_c$ . Contribution to the overlap is negligible for nearly the entire region  $r < R_c$  due to the fast oscillations in the inner parts of the both wavefunctions. Furthermore, the Condon point moves inward as the binding energy of the bound state molecules is increased. This causes overlap with the initial scattering state to decrease and correspondingly a decrease in the rate of molecule formation. Thus, photoassociation may be considered a long-range probe which can be used to measure and determine characteristics about the complex short-range potential.

Fig. b shows an alternative view of photoassociation in the dressed-state picture. In this formulation, photoassociation is naturally described by resonant scattering

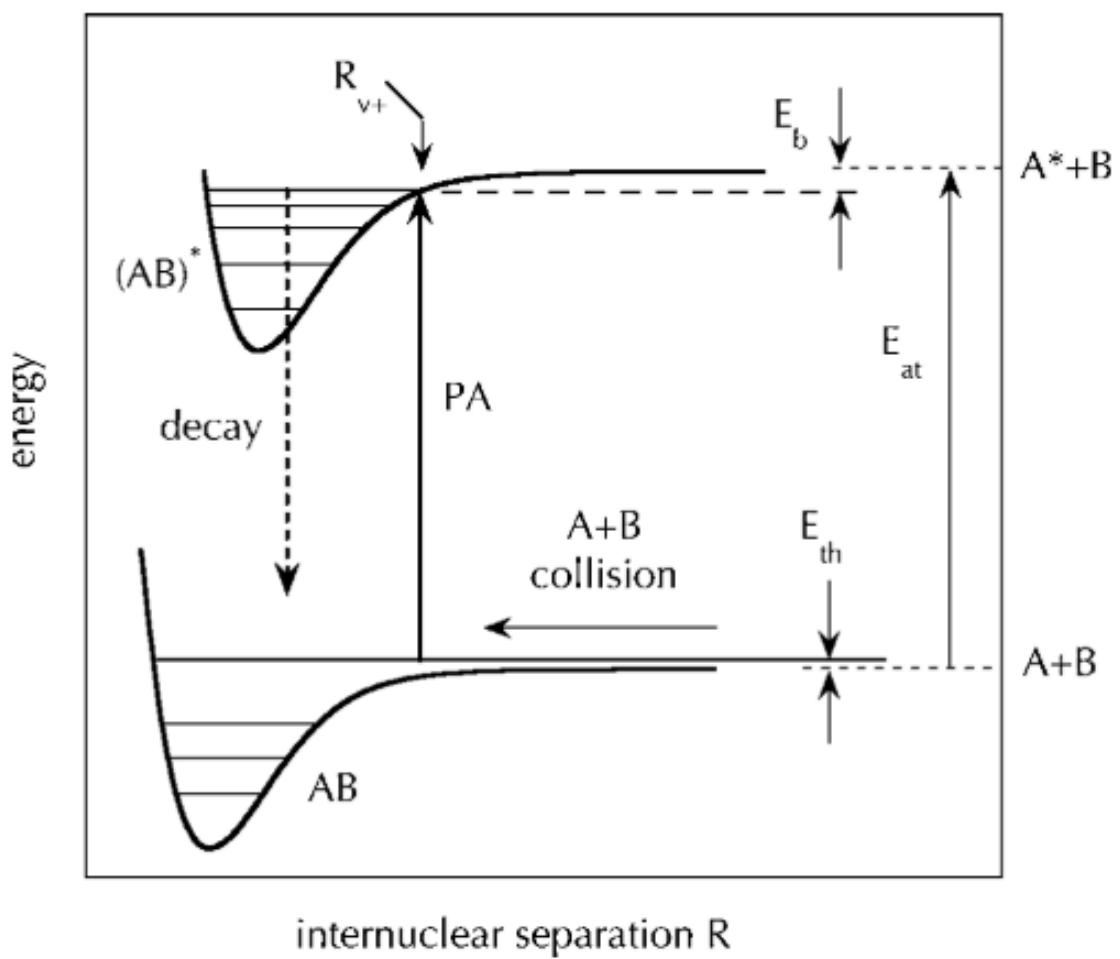


Figure 3.1 : Schematic of the photoassociation process

theory whereby bound states are considered embedded in a continuum of thermally distributed scattering states. Collisions between atoms are altered by the presence of light-field coupling that may, in general, lead to modification of the elastic scattering between atoms or introduce loss due to inelastic scattering [42] [Fan61, Tho87].

While the idea of photoassociation is fairly straightforward, a rigorous theoretical understanding of the process requires discussion of several key topics related to the behavior of ultracold gases. In particular, the rate of photoassociation of a trapped gas is sensitive to a number of energetic effects including the gases thermal kinetic energy, external potential energy from trapping potentials, and internal interaction energy due to inter-particle scattering [43]. The remainder of this chapter will discuss each of these in turn and end by formulating an approachable analytic description for modeling photoassociation spectra.

## 3.2 Theory of trapped boson gases

This section will briefly cover the statistical mechanics describing a trapped thermal bosonic gas. From this description we discuss the evolution of these densities under free expansion and discern how to extract physical parameters of the gas from absorption images.

In the limit of large, fixed particle number, the trapped density distribution  $n(\mathbf{r})$  is given by

$$n_{th}(\mathbf{r}) = \int \frac{d\mathbf{p}}{2\pi\hbar^3} \frac{1}{\exp((E_p(\mathbf{r}) - \mu)/k_B T) - 1} \quad (3.1)$$

where  $E_p(\mathbf{r}) = \frac{p^2}{2m} + V(\mathbf{r})$ . This semi-classical description assumes negligible occupation of the trap ground state. This integral can be evaluated by defining the

quantities

$$x = \frac{p^2}{2mk_B T} \quad z(\mathbf{r}) = e^{[\mu - V(\mathbf{r})]/k_B T} = \xi e^{-V(\mathbf{r})/k_B T}$$

where  $\xi$  is known as the fugacity [72]. After a change of variables from  $p$  to the dimensionless quantity  $x$ , Eq. 3.1 reduces to

$$n_{th}(\mathbf{r}) = \frac{2}{\sqrt{\pi}} \frac{1}{\lambda_T^3} \int dx \frac{\sqrt{x}}{z^{-1}e^x - 1} \quad (3.2)$$

where  $\lambda_T = \sqrt{\frac{2\pi\hbar^2}{mk_B T}}$  is the de Broglie wavelength. This is a common integral in problems of this type and may be rewritten as [24, 48, 72]

$$\begin{aligned} \int_0^\infty dx \frac{x^{\gamma-1}}{z^{-1}e^x - 1} &= \sum_{n=1}^\infty \int_0^\infty dx x^{\gamma-1} e^{-nx} z^n \\ &= \Gamma(\gamma) \text{Li}_\gamma[z] \end{aligned} \quad (3.3)$$

where  $\text{Li}_\gamma[z]$  is the polylogarithm function defined by  $\text{Li}_\gamma[z] = \sum_{n=1}^\infty \frac{z^n}{n^\gamma}$ . This function is also known as the Bose enhancement function [48] and describes the bunching of bosonic particles near degeneracy. The thermal distribution is then given by

$$\begin{aligned} n_{th}(\mathbf{r}) &= \frac{\text{Li}_{\frac{3}{2}}[z(\mathbf{r})]}{\lambda_T^3} \\ &= \frac{1}{\lambda_T^3} \text{Li}_{\frac{3}{2}}[\xi \exp(-V(\mathbf{r})/k_B T)] \end{aligned} \quad (3.4)$$

For harmonic traps  $V(\mathbf{r}) = \frac{m}{2} \sum_i \omega_i^2 r_i^2$  and the *in-situ* density profile is

$$n_{th}(\mathbf{r}) = \frac{1}{\lambda_T^3} \text{Li}_{\frac{3}{2}} \left[ \xi \exp \left( \sum_i \frac{-m\omega_i^2 r_i^2}{2k_B T} \right) \right] \quad (3.5)$$

In the classical, or high-temperature limit,  $\text{Li}_{\frac{3}{2}}[z(\mathbf{r})] \approx z(\mathbf{r})$  and we recover the classical Maxwell-Boltzmann description

$$n_{MB}(\mathbf{r}) = \frac{\xi}{\lambda_T^3} \exp \left( \sum_i \frac{-m\omega_i^2 r_i^2}{2k_B T} \right) \quad (3.6)$$

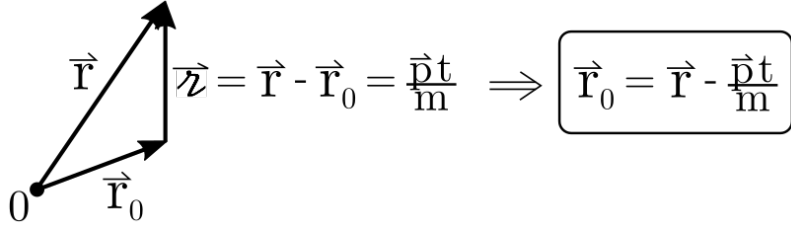


Figure 3.2 : Ballistic expansion of particles

Schematic representation particle displacement vectors used to determine how time-of-flight expansion transforms the initial density distribution

### 3.2.1 Extracting data from column densities

This description of thermal bosons in a trapping potential is useful but we must continue a step further and see how Eq. 3.5 evolve in free space. Once the trapping potential is removed, neglecting any collisions, atoms will expand according to

$$\frac{d\mathbf{r}}{dt} = \frac{\mathbf{p}}{m} \quad \text{and} \quad \frac{d\mathbf{p}}{dt} = 0 \quad (3.7)$$

Thus, an atom measured at position  $\mathbf{r}$  after the time-of-flight,  $t$ , will have traveled a distance  $\zeta = \frac{\mathbf{p}t}{m} = \mathbf{r} - \mathbf{r}_0$  from its initial position  $\mathbf{r}_0$ . This is shown schematically in Fig. 3.2. The spatial density evolves then

$$\begin{aligned} n_{th}(\mathbf{r}, t)' &= \int \frac{d^3\mathbf{r} d^3\mathbf{p}}{(2\pi\hbar)^3} \frac{1}{\exp\left(\left[\frac{\mathbf{p}^2}{2m} + V(\mathbf{r}') - \mu\right] \frac{1}{k_B T}\right) - 1} \delta^3\left(\mathbf{r} - \frac{\mathbf{p}t}{m} - \mathbf{r}'\right) \\ &= \int \frac{d^3\mathbf{p}}{(2\pi\hbar)^3} \frac{1}{\exp\left(\left[\frac{\mathbf{p}^2}{2m} + V\left(\mathbf{r} - \frac{\mathbf{p}t}{m}\right) - \mu\right] \frac{1}{k_B T}\right) - 1} \end{aligned} \quad (3.8)$$

Adding the harmonic potential, the free expansion after release from a harmonic trap is found to be self-similar and amounts to rescaling the the spatial coordinates [24]. Thus the scaled spatial profile is given by

$$n'_{th}(\mathbf{r}, t) = \frac{1}{\lambda_T^3} \left( \prod_{j=1}^3 \frac{1}{1 + \omega_j^2 t^2} \right) \text{Li}_{\frac{3}{2}} \left[ \xi \exp \left( \sum_{i=1}^3 \frac{-m\omega_i^2 r_i^2}{2k_B T} \frac{1}{1 + \omega_i^2 t^2} \right) \right] \quad (3.9)$$

Using this description of the spatial distribution after time-of-flight expansion, we must now consider how to relate our absorption images to the physically relevant variables of the gas.

Absorption imaging is the process of illuminating a gas of atoms with resonant (or near resonant) laser light and taking a spatially resolved image of the laser beam. When illuminated, the atoms will absorb and scatter photons out of the laser beam resulting in a "shadow". Using Beer's law [cite](#), we can relate the total absorption of photons to the number density of scattering particles along the optical path multiplied by the absorption cross section. This results in a measurement of the "optical depth" of the gas along a column density. Measurement along a particular direction limits our description of the gas to the two-dimensional plane orthogonal to the laser beam.

Experimentally, the optical depth is computed by taking the natural logarithm of the ratio of the images obtained from the camera. Using the analytic form of the expanded density profile in Eq. 3.2.1, the optical depth can be fit to extract physical quantities. We equate this OD image to be proportional to the spatial density profile after the time-of-flight expansion integrated along the optical path through the atoms.

$$\begin{aligned} \text{OD} &= \ln \left( \frac{\text{Atom Image}}{\text{Background Image}} \right) = \sigma_{\text{abs}} \int_{-\infty}^{\infty} dz n'_{th}(\mathbf{r}, t) \\ &= \frac{\sigma_{\text{abs}}}{\lambda_T^3} \left( \prod_{j=1}^3 \frac{1}{1 + \omega_i^2 t^2} \right) \int_{-\infty}^{\infty} dz \text{Li}_{\frac{3}{2}} \left[ \xi \exp \left( \sum_{i=1}^3 \frac{-r_i^2}{2\sigma_i^2} \right) \right] \end{aligned} \quad (3.10)$$

where  $\sigma_i^2 = \frac{k_B T}{m \omega_i^2} (1 + \omega_i^2 t^2)$  and  $\sigma_{\text{abs}}(\omega_{img})$  is the optical absorption cross section dependent on the imaging laser frequency,  $\omega_{img}$ .

Before proceeding, we'll rewrite the polylogarithm in terms of it's series representation and integrate over a particular direction to replicate the column density image

of the experimental data.

$$\int_{-\infty}^{\infty} dz \text{Li}_{\frac{3}{2}} \left[ \xi \exp \left( \sum_{i=1}^3 \frac{-r_i^2}{2\sigma_i^2} \right) \right] = \int_{-\infty}^{\infty} dz \sum_{n=1}^{\infty} \frac{\xi^n}{n^{3/2}} \exp \left( \frac{-x^2}{2\sigma_x^2} - \frac{y^2}{2\sigma_y^2} - \frac{z^2}{2\sigma_z^2} \right)^n \quad (3.11)$$

Defining  $\rho = \exp \left( \frac{-x^2}{2\sigma_x^2} - \frac{y^2}{2\sigma_y^2} \right)$  and expanding

$$= \int_{-\infty}^{\infty} dz \xi \rho e^{\frac{-z^2}{2\sigma_z^2}} + \frac{\xi^2}{2^{3/2}} \rho^2 e^{\left( \frac{-z^2}{2\sigma_z^2} \right)^2} + \frac{\xi^3}{3^{3/2}} \rho^3 e^{\left( \frac{-z^2}{2\sigma_z^2} \right)^3} + \dots \quad (3.12)$$

This expansion readily shows the dependence on  $z$  which we can integrate along this direction, noting  $\int_{-\infty}^{\infty} dz \sum_{n=1}^{\infty} \exp \left( \frac{-z^2}{2\sigma_z^2} \right) = \frac{\sqrt{2\pi}}{n^{1/2}} \sigma_z$ , Eq. 3.12 then reduces to

$$\begin{aligned} &= \int_{-\infty}^{\infty} dz \sum_{n=1}^{\infty} \frac{\xi^n \rho^n}{n^{3/2}} \exp \left( \frac{-z^2}{2\sigma_z^2} \right) \\ &= \sqrt{2\pi} \sigma_z \underbrace{\sum_{n=1}^{\infty} \frac{\xi^n \rho^n}{n^2}}_{\text{Li}_2[\xi \rho]} \end{aligned} \quad (3.13)$$

Returning to Eq. and using the result of integration.

$$OD(x, y) = \frac{\sqrt{2\pi}}{\lambda_T^3} \frac{\sigma_{\text{abs}} \sigma_z}{(1 + \omega_x^2 t^2)(1 + \omega_y^2 t^2)(1 + \omega_z^2 t^2)} \text{Li}_2 \left[ \xi \exp \left( \frac{-x^2}{2\sigma_x^2} - \frac{y^2}{2\sigma_y^2} \right) \right] \quad (3.14)$$

This equation still has one unknown,  $\sigma_z$ , that we cannot readily measure. This is solved by measuring a specific value of the optical depth, namely the peak optical depth,  $OD_{\text{peak}}(x = 0, y = 0)$ .

$$OD_{\text{peak}} = \frac{\sqrt{2\pi}}{\lambda_T^3} \frac{\sigma_{\text{abs}} \sigma_z}{(1 + \omega_x^2 t^2)(1 + \omega_y^2 t^2)(1 + \omega_z^2 t^2)} \text{Li}_2[\xi] \quad (3.15)$$

Thus the relation between the measured optical depth and the spatial density distribution is given by

$$OD(x, y) = \frac{OD_{\text{peak}}}{\text{Li}_2[\xi]} \text{Li}_2 \left[ \xi \exp \left( \frac{-x^2}{2\sigma_x^2} - \frac{y^2}{2\sigma_y^2} \right) \right] \quad (3.16)$$

with  $\sigma_i^2 = \frac{k_B T}{m\omega_i^2}(1 + \omega_i^2 t^2)$ . In the limit of long expansion time during time-of-flight, namely  $t \gg \omega_x^{-1}, \omega_y^{-1}, \omega_z^{-1}$  then the width approach  $\sigma_i^2 \rightarrow \frac{k_B T}{m} t^2$ . From long-time expansion, the atom temperature is given along each axis by

$$T_i = \frac{m\sigma_i^2}{k_B t^2} \quad (3.17)$$

The generally limiting factor in the allowed expansion time is due to center of mass motion of the cloud under the influence of gravity. In the Neutral apparatus we typically utilize drop times  $\approx 30$  ms before we can no longer view the atoms. For shallow traps,  $\omega_i$  on the order of  $< 10$  Hz, the applicability of the above approximation should be validated as cold atoms may not achieve fully ballistic expansion,  $\omega_i^2 t^2 \gg 1$ , before falling out of frame.

Finally, we can also determine the total number of atoms in the trapping potential by requiring the particle number to be fixed as  $n_{th}(\mathbf{r}) \Rightarrow n'_{th}(\mathbf{r}, t)$ .

$$\begin{aligned} N &= \int_{-\infty}^{\infty} d^3\mathbf{r} n_{th}(\mathbf{r}) = \int_{-\infty}^{\infty} d^3\mathbf{r} n'_{th}(\mathbf{r}, t) \\ &= \int_{-\infty}^{\infty} d^3\mathbf{r} \frac{\sigma_{abs}}{\lambda_T^3} \frac{1}{(1 + \omega_x^2 t^2)(1 + \omega_y^2 t^2)(1 + \omega_z^2 t^2)} \sum_{n=1}^{\infty} \frac{\xi^n}{n^{3/2}} \exp\left(\frac{-x^2}{2\sigma_x^2} - \frac{y^2}{2\sigma_y^2} - \frac{z^2}{2\sigma_z^2}\right)^n \end{aligned} \quad (3.18)$$

Applying the same expansion and identity as in Eq. 3.12, we find

$$N = \frac{(2\pi)^{3/2}}{\lambda_T^3} \frac{\sigma_x \sigma_y \sigma_z}{(1 + \omega_x^2 t^2)(1 + \omega_y^2 t^2)(1 + \omega_z^2 t^2)} \text{Li}_3[\xi] = 2\pi \frac{\sigma_x \sigma_y}{\sigma_{abs}} OD_{\text{peak}} \frac{\text{Li}_3[\xi]}{\text{Li}_2[\xi]} \quad (3.19)$$

### 3.3 Atomic collisions

Atomic collisions may be envisioned as an interferometer of the incoming and outgoing waves due to reflection by the short-range interatomic potential [42]. Through their interference a standing wave pattern is established that extends out to infinity. With this picture, we can begin to understand how the effects of short-range couplings

between atoms can influence their long-range behavior as any small change in the "interferometer" is reflected across the entire wave. A notable achievement of atomic collision theory has been the successful separation of length scales into regions that exhibit very different characteristic length and energy scales. Through this separation, a great deal of insight has led to the development of many practical methods for studying the scattering states and weakly bound molecular states near zero-energy ch.6 - [3, 4, 5, 6, 7, 8, 9, 10, 11].

### 3.3.1 Single channel scattering near threshold

Consider the collision of two structureless atoms interacting by a single adiabatic Born-Oppenheimer potential, which at long-range is given by  $V(r)_{\text{long}} \sim -\frac{C_6}{r^6}$ . We are interested in understanding the van der Waals interaction as it is the dominant term in the long-range interaction between two ground state neutral atoms. This potential has a characteristic length,  $R_{vdW} = \frac{1}{2} \left( \frac{2\mu C_6}{\hbar^2} \right)^{1/6}$ , and energy,  $E_{vdW} = \frac{\hbar^2}{2\mu R_{vdW}^2}$ . However, the closely related characteristic scales from Gribakin and Flambaum [31] prove to be more useful

$$\bar{a} = \frac{4\pi}{\Gamma(1/4)^2} R_{vdW} \quad \bar{E} = \frac{\hbar^2}{2\mu \bar{a}^2} \quad (3.20)$$

where  $\Gamma(x)$  is the Gamma function.

The wavefunction for relative motion is found by solving the radial Schrödinger equation

$$-\frac{\hbar^2}{2\mu} \frac{d^2\phi_\ell}{dr^2} \left( V(r) + \frac{\hbar^2 \ell(\ell+1)}{2\mu r^2} \right) \phi_\ell = E \phi_\ell \quad (3.21)$$

Solutions of Eq.3.21, for energies  $E > 0$  are the scattering states  $\phi_\ell(E)$  with collision wavevector  $k = \sqrt{2\mu E / \hbar^2}$ . In the region  $r \gg \bar{a}$ , the scattering states approach the

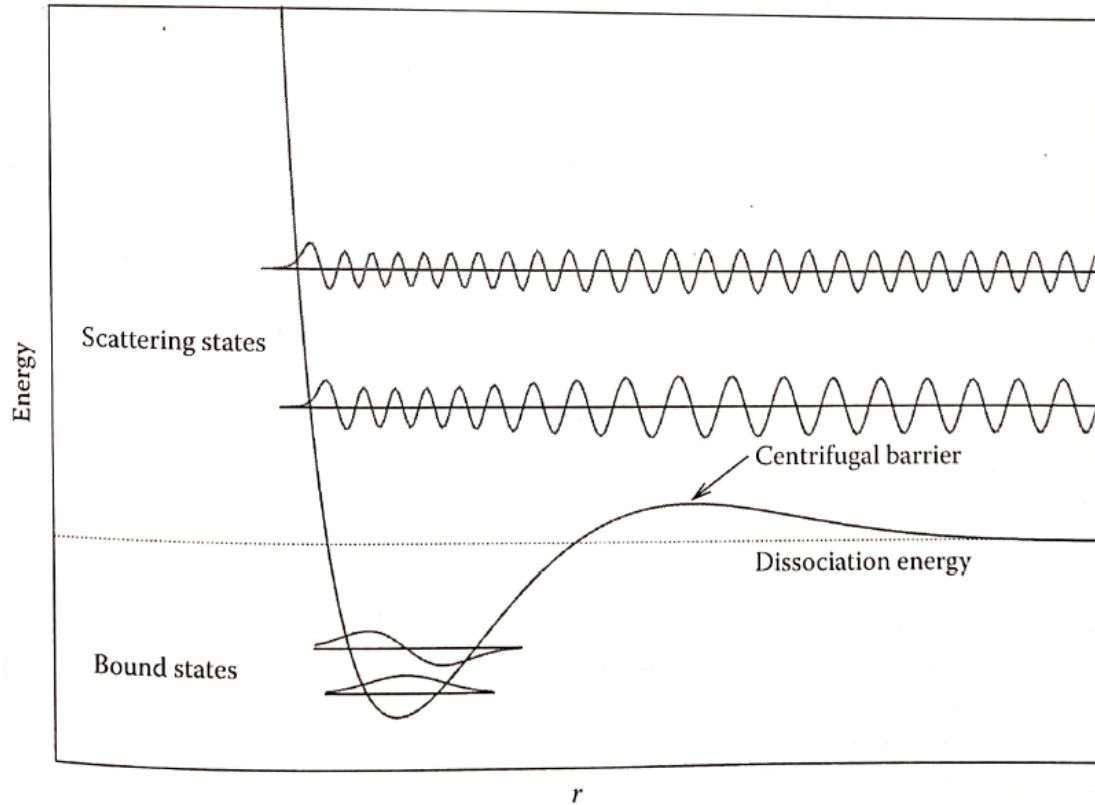


Figure 3.3 : Examples of scattering state solutions

free particle state

$$\phi_\ell(E) \rightarrow \frac{\sin(kR - \pi\ell/2 + \eta_\ell)}{\sqrt{k}} \quad (3.22)$$

with de Broglie wavelength  $\lambda = 2\pi/k$ .

The origin of the phase shift  $\eta_\ell$  in Eq. 3.22 can be seen by considering the scattering state  $\phi_\ell$  for several different energies as shown in Fig.. In this figure we see that, for low energy, as atoms near  $r \sim \bar{a}$  they are accelerated by the interatomic potential. This results in a shortening of the local de Broglie wavelength to  $\lambda_{\text{local}} = 2\pi\hbar/\sqrt{2\mu(E - V(R))}$  and a change in the overall phase of the wavefunction as it is pulled inward. In the limit  $E \rightarrow 0$ ,  $V(R)$  becomes the dominant energy scale

and the local de Broglie wavelength becomes independent of the incident energy. Thus near threshold, small changes in the collision energy do not change the oscillation frequency and the imparted phase shift, due to acceleration by the potential, is constant. This results in the s-wave scattering length,  $a$ . The scattering phase shift is related to  $a$  by

$$a = -\frac{\tan \eta_0(k)}{k} \quad (3.23)$$

where  $\eta_\ell$  is the additional phase in Eq. 3.22 and  $k = \sqrt{2\mu E/\hbar^2}$  is the collision wavevector. Finally, as energy is increased, the effect of the potential on the scattering state is reduced and the de Broglie wavelength once more remains constant for all interatomic distances.

From this simple picture, we see that changing the atom's reduced mass  $\mu$  and keeping  $V(r)$  fixed will also lead to a change in the local de Broglie wavelength when  $r < \bar{a}$ . This mass-scaling then appears like a change in the s-wave scattering length. This method has been highly successful in determining the scattering lengths of many isotopes [43].

A change in the reduced mass is not isolated to effecting the scattering states. In general, the binding energies of the bound states at  $E < 0$  will also change. In some case this may lead to changing the number of supported states in the potential. Gribakin and Flambaum [31] calculated the relationship between the scattering length and the potential as

$$a = \bar{a} \left[ 1 - \tan(\Phi - \frac{\pi}{8}) \right] \quad (3.24)$$

where

$$\Phi = \int_{R_i}^{\infty} \sqrt{\frac{-2\mu V(R)}{\hbar^2}} \quad (3.25)$$

Fig. 3.3.1 shows the effect of mass-scaling on a sample system. The change in the

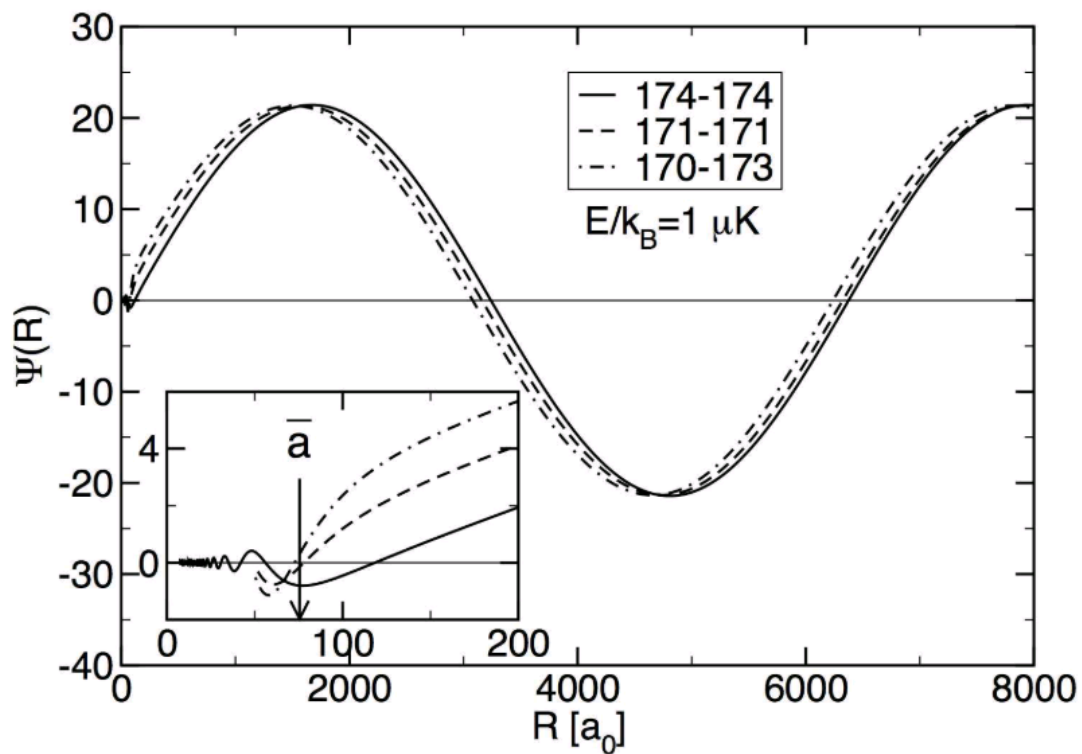


Figure 3.4 : Long range phase shift

note fast oscillations and that the amplitude goes as  $\sqrt{k}$

s-wave scattering length can be seen as a shift of the asymptotic wavefunctions at long-range.

Bound states also play an important role in scattering. In particular, in the simplest approximation, the binding energy of the least bound state is given by

$$E_{-1} = -\frac{\hbar^2}{2\mu a^2} \text{ as } a \rightarrow +\infty \quad (3.26)$$

However, accounting for the phase accumulation due to the long-range part of the van der Waals potential modifies the binding energy with  $\bar{a}$  [31].

$$E_{-1} = -\frac{\hbar^2}{2\mu(a - \bar{a})^2} \quad (3.27)$$

This approaches the universality limit when  $a \gg \bar{a}$ . Remarkably, a higher order correction to the van der Waals potential gives the binding energy as

$$E_{-1} = -\frac{\hbar^2}{2\mu(a - \bar{a})^2} \left[ 1 + \frac{g_1 \bar{a}}{a - \bar{a}} + \frac{g_2 \bar{a}^2}{(a - \bar{a})^2} + \dots \right] \quad (3.28)$$

where  $g_1 = \frac{\Gamma(1/4)^4}{6\pi^2} - 2$  and  $g_2 = \frac{5g_1^2}{4} - 2$  [28]. Ch. 5 will employ each of these estimates in analysis of the  $^{86}\text{Sr}$  halo molecule.

### 3.3.2 Remarks on *S*-matrix

In the previous section, we focused on interactions restricted to a single channel without any decay mechanism. Such interactions are necessarily elastic as the two-body scattering wavefunction cannot couple outside of its channel. However, most atoms used in laser-cooling exhibit a high degree of internal structure and a quantitative description of their collisions at short-range  $r < \sim \bar{a}$ , requires consideration of coupling among many different channels. While a full characterization of such methods is left to Refs.[37] refs, here we give the primary results which will be useful for describing photoassociation in the next section.

In this formalism, the atoms are consider in one of several quantum states, labeled the entrance channel and defined to have energy  $E = 0$ . Scattering channels are specified by a collective set of quantum numbers,  $\alpha$ , representing the state of each atom. Channels with  $E > 0$  are labeled closed, while those with  $E < 0$  are open. Upon solving a matrix formulation of Schrödinger equation, the effect of all short-range interactions during a collision with  $E > 0$  is summarized in the unitary  $S$ -matrix, and reflected in the scattering wavefunction for  $r \rightarrow \infty$ . Thus the  $S$ -matrix is the generalization of the energy-dependent phase shift,  $\eta_\ell(k)$ , across all the channels.

In the case of a single open channel scattering near threshold the  $S$ -matrix is reduced to a single element  $S(k) = e^{2i\eta(k)}$  represented by the complex energy-dependent phase shift  $\eta(k)$ . This phase shift also defines a complex energy-dependent scattering length

$$\alpha(k) = a(k) - ib(k) = -\frac{\tan \eta_0(k)}{k} = \frac{1}{ik} \frac{1 - S(k)}{1 + S(k)} \quad (3.29)$$

which is incredibly useful in the theory of magnetic and optical feshbach resonances, which are closely related to photoassociation [refs](#).

Finally, the  $S$ -matrix is also related to the elastic and inelastic cross sections by

$$\sigma_\alpha^{\text{el}}(k) = \frac{\pi g_\alpha}{k^2} |1 - S_{\alpha\alpha}(k)|^2 \quad (3.30)$$

$$\sigma_\alpha^{\text{in}}(k) = \frac{\pi g_\alpha}{k^2} (1 - |S_{\alpha\alpha}(k)|^2) \quad (3.31)$$

where  $g_\alpha$  is a channel specific collisional symmetry factor which is equal to 2 for describing inelastic collisions in a Maxwellian gas of two atoms of the same species in identical spin states [17].

### 3.4 Modeling of photoassociation lineshapes

With the section develops the theory we use to describe one- and two-photon photoassociative spectra with a focus on developing the equations necessary for modeling lineshapes presented in the following chapters.

Recall the classical result for the rate of two-body collisions in a monoenergetic gas is given by  $\Gamma = v \sigma n = Kn$ , where  $v$  is the velocity of each particle,  $\sigma$  is the scattering cross-section, and  $n$  is the particle density. Here  $K$  is identified as the two-body collision rate constant which for inelastic collisions governs the evolution of the density through  $\dot{n} = Kn^2$ .

Similarly, for scattering of quantum particles, the inelastic collision rate constant\* for a specific channel  $\alpha$ , is given by [69]

$$K_\alpha^{in}(k) = v \sigma_\alpha^{in}(k) \quad (3.32)$$

where  $v = \frac{\hbar k}{\mu}$  is the relative collision velocity in the center-of-mass frame for the atom pair with reduced mass  $\mu$  and  $\sigma_\alpha^{in}(k)$  is given by Eq. 3.31. We see that the inelastic cross section simply characterizes the coupling of channel  $\alpha$  to all other channels by recalling that the scattering  $S$ -matrix is unitary and thus

$$1 - |S_{\alpha\alpha}|^2 = \sum_{\alpha' \neq \alpha} |S_{\alpha\alpha'}|^2 \quad (3.33)$$

In the case of ultracold photoassociation, we are concerned with the evolution of a single ground state undergoing s-wave collisions that is coupled to one or few internal states leading to decay. Thus, at a fixed collision energy  $\epsilon = \hbar^2 k^2 / 2\mu$ , the loss rate constant due to inelastic collisions may be written as

$$K_{\text{loss}}(k) = g \frac{\pi \hbar}{\mu k} \sum_{\alpha' \neq \alpha} |S_{\alpha\alpha'}|^2 \quad (3.34)$$

---

\*also called the loss rate constant in literature

Finally, in order to compare to experimental data, we must consider a thermal average of the loss rate constant given by [43–45]

$$\langle K_{\text{loss}} \rangle = \int_0^\infty dv f_T(v) v \sigma_{in} \quad (3.35)$$

$$= \int_0^\infty d\epsilon f_T(\epsilon) g \frac{\pi \hbar}{\mu} \frac{\hbar}{\sqrt{2\mu\epsilon}} \sum_{\alpha' \neq \alpha} |S_{\alpha\alpha'}|^2 \quad (3.36)$$

$$= \frac{g}{h Q_T} \int_0^\infty d\epsilon \sum_{\alpha' \neq \alpha} |S_{\alpha\alpha'}|^2 e^{-\epsilon/k_B T} \quad (3.37)$$

where  $Q_T = (2\pi k_B T \mu / h^2)^{3/2}$  is the partition function. Here we have performed a change of variables using  $\mu v^2/2 = \epsilon$ . Eq. 3.35 assumes the relative collision energy distribution,  $f_T(\epsilon)$ , is a Maxwell-Boltzmann distribution.

$$f_T(\epsilon) = 2 \sqrt{\frac{\epsilon}{\pi}} \left( \frac{1}{k_B T} \right)^{3/2} e^{-\epsilon/k_B T} \quad (3.38)$$

With the expression for  $K_{\text{loss}}$  in Eq. 3.35, a description of photoassociation reduces to determining the relevant channel couplings and matrix elements needed from the scattering  $S$ -matrix and plugging them in. The most general approach for evaluating the  $S$ -matrix for scattering problems involving two or more channels is the coupled-channel method. Alternatively, analytic approximations for  $S$  exist if the scattering problem is in the isolated resonance regime. The isolated resonance approximation assumes that each molecular bound state is far from any molecular states and can be described by a local strength parameter independent of energy and molecular detuning [69]. Photoassociation is well described by an isolated resonance treatment as specific resonances are targeted and the number of relevant channels is relatively few. For the case of one- and two-color photoassociation, Bohn and Julienne derive approximate analytic expressions of the  $S$ -matrix elements using a multi-channel description of resonant scattering and applying a quantum defect treatment to approximate the wavefunctions in all channels [9, 10, 46].

We model both one- and two-photon PAS of ultracold atoms by first considering the evolution of a local density given by

$$\dot{n} = -2Kn^2 - \Gamma n \quad (3.39)$$

where  $\Gamma$  is the one-body loss rate due to background collisions and  $K$  is the loss rate constant. By integrating over the trapping volume, we find the evolution of the total number of trapped atoms is given by

$$N(t) = \frac{N_0 e^{-\Gamma t}}{1 + \frac{2N_0 \langle K \rangle V_q}{\Gamma V_1^2} (1 - e^{-\Gamma t})} \quad (3.40)$$

where  $N_0$  is the initial number of trapped atoms,  $\langle K \rangle$  is the trap-averaged loss rate constant, and  $V_q$  is the effective trap volume given by

$$V_q = \int_V d^3r \exp\left(-\frac{qU(\mathbf{r})}{k_B T}\right), \quad (3.41)$$

for trapping potential  $U(\mathbf{r})$ .

In one-color photoassociation, a single laser at frequency  $\omega_1$  couples pairs of colliding ground-state atoms with relative kinetic energy  $\epsilon$  to an excited bound state  $b_1$  with energy  $E_{b1}$  and decay rate  $\gamma_1$ . Here,  $\Delta_1 = \omega_1 - E_{b1}/\hbar$  is used to characterize the single photon detuning from the target state. Following the approach of Bohm and Julienne [10], the theoretical description of the bound state  $b_1$  is paired with an artificial, purely repulsive, potential  $a_1$  used to simulate decay from the bound state. State  $b_1$  is then allowed to couple to both the artificial channel and the ground state, while the ground state is defined to only couple to state  $b_1$ <sup>†</sup>. Thus the scattering probability  $|S_{\epsilon, a_1}|^2$  is the only relevant  $S$ -matrix element for describing inelastic loss due to one-photon PAS. This matrix element characterizes the probability that an

---

<sup>†</sup>This is discussed near Eq. 3.1 for one-photon PA scattering matrix in [10]

atom pair in the ground state with relative collision energy  $\epsilon$  scatters into the artificial loss channel  $a_1$  and is given by

$$|S_{\epsilon,a_1}|^2 = \frac{\gamma_1 \gamma_s(\epsilon)}{(\Delta_1 + \epsilon/\hbar)^2 + \left(\frac{\gamma_1 + \gamma_s(\epsilon)}{2}\right)^2} \quad (3.42)$$

where  $\gamma_s(\epsilon)$  is the stimulated width of  $b_1$  due to coupling to the initial scattering state by the PAS lasers, which for low energy can be expressed as [19, 71? ]

$$\gamma_s(\epsilon) = 2k\ell_{\text{opt}}\gamma_1, \quad (3.43)$$

The optical length  $\ell_{\text{opt}}$  characterizes the strength of coupling bound state  $b_1$  and is related to the overlap between the initial colliding state and  $b_1$ , and  $k = (2\mu\epsilon)^{1/2}/\hbar$ . Plugging  $|S_{\epsilon,a_1}|^2$  into Eq. 3.35 then the thermally averaged loss rate constant for one-photon PA is given by

$$\langle K_{\text{loss}} \rangle = \frac{2}{h Q_T} \int_0^\infty d\epsilon e^{-\epsilon/k_B T} \frac{\gamma_1 \gamma_s(\epsilon)}{(\Delta_1 + \epsilon/\hbar)^2 + \left(\frac{\gamma_1 + \gamma_s(\epsilon)}{2}\right)^2} \quad (3.44)$$

Similarly, two-color photoassociation also consider pairs of colliding atoms undergoing collisions in the presence of external fields. Here an additional laser at frequency  $\omega_2$  is also applied to couple a transition between state  $b_1$  and another bound state  $b_2$  with energy  $E_{b2}$  and decay rate  $\gamma_2$ . However, whereas in one-color PAS the frequency  $\omega_1$  is swept across the resonant energy of the bound state  $b_1$ , two-color PAS is most commonly performed in the Raman regime with a fixed intermediate state detuning  $\Delta_1 = \omega_1 - E_{b1}/\hbar$  from  $b_1$ . The two-photon detuning is given by  $\Delta_2 = \omega_1 - \omega_2 - E_{b2}/\hbar$ . As before, the bound states  $b_1$  and  $b_2$  are paired with artificial loss channels  $a_1$  and  $a_2$  respectively. Thus the relevant scattering probabilities for two-color PAS are  $|S_{\epsilon,a_1}|^2$  and  $|S_{\epsilon,a_2}|^2$ . Plugging these into  $\langle K_{\text{loss}} \rangle$ , a formal form of the loss rate constant is specified by

$$\langle K_{\text{loss}} \rangle = \frac{2}{h Q_T} \int_0^\infty d\epsilon \left[ |S_{\epsilon,a_1}|^2 + |S_{\epsilon,a_2}|^2 \right] e^{-\epsilon/k_B T} \quad (3.45)$$

where the explicit form of the matrix elements,  $S_{\epsilon,a_i}(\epsilon, \gamma_1, \gamma_2, \omega_1, \omega_2, \dots)$ , may be found in equations 4.8 and 4.9 of [10].

Typically, a simplifying assumption is applied at this point by considering loss from the state  $b_2$  at a rate  $\gamma_2$  to be negligible on the timescales of the experiment or in comparison to loss due to scattering from  $b_1$ . While this is usually an accurate assumption for PAS in alkali systems, it is not necessarily true in alkaline-earth system when using bound states of a narrow intercombination line transition as the two-photon intermediate state. However, taking  $\gamma_2 = 0$ , we recover the standard expressions for two-photon PA with scattering probability

$$|S_{\epsilon,a_1}|^2 = \frac{(\Delta_2 + \epsilon/\hbar)^2 \gamma_1 \gamma_s}{\left[ (\Delta_1 + \epsilon/\hbar + \delta_1)(\Delta_2 + \epsilon/\hbar) - \frac{\Omega_{12}^2}{4} \right]^2 + \left[ \frac{\gamma_1 + \gamma_s}{2} \right]^2 (\Delta_2 + \epsilon/\hbar)^2} \quad (3.46)$$

which includes a shift of the intermediate state  $\delta_1$  induced by laser 1 and the molecular Rabi frequency between states  $b_1$  and  $b_2$ . Finally, the thermally averaged loss rate constant simplifies to

$$\langle K_{\text{loss}} \rangle = \frac{2}{h Q_T} \int_0^\infty d\epsilon |S_{\epsilon,a_1}|^2 e^{-\epsilon/k_B T} \quad (3.47)$$

### 3.4.0.1 PAS near narrow intercombination transitions

In the previous section, Eq. 3.35 was presented with an implicit assumption that the loss rate is dependent only on the relative collision energy distribution. Once again, this is a good approximation for photoassociation with alkali atoms using dipole-allowed transitions. However, PAS using narrow intercombination line transitions may also be sensitive to Doppler broadening due to the center-of-mass momentum of the colliding pair [20]. To see this, we once again consider Eq. 3.35 written as a thermal average.

$$\langle K \rangle = \int_0^\infty d^3 \mathbf{p}_1 \int_0^\infty d^3 \mathbf{p}_2 \frac{2\pi\hbar^2}{|\mathbf{p}_1 - \mathbf{p}_2|\mu} f_2(\mathbf{p}_1, \mathbf{p}_2) |S(\mathbf{p}_1, \mathbf{p}_2, \omega_1, \omega_2, \dots)|^2 \quad (3.48)$$

If we assume that particle collisions are not correlated, or equivalently, that collisions occur rapidly enough that  $\mathbf{p}_1$  and  $\mathbf{p}_2$  are independent then we can write the two-particle momentum distribution function,  $f_2(\mathbf{p}_1, \mathbf{p}_2)$ , as the product of two single particle distributions.

$$\begin{aligned} f_2(\mathbf{p}_1, \mathbf{p}_2) &= f^1(\mathbf{p}_1)f^1(\mathbf{p}_2) \\ &= \left( \frac{1}{2\pi m k_B T} \right)^3 \exp \left( \frac{-(p_1^2 + p_2^2)}{2m k_B T} \right) \end{aligned} \quad (3.49)$$

where  $m$  is the single particle mass for a sample at temperature  $T$ .

Eq. 3.48 may be reduced to the earlier equations for  $\langle K_{\text{loss}} \rangle$  by performing a coordinate transform into center-of-mass and relative coordinates and integrating over the center-of-mass. We will consider a special case of this procedure in Ch. 5 when discussing the truncation of the relative collision energies of particles in a trapped gas.

Ref. [20] develops a rigorous extension of the standard Bohn and Julienne theory for one-photon photoassociation near an intercombination line which accounts for Doppler broadening and the photon recoil.

## Chapter 4

### High intensity PAS of a halo molecule

#### 4.1 Probing the ground state potential

In this chapter we study the least-bound vibrational level of the  $X^1\Sigma_g^+$  electronic ground state of the  $^{86}\text{Sr}_2$  dimer in a high intensity regime. Previous studies of the molecular states of the  $X^1\Sigma_g^+$  ground state potential have been performed using strontium-88, due to its high natural abundance, and strontium-84, because of it's amenable scattering properties. [refs.](#)

This work presents the first two-photon photoassociation study of the ground state of  $^{86}\text{Sr}$ . All previous PA experiments with this isotope have been one-photon photoassociation to excited electronic states [Yu 25-27](#). The large s-wave scattering length,  $\sim 800 \text{ a}_0$ , for this isotope is indicative of a near-threshold bound state known as a halo molecule. Direct photoassociation to this halo state revealed several unanticipated phenomena discussed in this chapter including AC Stark shifts comparable to the halo molecule binding energy and multi-photon resonance processes.

This work is expanded upon in Ch. 5 with a low intensity study that precisely determined the halo binding energy and using this measurement, improves upon the previous best determinations of the scattering lengths of all strontium isotopes via mass-scaling. In these initial experiments, we'll explore some of the novel effects of photoassociation to a halo state with a focus on understanding the AC Stark shifts and developing a useful theoretical framework for describing this unique photoassociation

regime.

As discussed in the previous chapter, two-photon PAS can be used to directly populate molecular levels and described with the formalism of Bohn and Julienne. However, this approach assumes the two driving lasers are of sufficiently different frequencies that each independently drives a specific transition, as in the typical  $\Lambda$ -model [Yu, 20 21]. In the regime of PAS to a halo state, the laser frequencies differ by only up to  $\sim 300$  kHz, much smaller than the typical intermediate state detuning of several MHz. Thus, both lasers must be considered to act on each leg of the transition simultaneously. We explored the effects of this bichromatic coupling through a collaboration with the theory group of Kaden Hazzard to develop simple models that are able to reproduce the key experimental observations and features.

In the following, we present the experimental results of high-intensity PA to the halo state and develop lineshape models based on the theory of Bohn and Julienne to extract the halo state binding energy. Next, we'll compare our experimental data to the numerical solution of a three-level model. This model subsequently becomes the basis of a Floquet treatment which results in an analytic form for describing and predicting AC Stark shifts of the halo state. This is used to consider the observed frequency dependence of the halo state energy and estimate the bound-bound coupling strength between the intermediate and halo states.

## 4.2 Experimental setup

Fig. 4.1 shows the excitation scheme used to probe the halo state in  $^{86}\text{Sr}$  using two-photon Raman photoassociation [? ], in which two laser fields couple colliding atoms to the least-bound state of the ground molecular potential.  $^{86}\text{Sr}$  has no nuclear spin and a  $^1S_0$  electronic ground state, leading to a single  $X^1\Sigma_g^+$  ground electronic

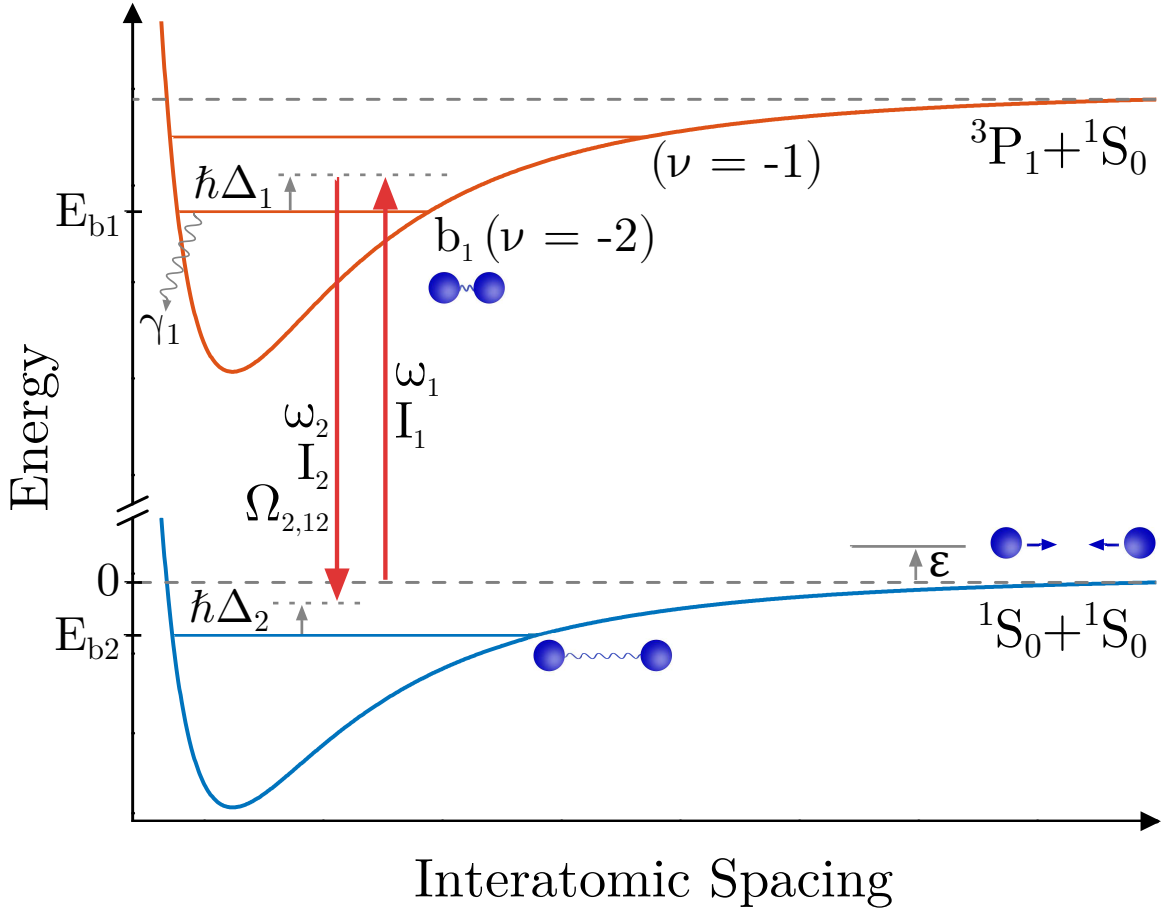


Figure 4.1 : Strontium PAS potential

Two-photon photoassociation diagram. The energy of two well-separated  ${}^1S_0$  atoms at rest is taken as zero.  $\epsilon$  is the kinetic energy of the colliding atom pair.  $E_{b1}$  is the unperturbed energy of the bound state of the excited molecular potential that is near resonance with the free-bound laser, which in these experiments is the second-least bound level of the excited molecular potential ( $\nu = -2$ ).  $E_{b2} (< 0)$  is the energy of the least bound state of the ground molecular potential. The photon of energy  $\hbar\omega_1$  is detuned from  $E_{b1}$  by  $\hbar\Delta_1$  for  $\epsilon = 0$ , while the two-photon detuning from  $E_{b2}$  is  $\hbar\Delta_2$ . The decay rate of  $b_1$  is  $\gamma_1$ . Stark and collisional frequency shifts are neglected in this schematic.

molecular potential. The target state for the two-photon transition has total angular momentum  $J = 0$  and halo state energy  $E_{b2}(< 0)$ , which we label as  $b_2$ . The dominant intermediate state,  $b_1$ , with energy  $E_{b1}$ , is the  $J = 1$  rotational state of the second least-bound  $\nu = -2$  vibrational level on the  $0_u^+$  molecular potential, which asymptotically connects to the  ${}^1S_0 + {}^3P_1$  asymptote at long range[? ]. This state is bound by 44.246(10) MHz [? ]. We define  $\Delta_1 = \omega_1 - E_{b1}/\hbar$  and  $\Delta_2 = \omega_1 - \omega_2 - E_{b2}/\hbar$  as the one-photon detuning from state  $b_1$  and two-photon detuning from state  $b_2$  respectively for an initial scattering state with collision energy  $\epsilon = 0$ . The Rabi frequency,  $\Omega_{2,12}$ , characterizes coupling between states  $b_1$  and  $b_2$  due to the laser field at  $\omega_2$  with single-beam intensity  $I_2$ . Because the binding energy of the halo molecule is very small compared to  $\Delta_1$ , both laser frequencies are near resonance with the  $\nu = -2$  state. The least-bound  $\nu = -1$ ,  $J = 1$  excited molecular state, bound by 1.633(1) MHz, and the excited atomic state lie near enough in energy to the  $\nu = -2$  state that they can also effect our observations.

The small detuning between  $\omega_1$  and  $\omega_2$  results in an atypical consideration of the accessible resonance conditions during the Raman process. Fig. 4.2a shows the two scenarios which lead to resonance with the halo state when  $\omega_1$  is held fixed and  $\omega_2$  is varied. The left panel, when  $\omega_2 \geq \omega_1$ , shows  $\Delta_1$  remains fixed while scanning the two-photon energy. This holds constant the bound-bound coupling between the halo and intermediate state. In the opposite case, when  $\omega_2 \leq \omega_1$ , the halo resonance condition can still be satisfied as  $\omega_2$  is varied, though at the expense of also varying  $\Delta_1$ . This behavior is equivalent to fixing  $\omega_2$  and scanning  $\omega_1$  in a typical  $\Lambda$ -type Raman scheme, but warrants our attention because of the interchangeability of the excitation lasers.

The latter configuration, which couples  $\omega_2$  and  $\Delta_1$ , was used during our pho-

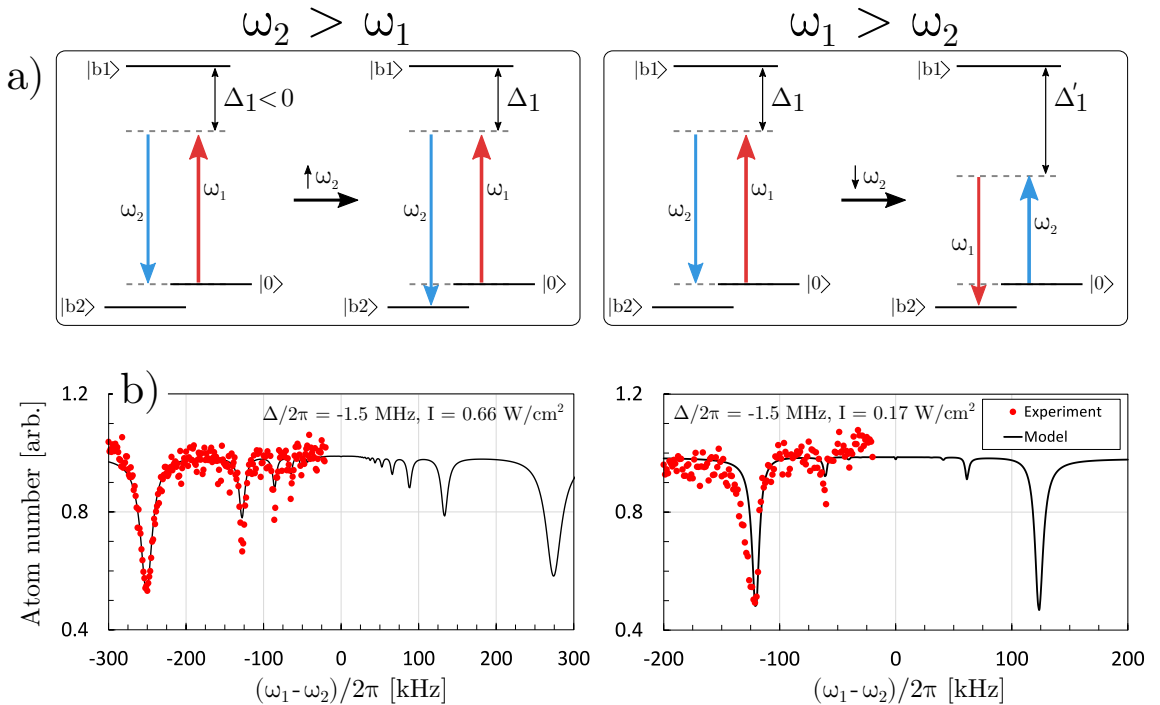


Figure 4.2 : Accessible halo resonance PAS processes

Effects of fixing  $\omega_1$  and varying  $\omega_2$ . Consider the state  $|b2\rangle$  to be fixed. a) The left and right panels illustrate scanning  $\omega_2$  relative to  $\omega_1$ . Within each panel, the lasers start with  $\omega_1 = \omega_2$  and  $\Delta_2 = -E_b/\hbar$ . Scanning  $\omega_2$  will fulfill the resonance condition in both scenarios but also lead to a change in  $\Delta_1$  if  $\omega_1 > \omega_2$ . b) Example simulated spectra compared with experimental PAS. The development of the model is described in Sec. 4.3.1. For both simulations, the "positive" axis is the configuration where  $\omega_2 \geq \omega_1$  and the negative axis is the opposite. Note the asymmetry in the resonance frequency for  $I = 0.66$  W/cm<sup>2</sup>.

toassociation experiments. The effects on the observable spectra between these two schemes was considered using a three-level model, Sec. 4.3.1, to evaluate both scenarios of laser detuning across the complete range of our data. Fig. 4.2b shows two simulated spectra in the regime of strongest coupling accessible by our experiments. The higher intensity spectrum,  $I = 0.66 \text{ W/cm}^2$ , shows that coupling between  $\Delta_1$  and  $\omega_2$  can noticeably shift the resonance energy of the halo state. Importantly, this prediction is in a regime where  $E_{b2} \sim \Delta_1$ , which applies to only a small subset of our measurements. Most of our data is in a regime where  $\Delta_2 \ll \Delta_1$  thus we neglect variation of the AC Stark shift with  $\omega_2$ .

Spectroscopy is performed in the crossed beam optical dipole trap generated from a 1064-nm laser propagating perpendicular to gravity with spot sizes at the atoms of  $300 \mu\text{m} \times 60 \mu\text{m}$  and  $400 \mu\text{m} \times 40 \mu\text{m}$ , with the short axis parallel to gravity. Further details are available in Sec. 2.3.3. Typical atom numbers are several hundred thousand and sample temperatures of approximately 300 nK. Peak densities are between  $n_0 = 1 - 2 \times 10^{12} \text{ cm}^{-3}$ . Following forced evaporative cooling, the atoms thermally equilibrate before they are illuminated by the photoassociation beam for 1 - 10 milliseconds. The number of ground-state atoms remaining and the sample temperature are then measured with time-of-flight absorption imaging. Trap oscillation frequencies are determined by measuring dipole and breathing collective mode frequencies, which allow determination of trap volume and sample density.

We generate the two photons for spectroscopy as shown in Fig. 4.3. Using an AOM, these photons are derived from the output of a slave diode laser that is injected locked from the master 689 nm laser. Two precisely controlled RF frequencies are applied to a single AOM. These frequencies are separated by less than 300 kHz, and the diffracted beams corresponding to each frequency component appear as a single beam

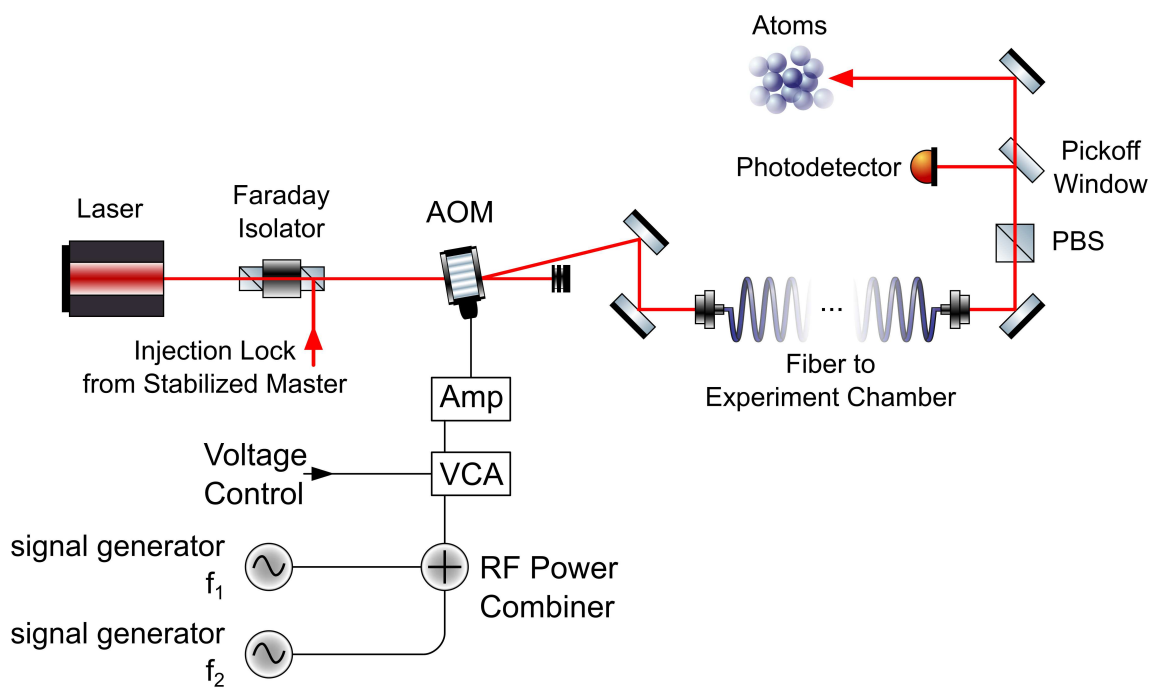


Figure 4.3 : Schematic of PAS light generation

Light for these experiments is generated by the spectroscopy slave laser setup discussed in Sec. 2.3.4.2. Light at two controllable frequencies is generated with a single acousto-optic modulator (AOM) and delivered to the atoms with an optical fiber. The beat note between the two frequencies is monitored after the fiber.

that is coupled into a single-mode, polarization-maintaining fiber. The output light is linearly polarized such that the polarization vector is parallel to gravity.

This fiber output is launched near the science chamber and shaped with output optics that yield a  $450\,\mu\text{m}$  waist at the atoms, much larger than the size of the atom cloud. The optical fiber ensures that the wavevector of the two photons will be parallel. This allows us to neglect any effects of Doppler broadening that might result from photoassociation near an intercombination line.

By using a single laser source and applying both frequencies to a single acousto-optic modulator, we establish phase coherence and RF precision frequency differences between the  $\omega_1$  and  $\omega_2$  photons. Reduction of the beat note contrast is the primary limiting factor of the available scan range for this spectroscopy setup. This is due to the misalignment into the optical fiber resulting from the varying angular deviation out of the AOM. We partially compensate for this misalignment by increasing the RF amplitude of one drive frequency to maintain high beat note contrast. We observe significant reduction in contrast, which we were unable to compensate for, when the two drive frequencies differ by more than  $\approx 300$  kHz.

During the course of our experiments we found that mild environmental perturbations resulted in slow variation (on the order of 1 s) of the light coupling through the fiber. Such amplitude modulations are not uncommon in laser systems and are typically compensated by using a closed loop intensity stabilization circuit. However, this circuit was inadequate for short-time exposures due to the acquisition process being long compared to our desired pulse width. This led us to implement the digital based infinite sample and hold mechanism for reduced intensity variability described in detail in Sec. 2.3.4.2. The sample and hold system provided increased intensity stability with a 5% standard deviation during a typical experiment. The beat sig-

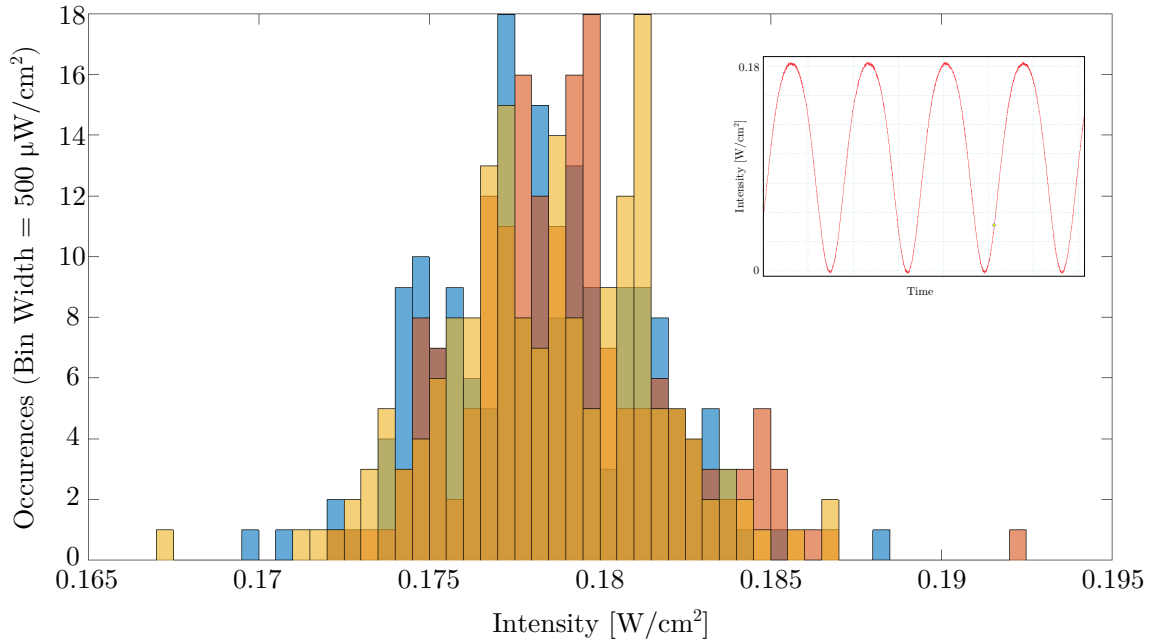


Figure 4.4 : Histogram of PAS beam intensity variation

Sample intensity variation during a set of photoassociation scans. Different colors denote multiple scans separated in time which are averaged. The inset shows a sample beat note and typical contrast.

nal of the two light fields after the fiber is monitored on a photodiode and the RF powers are adjusted to ensure matched intensities for the two frequency components ( $I_1 = I_2 \equiv I$ ). Fig. 4.4 shows a typical histogram of the recorded intensities and a sample beat note.

### 4.3 Modeling of the photoassociative loss

We observe photoassociation as a loss of atoms from the trap. Fig. 4.5a shows several example spectra of PA to the  $^{86}\text{Sr}$  halo state. Intensities given here are the single-beam intensities,  $I$ , with the average total near-resonant intensity illuminating the

atoms given by  $I_{689} = 2I$ . We clearly see the asymmetric tail, which is characteristic of a photoassociation process that maps out the relative collision energy distribution of the trapped atoms. Each spectrum is averaged over several scans and the error bars represent the standard error.

We model this atom loss following the two-color PA theory of Bohn and Julienne and introduced in Sec. 3.4. Recall that the evolution of the total number of trapped atoms is given by

$$N(t) = \frac{N_0 e^{-\Gamma t}}{1 + \frac{2N_0 \langle K \rangle V_2}{\Gamma V_1^2} (1 - e^{-\Gamma t})} \quad (4.1)$$

with  $\Gamma$  the one-body loss rate,  $N_0$  the initial number of trapped atoms before applying PAS, and  $V_q$  the effective volumes defined in Eq. 3.41. When fitting to experiments, we find it advantageous to account for the two-body average density distribution within the trap by considering the thermally averaged  $\langle K \rangle$  (Eq. 3.47) at each  $\mathbf{r}$  contained within the trapping volume. This trap averaged  $\langle K \rangle$  is given by

$$\langle K \rangle = \frac{1}{V_2} \int_V e^{-2U(\mathbf{r})/k_B T} \frac{1}{h Q_T} \int_0^{\epsilon_{\max}(\mathbf{r})} d\epsilon |S|^2 e^{-\epsilon/k_B T} \quad (4.2)$$

In addition to the spatially dependent density weighting, we have also introduce a spatial dependence into the collision energy distribution  $\epsilon$ , with an energy cutoff  $\epsilon_{\max}(\mathbf{r})$  defined by the local trap depth  $\epsilon_{\max}(\mathbf{r}) = U_{\text{depth}} - U(\mathbf{r})$ . Here,  $U(\mathbf{r})$  is the trapping potential and  $U_{\text{depth}}$  is the overall trap depth defined from the trap minimum to the lowest saddle point. Examples of analytic form of the trapping potential  $U(\mathbf{r})$  are given in Sec. 2.3.3.1. The partition function  $Q_T = \left(\frac{2\pi k_B T \mu}{h^2}\right)^{3/2}$  is determined for sample temperature  $T$  and reduced mass  $\mu = m/2$  with mass  $m$  the mass of  $^{86}\text{Sr}$ .

We note that the energy cutoff introduced in Eq. 4.2 provides the correct normalized thermal average when the ratio of the sample temperature to trap depth is large,  $U_{\text{depth}}/k_B T \gtrsim 4$ , which is accurate for the data presented here. The next chapter

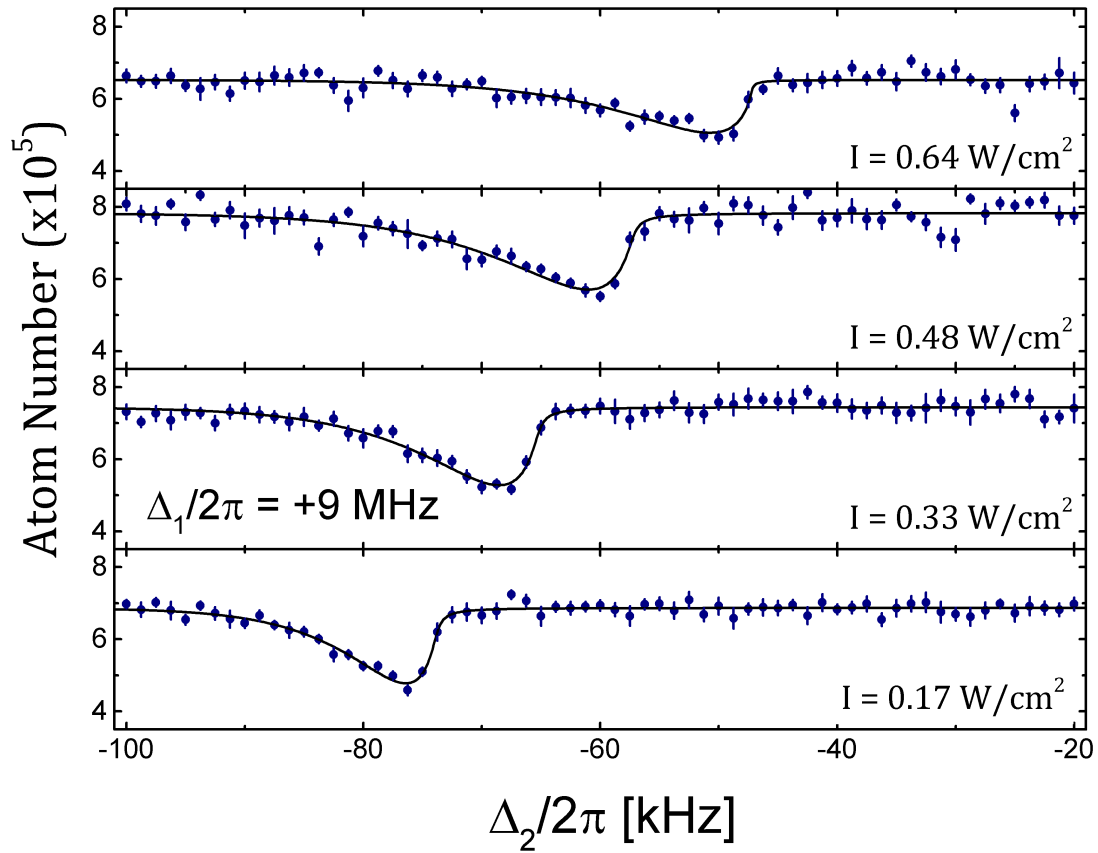


Figure 4.5 : Halo molecule spectroscopy

Characteristic spectra of the halo molecule spectroscopy at various single-beam intensities,  $I$ , and fixed detuning  $\Delta_1/2\pi = +9 \text{ MHz}$ . The procedure used to fit these lineshapes is discussed in the text.

will consider the effects of this energy truncation further. Finally, we also assume a fixed temperature throughout the exposure time. Consideration of the temperatures measured from time-of-flight images showed no more than 15% variation as  $\Delta_2$  was scanned.

We assume the dominant loss process to occur via the intermediate state  $b_1$  and therefore use the scattering probability,  $|S|^2$  given in Eq. 3.46

$$|S|^2 = \frac{(\Delta_2 + \epsilon/\hbar)^2 \gamma_1 \gamma_s}{\left[ (\Delta_1 + \epsilon/\hbar)(\Delta_2 + \epsilon/\hbar) - \frac{\Omega_{12}^2}{4} \right]^2 + \left[ \frac{\gamma_1 + \gamma_s}{2} \right]^2 (\Delta_2 + \epsilon/\hbar)^2} \quad (4.3)$$

where  $\gamma_1 = 2\gamma_{\text{atomic}}$ , and  $\gamma_{\text{atomic}} = 4.7 \times 10^4 \text{ s}^{-1}$  is the decay rate of the atomic  ${}^3P_1$  level.  $\gamma_s(\epsilon)$  is the stimulated width of  $b_1$  due to coupling to the initial scattering state by the PAS lasers, which for low energy can be expressed as [19, 71? ]

$$\gamma_s(\epsilon) = 2k l_{\text{opt}} \gamma_1, \quad (4.4)$$

where the optical length ( $l_{\text{opt}} \propto I_{689}$ ) is related to the overlap between the initial colliding state and  $b_1$ , and  $k = (2\mu\epsilon)^{1/2}/\hbar$ . Our chosen intermediate state has optical length  $l_{\text{opt}}/I = (1.5 \pm 0.3) \times 10^4 a_0 / (\text{W/cm}^2)$  [? ], where  $a_0 = 5.29 \times 10^{-11} \text{ m}$  is the Bohr radius.

Since we are primarily concerned with measuring light shifts on the halo state, the statement of  $|S|^2$  above omits any explicit inclusion of light shifts in contrast to the original theory. This includes the shift of  $b_1$  due to coupling to the ground state scattering continuum which was found to be a sufficient approximation for describing previous two-photon spectroscopy in  ${}^{88}\text{Sr}$  [59]. Furthermore, lacking a model of coupling outside of our system, the scattering probability neglects explicit dependence on shifts due to the trapping or photoassociation lasers coupling to states outside of this model.

For the experiments reported here, we maintain significant intermediate state detuning,  $\Delta_1$ , for which  $|\Delta_1| \gg \Omega_{12}$ . Thus we are in the Raman regime and may further simplify Eq. 4.3 by considering its behavior as a function of  $\Delta_2$ . A maximum for this function occurs when  $\Delta_2 + \epsilon/\hbar = \Omega_{12}^2/4\Delta_1$ . By restricting the range of  $\Delta_2$  to be near two-photon resonance and maintaining  $|\Delta_1| \gg \Omega_{12}, \gamma_1, \gamma_s$ , then we can approximate  $|S|^2$  by a Lorentzian [70, 71].

$$|S|^2 \approx \frac{A(\epsilon)}{\left(\Delta_2 + \epsilon/\hbar - \frac{\Omega_{12}^2}{4(\Delta_1 + \epsilon/\hbar)}\right)^2 + [\Gamma_L(\epsilon)/2]^2} \quad (4.5)$$

where

$$A(\epsilon) = \frac{\Omega_{12}^4 \gamma_1 \gamma_s(\epsilon)}{16(\Delta_1 + \epsilon/\hbar)^4} \quad (4.6)$$

$$\Gamma_L(\epsilon) = \frac{\Omega_{12}^2 [\gamma_1 + \gamma_s(\epsilon)]}{4(\Delta_1 + \epsilon/\hbar)^2} \quad (4.7)$$

There are several concerns regarding this formulation of the Bohn and Julienne theory for our experiment. First, it assumes an isolated intermediate state, which is not always a good approximation due to the proximity of the intermediate state  $b_1$  to the  ${}^1S_0 + {}^3P_1$  asymptote and to the  $\nu = -1$  state. Second, Eq. 4.3 is derived assuming only a single near resonant laser beam along each leg of the two-photon transition. This condition is clearly violated for two-photon spectroscopy to a halo state where  $\omega_1 - \omega_2 \approx -E_{b2} \ll |\Delta_1|$ . Thus, we expect pairs of colliding atoms will experience inelastic scattering processes in both fields simultaneously which will contribute to the overall observed transition strengths and light shifts. During the photoassociation exposure time the total 689 nm intensity,  $I_{689}$ , oscillates with near 100% contrast according to  $I_{689} = I_1 + I_2 + 2\sqrt{I_1 I_2} \cos[(\omega_1 - \omega_2)t] = 2I \{1 + \cos[(\omega_1 - \omega_2)t]\}$ . We assume an ansatz dependence of the bound-bound coupling,  $\Omega_{12} \propto \langle I_{689} \rangle^{1/2}$  where

$\langle I_{689} \rangle$  is the time averaged intensity which neglects the interference term between the lasers.

In the absence of a more rigorous theory treating these effects, we analyze loss spectra using the effective expression given by Eq. 4.8, where the observed molecular binding energy,  $E'_{b2}$ , includes any perturbations due to AC Stark shifts.

$$|S|^2 = \frac{\Gamma_L(\epsilon) + \gamma_{\text{eff}}}{\Gamma_L(\epsilon)} \frac{\eta A(\epsilon)}{(\omega_1 - \omega_2 + \epsilon/\hbar - E'_{b2}/\hbar)^2 + \left[ \frac{\Gamma_L(\epsilon) + \gamma_{\text{eff}}}{2} \right]^2} \quad (4.8)$$

This formulation of the  $|S|^2$  has been further modified with two additional parameters,  $\eta$  and  $\gamma_{\text{eff}}$ , while maintaining the required unit normalization of the scattering probability. These parameters were added to account for deviations of the signal strength,  $\eta$ , and observed width,  $\gamma_{\text{eff}}$ , which may not be accounted for in a naive treatment of the inelastic scattering.

When performing fits of the atom loss lineshapes using Eqs. 4.1,4.2,5.6, we utilize independently determined simulations of the trapping potential  $U(\mathbf{r})$ . The sample temperature,  $T$ , is measured from the time-of-flight and used to characterize the energy distribution of  $\langle K \rangle$ . As a check of our lineshape model, we allowed the sample temperature to vary as a fit parameter and found reasonable agreement between the temperature estimated by the asymmetric tail of the lineshape and the time-of-flight temperature. However, this process makes the fitting routine proceed much more slowly so we generally leave it fixed to the value measured via time-of-flight. The one-body loss rate  $\Gamma$  was also measured and found to be  $\approx 5 \text{ s}^{-1}$ . All other values such as  $\gamma_s$ ,  $\gamma_1$ ,  $\Omega_{12}$ , etc. are calculated for each spectrum using known physical values or locally measured estimates. Thus, the remaining parameters  $E'_{b2}$ ,  $N_0$ ,  $\eta$ , and  $\gamma_{\text{eff}}$  are independently fit and estimated for each spectrum.

Note that for each set of experimental conditions,  $I_{689}$  and  $\Delta_1$ , several scans of

the photoassociation process were accumulated. When determining the parameter estimates,  $E'_{b2}$ ,  $N_0$ , etc., for a specific set of conditions, we independently fit and extract the coefficient values from each of the individual scans. Then calculate the average and standard error for each parameter for those conditions.

In this work, we are primarily concerned with the variation of the halo resonance energy with the excitation laser intensity and intermediate state detuning as shown in Fig. 4.6a. The estimate of  $E'_{b2}$  from the spectra is largely determined by the sharp edge on the blue end of the spectra. While we cannot determine if the halo resonance energies are sensitive to other interactions causing shifts of the halo state, we do observe a striking dependence on the 689 nm excitation intensity,  $I_{689}$ , as shown in Fig. 4.5. We model the relationship between the measured resonance positions and the unperturbed binding energy  $E_{b2}$  as

$$E'_{b2} = E_{b2} + h\chi_{689}I_{689} \quad (4.9)$$

We characterize the effects of varying  $\Delta_1$  on the AC Stark shift by determining the slope of those intensities which exhibit linear scaling for each  $\Delta_1$ . This estimates the susceptibility of the halo state,  $\chi_{689}(\Delta_1)$ , which are plotted as a function of  $\Delta_1$  in Fig. 4.6b.

#### 4.3.1 Frequency dependence of the binding energy

Collaborating with Kon Wen Yu, of the Hazzard group, the data shown in Fig. 4.6 was used to develop and assess several theoretical descriptions in order to reproduce and predict the resonance positions and susceptibility of the halo molecule state [51]. Additionally, we evaluated the effect of a bichromatic drive on the observed halo resonance energies and reproduced the emergence of higher-order loss processes observed in the experiment.

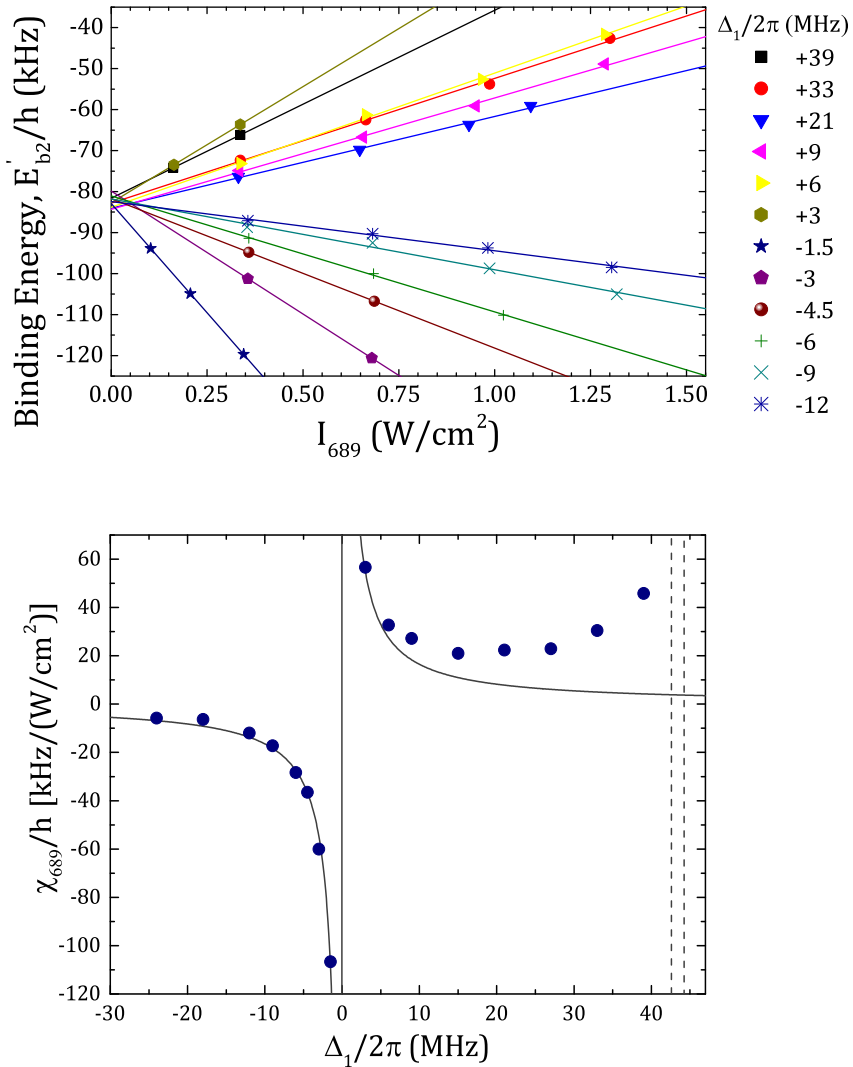


Figure 4.6 : Halo state resonances and susceptibilities,  $\chi_{689}$

Summary of the halo PAS experimental results. Top: A selection of two-photon PA resonance positions as a function of twice the single-beam excitation intensity,  $I_{689} = 2I$ , for various intermediate state detunings  $\Delta_1$ . The solid lines are fits used to determine  $\chi_{689}$  at each detuning. Bottom: The susceptibility,  $\chi_{689}$ , across all intermediate state detunings probed in this study. Dashed lines indicate the positions of the  $\nu = -1$ ,  $J = 1$  excited molecular state, bound by 1.633(1) MHz, and the  ${}^1S_0 + {}^3P_1$  continuum. Dark solid line is a guide to the eye  $\propto 1/\Delta_1$ .

These theoretical approaches began with the setup and numerical evaluation of a time-dependent three-level system. This model was then analyzed using Floquet and perturbation theory to develop an approximate analytic formula for predicting the halo resonance shift. Throughout this analysis, we neglect the motional degrees of freedom for the initial state of two free atoms. This greatly simplifies the physical processes we must consider and allows us to deduce an analytic result for the scaling of the binding energy. For the remainder of this chapter, our discussion will focus on the results of Yu's analyses and leave the details of his derivation to Ref. [51].

The photoassociation experiment is modeled using a three-level system composed of - two well-separated atoms  $|0\rangle$ , an intermediate dimer state in an excited electronic potential  $|b_1\rangle$ , and a dimer in the ground electronic state  $|b_2\rangle$ . This setup is outlined in Fig. 4.1 where we have defined  $|0\rangle$  to be pair of atoms with  $\epsilon = 0$  relative collision energy. The Hamiltonian for this system is

$$H = \begin{bmatrix} 0 & \Omega_{1,01}\cos(\omega_1 t) + \Omega_{2,01}\cos(\omega_2 t) & 0 \\ \Omega_{1,01}\cos(\omega_1 t) + \Omega_{2,01}\cos(\omega_2 t) & E_{b1} - i\frac{\Gamma_1}{2} & \Omega_{1,12}\cos(\omega_1 t) + \Omega_{2,12}\cos(\omega_2 t) \\ 0 & \Omega_{1,12}\cos(\omega_1 t) + \Omega_{2,12}\cos(\omega_2 t) & E_{b2} - i\frac{\Gamma_2}{2} \end{bmatrix} \quad (4.10)$$

Unlike the typical  $\Lambda$ -model considered in the Bohn and Julienne formalism, Eq. 4.10 considers both lasers 1 and 2 to drive the transition  $|0\rangle \rightarrow |1\rangle$  and  $|1\rangle \rightarrow |2\rangle$ . Decay terms are included to describe atom loss with  $\Gamma_1$  representing spontaneous emission from the intermediate bound state due to natural decay and  $\Gamma_2$  representing loss from the halo state due to collisions with background atoms.

The time-evolution of Eq. 4.10 begins in  $|0\rangle$  and proceeds for a time  $\tau$  using similar optical couplings and oscillating optical intensity as present during the photoassocia-

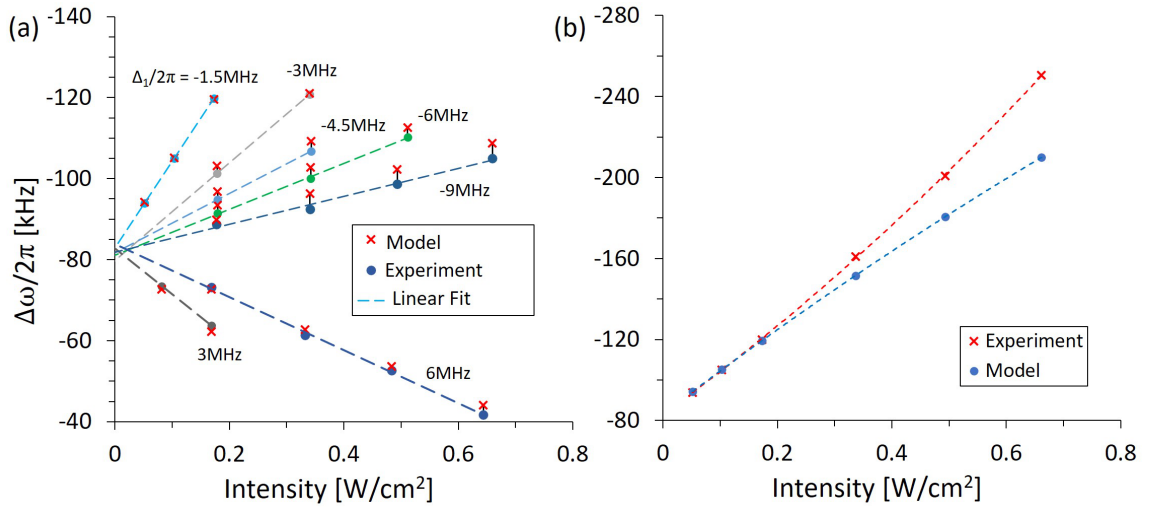


Figure 4.7 : Comparison of a three-level model to experimental halo PAS

a) The resonance energies,  $E'_{b2}$ , determined from the experiments as well as the corresponding predicted resonance position from numerical simulation of three-level model given by Eq. 4.10. Linear fits to the experimental data are also shown which are used to determine the halo state susceptibility at 689 nm and subsequently the variation of susceptibility with  $\Delta_1$ . b)  $\Delta_1/2\pi = -1.5$  MHz data over a larger range of intensities for which the experimental results are not well described by linear scaling as predicted by the three-level model. Quadratic fits are shown as a guide to the eye.

tion experiments. The model is numerically solved to generate a simulated spectrum as shown in Fig. 4.2. From these spectra, we estimate the halo resonance energy by determining the frequency of peak loss. The results of these simulations are shown in Fig. 4.7. The predicted halo resonance energies generally agrees with experimental data and reproduces a linear scaling of the binding energy consistent with the experimental observations. This indicates that effects missing from this theory – the motion of the atoms [21], interaction shifts due to molecules and atoms scattering

off of other molecules and atoms [22], and the varying density within the trap [18] – are not necessarily relevant for considering the effects of the bichromatic drive and determination of the internal interaction strengths. [refs from hazzard paper](#)

However, as intensity is increased the model begins to deviate from the experimental data, limiting its regime of applicability. Fig. 4.5b shows an example where the three-level model tends to underestimate the resonance energy at higher intensities. This behavior is suggestive of additional interactions between the halo molecule state and one or more levels outside of our model.

We expect the predictive capability of the three-level system to prove useful for future studies of the  $^{86}\text{Sr}$  halo molecule. However, the numerical time-evolution is time intensive and would require solving multiple simulations when using the halo resonance position in the development of further theories. Thus, to obtain analytic insight into the three-level model, the Hamiltonian of Eq. 4.10 was treated under Floquet theory. We leave the details of this expansion to Ref. [51] but note that once the Floquet Hamiltonian has been found, a perturbative expansion can be applied in the region around  $|\omega_1 - \omega_2| \approx -E_b^0$  by assuming  $|\Delta_1| \gg \Omega_{01}, \Omega_{12}, \Delta_2, |\omega_1 - \omega_2|$ , where  $\Delta_2 = \omega_1 - \omega_2 - E_b^0$ . Additionally, we assume  $\Omega_{12} \gg \Omega_{01}$ . The resulting expression for the shift of the halo resonance energy is then

$$\Delta\omega = \frac{\Omega^2}{4} \left( \frac{1}{\Delta_1 + E_b^0 + \Delta\omega} + \frac{1}{\Delta_1 + E_b^0} \right) \quad (4.11)$$

where  $\Delta\omega$  is the shift from the natural binding energy  $E_b^0$  and we have defined  $\Omega_{1,12} = \Omega_{2,12} = \Omega$  in the case that  $I_1 = I_2$ . Comparison of this analytic formula with results from the numerical simulations show excellent agreement, even outside the region of strict validity of the perturbative expansion. Eq. 4.11 also agrees with our initial hypothesis, applied when fitting the halo molecule lineshapes in the previous section, that the AC Stark shift scales as nearly twice the single-beam intensity

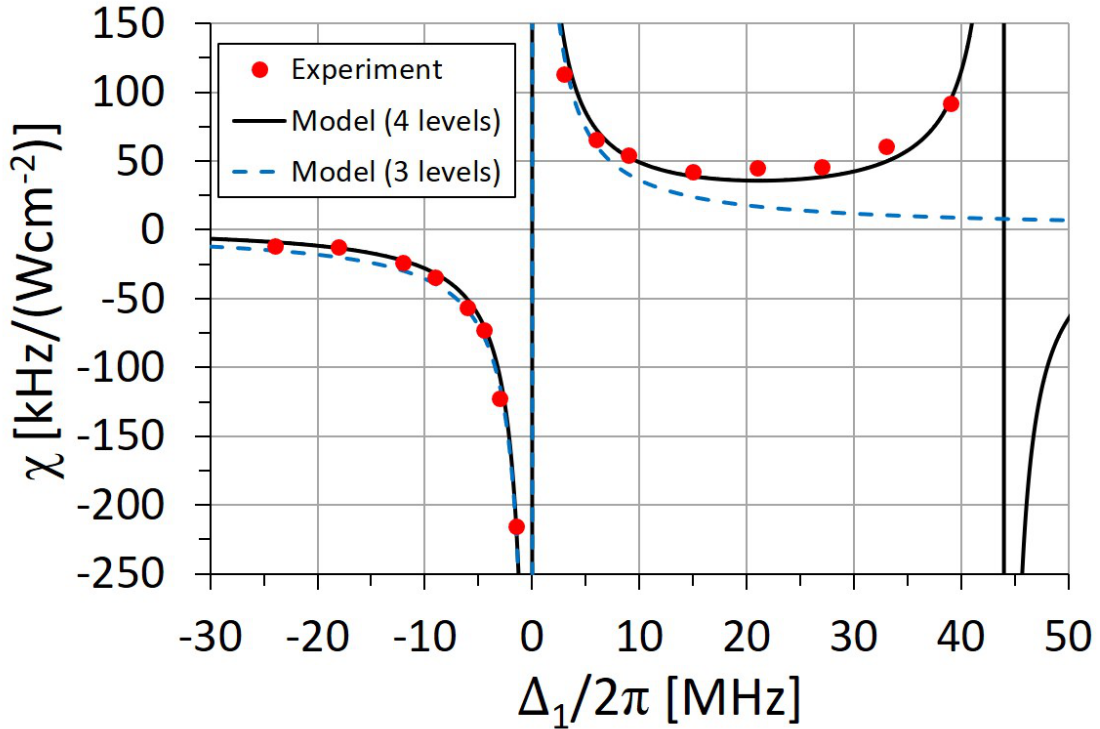


Figure 4.8 : Analytic approximation of the susceptibility

Plot of the experimental susceptibility data shown in Fig. 4.6b. These points are fit with the analytic susceptibility predicted from the Floquet treatment of the three-level and four-level models.

and is consistent with approximations of light shifts made in previous experiments. (Yu 22 and 44).

As an application of Eq. 4.11, we note that  $\frac{d\Delta\omega}{dT}$  determines the susceptibility  $\chi_{689}(\Delta_1)$  of the halo state. Fig. 4.8 plots the analytic susceptibility over  $\Delta_1$  resulting from fitting the coupling parameter in  $\frac{d\Delta\omega}{dT}$ . Once more we see that the three-level model cannot reproduce the experimental observations as intermediate state detuning is increased. This is most likely due to coupling with the  $\nu = -1, J = 1$  excited molecular state and the  $^1S_0 + ^3P_1$  continuum. Experimentally we were unable to isolate

and determine the separate effects of these states. Thus as an approximate theoretical approach, the three-level model is extended with a virtual fourth-level,  $|X\rangle$ , specified by

$$H' = H_0 + E_X |X\rangle \langle X| + [\Omega_{1,0X} \cos(\omega_1 t) + \Omega_{2,0X} \cos(\omega_2 t)] |0\rangle \langle X| + \text{h.c.} \quad (4.12)$$

where  $H_0$  is the three-level Hamiltonian in Eq. 4.10. The virtual state  $|X\rangle$  may, in general, have couplings  $\Omega_{0X}$  and  $\Omega_{2X}$ . We choose to set  $\Omega_{2X} = 0$  in Eq. 4.12 and consider the dominant coupling between states  $|0\rangle$  and  $|X\rangle$ . This approximation is motivated by the positive slope of the observed susceptibilities as  $\Delta_1$  is varied towards the  $^1S_0 + ^3P_1$  asymptote which suggests that the ground state is shifting faster than the halo state. If instead we assumed that  $\Omega_{2X} \gg \Omega_{0X}$ , the sign of the AC Stark shift would be negative at red-detuning, which is inconsistent with our observations. Additionally, we choose to set the energy of the virtual state to the energy of the  $^1S_0 + ^3P_1$  asymptote,  $E_X = E_{b1} + 2\pi\hbar \times 44.2 \text{ MHz}$ .

A fit of the Floquet treatment of the four-level model is shown in Fig. 4.8 and yields  $\Omega_{12}/2\pi = 850 \text{ kHz}$  for  $I = 1 \text{ W/cm}^2$ . Note that  $\Omega_{12}$  as defined here would be the splitting of the Autler-Townes doublet [71], which differs from the Bohn-Julienne definition of the molecular Rabi coupling [? ].

Using the measured  $\Omega_{12}$ , one can extract the Franck-Condon factor,  $f_{\text{FCF}}$ , reflecting the overlap of the ground and intermediate molecular states through

$$\Omega_{12} = \sqrt{f_{\text{ROT}}} \sqrt{f_{\text{FCF}}} \gamma_{\text{atomic}} \sqrt{\frac{I}{2I_{\text{sat,atom}}}} \quad (4.13)$$

where  $I_{\text{sat,atom}} = 2\pi^2\hbar c \gamma_{\text{atomic}} / (3\Lambda^3) = 3 \mu\text{W/cm}^2$  is the atomic saturation intensity for the  $^1S_0 \rightarrow ^3P_1$  transition and  $I = I_{689}/2$  is the single-beam intensity. The rotational factor  $f_{\text{ROT}}$  accounts for the change in dipole moment from atom to molecule due to symmetry of the wave function and projection on a rotating molecular axis.

Following the formalism described in [71],  $f_{\text{ROT}} = 2$  for the  $J = 1 \rightarrow 0$  bound-bound molecular transition studied here. This yields  $f_{\text{FCF}} = 0.03$ .

#### 4.4 Multi-photon loss processes

In the regime of strongest coupling between the halo state and intermediate excited molecular state, we observe the emergence of higher order loss features absent in the typical  $\Lambda$ -model due to the separability of the excitation lasers. Fig. 4.9 shows a series of spectra close to resonance which demonstrates the appearance of these loss features. At low intensity a single prominent PAS lineshape around  $\Delta_2 \approx -100$  kHz is observed. Then, as the intensity is increased, the resonance energy of the primary loss feature, defined as  $E_{b2}$ , shifts significantly more deeply into the ground state potential. Accompanying this shift, additional loss features continue to emerge in the spectrum as the intensity is further increased. These satellite features also appear to scale with intensity and the position of the primary loss feature. Increasing intensity also results in an increase in the linewidth as the lineshape broadens from an asymmetric feature into a fully symmetric profile. This is indicative of power broadening of the two-photon transition as population is cycled between the halo and continuum states.

Two conclusions drawn from these spectra are of particular note. First, the shift of the halo state to a binding energy of  $\approx 250$  kHz for the highest intensity spectrum represents a significant change in the scattering length of freely colliding atoms in the  ${}^1S_0 + {}^1S_0$  continuum. In the next chapter we will discuss our precise determination of the halo molecule resonance energy which we measure to be  $E_{b2} = -83$  kHz. Presuming this value of  $E_{b2}$  for the moment, we can estimate the change in scattering length due to a 250 kHz change in the halo state resonance energy using  $E_{b2} = -\hbar^2/(2\mu a^2)$ , where  $\mu$  is the reduced mass of the strontium-86 halo molecule and  $a$  is the s-wave

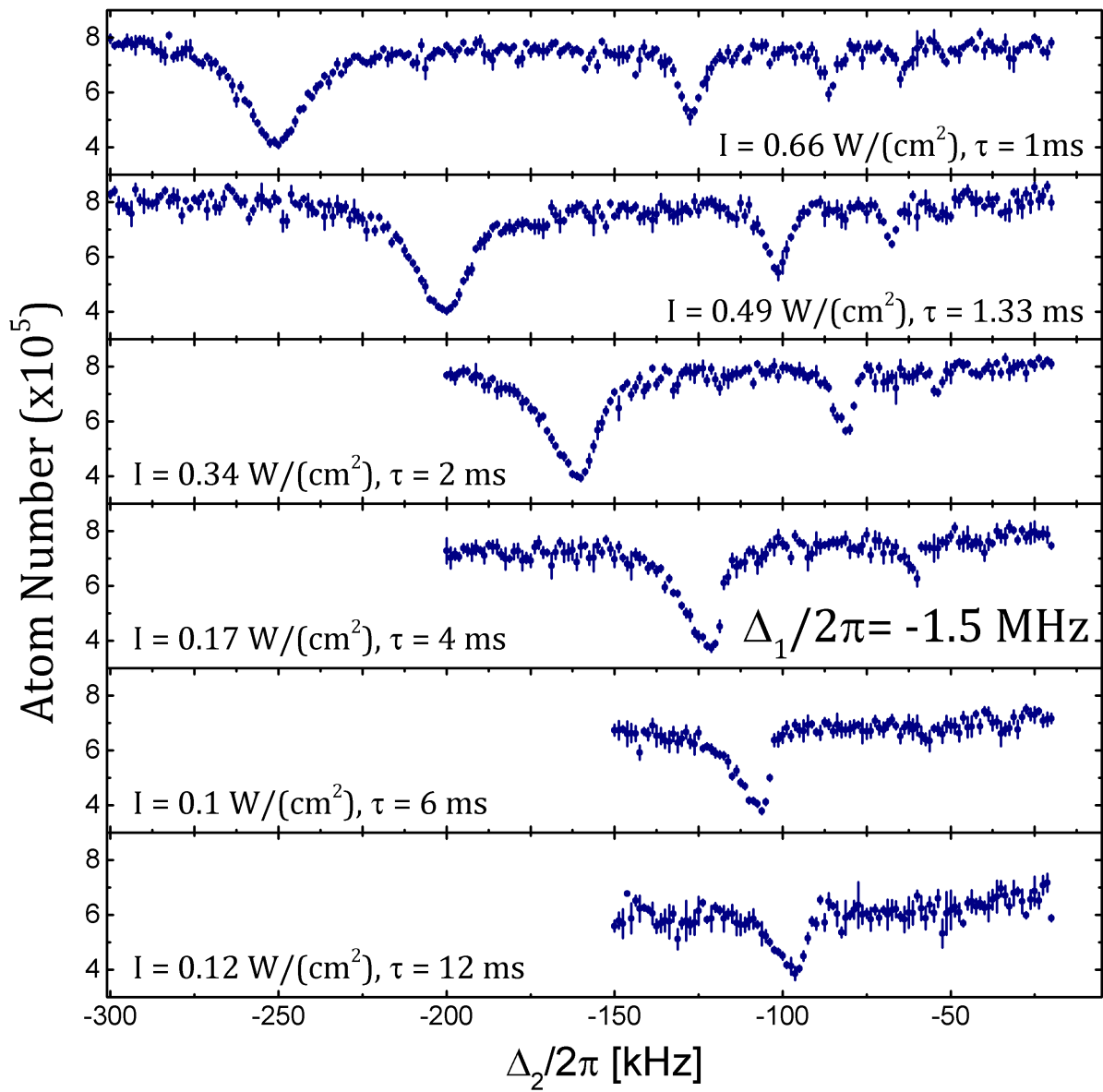


Figure 4.9 : Observation of higher order Raman processes

scattering length. From the highest intensity spectrum, the primary loss feature is shifted by approximately  $3 \times$  the natural binding energy. This reduces the 86-86 scattering length to  $\sim 500 a_0$ , or approximately 60% of its natural value. The proximity of  $^{86}\text{Sr}$  to a scattering resonance and the susceptibility of the halo binding energy to the intensity of the excitation light suggests using light to tune the binding energy and scattering length as was done with optically assisted magnetic Feshbach resonances [4, 21]. This complements previous work on the use of optical Feshbach resonances in strontium [7, 85, 90, 92? ].

Second, consideration of the peak loss positions in Fig. 4.9 shows that each higher order process is related to the position of the primary loss by approximately  $E_{b2}/2$ .  $E_{b2}/3$ , . . . . This scaling suggests a non-linear process whereby multiple photons from the excitation light fields are absorbed and emitted to reach the final state. This is possible because of the small overall detuning,  $\Delta_2$ , and strong coupling between the halo and intermediate state. This hypothesis can be tested using time-evolution of the three-level model to predict the spectra under similar conditions. Fig. 4.10 shows a schematic example of the multi-photon process as well as the result of the numerical evaluation for a selection of the strongly coupled spectra shown in the previous figure. Despite its simplicity, the three-level model captures the relevant physics and accurately predicts the emergence of multi-photon loss features near the positions of the experimentally measured loss. Furthermore, at high intensity, this model reproduces the symmetric lineshape profile indicating that power broadening is becoming the dominant source of the width. This shows that at high intensity, the scattering nature of the problem, in which the initial state is embedded in a continuum of free atoms, is relatively unimportant.

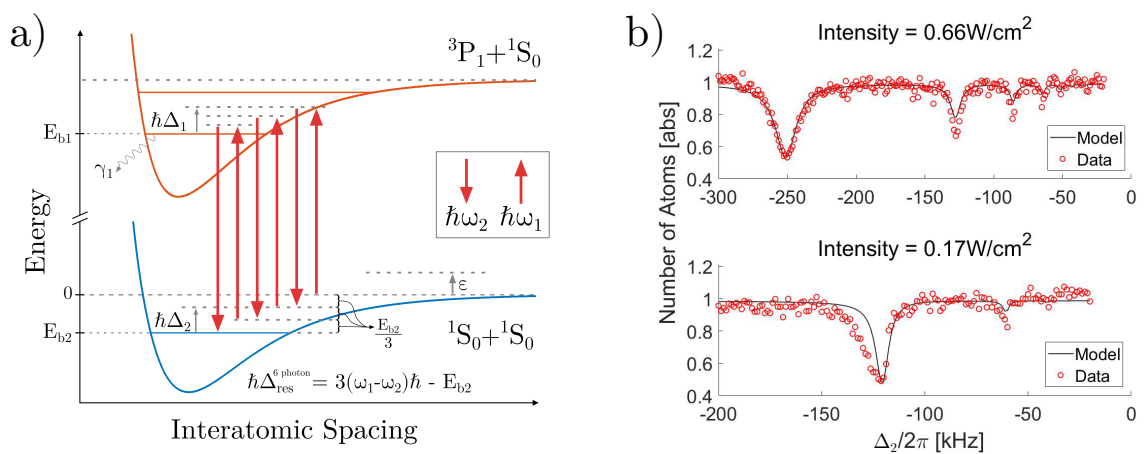


Figure 4.10 : Multi-photon Raman processes

a) The excitation process for observing multi-photon Raman processes. Shown is a 6-photon process which results in atom loss at  $E_{b2}/3$  where  $E_{b2}$  is the AC stark shifted halo molecule resonance energy of the fundamental process. b) Numerical simulation of the three-level model which reproduces the observed higher order loss processes.

## Chapter 5

### Binding energy of the $^{86}\text{Sr}_2$ halo molecule

Weakly bound ground-state dimers are of great interest in ultracold atomic and molecular physics. These molecular states exhibit the strongest dependence on the long-range portion of the interaction potential between atoms. Accurate description of the long-range part of this potential allows the scattering length,  $a$ , to be determined which is of the utmost importance in characterizing ultracold atomic physics. Measurement of the binding energy precisely determines the associated  $s$ -wave scattering length ( $a$ ) for free-atom collisions.

binding energy and scattering length are inversely correlated. Atoms with large scattering lengths will have molecular resonances nearby zero collision energy. given by E=hma2 Plugging in the values for 86 we estimate the most weakly bound level to have a binding energy of 86 kHz. Such extremely weakly bound molecules have special properties and are known as halo molecules. As discussed in Chap 1, halo molecules are Fig. 5.1 shows the halo state for 86

Of particular interest, the most weakly bound molecules are known as halo molecules which exhibit universality, meaning that molecular properties such as size and binding energy can be parameterized by the single quantity  $a$  independent of other details of the atom-pair interaction [12? ].

Atomic interaction potentials are difficult to understand a priori due to the complicated nature of multi-electron atoms. Even more so in the case of two valence electron atoms such as strontium. as we've needed to understand the potentials bet-

ter, we've developed analytic models for describing portions of the potential. GF considered a pure van-der-waals C6 potential and found that it can be analytically solved for the binding energies. By extending their model, they described interaction potentials that asymptote to a van-der-Waals form using an additional parameter, the van der Waals length  $l_{\text{vdW}}$ , which defines a length scale beyond which the C6 portion of the potential dominates. This provided a way to estimate the binding energy for weakly bound molecular states. For systems which exists near a scattering resonance, the analytic approximations of GF are expected to be quite accurate.

Efimov trimers also exist in systems near a scattering resonance, influencing dimer and atomic scattering properties and introducing additional universal phenomena [13, 68].

The known scattering properties of strontium are mass scaled from 88 is this somehow not as good for 86? Also, where are the most up to date scattering lengths for Sr from? The '10 Fourier paper but by probing the 86 ground state potential directly we can obtain a more accurate measurement of the 86-86 scattering length.

In the previous chapter we explored the coupling of the intermediate state and halo state via measuring the susceptibility as a function of the light intensity and detuning from the intermediate state.

This revealed that it is strongly coupled and that our initial experiments were in a strongly coupled regime.

In order to gain a more precise determination of the natural binding energy of the halo binding energy, we repeated similar experiments as before where we varied the laser intensity at a single fixed detuning.

We also varied the trap depth to look for any differences in susceptibility between the halo state and the asymptote.

In the extreme case of a scattering resonance, the least-bound state represents an example of a quantum halo system [40] with spatial extent well into the classically forbidden region.

We accurately determine the  $^{86}\text{Sr}_2$  binding energy, considering possible collisional frequency shifts and AC Stark shifts due to trapping and excitation lasers. Using the universal prediction for the binding energy, including corrections derived for a van der Waals potential [27, 28, 31], we derive a more accurate value of the *s*-wave scattering length for  $^{86}\text{Sr}$  atomic collisions [? ? ].

Finally, we consider the strontium interaction potential given by Tiemann. From our measurement of the 86 binding energy we estimate the value of C<sub>6</sub> for strontium and use a modified version of the potential to estimate improved scattering lengths for all isotopes via mass scaling.

In our first experiments probing the 86 halo, presented in the previous chapter, we probed the regime of strong coupling and observed large AC stark shifts and higher order Raman processes. These processes strongly perturbed the bare halo molecular state. Therefore, our next experiments choose to examine the weak coupling regime by applying low intensity excitations. This allows us to apply a simple isolated resonance model and precisely determine the effects of excitation lasers via intensity variation. Furthermore, we explored the

## 5.1 Modeling the PA spectra

Excitation to the halo state proceeded following the same general prescription as the photoassociation experiments presented in the previous chapter. However, the trap geometry was slightly modified to produce a larger trapping volume. This allowed us to maintain similar overall densities compared to our previous work, while allowing

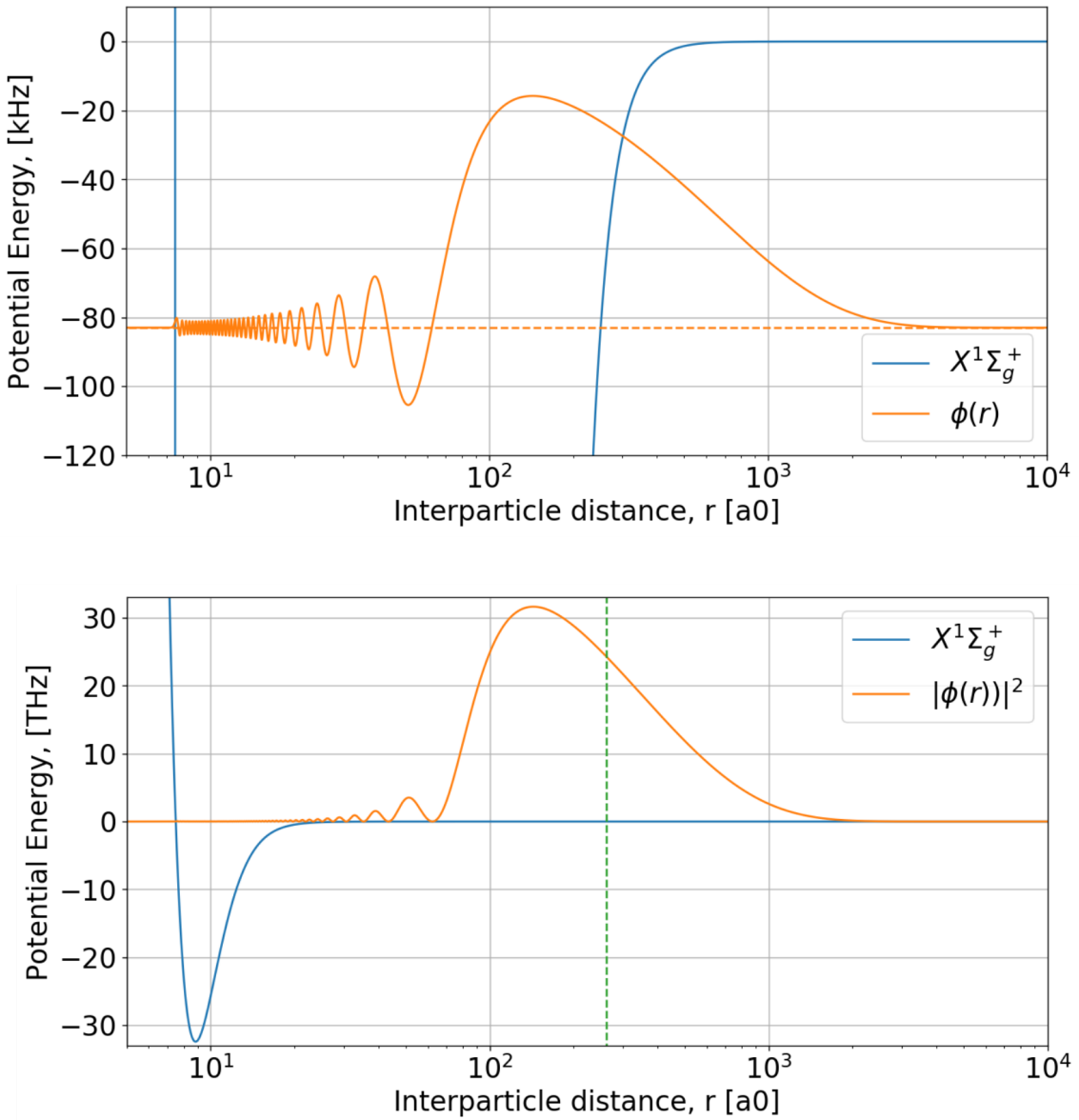


Figure 5.1 :  $^{86}\text{Sr}$  halo molecule wavefunction

The wavefunction (top) and probability amplitude (bottom) of the halo molecule calculated using the strontium ground state potential from Tiemann [ref.](#) Note the difference in energy scales to illustrate the weakest portion of the ground state potential. The wavefunction and probability amplitude have been scaled to be visible on each figure and are not normalized. As expected the halo molecule extends far into the classically forbidden region with the classical turning point, given by Eq. [something](#),

$$r_{clas} = \left( \frac{a^2 m C_6}{\hbar^2} \right)^{1/6} \approx 260 a_0$$

variation of the trap intensity to search for a difference in the AC Stark shift at 1064 nm between the free-atom asymptote and halo molecule state.

The single-beam optical dipole trap is generated from a 1064 nm laser propagating perpendicular to gravity produced this high volume trap. After forced evaporative cooling, we achieve atom temperatures between 30 nK - 1000 nK with typical atom numbers several hundred thousand and peak densities  $\approx n_0 = 1 \times 10^{12} \text{ cm}^{-3}$ . The number of atom number and sample temperature are measured using time-of-flight absorption imaging and trap oscillation frequencies are determined by measuring dipole and breathing collective mode frequencies.

As discussed in Chap 3, a description of photoassociative loss processes can be reduced to determining the inelastic loss rate coefficient  $K$ . This discussion of the rate loss constant assumed we could describe the spatial distribution of the atomic density profile analytically. This is a valid supposition given two key assumptions, 1) the sample temperature remains constant during the PA exposure and 2) the trap is of sufficient depth that we can reasonably approximate it as a harmonic trap. [cite Mi's trap paper](#). This simplifies the description of the density and velocity distributions within the trap.

result of fitting is a series of lorentzians. energy A value causes the amplitude to grow boltzmann factor occupation probability causes it to decrease

A discussed in the previous chapter, there are several concerns regarding the rigorous application of the Bohn and Julienne theory [? ] to these halo experiments. The first being that it assumes an isolated intermediate state which we demonstrated breaks down as  $\Delta_1$  or intensity is increased, (Fig.[something](#)). However, for our experiments here at fixed  $\Delta_1 = +9 \text{ MHz}$  and low intensities, any perturbations from additional states are expected to be negligible.

### 5.1.1 Consideration of the trap depth

The trapping potential is given by  $U(\mathbf{r}) = mgz + h\chi_{1064,g}I_{1064}(\mathbf{r}) - \tilde{U}_{\min}$ , where  $mgz$  is the gravitational potential at height  $z$ ,  $I_{1064}(\mathbf{r})$  is the intensity of the trapping light, and  $\chi_{1064,g} = 11 \text{ Hz}/(\text{W/cm}^2)$  [? ] is proportional to the polarizability of ground state atoms due to 1064 nm light.

If the single-particle kinetic-energy distribution function is a Boltzmann truncated at  $U_{\text{depth}} - U(\mathbf{r})$ , then the collision-energy distribution follows a Boltzmann distribution at low energies [ $\epsilon \ll U_{\text{depth}} - U(\mathbf{r})$ ] and falls off more quickly at larger energies, reaching zero at  $2[U_{\text{depth}} - U(\mathbf{r})]$ .

Three effects to discuss, the non analytic density distribution, the truncation of the energy, and the non-ergodicity. Density distribution because we need to know the spatial weighting at each position in space. Truncation of energy because the position in space leads to a spatially dependent maximum kinetic energy. The non-ergodicity because it means we don't actually know what the maximum kinetic energy should be.

This provides an analytically simply relationship between the spatial coordinates and the atoms potential energy due to the trapping potential. Such a description is typically valid when the ratio of the trap depth to the sample temperature is  $> 4$  ref. We define this ratio to be  $\eta = U_{\text{depth}}/k_B T$ .

Second, we consider the spatial density profile of the atomic sample and consider the number of atoms available in each region of the cloud.

In a typical high-eta trap, a Boltzmann profile is sufficient to describe the velocity distribution of the atoms and when we consider the distribution of relative energies that is important for PAS expeirments, we recover a simple bolztmann weighting for the distribution of energy probabilities. This is shown in [sopme app](#).

Then we have to figure out the distribution of collision energies. Following the example in [ref](#), chapter 3 considers two additional albeit related effects.

First, we consider the truncation of the collision energy interval. For traps of finite depth, we expect each atom to have kinetic energy up to  $U_{\text{depth}}/k_B T$ . We define this ratio as the trap- $\eta = U_{\text{depth}}/k_B T$ . Therefore, the maximum collision energy is  $2\eta$  between two particles each with kinetic energy  $\eta$ .

shift of the ground state energy by the trapping potential for each shell of density. decide to fit both 1ud and 2ud as limiting cases because we aren't sure which energies contribute to the atomic loss

$\tilde{U}_{\min}$  is subtracted to set the potential at the trap minimum to zero. The spatial integral is restricted to regions around the trapping local minimum with  $U(\mathbf{r})$  less than the trap depth [? ].

Downhill regions on the other side of the saddle point defining the trap depth are excluded. The laser intensity profile is measured independently, and the potential is found to be consistent with measured trap oscillation frequencies.

The partition function is  $Q_T = \left(\frac{2\pi k_B T \mu}{\hbar^2}\right)^{3/2}$  for reduced mass  $\mu = m/2$  and sample temperature  $T$ , for atoms of mass  $m$ .

Equation (??) provides the correct thermal average when the collision-energy distribution does not need to be truncated ( $\epsilon_{\max} \rightarrow \infty$ ).

For our data, however, the ratio of sample temperature to trap depth is  $k_B T/U_{\text{depth}} \approx 3$  for samples with temperature above 100 nK and drops to unity for 30 nK samples, so truncation effects are important.

We find that this treatment predicts a narrower distribution on the red side of the spectral line than we observe in our data, suggesting the presence of atoms in non-ergodic orbits with energies above the saddle point of the trap.

This is not surprising given the large collisional loss rate associated with near-resonant scattering in this isotope.

Analysis of the trapping conditions following acquisition of the PAS data revealed that this second assumption was not maintained during these low-intensity experiments. Lacking an analytic expression for the density distribution, a description of the bulk properties is possible by discretizing the trap and considering its local properties. Fig. 5.2 shows the potential energy surface for a characteristic trap used in this experiment. Recalling that the trap depth is defined between the trap minimum and the lowest saddle point, we see that this point is along a non-trivial trajectory. Thus atoms at high kinetic energies may remain trapped in the region and the timescale to reach equilibrium is long. Due to this ambiguity

In addition to the modified spatial distribution, we must also consider the effect of the trap depth on the energy profile of the trapped gas.

This is troublesome as it means we must numerically consider the density distribution over space when solving for the rate loss constant K.

However, the case of a low- $\eta$  trap we must define a local cutoff energy at each point in space within the trap as atoms that have an energy higher than the local  $\eta$  value are assumed to be lost from the trap.

Derivation of this truncated relative energy probability distribution is given in some app and results in a stronger weighting of the coldest atoms near the bottom of the trap. For deep traps, the effects of the energy truncation due to the finite trap depth become negligible and the relative collision energy likelihood approaches a Maxwell-Boltzmann. Details of this limiting behavior are given in App. ??.

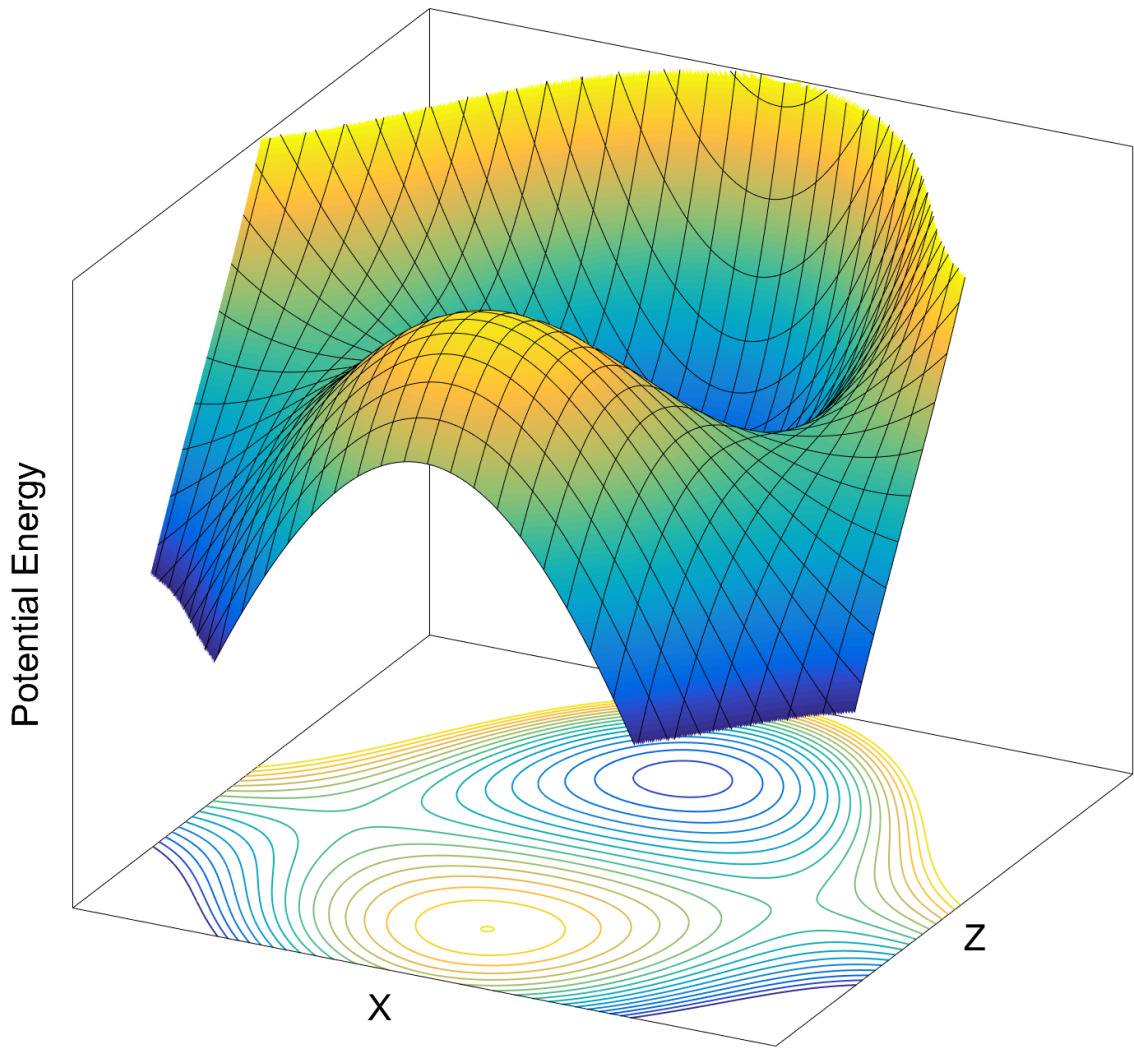


Figure 5.2 : Surface plot of the trapping volume in single beam trap

The spatial dependence along the XZ plane with Y=0 of the ground state potential energy during the halo molecule excitation. Note, this coordinate system assumes the laser wavevector is propagating along +X and gravity is aligned along -Z. We can clearly see the trap depth is defined along a trajectory where a particle is simultaneously moving away from the beam waist and down under the influence of gravity.

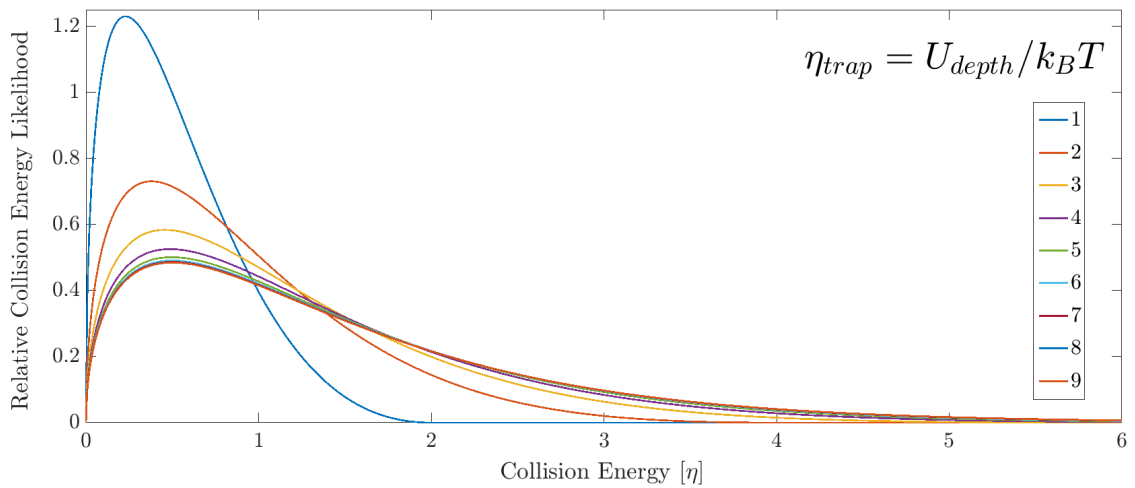


Figure 5.3 : Relative collision energy distributions for various trap depths

The effects of energy truncation on the likelihood of collisions at different various trap depths where the total collision probability for each curve is normalized to unity. Energy is specified in units of  $\eta = U_d/k_B T$ . Each trap has a maximum collision energy of  $2\eta_{trap}$  between two particles each with maximum kinetic energy  $\eta$ .

### 5.1.2 Fitting the thermally averaged spectra

Fortunately, the molecular binding energy is strongly determined by the sharp edge of the spectrum on the blue side of the line, which is relatively insensitive to the description of the red tail.

Our data is fit well with a truncated Boltzmann distribution of collision energies [Eq. (??)].

To estimate the systematic uncertainty introduced by this treatment, we perform fits with  $\epsilon_{\max}$  equal to  $2[U_{\text{depth}} - U(\mathbf{r})]$  and  $U_{\text{depth}} - U(\mathbf{r})$  and take the mean of the two results as the best value for the binding energy and half the difference as a systematic uncertainty  $\sigma_{\epsilon_{\max}} \approx 100 \text{ Hz}$ .

This procedure does not correctly represent the overall normalization of  $\langle K \rangle$ , but we are not concerned with overall signal amplitude in this study.

Atom temperatures vary by no more than 20% during the interaction time, so assuming a constant sample temperature is reasonable.

In Ch. somewhere we discussed the usual situation for observing loss due to photoassocition. This experiment was similar to the 88 autler townes experiment.

Two notable features, 1) the linewidth on the right side starts broad and becomes more narrow as the maximum collision energy is increased. Conversely, the these are fits so when the model is not appropriate the algorithm will broaden out the line and shift the binding energy to try and describe the data. For max coll of 2, we see a broad linewidth was

The tail is given by atoms near the center of the trap. These are high enegy atoms which are only possible

this data did not show an increase in tmperature and the timescales used are apprpriate for a frozen gass approximation. The hottest atoms must be near the

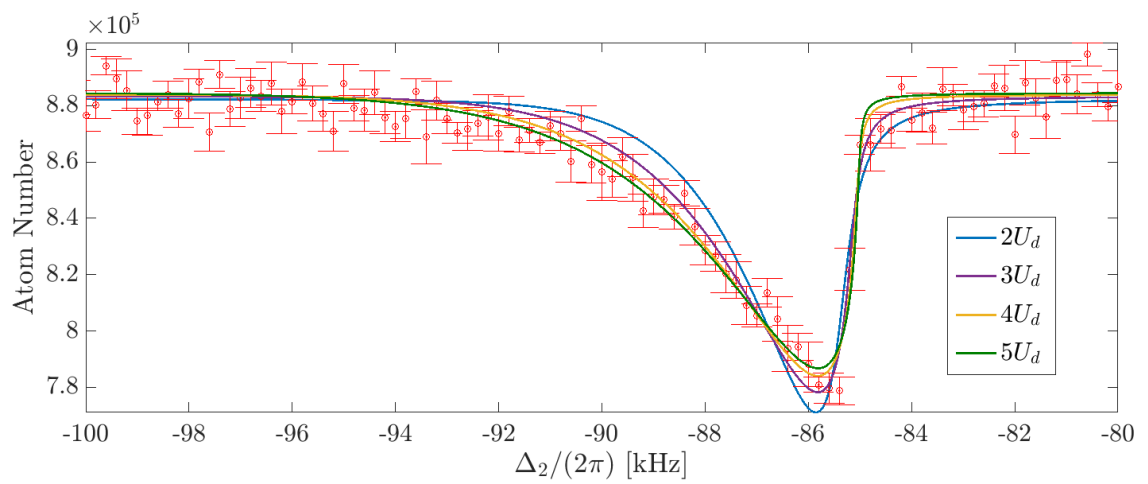


Figure 5.4 : Comparison of lineshape fits at various  $\epsilon_{\max}$

Using a constant trap geometry (eg. Fig. [trapFig](#)) with a trap depth  $U_d$ , the spectra is fit with varying maximum collision energy,  $\epsilon_{\max}$ . The solid lines give the maximum single particle kinetic energy such that the collision energy is twice Temperature of this sample is 100 nK

center of the trap since this is the only region deep enough to keep them trapped. Conversely, cold atoms appear near the edges of the trap for the same reason. Thus we can see that for a max collision energy of  $2U$ , the linewidth biases towards large values and the binding energy shifts. This suggests that the model is incomplete at this energy and we are missing contributions from hotter atoms. As we increase the maximum collision energy, the linewidth decreases and begins to better describe the observed data. At the same time, we begin accurately accounting for the thermal portion of the spectrum. Since it is not clear which description is most accurate for our scenario, we choose to fit the data at the limits of  $2U$  and  $4U$  as shown in Fig. something.

Bohn and Julienne [? ] provide an expression for  $|S(\epsilon, \omega_1, \omega_2, \dots)|^2$  for a collision on the open channel of two ground state atoms (g) with total energy  $\epsilon$  leading to loss-producing decay from the excited state  $b_1$  with rate  $\gamma_1$  (Fig. ??),

$$|S|^2 = \frac{(\Delta_2 + \epsilon/\hbar)^2 \gamma_1 \gamma_s}{\left[ (\Delta_1 + \epsilon/\hbar)(\Delta_2 + \epsilon/\hbar) - \frac{\Omega_{12}^2}{4} \right]^2 + \left[ \frac{\gamma_1 + \gamma_s}{2} \right]^2 (\Delta_2 + \epsilon/\hbar)^2}. \quad (5.1)$$

For simplicity, we have omitted the light shift of  $b_1$  due to coupling to the scattering continuum [? ].

This approach was found to be sufficient for describing two-photon spectroscopy to a more deeply bound molecular level in  $^{88}\text{Sr}$  [? ].

Equation (??) neglects all light shifts due to the trapping laser. Light shifts due to the photoassociation lasers coupling to states outside our model (Fig. ??) are also neglected.

The thermal energy is much greater than the zero-point energy for trap motion,  $T \gg h\nu_{\text{trap}}/k_B$ , so confinement effects are negligible [? ].

$\gamma_1 = 2\gamma_{\text{atomic}}$ , where  $\gamma_{\text{atomic}} = 4.7 \times 10^4 \text{ s}^{-1}$  is the decay rate of the atomic  ${}^3P_1$  level.

$\gamma_s(\epsilon)$  is the stimulated width of  $b_1$  due to coupling to the initial scattering state by laser 1, which for low energy can be expressed as [19, 71? ]

$$\gamma_s(\epsilon) = 2kl_{\text{opt}}\gamma_1, \quad (5.2)$$

where the optical length ( $l_{\text{opt}} \propto I_1$ ) is related to the overlap between the initial colliding state and  $b_1$ , and  $k = (2\mu\epsilon)^{1/2}/\hbar$ .

We take the intermediate state  $b_1$  as the  $\nu = -2$  state, for which  $l_{\text{opt}}/I = (1.5 \pm 0.3) \times 10^4 a_0/(\text{W/cm}^2)$  [? ], where  $a_0 = 5.29 \times 10^{-11} \text{ m}$  is the Bohr radius.

For the experiments reported here, we maintain significant intermediate-state detuning,  $\Delta_1$ , for which  $|\Delta_1| \gg |\Omega_{2,12}|$ .

Thus we are in a Raman configuration, and not in the Autler-Townes regime [? ].

In the Raman regime, Eq. ?? shows a maximum near two-photon resonance at  $\Delta_2 + \epsilon/\hbar = \Omega_{2,12}^2/4\Delta_1$ .

Following a treatment discussed recently for a similar experiment in calcium [71], if the detuning is restricted to near two-photon resonance then  $|S|^2$  can be approximated as a Lorentzian

$$|S|^2 \approx \frac{A(\epsilon)}{\left(\Delta_2 + \epsilon/\hbar - \frac{\Omega_{2,12}^2}{4(\Delta_1 + \epsilon/\hbar)}\right)^2 + [\Gamma_L(\epsilon)/2]^2}, \quad (5.3)$$

where

$$A(\epsilon) = \frac{\Omega_{2,12}^4 \gamma_1 \gamma_s(\epsilon)}{16(\Delta_1 + \epsilon/\hbar)^4} \quad (5.4)$$

$$\Gamma_L(\epsilon) = \frac{\Omega_{2,12}^2 [\gamma_1 + \gamma_s(\epsilon)]}{4(\Delta_1 + \epsilon/\hbar)^2}. \quad (5.5)$$

In the absence of a more complete theory treating these effects, we analyze loss spectra using the effective expression given by Eq. (5.6), where the observed molecular

binding energy ( $E'_{b2}$ ) includes any perturbations due to AC Stark or collisional shifts.

$$|S|^2 = \frac{\Gamma_L(\epsilon) + \gamma_{\text{eff}}}{\Gamma_L(\epsilon)} \times \frac{\eta A(\epsilon)}{(\omega_1 - \omega_2 + \epsilon/\hbar - E'_{b2}/\hbar)^2 + \left[\frac{\Gamma_L(\epsilon) + \gamma_{\text{eff}}}{2}\right]^2}, \quad (5.6)$$

Parameters have been added in Eq. (5.6) to account for deviations of the signal strength ( $\eta$ ) and width ( $\gamma_{\text{eff}}$ ) from the predictions of [? ].

If deviations from Eq. (??) are small, we expect  $\eta \sim 1$ ,  $\gamma_{\text{eff}} \sim 0$ , and  $E'_{b2} \sim E_{b2} + \Omega_{2,12}^2/4(\Delta_1 + \epsilon/\hbar)$ .

Light shifts (AC Stark shifts) due to the trapping lasers and collisions with ground-state atoms (density  $n$ ) should contribute to shifts of molecular resonance.

Similar effects were taken into account in a recent, high-precision study of weakly bound molecular states of ultracold ytterbium atoms [83].

In addition, we expect that both 689-nm excitation lasers will shift the line, not just  $I_2 \propto \Omega_{2,12}^2$ . We model the relationship between the measured resonance positions and the unperturbed binding energy  $E_{b2}$  as

$$E'_{b2} = E_{b2} + h\chi_{689}I_{689} + h\chi_{1064}I_{1064}(\mathbf{r}) + h\chi_n n(\mathbf{r}). \quad (5.7)$$

## 5.2 Determination of energy shifts

Figure 5.5 shows a series of spectra for different final trap depths and sample temperatures.

The characteristic asymmetric lineshape for excitation of a thermal sample is evident, with width decreasing as sample temperature decreases.

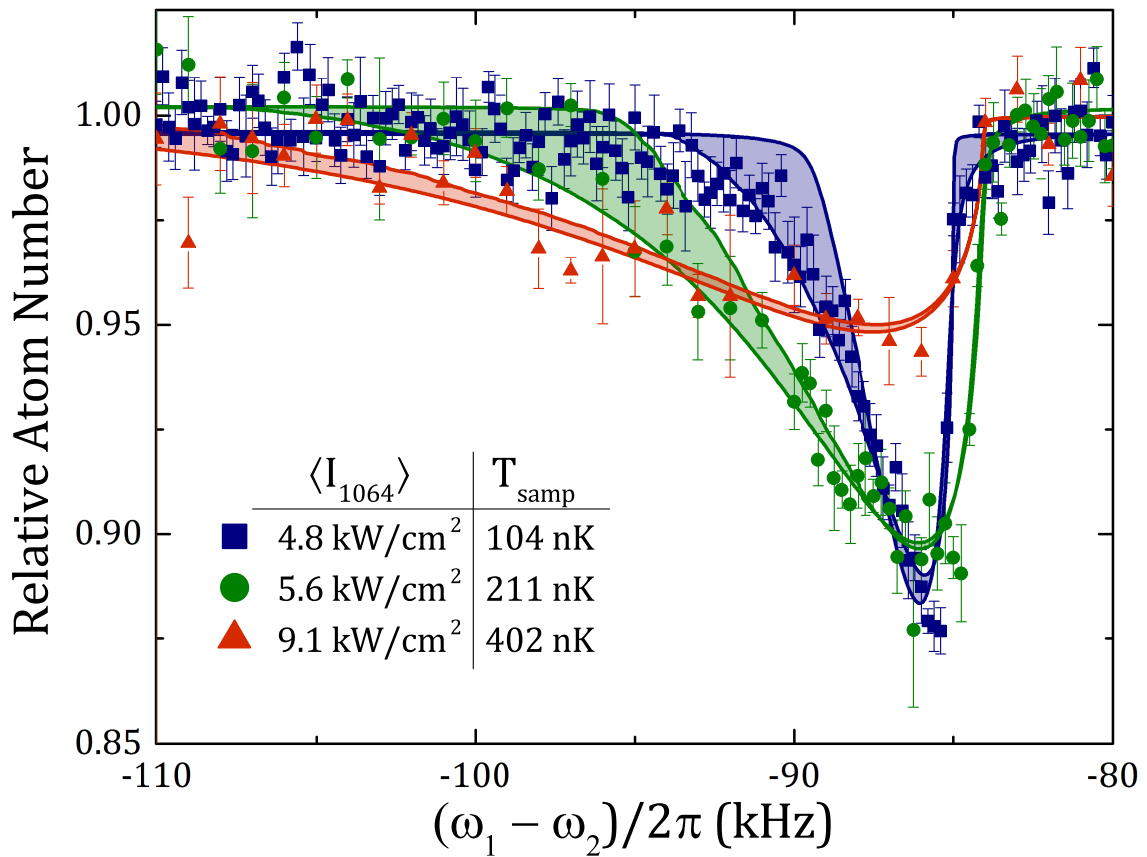


Figure 5.5 : Variation of 1064 nm trap depth

Atom-loss spectra as a function of two-photon difference frequency  $(\omega_1 - \omega_2)/2\pi$  for intermediate detuning  $\Delta_1/2\pi = -9 \text{ MHz}$ . Sample temperature and average trapping laser intensity are indicated in the legend. The single-beam excitation laser intensity is  $I = 25 \text{ mW}/\text{cm}^2$  for the 104 nK spectrum and  $I = 48 \text{ mW}/\text{cm}^2$  for the 211 nK and 402 nK spectra. Fits are described in the text, with the two boundaries of each band given by the fits with collision-energy truncation  $\epsilon_{\max}$  equal to  $2[U_{\text{depth}} - U(\mathbf{r})]$  and  $U_{\text{depth}} - U(\mathbf{r})$ .

The molecular binding energy is close to the sharp edge on the blue side of each spectrum.

We fit atom-loss spectra with Eq. (??) for the evolution of atom number with time, using the phenomenological expression Eq. (5.6) for the scattering probability and Eq. (??) for the average of the collision event rate constant over the trap volume and collision energy.

The sample temperature, perturbed resonance frequency  $E'_{b2}$ ,  $\eta$ , and  $\gamma_{\text{eff}}$  are taken as fit parameters.

In the final analysis, temperatures are set to values determined from time-of-flight imaging of the atoms, but when they are allowed to vary, the fit values differ by no more than 10%.

Approximately 10 spectra are recorded for each set of experimental parameters, and the spread of resulting fit values are used to determine best values and uncertainties.

The susceptibilities, in Hz per unit intensity or density, will be determined from experimental data or theoretical considerations.

The variation with position of the trapping laser intensity ( $I_{1064}$ ) and the density give rise to the spatial dependence of  $|S|^2$  and the need for a spatial average in Eq. (??).

We take  $I_{689}$  as twice the single-beam intensity  $I_{689} = 2I$ . The 689-nm excitation beam is large enough compared to the atom sample to neglect spatial variation.

The functional form for the AC Stark shift due to the excitation lasers is discussed in Sec. ??.

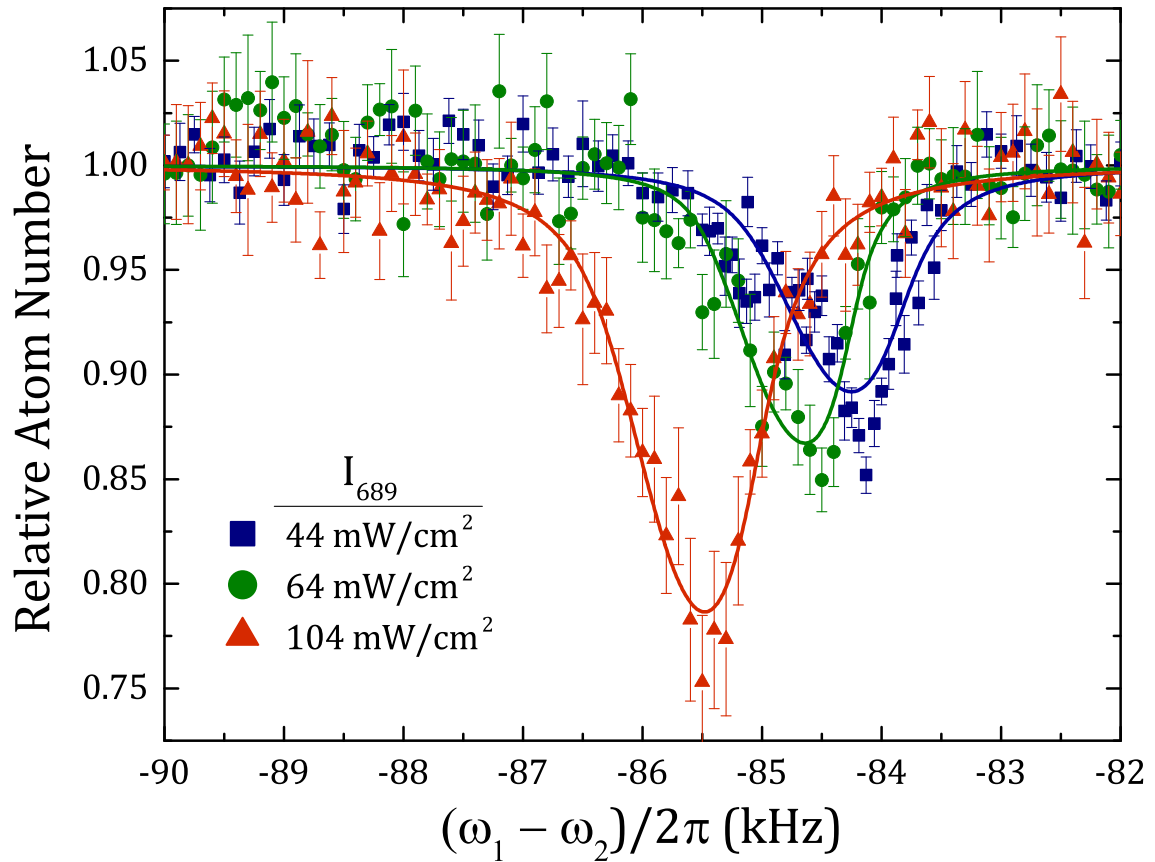


Figure 5.6 : Variation of 689 nm excitation

Atom-loss spectra as a function of two-photon difference frequency  $(\omega_1 - \omega_2)/2\pi$  for intermediate detuning  $\Delta_1/2\pi = -9 \text{ MHz}$  and various 689-nm excitation laser intensities . Twice the single-beam intensity  $I_{689} = 2I$  is indicated in the legend.

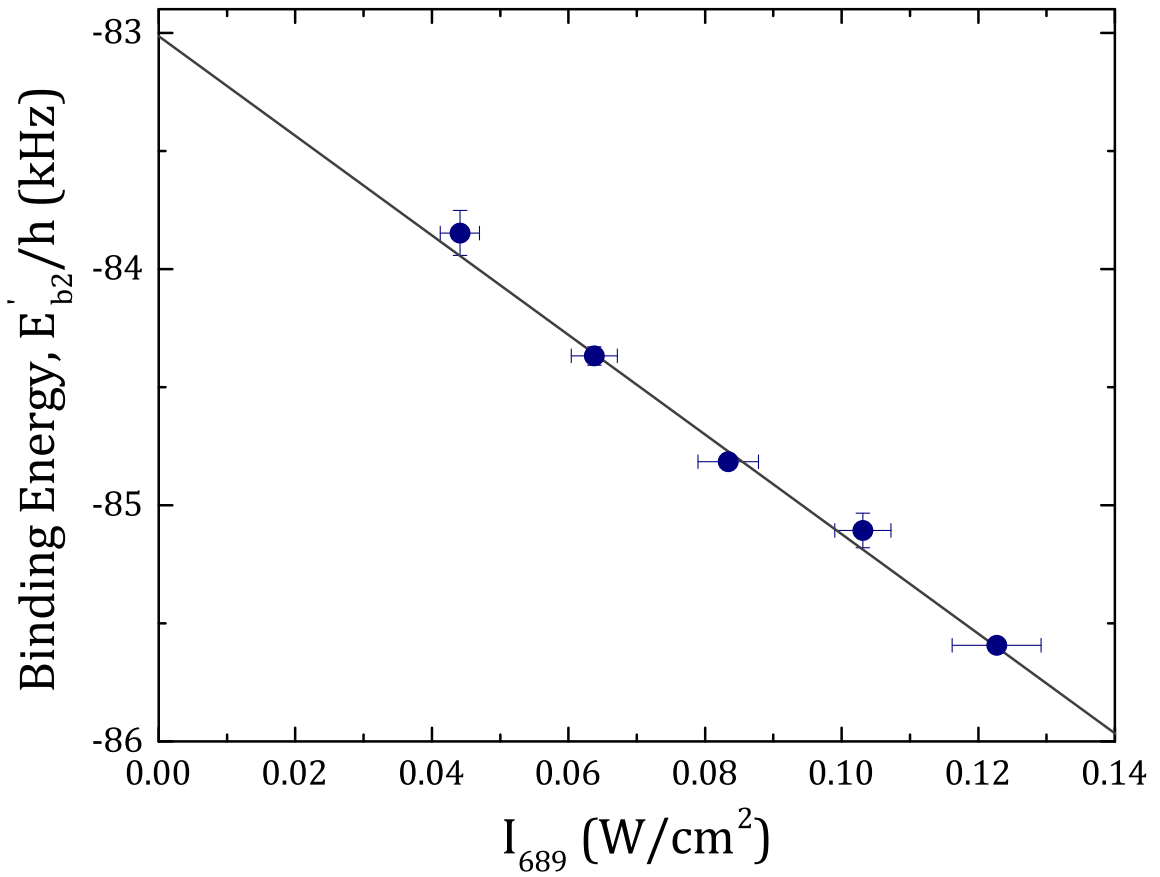


Figure 5.7 : Fit of 689 nm AC Stark shift

Measured resonance position  $E'_{b2}$  plotted versus twice the single-beam intensity  $I_{689} = 2I$ . The linear fit provides the AC Stark shift parameter  $\chi_{689}$ .

### 5.2.1 AC Stark shift due to excitation lasers

The most significant perturbation to the resonance position is the AC Stark shift due to the excitation laser intensity, as shown in Fig. 5.6.

For this data, the trap parameters, temperature ( $T = 30\text{ nK}$ ), and initial peak sample density ( $n_0 = 2 \times 10^{12}\text{ cm}^{-3}$ ) are held constant.

We vary the single-beam excitation intensity from  $I = 0.02 - 0.06\text{ mW/cm}^{-2}$ , and the excitation time is 50 ms.

The observed shifts are comparable to the thermal width of the spectrum, allowing a precise determination of  $\chi_{689} = -21(1)(2)\text{ kHz/(W/cm}^2)$  from a linear fit to the resonance positions,  $E'_{b2} \propto h\chi_{689}I_{689}$  (Fig. 5.7).

The first quoted uncertainty is statistical and it arises from variations in parameters and fluctuations in the measured intensity during the scans.

The second value is systematic, reflecting uncertainty in laser-beam size and intensity profile at the atoms.

All parameters beside the 689-nm laser intensity are held fixed for this data set, and the AC Stark shift is not correlated with any other variable, such as density or trap intensity.

We thus obtain an accurate measure of  $\chi_{689}$  without attempting to account for other systematic shifts of  $E'_{b2}$  in this data.

A study of the dependence of  $\chi_{689}$  on detuning from the excited molecular state will be discussed in Sec. ??.

Broadening to the red of the spectrum reflects the distribution of atom-atom collision energies, while broadening to the blue is most sensitive to decay of the intermediate state ( $\Gamma_L$ ) and the phenomenological broadening term  $\gamma_{\text{eff}}$  [Eqs. (5.5) and (5.6)].

The long lifetime of the excited state and the significant detuning  $\Delta_1$  result in a width  $\Gamma_L(\epsilon)$  less than 5 Hz for all conditions.

This is extremely small compared to observed width, which yields values of  $\gamma_{\text{eff}}$  on the order of 300 Hz.

We hypothesize that this width reflects decay of molecules in the electronic ground-state due to collisions with background atoms.

### 5.2.2 Density-dependent frequency shift

A shift of the two-photon resonance position is possible due to differing mean-field shifts of initial atomic and final molecular states arising from interaction with the background of ground-state atoms.

Such a shift would be proportional to the atom density and depend upon the *s*-wave scattering lengths for atom-atom and atom-dimer collisions,  $a_{86}$  and  $a_{\text{ad}}$  respectively.

This was observed in a Rb Bose-Einstein condensate (BEC) in [89]. For a non-degenerate gas, this effect yields  $\chi_n = \hbar(\frac{a_{\text{ad}}}{\mu_{\text{ad}}} - 4\frac{a_{86}}{\mu_{\text{aa}}}) = \frac{\hbar}{m}(\frac{3}{2}a_{\text{ad}} - 8a_{86})$ , where  $\mu_{\text{ad}}$  and  $\mu_{\text{aa}}$  are the reduced masses for molecule-atom and atom-atom collisions respectively.

Note that the shift would vanish for  $a_{\text{ad}} = (16/3)a_{86}$ .

The largest density used in our experiment ( $\sim 1 \times 10^{12} \text{ cm}^{-3}$ ) is relatively low compared to typical BEC densities, and at this time we are unable to accurately measure a variation of resonance position with density.

However, the atom-atom scattering is close to resonance and thus Efimov physics can provide information on  $a_{\text{ad}}$  [13, 68] and an estimate of the systematic error introduced by any residual density-dependent frequency shifts.

For a zero-range interaction, the atom-dimer scattering length is related to the

atom-atom scattering length through the three-body Efimov parameter  $\kappa_*$  according to [13]

$$a_{\text{ad}} = a_{86} \{1.46 + 2.15 \cot[s_0 \ln(14.1 \kappa_* a_{86})]\} \quad (5.8)$$

where  $s_0 = 1.006$ <sup>\*</sup>.

In principle, the atom-dimer scattering length can take any value.

However, for a deep atom-atom potential, such as for the ground-state strontium dimer [?], there is a universality of the three-body physics that sets  $\kappa_* = 0.226(2)/l_{\text{vdW}}$  [86].

Here,  $l_{\text{vdW}} = (2\mu C_6/\hbar^2)^{1/4}/2 = 74.6 a_0$  is the van der Waals length associated with the  $C_6$  coefficient of the long-range Sr<sub>2</sub> ground-state potential.

We use  $C_6 = 3.03(1) \times 10^{-76}$  J m<sup>6</sup> found from a fit of potential parameters to spectroscopic data [?], which is consistent with a recent *ab initio* calculation [93].

This yields  $\kappa_* = 5.72 \times 10^7$  m<sup>-1</sup> =  $(330 a_0)^{-1}$ . Equation (5.8) then predicts  $a_{\text{ad}} = 6.4 a_{86}$ , which leads to a small density-dependent frequency shift parameter of  $\chi_n = 50$  Hz/(10<sup>12</sup> cm<sup>-3</sup>).

A numerical calculation including a finite-range correction for the atom-atom interaction [62] results in  $a_{\text{ad}} = 3.5 a_{86}$  and  $\chi_n = -90$  Hz/(10<sup>12</sup> cm<sup>-3</sup>).

Thus, a very small shift is expected for the densities used here.

We incorporate  $\chi_n = 0 \pm 90$  Hz/(10<sup>12</sup> cm<sup>-3</sup>) as a set parameter in our model of the spectrum, where we set the systematic uncertainty to reflect the spread of theory predictions.

This uncertainty will be significant for our determination of the unperturbed halo binding energy.

---

\*The Efimov parameter is related to  $E_{3b}^0$  through  $\kappa_* = (m|E_{3b}^0|/\hbar^2)^{1/2}$ , where  $E_{3b}^0$  is the binding energy the lowest Efimov trimer would have in the case of resonant atom-atom interactions.

### 5.2.3 AC Stark Shift due to Trapping Lasers

There is an additional effect we considered which accounts for the spatial dependence of the AC Stark shift due to the variation in intensity of the 1064 nm trapping laser. We tested simulations accounting for this effect and found no noticeable deviations of the complete lineshape within our knowledge of the exact trapping potential. Inclusion of this effect significantly increases the computation time of the lineshape so we approximated this effect by calculating a two-body weighted average intensity of the 1064 nm laser to characterize the average shift experienced by the atoms due to the trapping potential.

With an accurate determination of  $\chi_{689}$  and a value for  $\chi_n$ , we use the data shown in Fig. 5.5 to determine the susceptibility for the AC Stark shift from the trapping laser,  $\chi_{1064}$ , and the unperturbed halo binding energy  $E_{b2}$ .

Figure 5.8 shows a plot of  $E'_{b2} - \chi_{689}I_{689} - \chi_n\langle n \rangle$  versus  $\langle I_{1064} \rangle$ , where  $E'_{b2}$  is the resonance position from each fit and  $\langle \dots \rangle$  indicates a weighted average of the quantity over the trapped sample, with a weighting given by the square of atom density.

This weighting reflects the contribution to photoassociative loss, a two-body process.

The plotted uncertainties in  $E'_{b2} - \chi_{689}I_{689} - \chi_n\langle n \rangle$  are from statistical variation in the fit parameters.

The typical average density is  $\langle n \rangle \approx 1 \times 10^{12} \text{ cm}^{-3}$ . The linear fit function is to  $E_{b2} + \chi_{1064}\langle I_{1064} \rangle$ .

In addition to statistical uncertainty, we have systematic uncertainty from  $\chi_n$  and treatment of the truncation of the collision-energy integral [Eq. (??)].

The dashed lines shown in Fig. 5.8 are resulting fits when the values of  $E'_{b2} - \chi_{689}I_{689} - \chi_n\langle n \rangle$  are shifted by the sum of these systematic uncertainties.

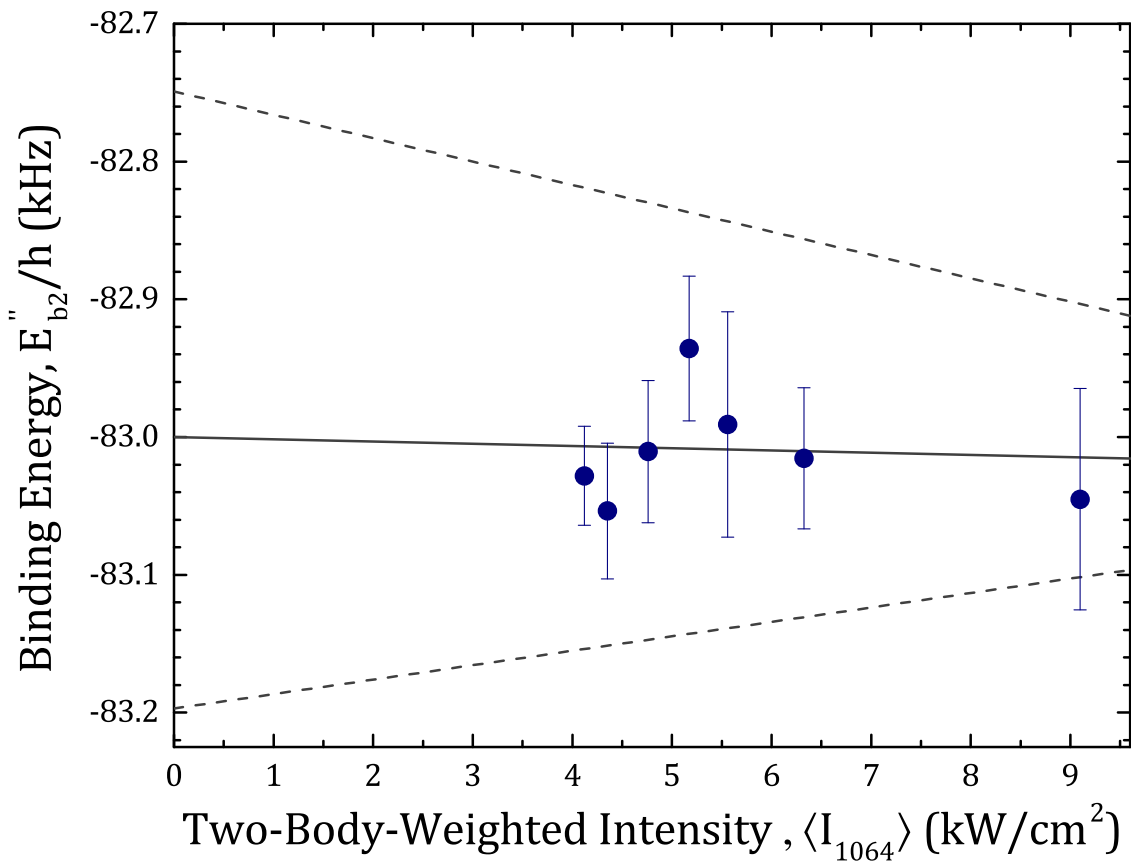


Figure 5.8 : Measurement of halo state susceptibility,  $\chi_{1064}$

Measured resonance positions corrected for excitation-laser AC Stark shift and collisional frequency shift,  $E'_{b2} - \chi_{689}I_{689} - \chi_n\langle n \rangle$ , as a function of average trap laser intensity  $\langle I_{1064} \rangle$  for the data such as in Fig. 5.5 . The trend line and confidence intervals are described in the text.

The resulting value for the unperturbed binding energy is  $E_{b2}/\hbar = -83.00(7)(20)$  kHz, where the first uncertainty is statistical, and the second is systematic.

We observe a susceptibility to  $I_{1064}$  of  $\chi_{1064} = 0 \pm 10$  Hz/(kW/cm<sup>2</sup>).

For two-photon spectroscopy to a weakly bound dimer, it is typical to neglect any potential AC Stark shift due to far-off-resonant trapping lasers because the atoms contribute to the overall polarizability approximately as free atoms.

But the high precision of our measurement allows us to detect a small shift.

This corresponds to a relative differential polarizability of  $\chi_{1064}/2\chi_{1064,g}g = (\chi_{1064,b2} - 2\chi_{1064,g}g)/2\chi_{1064,g}g \approx 0.0001$ , or  $xx$ .

### 5.3 Discussion of the halo binding energy

In the limit of extremely small binding energy, and thus resonant atom-atom interactions, the binding energy of a halo molecule is approximately given by [? ]

$$E_b = -\hbar^2/2\mu a^2. \quad (5.9)$$

For interactions described at long-range by the van-der-Waals form,  $V(r) = -C_6/r^6$ , as with ultracold atoms, a convenient figure of merit for quantifying how accurate this simple expression should be is given by the ratio of the *s*-wave scattering length to the mean scattering length or interaction range, closely related to the van der Waals length through [18, 31]

$$\bar{a} = l_{\text{vdW}} \frac{\Gamma(\frac{3}{4})}{\sqrt{2}\Gamma(\frac{5}{4})}. \quad (5.10)$$

Slightly away from resonance, corrections to the binding energy for the van der Waals potential were worked out in [27, 28], yielding

$$E_{b2} = -\frac{\hbar^2}{2\mu(a - \bar{a})^2} \left[ 1 + \frac{g_1 \bar{a}}{a - \bar{a}} + \frac{g_2 \bar{a}^2}{(a - \bar{a})^2} + \dots \right], \quad (5.11)$$

where  $g_1 = \Gamma(1/4)^4/6\pi^2 - 2 = 0.918\dots$  and  $g_2 = (5/4)g_1^2 - 2 = -0.947\dots$ . The range of validity of this expression is  $a \gtrsim 2\bar{a}$ .

The accuracy of the first term in this expansion has been experimentally confirmed for various systems such as  $^{85}\text{Rb}$  [22, 49],  $^{40}\text{K}$  [66, 73] and  $^6\text{Li}$  [3].

This derivation of Eq. (5.11) assumes that the influence of short-range physics, which can be expressed through a quantum defect, varies negligibly from threshold to the molecular binding energy.

We expect this to be an excellent approximation, since, as shown in Ref. [27] the corrections are typically less than about 1% even for GHz binding energies.

For ground-state  $^{86}\text{Sr}$  atoms,  $\bar{a} = 71.3 a_0$ .

The most accurate value available for the s-wave scattering length is  $a = 798(12) a_0$  [? ], satisfying the requirement of  $a \gg \bar{a}$  for the least-bound state on the ground molecular potential to be a halo molecule.

Nonetheless,  $\bar{a}/(a - \bar{a}) = .10$ , and the corrections given by Eq. (5.11) are significant.

Figure 5.9 shows the importance of the correction terms.

Equation (5.11) and the previous best value of the scattering length [? ] predict a binding energy of  $E_{b2} = -86(3)$  kHz.

This agrees with our measurement, but by inverting Eq. (5.11), we can use our increased accuracy in  $E_{b2}$  to extract an improved value of the scattering length of  $a = 810.6(3)(9) a_0$ , where uncertainties reflect statistical and systematic uncertainties in  $E_{b2}$  respectively.

The next higher-order term in  $x_0 = \bar{a}/(a - \bar{a})$  is likely to introduce a correction on the order of 100 Hz in Eq. (5.11), creating a systematic uncertainty in  $a$  that is about one third of the uncertainty from our measurement.

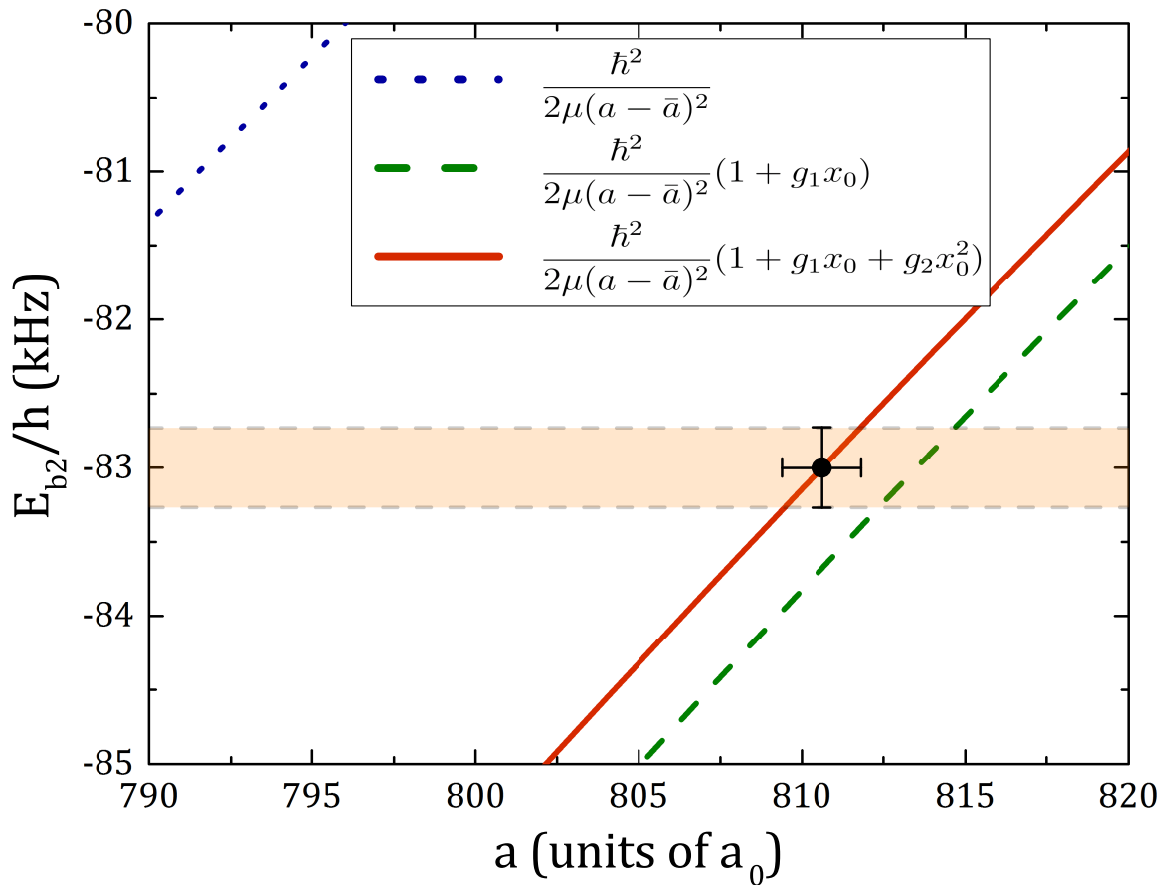


Figure 5.9 : Determination of  ${}^{86}\text{Sr}$  scattering length

Halo binding energy versus  $s$ -wave atom-atom scattering length for  ${}^{86}\text{Sr}$ . The shaded region indicates our experimental measurement. The lines are predictions of Eq. 5.11 retaining up to the first, second, and third terms as indicated in the legend [ $x_0 = \bar{a}/(a - \bar{a})$ ]. The data point is the prediction of Eq. (5.11) for the recommended value of the measured binding energy.

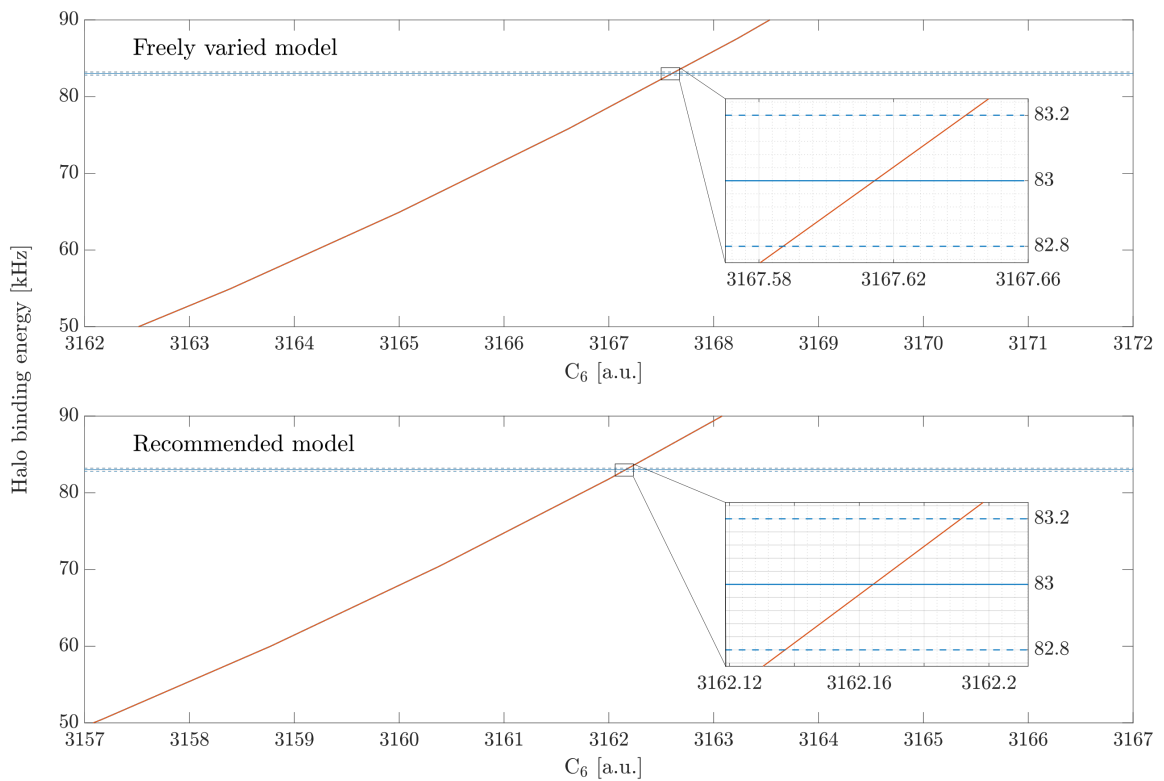


Figure 5.10 : Comparison of  $C_6$  coefficient estimates

Binding energy estimated from GF

We consider the collisional wavefunction and estimate the 86 scattering length via the position of the last node. Using the two different values of C6 we calculate the wavefunction with a collision energy of 10nK to estimate the

Another way to estimate the scattering length is via a numerical integration of the ground state potential.

This method lets us quickly calculate the scattering length across a range of reduced masses in order to mass scale our model.

From the formula for the line shape we can see that it depends on the spatial distribution of the atoms.

The standard approximation made when measuring these types of systems is to ensure loss does not cause heating of the atoms during photoassociation.

Heating results in re-equilibration of the atomic density distribution, which in turn effects the rate of loss creation.

Without independent controls to keep the system in thermal (and therefore spatial density) equilibrium.

What are the things the rate equation deals with?

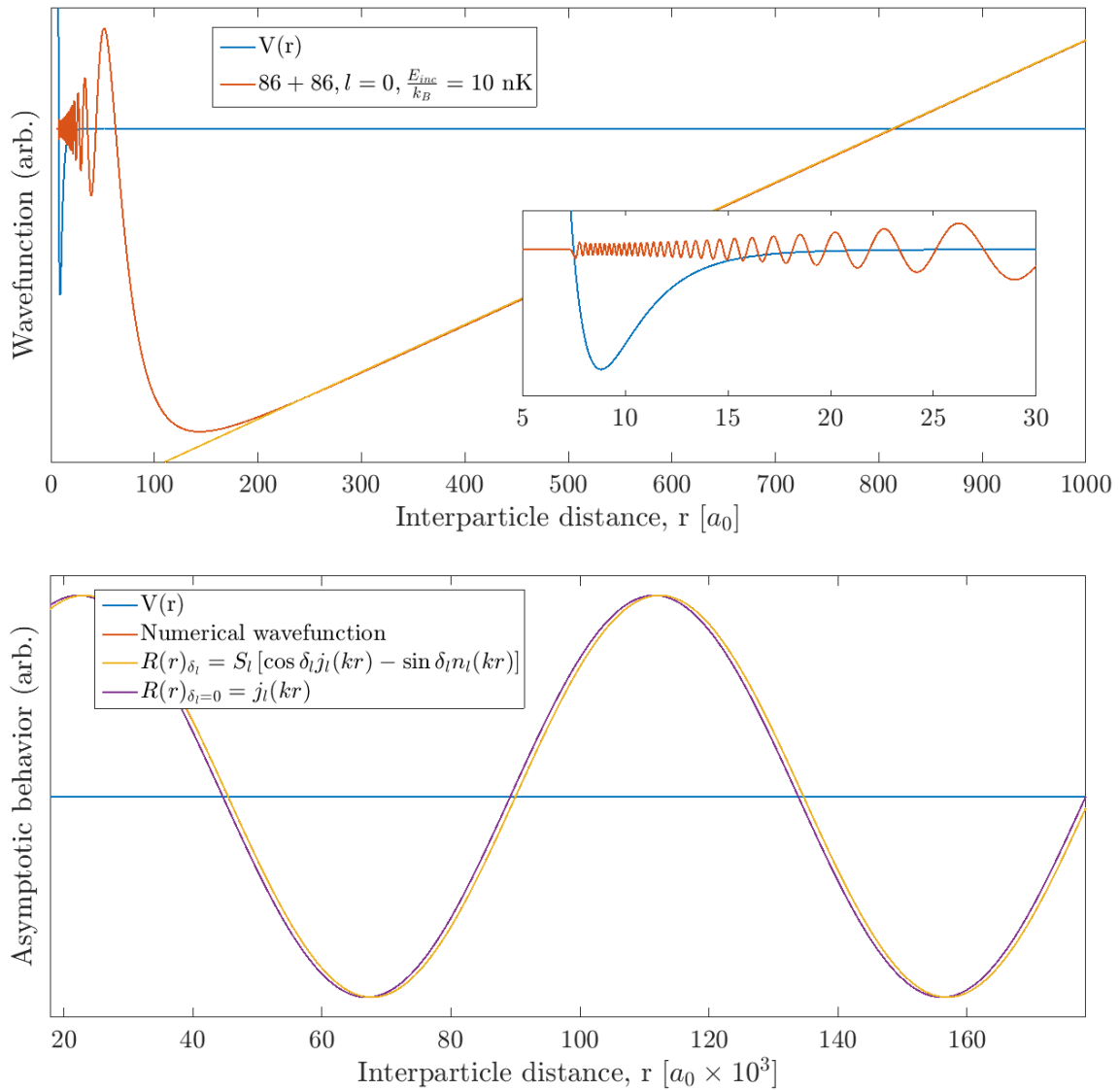
We need the desnity distribution.

In a harmonic trap, there if a simp[le anayltic form to the density distribution of a thermal gas.

From Mi's work (and others) we know that this is only an approximation that is valid when eta is approx greater than 4.

When greater than 4 we can apply the high-eta approx and the trap frequencies along a particular direction reduce to  $\omega_{eq}$ .

However, the trap we did this experiment in were at eta's of 1 or less so we don't have an analytic solution to the spatial distribution.

Figure 5.11 :  $^{86}\text{Sr}$  collision wavefunction

Estimate scattering length via position of the last node.

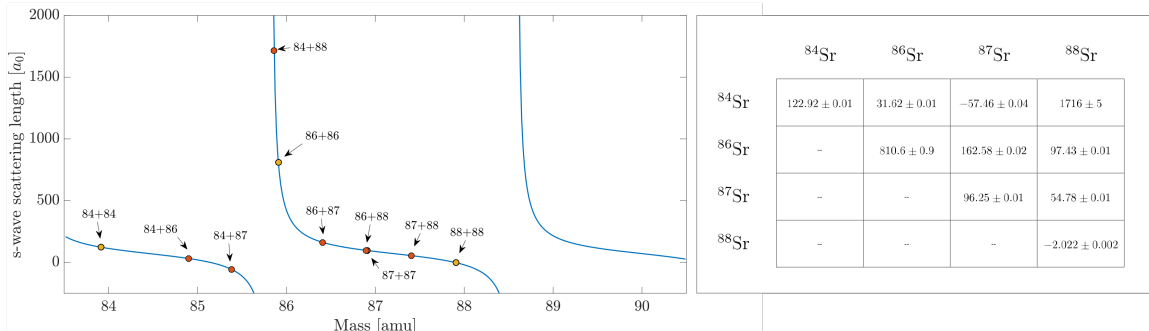


Figure 5.12 : Estimation of scattering lengths via mass scaling

Using estimates of  $C_6$  can mass scale

Since this could be a problem we need to know what the trap looks like.

We measure trap oscillation freq. at several different powers and model the trap using the utility outlined somewhere else.

From the numeric model, we can define a spatially dependent eta which is determined by the local trap depth which is simply the difference between the local potential energy and the global depth. This is illustrated in fig something.

The spatial information is not only important for the density determination, but also for the range of available thermal energies.

Consider two atoms near the local bottom of the trap. By definition, in equilibrium, a single atom may only have up to the trap depths worth of energy since any additional energy would result in its expulsion from the trap.

In this case, in a relative momentum frame, the allowed collision energies range from zero to two times the trap depth.

Similarly, as we move towards the edge of the trap the range of accessible collision energies shrinks.

This additional weighting factor may be viewed as having a local truncated Boltz-

mann ditribution at every point in space.

Normally the BZ dist goes to infinity but here we have a cutoff at 2 trap depth. The most naive approx would be to simply consider the BZ and harshly truncate at 2 trap depth. We tried this

We know this is unphysical since we should expect that the probability of observing a certain momenta at a certain point in space, should smoothly tend zero towards as we approach the edge of the trap.

To see what this looks like we (and determine how important the effect is) we rederive the relative momentum distribution.

{Some stuff about center of mass and relative;}

What were all the cases and conclusions of having done this? Remember to consider what the different cases are.

If the total relative energy can be X then how does that get split up? Use the plots to show this limiting behavior.

Like if particle 1 has all the energy then there is only one possible value for particle 2 (and vice versa).

DERIVATION for truncated trap below

Need to lookup references for this molecular chaos assumption. What about ergodicity? How to discuss that we may not be completely ergodic?

What does my potential look like? Can I make it a piecewise function? How should I introduce this part?

Where does the f equation come from? I believe this is just the normalized boltzmann factor for probability to occupy a particlar state.

We can truncate this single particle distribution by

$$f_{\mathbf{r}}(\mathbf{p}) = A \left( \frac{1}{2\pi k_B T} \right)^{3/2} e^{\left( \frac{-p^2}{2m k_B T} \right)} \Theta \left( \epsilon_{max} - U(\mathbf{r}) - \frac{p^2}{2m} \right) \quad (5.12)$$

where A is a normalization constant which ensures  $\int_0^\infty f_{\mathbf{r}}(\mathbf{p}) d\mathbf{p} = 1$  and  $\Theta(x)$  is the Heaviside function defined by

$$\Theta(x) = \begin{cases} 1 & \text{if } x \geq 0, \\ 0 & \text{if } x < 0 \end{cases} \quad (5.13)$$

We got a certain answer with the way shown in the paper.

We can also use a completely different method that ignores all the considerations of the last few sections. As was done in the calcium paper, we could simply fit the blue edge of the feature using a model function which can capture the high level features of the lineshape. Get the same answer. SHOW PLOTS TO THIS AFFECT AND COMPARE

Maybe go a little into the isolated resonance model (or at least recall), then tie into how we can measure the susceptibility across several different detunings which can give us the coupling to intermediate level. The first order analysis of this data suggest a bound-bound rabi frequency of **BLAH**.

Point out the curling up at the end and say how the simple isolated resonance model cannot predict.

A full coupled channel calculation probably could but in the spirit of the Bohm and Julianne semi-classical approach, we set out to derive an approximate analytic expression to determine the binding energies.

This is presented in the next chapter.

Lastly, we note that in the context of photoassociation, the center-of-mass component of Eq.A.3 is not typically considered as typical PAS experiments are performed utilizing broad dipole allowed transitions which have linewidths much greater than the doppler width thus only the relative momentum between particles is important

for determining the loss rate coefficient K discussed in [somewhere].

The case of PA using narrow intercombination line transitions found in alkaline-earth-metal atoms

In general K is considered as a boltzmann average over a single loss rate constant  
This can be seen in [20] Eq. 1 where the loss rate constant is given by

$$\begin{aligned} K(\Delta, T) &= \langle \mathcal{K}(\Delta, \mathbf{P}_c, \mathbf{p}_r) \rangle \\ &= \int d^3 \mathbf{P}_c f_M(\mathbf{P}_c) \int d^3 \mathbf{p}_r f_\mu(\mathbf{p}_r) \mathcal{K}(\Delta, \mathbf{P}_c, \mathbf{p}_r) \end{aligned} \quad (5.14)$$

To this end we can integrate out the center of mass component to obtain the distribution most typically relevant to photoassociation.

By the time I've gotten to this I have already introduced K and that is not what I wanted to do.

conclusion here is the modified version of K we need for a trap that has a truncated energy distribution

to get there normal version of K is given in ch3 this K can be given in terms of f?  
this version of f is given in the appendix why do I integrate out the com component?

typical PAS experiments utilize dipole allowed transitions which have linewidths many times larger than the

We now perform a change of variables using Eq. and Eq.A.2 can be rewritten as

In the s-wave limit I need to write K as a function of f(p) (should do this in the appendix proof and reference in body). Given the form of the loss rate constant K, our problem reduces to determining the form of f(p) when eta is finite.

Ok, so need to reference [20] to motivate usage of center of mass. Then use [69]  
Eq. 43 to reference the particular form

what is the throughline I want to make? Develop  $K_{in} \rightarrow$  recast in terms of P distribution  $\rightarrow$  show how we can replace the normal dist with a truncated dist  $\rightarrow$  explore the effects of that truncation

## Chapter 6

### Progress towards studies of quantum magnetism

A straightforward extension of the work presented in this thesis would be to control interparticle spacing via an optical lattice. For these and additional experiments using quantum degenerate fermionic strontium we purchased and installed an optical lattice system. Our lattice is implemented using a Coherent Verdi V-18 which is shaped and propagated to our science chamber in free space. Fig shows the optical path for each arm of our cubic lattice.

Unfortunately, complications due to heating when loading the lattice has limited our success in this optical trap. I want to go over what we have been able to do so far with the lattice.

How did we characterize? Kaptiza-dirac extension

What convinced us we were having problems?

What are some ideas we could do in the lattice? Zeno faster cooling via stimulated raman potentially? (can I model this somehow?) repulsively bound molecules? use interaction control in lattice with the zeno thing

#### 6.1 Optical lattice trap: 532 nm

Until recently, experiments on the Neutral apparatus were confined to work with bulk gases in an optical dipole trap. While optical dipole traps are useful for efficient evaporation and thermalization of an ultracold gas, optical lattices greatly extend our

capabilities for studying ultracold molecules and novel many-body quantum states  
give some refs.

Optical lattices are formed by a standing wave of light which creates a defect free periodic potential. These traps are extremely versatile and have enabled the observation of the superfluid - Mott insulator transition [29], artificial gauge fields for neutral atoms [53], quantum microscopy with single-site resolution [? ], and investigations of quantum magnetism [? ? ]. They are among the most well-established techniques for controlling a quantum state and have proven to be great tools for exploring the connection between few- and many-body systems [? ].

#### 6.1.0.1 Background

An optical lattice is created by counterpropagating two laser beams to form a standing wave pattern, which for two plane waves in one dimension results in a periodic potential given by

$$V(x) = V_{lat} \sin^2(k_L x) \quad (6.1)$$

where  $V_{lat}$  is the lattice depth determined by the polarizability of the atom for a given trapping wavelength  $\lambda$  and laser intensity  $I$ , and  $k_L$  is the lattice wavevector. This potential can be readily extended to three dimensions using two additional pairs of counterpropagating laser beams along the  $y$  and  $z$  directions which results in a 3D cubic lattice. Depth of the trapping potential,  $V_{lat}$ , is controlled by varying the intensity of the lattice beams.

Periodic potentials are powerful because they break the translational invariance of space which results in the formation of band structure and the opening of bandgaps or disallowed particle energies [5]. Because of this broken invariance,  $p$  is no longer a good quantum number and must be replaced by two new quantum numbers: the band

index,  $n$ , and the quasimomentum,  $q$ . In one dimension, quasimomentum is specified by  $q = p - nG$ , where  $G = 2\pi/a$  is a reciprocal lattice vector, and  $a$  is the real space lattice constant. Fig. 6.1.0.1 shows how the band structure varies as the lattice depth is increased. Optical lattices have a lattice spacing  $a = \lambda/2$  which determines the reciprocal lattice vector  $G = 4\pi/\lambda = 2\hbar k_L$  and a natural energy scale  $E_r = \frac{\hbar^2 k_L^2}{2m}$  where  $m$  is the atomic mass and  $k_L$  is the lattice wavevector,  $k_L = 2\pi/\lambda$ . From the band structure, we see that the bandwidth of each band, given by  $\Delta E = E_{q=\hbar k_L} - E_{q=0}$ , decreases as the lattice depth is increased. In the limit that  $V_{lat} \rightarrow \infty$  the band structure reduces to a ladder of harmonic oscillator levels spaced by  $\hbar\omega_{ho} = \sqrt{4V_{lat}E_r}$ . Although, for moderately deep lattices,  $V_{lat} \gtrsim 5 E_r$ , this approximation is valid near the center of the Brillouin zone,  $q = 0$ , and provides a simple form to estimate the energy gaps between bands [39? ].

Solutions to the Schrödinger equation in a periodic potential are given by the Bloch functions [5]

$$\phi_q^{(n)}(x) = e^{iqx/\hbar} u_q^{(n)}(x) \quad (6.2)$$

These eigenstate wavefunctions are specified for a given quasimomentum  $q$ , and band index  $n$ . Their corresponding energy eigenvalues define the band structure of the lattice shown in Fig. 6.1.0.1. From Eq. 6.2 we see that the Bloch functions are the product of plane waves modulated by a function  $u_q^{(n)}(x)$ , which shares the periodicity of the underlying lattice potential [5]. For an optical lattice this modulating function can be expanded in a basis of plane waves through a Fourier decomposition of the lattice potential in Eq. ??, which gives [2],

$$u_q^{(n)}(x) = \sum_l c_l^{(n,q)} e^{i2lk_L x} \quad (6.3)$$

Here  $c_l^{(n,q)}$  are the coefficients for each plane wave in the basis expansion that are

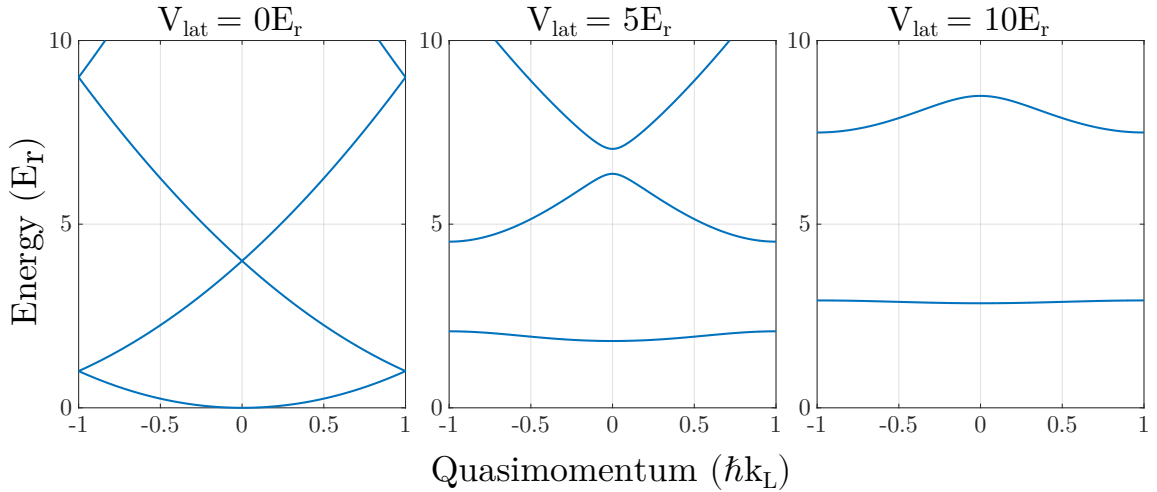


Figure 6.1 : 1D band structure as a function of lattice depth

One dimensional band structure for an optical lattice as the lattice depth is increased. The band energies are found by solving the Schrödinger equation using the Bloch functions of Eq. 6.2.

found by diagonalizing the lattice Hamiltonian [2].

Often, we are interested in the dynamics of particles on a particular lattice site, but since Bloch functions are delocalized over the entire lattice, it is useful to instead use the Wannier functions. These functions provide an orthogonal and normalized set of wavefunctions that are maximally localized to a specific lattice site. The Wannier function for a localized particle in the  $n^{th}$  band of a lattice site located at position  $x_i$  is given by [39]

$$w_n(x - x_i) = \mathcal{N}^{-1/2} \sum_q e^{iqx_i/\hbar} \phi_q^{(n)}(x) \quad (6.4)$$

where  $\mathcal{N}$  is a normalization constant and  $\phi_q^{(n)}(x)$  are the Bloch functions of Eq. 6.2.

This localized description of particles allows us to calculate important physical quantities which govern dynamical properties of the lattice such as the tunneling rate,

$J/\hbar$ , and on-site interaction energy,  $U$ . As  $V_{lat} \rightarrow \infty$ , the Wannier functions approach the eigenfunctions of the harmonic oscillator, which allows us to estimate the spatial extent of an atomic wavefunction by  $a_{ho} = \sqrt{\frac{\hbar}{m\omega_{ho}}}$  [39].

### 6.1.0.2 Setup and alignment

#### Setup

Our optical lattice operates at  $\lambda = 532$  nm and is derived from a Coherent Verdi V-18 single mode laser which is sent through separate AOMs for intensity control of each arm before propagating in free space to the atoms. We label these arms A, B, & C as noted in Fig. 6.2. Figs. 6.3 - 6.5 show the detailed beam profiles for the lattice and specify the spot size at the atoms for each pass of all three arms. The horizontal arms are linearly polarized with the polarization vector aligned along the  $z$  direction, parallel to gravity. The vertically propagating beam is also initially linearly polarized, however when propagating vertically, this polarization appears as a superposition of  $\sigma+$  and  $\sigma-$  vectors in the frame of the atoms. With this configuration we can achieve lattice depths  $\gtrsim 30E_r$  in an isotropic lattice.

#### Aligning the first pass:

The following is a technique conveyed to our lab from Trey Porto. We have successfully used this technique to reproducibly align the first pass of the optical lattice to maximize overlap with the 1064 nm optical dipole trap. This process relies on co-locating the trapping regions of the 532 nm and 1064 nm traps by observing the change in amplitude of center-of-mass oscillations due to misalignment of 532 nm. Additionally, we have observed breathing mode oscillations when the 532 nm and 1064 nm traps are well overlapped due to the change in trap depth, and correspondingly the

	Label	Part	Position [cm]	Distances [cm]	
Arm A	AOM	IntraAction AFM-804A1	-126.5	AOM → A1	24.1
	PBS	Thorlabs PBS12-532-HP	-117.8	A1 → A2	22.3
	Lens	CVI PLCX-25.4-772.6-UV-532	-106.5	A2 → A3	35
	Dichroic - 1	Thorlabs HBSY12	-30.6	A3 → A4	4.5
	Dichroic - 2	Thorlabs HBSY12	43.6	A4 → AD1	10
	Retro mirror	CVI Y2-1025-0-0.30CC	69.9	AD1 → Atoms	30.6
Arm B				Atoms → AD2	43.6
				AD2 → ARM	26.3
	AOM	IntraAction AFM-803A1	-167.1	AOM → B1	19
	PBS	Newport PBS-5811	-154.6	B1 → B2	25
	Lens	CVI PLCX-25.4-772.6-UV-532	103.1	B2 → B3	46
	Dichroic - 1	Thorlabs HBSY12	-36.1	B3 → B4	23.5
Arm C	Dichroic - 2	Thorlabs HBSY12	30.5	B4 → B5	14
	Retro mirror	CVI Y2-1025-0-0.30CC	73.5	B5 → BD1	3.5
				BD1 → Atoms	36.1
				Atoms → BD2	30.5
				BD2 → B6	25
				B6 → BRM	18
Arm C	AOM	IntraAction AFM-803A1	-117.5	AOM → C1	45.5
	PBS	Thorlabs PBS12-532-HP	-109.5	C1 → C2	25.5
	Lens-1	CVI PLCX-25.4-772.6-UV-532	-89.5	C2 → C3	15
	Retro lens	CVI PLCX-25.4-149.9-UV-532	14.6	C3 → C4	5.5
	Retro mirror	CVI Y2-1025-0	18.2	C4 → Atoms	26
				Atoms → CRM	18.2

Table 6.1 : Lattice optics details

All measurements are specified in centimeters. The optics position is given with respect to zero defined at the atom position. Distances are referenced to the optics labels given in Fig. 6.2.

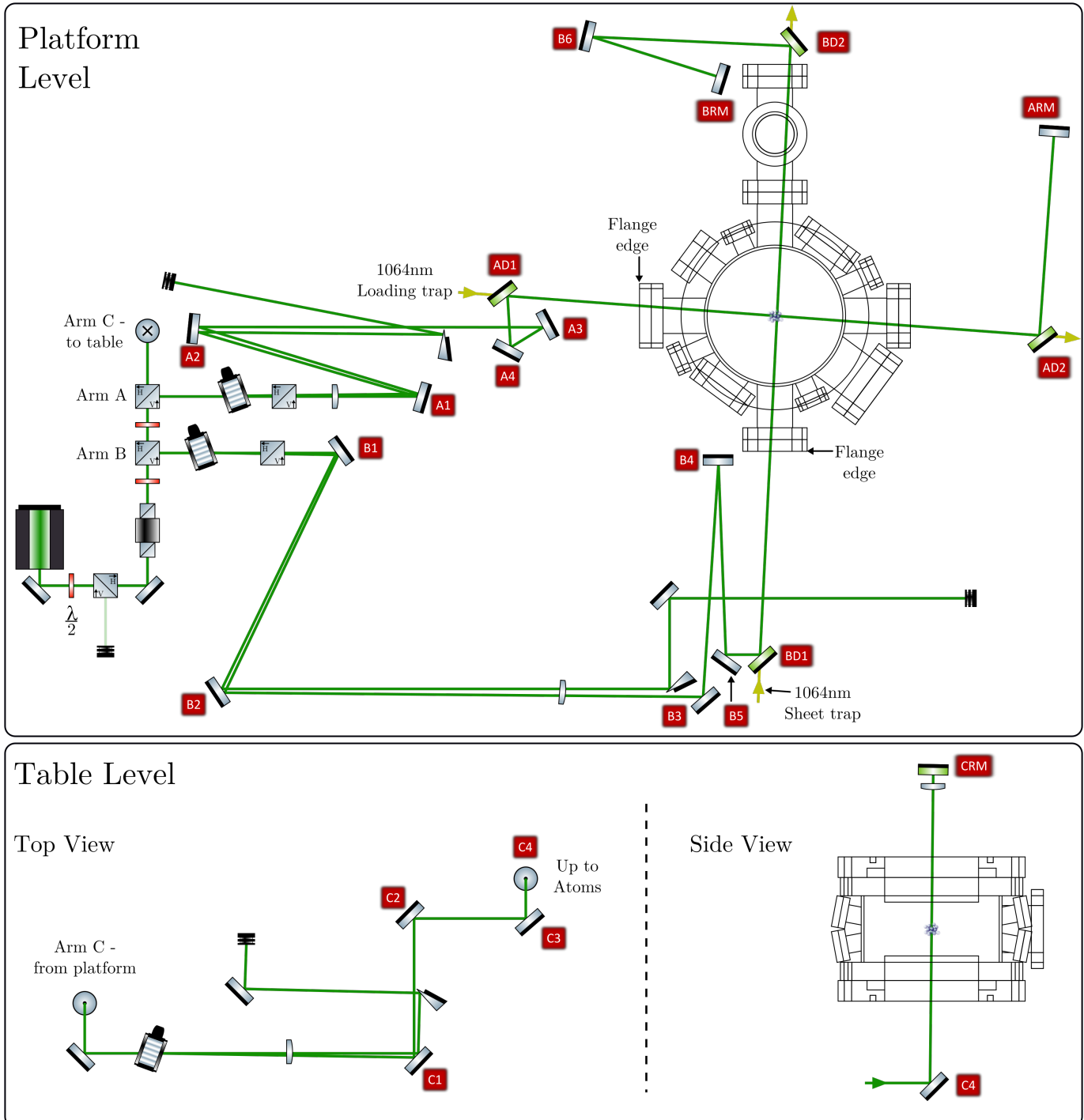


Figure 6.2 : Lattice optical schematic

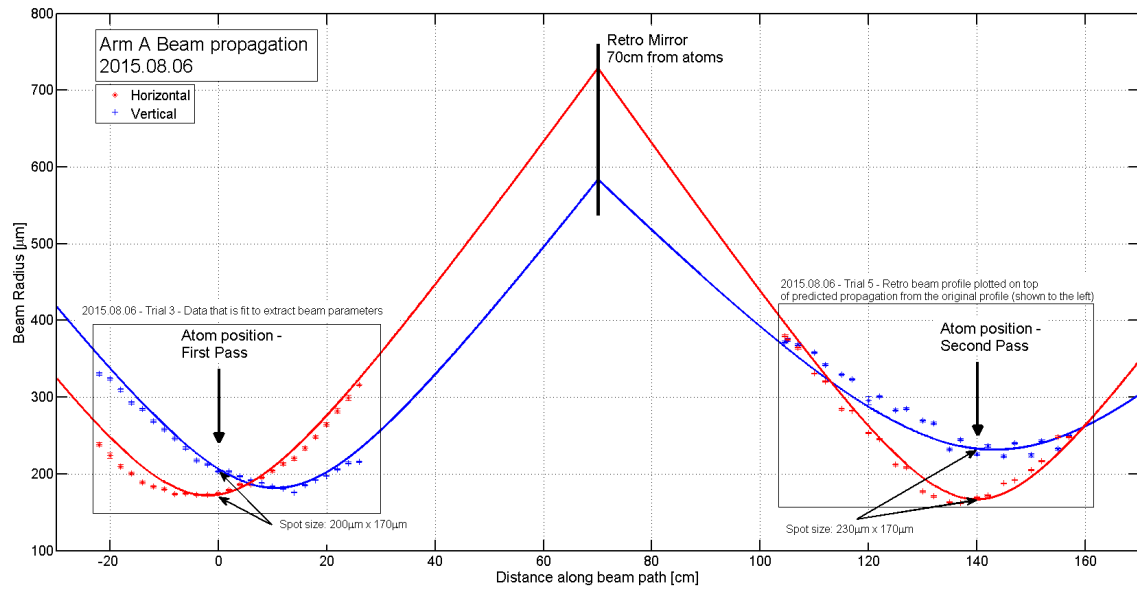


Figure 6.3 : Lattice Arm A profile

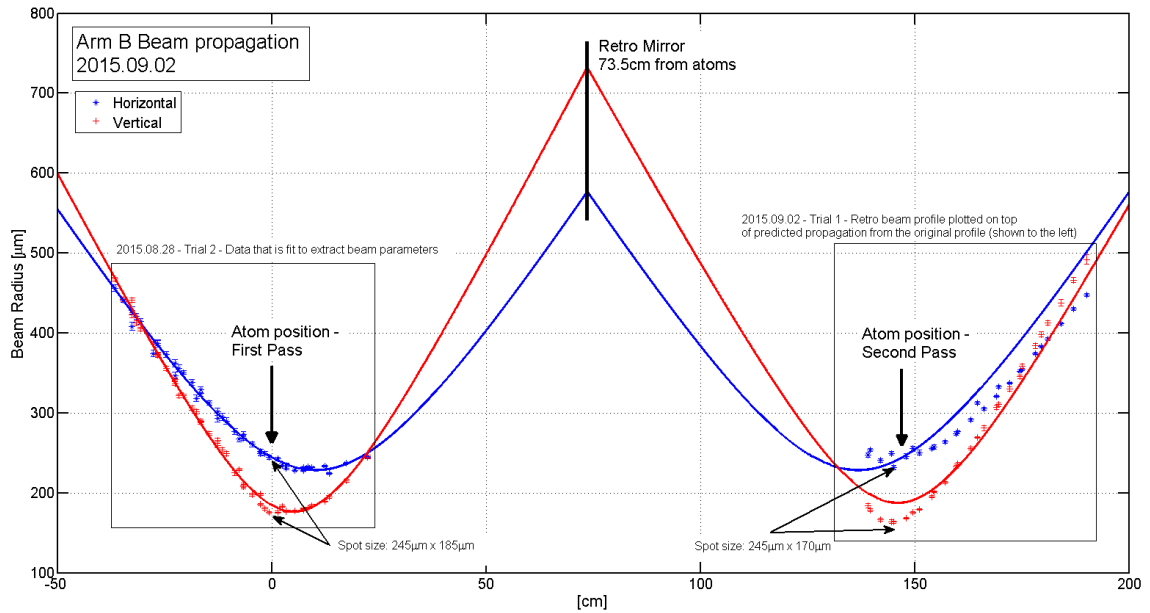


Figure 6.4 : Lattice Arm B profile

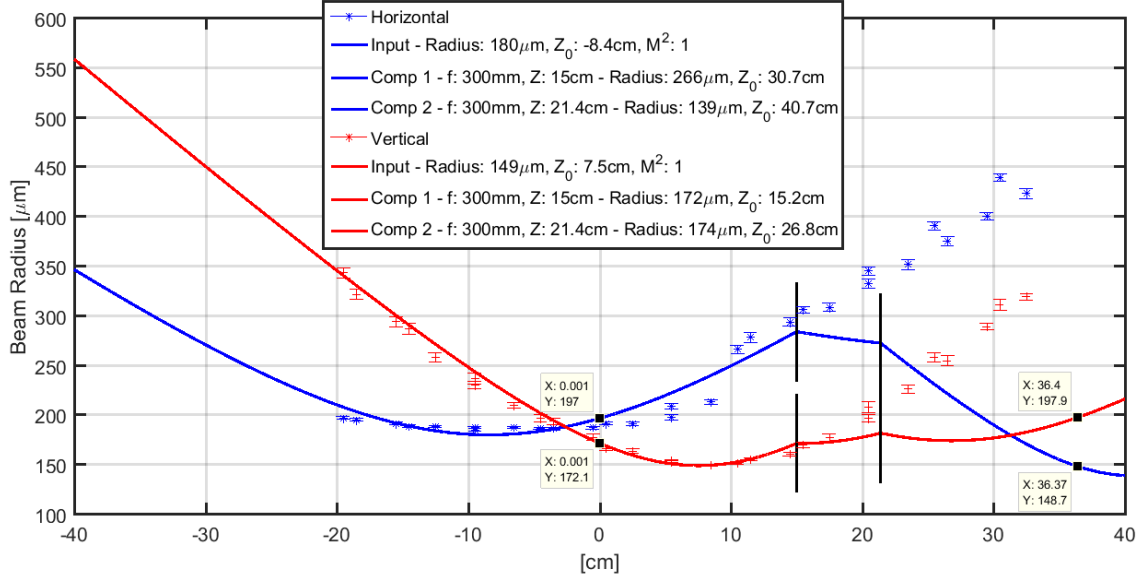


Figure 6.5 : Lattice Arm C profile

potential energy of the atoms, when flashing off the 532 nm light.

Below is our prescription for overlapping the first pass of the lattice with the IR trap.

I. This process requires the oscillations start from a consistent equilibrium. We achieve this through the following experimental sequence:

- Typical trapping sequence of blue MOT, repump, red MOT broadband, red MOT single frequency + ODT load
- After loading the ODT, evaporate to a reasonable depth for the given loading time. Note that we have observed thermal effects from the ODT which may lead to inconsistent spatial behavior. Therefore, the point where the beam overlap should be optimized is at or near the desired IR trap depth for the proposed experiments.

- C. Following the forced evaporation, hold in the 1064 nm trap while ramping up the lattice arm being studied to full power. We generally find a ramp of  $\sim$ 200 - 300 ms worked best for strontium 84.
  - D. Once the green is at full power, we additionally hold for  $\sim$ 250 ms in the combined 532 + Crossed IR ODT trap to allow for the equilibration of the atoms in the modified trapping potential.
  - E. After the 250 ms hold, the green is flashed off to excite an oscillation within the IR ODT.
  - F. Image the cloud as it oscillates
- II. To evaluate the procedure above, first focus on in-situ images of the cloud, where atoms are held in the combined 1064 + 532 nm trap\*.
- III. When turning off the lattice and allowing the cloud to oscillate, identify the 1/4th period time of the oscillation. This is the point of maximum displacement and provides the most sensitive probe for observing how changes to the alignment may vary the oscillation amplitude. As the alignment is improved the maximum displacement is minimized, this is the signature of improving the overlap. If unsure about the oscillation period, vary the evolution time after extinguishing the 532 nm and observe the dynamics of the cloud to resolve a full oscillation.
- IV. Each lattice arm (A,B,C) can then be varied along both dimensions (horizontal and vertical) while monitoring the oscillation amplitude. Lower amplitude

---

\*Start by moving the VI cursor positions to be on the cloud center and drawing a box around the cloud location. This will help to identify small movements of the cloud as well as recording your start position.

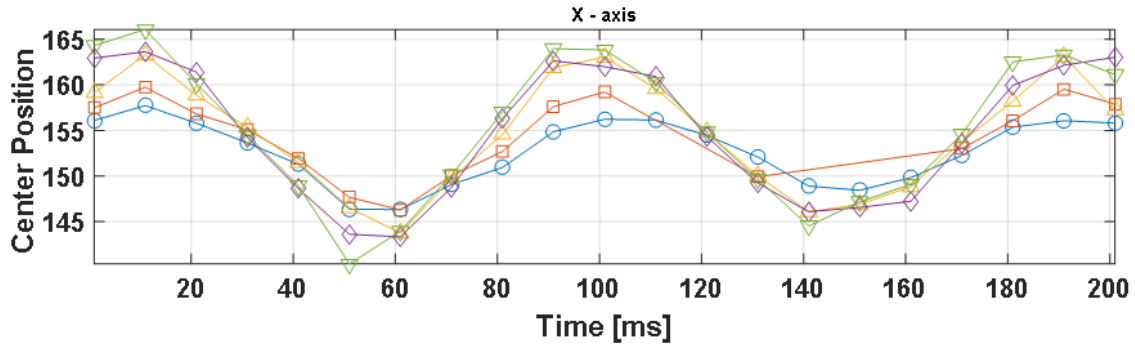


Figure 6.6 : Center-of-mass amplitude suppression when overlapping traps

Each subsequent scan is a small variation in the pointing of the last mirror directing the 532 nm light before the chamber. Note that the Y-axis is in arbitrary units.

indicates better alignment, but one must be extremely careful, as it is possible to obtain a flat response of the oscillation amplitude when severely misaligned. We have found that around the minimum in the oscillation amplitude, we are able to flip the phase of the 1/4 period oscillation as we move through the minimum. This phase flip along with the emergence of breathing mode oscillation are robust measures of good overlap between the beams.

Fig. 6.6 shows an example of the above process where for each scan we have varied the beam alignment slightly and can clearly observe a suppression of the oscillation amplitude. However, extended time series data in this fashion is arduous and we have found similarly effective alignment to result from the single-point measurement as outlined above.

Additionally, Fig. 6.7 shows the emergence of a breathing mode when the traps are well overlapped. Observation of oscillatory behavior of the cloud radius with reduced deviation of the cloud center is a robust measure of the overlap of the 532 and 1064

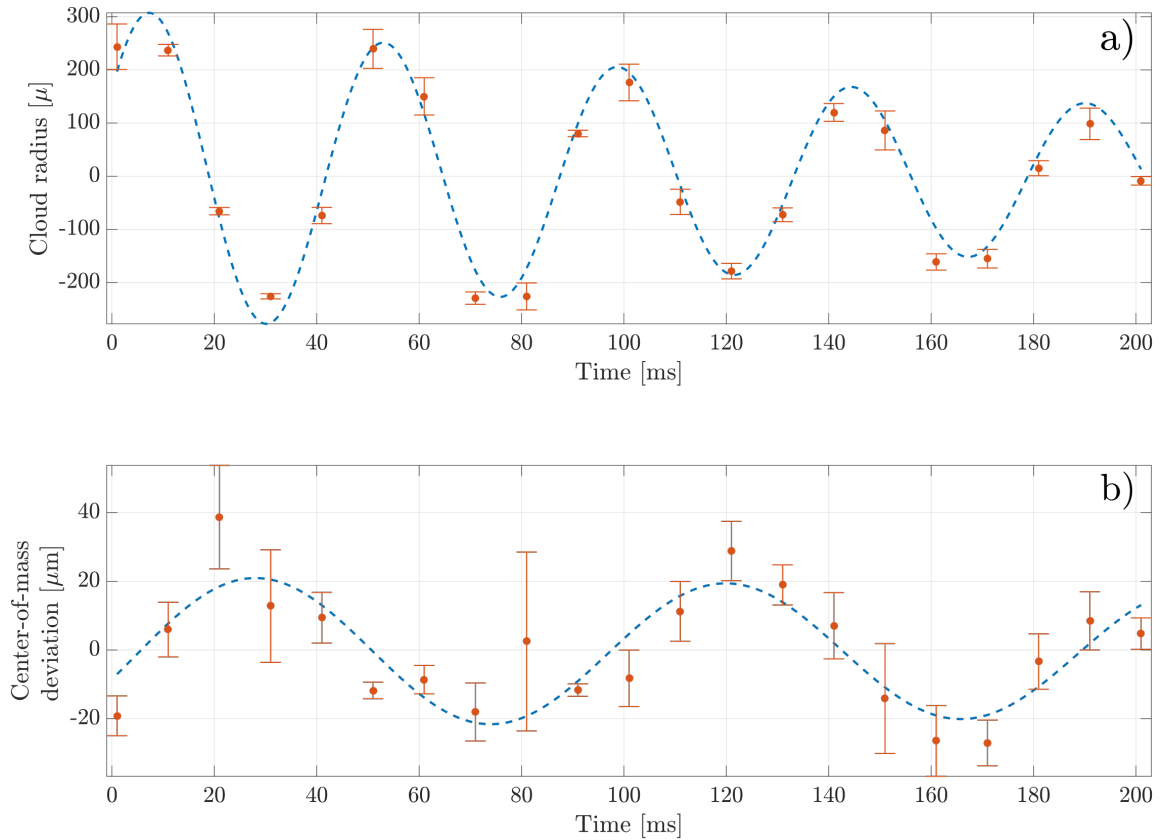


Figure 6.7 : Observation of breathing mode oscillation

a) The measured radius and b) the cloud center deviation along the horizontal axis.

traps.

### Aligning the retro-reflection:

The retro-reflection is optimized via the 2-band Kapitza-Dirac method. For a quantum degenerate gas in shallow lattice depths,  $\sqrt{10} E_r$ , only the  $\pm 1$  plane waves will be populated. Furthermore, for short pulses the amplitude of the population in these plane waves is linearly increasing with lattice depth. This provides a simple single point measurement which can be used for optimizing the lattice depth. However, an

iterative approach may be needed to ensure that the alignment is only optimized during the first quarter period before the population of the orders is maximized. Fig. 6.8 shows an example oscillation.

As our lattice is free space, the first order alignment of the retro-reflection is to overlap the incoming and retro-reflected beam over a long distance. This tends to overlap the two beams closely enough in the region of the atoms so as to begin observing diffraction effects when performing a short high intensity pulse of the 532 nm light.

Second, once we can observe diffraction, the gimbal mounted retro mirrors are adjusted to maximize the population of the diffracted plane waves<sup>†</sup>. As the diffracted population is oscillatory and depends on laser intensity we have found that using an exposure time of approximately 2 - 3  $\mu$ s and varying the laser intensity has led to the most successful alignments of the retro. We generally start with this short time pulse of a few microseconds using the highest intensity pulse possible and systematically decrease the laser power into the lattice arm as the alignment is improved. Finally we note that, as Kapitza-Dirac happens on very short timescales, the power stabilization circuits must be bypassed for this procedure. Instead, we directly drive the RF sources with fast analog IC switches (switching time on the order of 10's ns) to apply the desired power to the lattice arm.

---

<sup>†</sup>This alignment is extremely sensitive and may ultimately benefit from a more reproducible method of adjustment as mount backlash can strongly effect this process.

### 6.1.0.3 Measurement and results

#### Kaptiza-Dirac Scattering

Kapitza-Dirac diffraction can be viewed as a diabatic projection from an initial eigenstate to a new set of eigenstates which results in an oscillation of the wavefunctions probability amplitudes over the new eigenstates of the system [33]. As was discussed in Sec. 6.1.0.1, the free space eigenstates are not the eigenstates of the lattice Hamiltonian. Thus a pure  $p = 0$  plane wave,  $|\phi_{p=0}\rangle$ , suddenly loaded into an optical lattice can be written as a superposition of the Bloch states given by Eq. 6.2, here denoted by  $|n, q\rangle$ .

$$|\Psi(t=0)\rangle = \sum_{n=0}^{\infty} |n, q\rangle \langle n, q| \phi_{p=0} \rangle \quad (6.5)$$

The time evolution of this state is then given by

$$|\Psi(t)\rangle = \sum_{n=0}^{\infty} |n, q\rangle \langle n, q| \phi_{p=0} \rangle \exp\left(\frac{-iE_n(q)t}{\hbar}\right) \quad (6.6)$$

where  $E_n(q)$  is the energy of the Bloch state at a specified  $q$  and  $n$  shown in Fig. 6.1.0.1. The exponential factor of Eq. 6.6 introduces oscillations among Bloch states and after a second diabatic projection back to the plane wave basis, we can relate evolution of plane wave population to the bandgap energy. From this analysis we find that for relatively weak lattices,  $V_{lat} \lesssim 10E_r$ , the plane wave population will vary as  $\omega_{osc} = (E_2 - E_0)/\hbar$ . Where  $E_i$  is the band energy of the  $i^{th}$  band with  $q = 0$  as is the case when performing Kapitza-Dirac with a Bose-Einstein condensate.

Fig. 6.8 shows a typical Kapitza-Dirac oscillation pattern which we use to maximize beam overlap near the atoms and calibrate our achievable lattice depths. Kapitza-Dirac is useful as an alignment tool since measurement of the population oscillation frequency can be highly accurate and directly relates to the bandgap energy in the lattice, shown in Fig. 6.1.0.1.

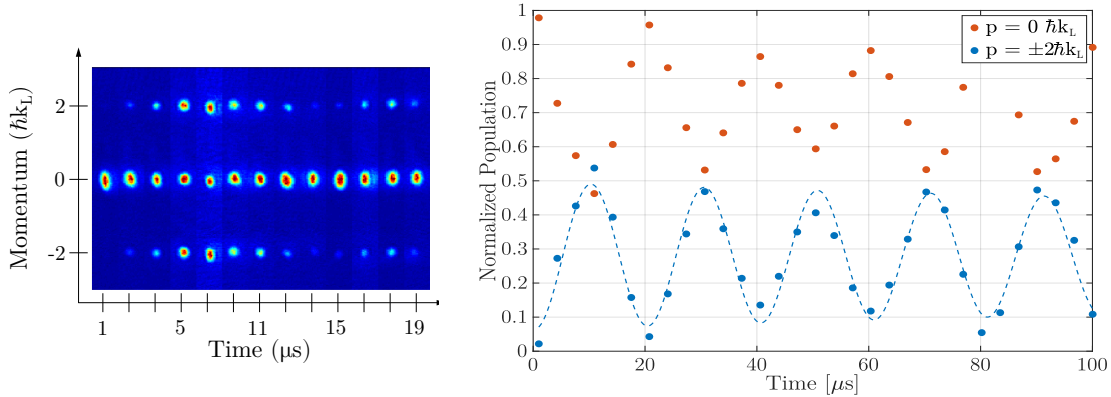


Figure 6.8 : Evolution of plane wave population using Kapitza-Dirac

Left: Time of flight slices for several realizations of Kapitza-Dirac with varying hold time in the lattice. Right: Normalized population from fits of time-of-flight images. Oscillations are fit with a decaying sinusoidal and the best-fit frequency is used to determine the lattice depth.

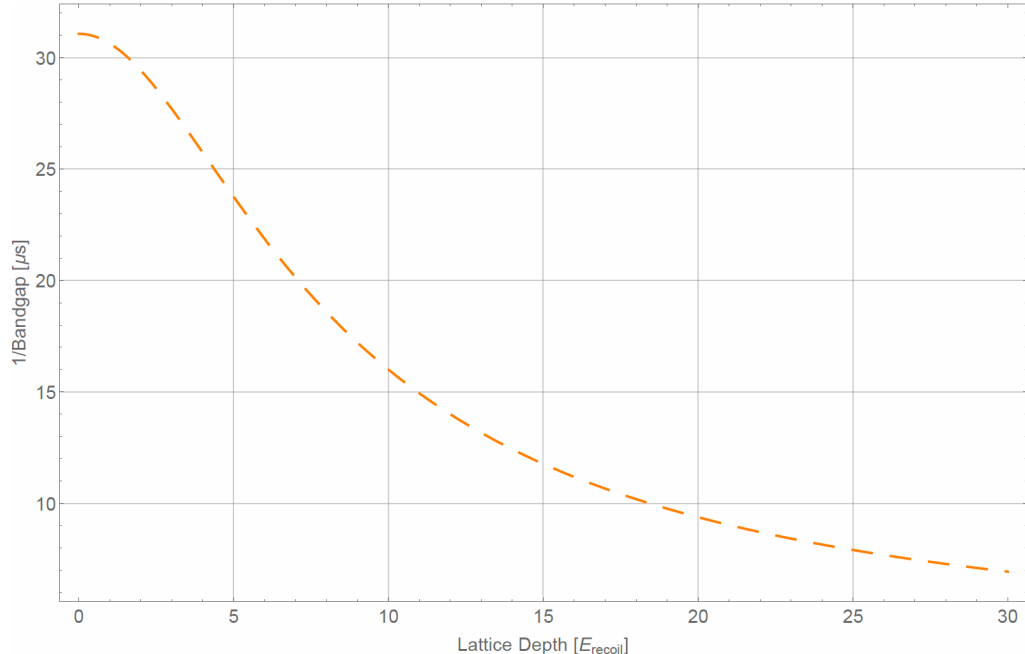


Figure 6.9 : Oscillation period between  $n = 0 \rightarrow n = 2$  band at  $q = 0$

Calculated for a 532 nm lattice acting on strontium-84.

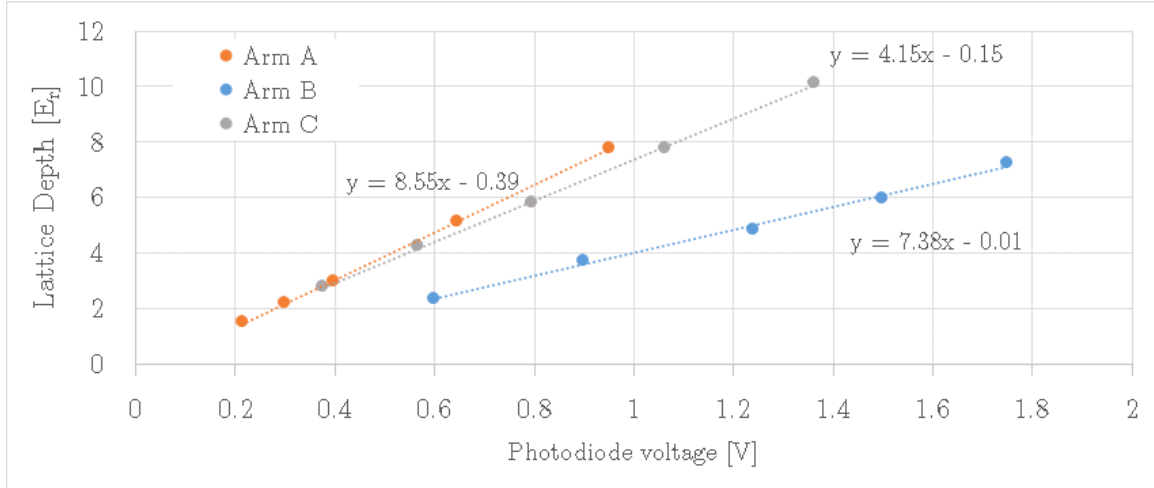


Figure 6.10 : Lattice depth calibration

Calibration was performed using the two-band Kapitza-Dirac technique. Maximum photodiode voltage for each arm is 10 V

For reference, Fig. 6.10 shows the resulting lattice depth calibration for our most recent alignment.

**Higher order Kapitza-Dirac:** The simple two-band model is a straightforward method for determining the lattice depth but one that requires a time-series measurement over varying lattice depths. Gadway et. al. [26] derived a complementary depth calibration method which requires only a single time-series measurement at high lattice depth. This process relies on the quantum interference of the oscillating populations which produces a complex beat note. An undergraduate report from Alex Wikner [87], follows the original Gadway construction to develop an algorithm using Matlab<sup>TM</sup> for applying this technique to the Neutral apparatus. The cited report provides sample code as well as benchmark calculations for comparison. However, application of this work to calibrate the lattice depth has been stymied by

a consistent heating concern we have observed when applying the lattice beams for significant periods at high lattice depths.

### Heating of a quantum degenerate gas

While Kapitza-Dirac diffraction is useful as a characterization tool, we typically wish to maintain equilibrium when loading condensates into the lattice. Thus slowly ramping up the lattice laser intensity will adiabatically transform a plane wave ground state into the ground Bloch state of the lattice [74]. Strictly speaking, in order to adiabatically connect the free space eigenstates and the lattice eigensates, the lattice must be turned on infinitely slowly due to the infinitesimal bandgaps which open near the band edges. Although near the band center,  $q = 0$ , the adiabaticity requirement relaxes to  $dV_{lat}/dt \ll 16E_r^2/\hbar$ , [33] which for strontium in a 532 nm lattice is  $\approx 5\ \mu\text{s}/E_r$ . However, in practice we find that our condensate fraction is reduced during fast ramps into the lattice. Instead, we slowly ramp on the lattice over 100 ms which reduces heating caused by the ramp. We have experimented with various functional forms of this pulse shape and currently rely on an S-shaped curve given by Eq. 6.7

$$V_{sCurve}(A, B, C, t) = \frac{A - C}{2} [\tanh(2\pi B[t - 1]) + 1] + C \quad (6.7)$$

where A is the overall amplitude starting from zero, B is the timescale for one period, and C is a constant offset term.

As shown in Fig. 6.11, we observe a large condensate fraction after ramping the lattice up and back down in this manner to demonstrate restoration of BEC coherence. Further characterization of the lattice required us to measure the reduction of atom population over long times due off-resonant light scatter. For our red detuned optical lattice we expect the off-resonant scattering rate to be well approximated by a simple

two level approach. In this model, the effective scattering rate is given by [39]

$$\Gamma_{eff} \approx \frac{\Gamma V_{lat}}{\hbar \delta_{lat}} \quad (6.8)$$

where  $\Gamma$  is linewidth of the dipole transition between the two states,  $V_{lat}$  is the lattice depth, and  $\delta_{lat}$  is the detuning of the optical lattice from the two level transition frequency. In strontium, the  $^1S_0 \rightarrow ^1P_1$  transition strongly dominates the polarizability of the ground state and therefore can be used to estimate the effective off-resonant scattering rate. For this transition  $\Gamma = 2\pi \times 30.5$  MHz and a 532 nm lattice is detuned by  $\delta_{lat} \approx 2\pi \times 87$  THz. With a lattice depth of  $V_{lat} = 10 E_r$ , we expect a scattering rate of  $\Gamma_{eff} \approx 2 \times 10^{-1} s^{-1}$ , which is negligible for the timescales of our proposed experiments. From Fig. 6.11, we see that there is not an appreciable loss of atoms over a one second timescale. Unfortunately, we have recently observed that attempts to load a degenerate gas into a deep lattice,  $\gtrsim 15 E_r$ , and hold over long timescales leads to unacceptable heating of the atomic sample. Currently, we hypothesize that this may result from the freespace nature of the lattice or an intrinsic instability (frequency or power) of the Verdi. The latter of these has been tested by monitoring the 532 nm light in a spectrum analyzer where no obvious deficiencies have been observed. To test our stability hypothesis, we are currently investigating fiber coupling one of the arms of the lattice but as of spring 2019, this project is ongoing.

## 6.2 Spin manipulation of $^{87}\text{Sr}$

Here is where I need to introduce and characterize the LCR

Averaging images together (how to use this code specifically)

don't forget to talk about optimizing the polarization of the fixed waveplate

Fig. something shows the variation of the retardance angle for 689 nm light.

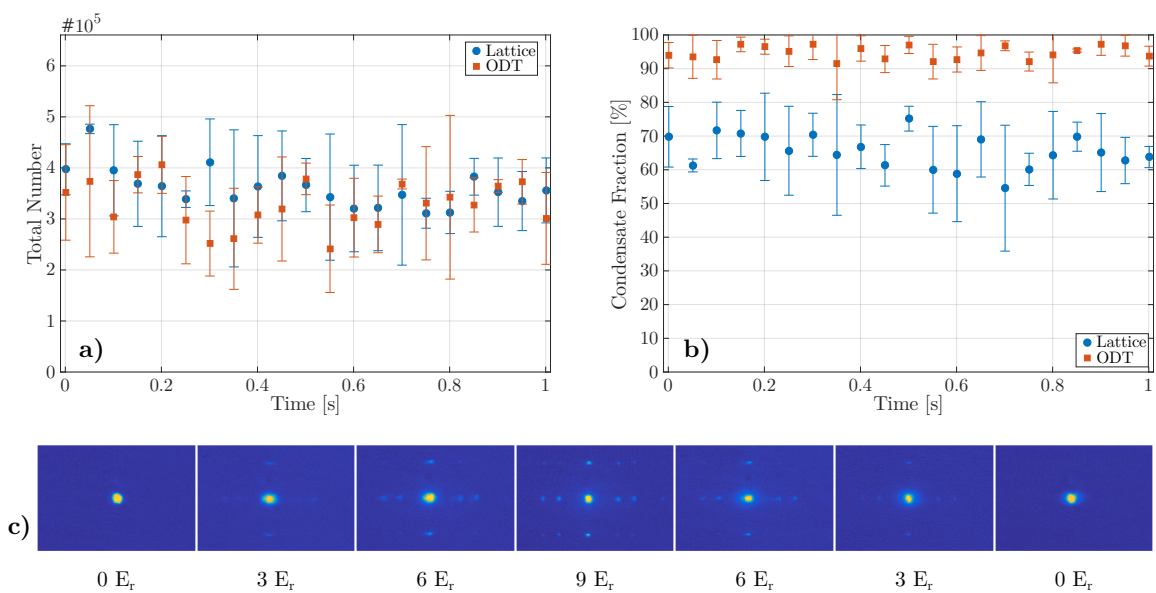


Figure 6.11 : Characterization of heating in the optical lattice

Evolution of condensate fraction over time after adiabatically ramping on the lattice to  $9 E_r$ . a,b) Comparison of total number and condensate fraction for a sample held in the optical dipole trap (red squares) or in a deep lattice (blue circles). c) Time of flight images after ramping on the lattice and diabatically projecting back to plane wave states.

For reference, Fig. 6.12 reproduces the Clebsch-Gordan coefficient diagrams originally created by Pascal. From this diagram we can easily see how optical pumping works. Let us consider an atom starting in the  $m_F = -9/2$  ground state and being exposed to *sigma+* photons acting on the  $F = 9/2 \rightarrow F = 11/2$  hyperfine transition. Absorbing a photon promotes the atom to the  $F = 11/2, m_F = -7/2$  state. From here we can consult Fig. 6.12 to find the dominate decay path to be to the  $F = 9/2, m_F = -5/2$  state due to the Clebsch-Gordan coefficients.

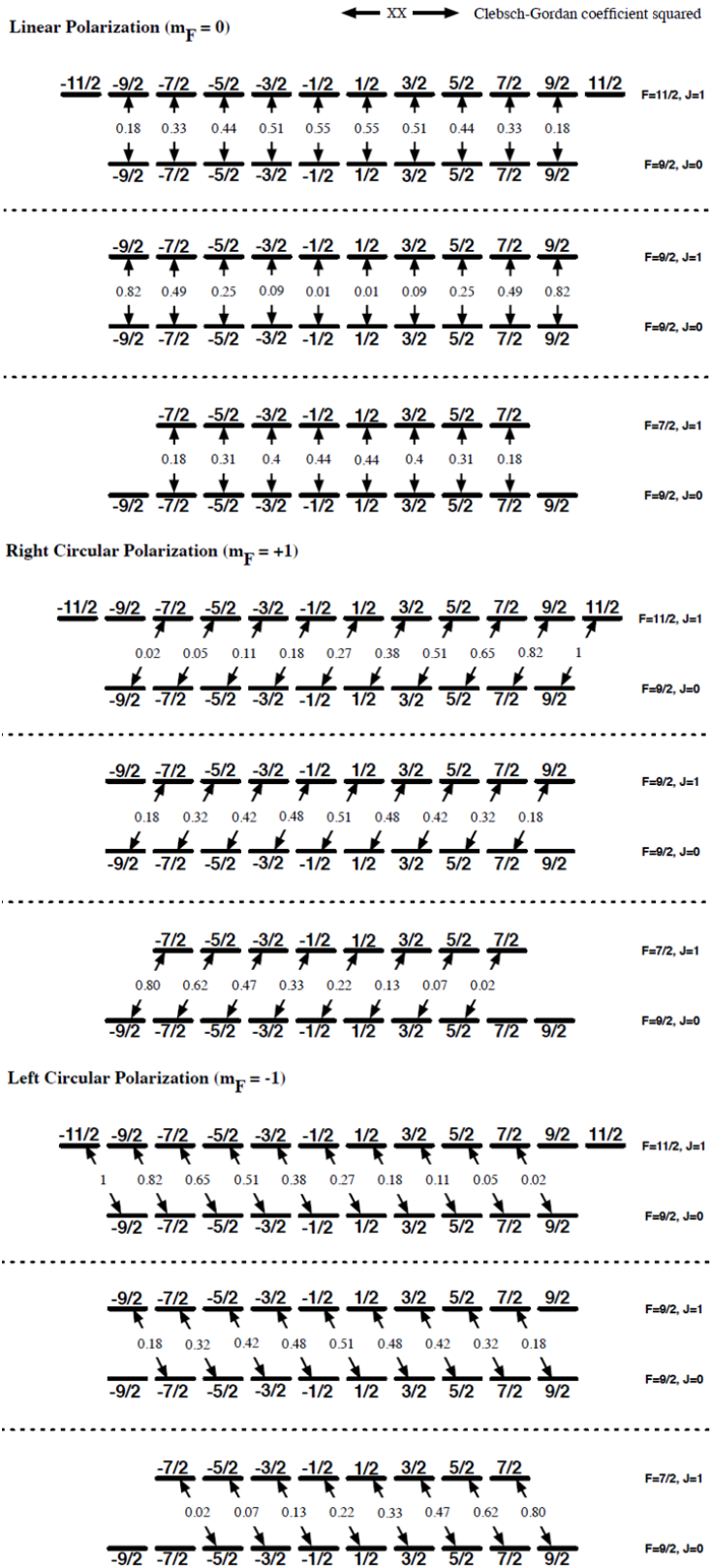
Now we have a couple of options, by taking advantage of the CG coefficients we see that we will probabilistically promote population towards a polarized state. In the absence of a bias field the magnetic sub-levels are degenerate so this could be an efficient process. In practice we find this to heat the atom population significantly. Therefore, in a bias field, we split out the levels by approx. 200 kHz to and address each sub-level transition individually. This allows us to minimize the number of photon scattering events which we hypothesize to be the cause of the observed heating.

can individually address the separate hyperfine sub-level transitions and sequentially pump population towards one a polarized state

Be sure to define convention for what we determined was plus and minus

### 6.3 Search for narrowline PA molecules using various spin mixtures

”Lorem ipsum dolor sit amet, consectetur adipiscing elit, sed do eiusmod tempor incididunt ut labore et dolore magna aliqua. Ut enim ad minim veniam, quis nostrud exercitation ullamco laboris nisi ut aliquip ex ea commodo consequat. Duis aute irure dolor in reprehenderit in voluptate velit esse cillum dolore eu fugiat nulla pariatur.

Figure 6.12 :  $^{87}\text{Sr} \ ^1S_0 \rightarrow ^3P_1$  hyperfine structure

Excep**teur** sint occaecat cupiditat non proident, sunt in culpa qui officia deserunt  
mollit anim id est laborum."

## Chapter 7

### Conclusion

We have measured the binding energy of the least-bound vibrational level of the ground electronic state of the  $^{86}\text{Sr}_2$  molecule with two-photon photoassociative spectroscopy. Using the universal prediction for the binding energy of a halo state including corrections derived for a van der Waals potential [Eq. (5.11)] [27, 28, 31], we extract an improved value of the *s*-wave scattering length.

We also characterized the AC Stark shift of the halo-state binding energy due to light near resonant with the single-photon photoassociation transition. A model only accounting for a single excited-state channel [? ] cannot explain the observed frequency dependence of the AC Stark shift, which can be attributed to the proximity of other excited states.

Large AC Stark shifts of the halo state point to the possibility of optically tuning the  $^{86}\text{Sr}$  scattering length, similar to recent demonstrations of optical tuning of magnetic Feshbach resonances [4, 21]. This is attractive because ground-state strontium lacks magnetic Feshbach resonances. With improved measurement of the photoassociation resonance frequency and its dependence on background atom density, perhaps combined with optical manipulation of the scattering length, it may also be possible to study the landscape of Efimov trimers associated with this naturally occurring scattering resonance. This work also points to the need for improved theory, such as an improved calculation of the Sr ground-state molecular potential and  $C_6$  coefficient, which could be compared with this high-accuracy measurement of the halo binding

energy.

The work presented in this proposal is a natural extension of previous work done in our lab using an optical Feshbach resonance and one color photoassociation to manipulate the quantum state of a Bose-Einstein condensate. The creation and characterization of a novel type of Feshbach molecule is of fundamental interest to complete the analogy between optical and magnetic Feshbach resonances as well as to test the mechanism of Feshbach molecule stability in the presence of closed channel decay. This experiment provides a practical first demonstration of an optical lattice on our apparatus, which can be readily extended to a number of experiments such as out of equilibrium unitarity quenches [56], strongly interacting Bose gases stabilized by the quantum zeno effect [81, 88, 95? ], and the observation of exotic spin phases [6, 16? ]. Moreover, additional insight might also be drawn from revisiting OFR and photoassociation in an optical lattice and employing new measurement techniques in the lattice [82]. These and future experiments will take advantage of the variety of interactions and narrow intercombination transitions available in strontium as well as the control and selectivity afforded through an optical lattice.

## Bibliography

- [1] Aman, J. A., J. C. Hill, R. Ding, W. Y. Kon, K. R. Hazzard, and T. C. Killian, 2018, Physical Review A **98**(5), 053441, ISSN 24699934, URL <https://link.aps.org/doi/10.1103/PhysRevA.98.053441>.
- [2] Anker, T., 2005, *Ultracold quantum gases in one-dimensional optical lattice potentials*, Ph.D. thesis, Ludwig-Maximilians-Universität München, URL [https://edoc.ub.uni-muenchen.de/968/1/Greiner\\_{ }Markus.pdf](https://edoc.ub.uni-muenchen.de/968/1/Greiner_{ }Markus.pdf).
- [3] Bartenstein, M., A. Altmeyer, S. Riedl, R. Geursen, S. Jochim, C. Chin, J. H. Denschlag, R. Grimm, A. Simoni, E. Tiesinga, C. J. Williams, and P. S. Julienne, 2005, Physical Review Letters **94**(10), 103201, ISSN 00319007.
- [4] Bauer, D. M., M. Lettner, C. Vo, G. Rempe, and S. Durr, 2009, Nature Physics **5**, 339.
- [5] Bergman, D. J., and D. Stroud, 1992, *Solid state Physics* (Saunders College), ISBN 047141526X.
- [6] Beverland, M. E., G. Alagic, M. J. Martin, A. P. Koller, A. M. Rey, and A. V. Gorshkov, 2016, Physical Review A **93**(5), 051601, ISSN 24699934, URL <http://link.aps.org/doi/10.1103/PhysRevA.93.051601>.
- [7] Blatt, S., T. L. Nicholson, B. J. Bloom, J. R. Williams, J. W. Thomsen, P. S. Juli-

- enne, and J. Ye, 2011, Physical Review Letters **107**(7), 073202, ISSN 00319007, URL <http://link.aps.org/doi/10.1103/PhysRevLett.107.073202>.
- [8] Boffard, J. B., M. L. Keeler, G. A. Piech, L. W. Anderson, and C. C. Lin, 2001, Physical Review A **64**(3), 032708, ISSN 1050-2947, URL <https://link.aps.org/doi/10.1103/PhysRevA.64.032708>.
- [9] Bohn, J. L., and P. S. Julienne, 1996, Physical Review A - Atomic, Molecular, and Optical Physics **54**(6), R4637, ISSN 10941622, URL <http://link.aps.org/doi/10.1103/PhysRevA.54.R4637>.
- [10] Bohn, J. L., and P. S. Julienne, 1999, Physical Review A - Atomic, Molecular, and Optical Physics **60**(1), 414, ISSN 10941622, URL <https://link.aps.org/doi/10.1103/PhysRevA.60.414>.
- [11] Borkowski, M., R. Ciuryło, P. S. Julienne, S. Tojo, K. Enomoto, and Y. Takahashi, 2009, Physical Review A - Atomic, Molecular, and Optical Physics **80**(1), 1, ISSN 10502947, URL <http://arxiv.org/abs/0905.0958>.
- [12] Braaten, E., and H. W. Hammer, 2006, Physics Reports **428**, 259, ISSN 03701573.
- [13] Braaten, E., and H.-W. Hammer, 2007, Annals of Physics **322**(1), 120, ISSN 00034916, URL <http://linkinghub.elsevier.com/retrieve/pii/S0003491606002387>.
- [14] Bradley, C. C., C. A. Sackett, J. J. Tollett, and R. G. Hulet, 1995, Physical Review Letters **75**(9), 1687, ISSN 00319007, URL <http://link.aps.org/doi/10.1103/PhysRevLett.75.1687>.

- [15] Camargo, F., 2015, *Strontium Laser Cooling and Trapping Apparatus*, Masters, Rice University, URL <http://ultracold.rice.edu/publications/2015CamargoMasters.pdf>.
- [16] Chen, G., K. R. A. Hazzard, A. M. Rey, and M. Hermele, 2015, Physical Review A **93**(6), ISSN 24699934, URL <http://arxiv.org/abs/1501.04086>{%}0A<http://dx.doi.org/10.1103/PhysRevA.93.061601>.
- [17] Chin, C., R. Grimm, P. Julienne, and E. Tiesinga, 2010, Reviews of Modern Physics **82**(2), 1225, ISSN 00346861, URL <https://link.aps.org/doi/10.1103/RevModPhys.82.1225>.
- [18] Chin, C., and P. S. Julienne, 2005, Physical Review A - Atomic, Molecular, and Optical Physics **71**(1), 12713, ISSN 10502947.
- [19] Ciurylo, R., E. Tiesinga, and P. S. Julienne, 2006, Physical Review A **74**, 22710.
- [20] Ciuryło, R., E. Tiesinga, S. Kotchigova, and P. S. Julienne, 2004, Physical Review A - Atomic, Molecular, and Optical Physics **70**(6), 062710, ISSN 10941622, URL <http://link.aps.org/doi/10.1103/PhysRevA.70.062710>.
- [21] Clark, L. W., L. C. Ha, C. Y. Xu, and C. Chin, 2015, Physical Review Letters **115**, 155301, ISSN 10797114.
- [22] Claussen, N. R., S. J. J. M. F. Kokkelmans, S. T. Thompson, E. A. Donley, E. Hodby, and C. E. Wieman, 2003, Physical Review A **67**(6), 60701, ISSN 1050-2947, URL <https://link.aps.org/doi/10.1103/PhysRevA.67.060701>.
- [23] Cooper, A., J. P. Covey, I. S. Madjarov, S. G. Porsev, M. S. Safronova, and M. Endres, 2018, [1810.06537](https://arxiv.org/abs/1810.06537), URL <https://arxiv.org/abs/1810.06537>.

- [24] Demarco, B., 1998, *Quantum Behavior of an Atomic Fermi Gas*, Ph.D. thesis, University of Colorado.
- [25] DeSalvo, B. J., M. Yan, P. G. Mickelson, Y. N. Martinez de Escobar, and T. C. Killian, 2010, Physical Review Letters **105**(3), 030402, ISSN 0031-9007, URL <https://link.aps.org/doi/10.1103/PhysRevLett.105.030402>.
- [26] Gadway, B., D. Pertot, R. Reimann, M. G. Cohen, and D. Schneble, 2009, Optics Express **17**(21), 19173, ISSN 1094-4087, URL <http://arxiv.org/abs/0907.3507>{%}0A<http://dx.doi.org/10.1364/OE.17.019173>.
- [27] Gao, B., 2001, Physical Review A - Atomic, Molecular, and Optical Physics **64**, 10701, ISSN 10941622.
- [28] Gao, B., 2004, Journal of Physics B: Atomic, Molecular and Optical Physics **37**(21), 4273, ISSN 0953-4075, URL <http://stacks.iop.org/0953-4075/37/i=21/a=004?key=crossref.2818e17c48ea9c152598f4de6d7b11ce>.
- [29] Greiner, M., O. Mandel, T. Rom, A. Altmeyer, A. Widera, T. W. Hänsch, and I. Bloch, 2003, Physica B: Condensed Matter **329-333**(6867), 11, ISSN 09214526, URL <http://www.nature.com/doifinder/10.1038/415039a>.
- [30] Greiner, M., C. A. Regal, and D. S. Jin, 2003, Nature **426**, 537.
- [31] Gribakin, G. F., and V. V. Flambaum, 1993, Physical Review A **48**(1), 546, ISSN 1050-2947, URL <https://link.aps.org/doi/10.1103/PhysRevA.48.546>.
- [32] Grimm, R., M. Weidemüller, and Y. B. Ovchinnikov, 1999, Optical dipole traps for neutral atoms, **9902072**, URL <https://arxiv.org/abs/physics/9902072>.

- [33] Hecker Denschlag, J., J. E. Simsarian, H. Häffner, C. McKenzie, A. Browaeys, D. Cho, K. Helmerson, S. L. Rolston, and W. D. Phillips, 2002, Journal of Physics B: Atomic, Molecular and Optical Physics **35**(14), 3095, ISSN 09534075, URL <http://stacks.iop.org/0953-4075/35/i=14/a=307?key=crossref.143851fb4f795110e47d745ef41278c>.
- [34] Hill, J. C., 2017, *Design and Construction of an Apparatus for Optically Pumping <sup>87</sup>Sr*, Masters, Rice University, URL [http://ultracold.rice.edu/publications/Hill{\\_}MS.pdf](http://ultracold.rice.edu/publications/Hill{_}MS.pdf).
- [35] Huang, B., R. Grimm, S. Stellmer, F. Schreck, and M. K. Tey, 2009, Physical Review Letters **103**(20), 200401, ISSN 0031-9007, URL <http://link.aps.org/doi/10.1103/PhysRevLett.103.200401>.
- [36] Huang, Y., 2013, *A New Optical Trap System for Ultracold Strontium*, Masters, Rice University, URL [http://ultracold.rice.edu/publications/Ying{\\_}Huang{\\_}master.pdf](http://ultracold.rice.edu/publications/Ying{_}Huang{_}master.pdf).
- [37] Hutson, J. M., 2007, New Journal of Physics **9**(5), 152, ISSN 1367-2630, URL <http://stacks.iop.org/1367-2630/9/i=5/a=152?key=crossref.21a092de740716c0280b5f41edc5d848>.
- [38] Ido, T., Y. Isoya, and H. Katori, 2000, Physical Review A - Atomic, Molecular, and Optical Physics **61**(6), 4, ISSN 10941622, URL <http://link.aps.org/doi/10.1103/PhysRevA.61.061403>.
- [39] Jaksch, D., and P. Zoller, 2005, Annals of Physics **315**(1), 52, ISSN 00034916, URL <http://linkinghub.elsevier.com/retrieve/pii/S0003491604001782>.

- [40] Jensen, A. S., K. Riisager, D. V. Fedorov, and E. Garrido, 2004, Reviews of Modern Physics **76**(1), 215, ISSN 00346861, URL <https://journals.aps.org/rmp/pdf/10.1103/RevModPhys.76.215>.
- [41] Jochim, S., M. Bartenstein, A. Altmeyer, G. Hendl, S. Riedl, C. Chin, J. Hecker-Denschlag, and R. Grimm, 2003, Science **302**, 2101.
- [42] Jones, K. M., E. Tiesinga, P. D. Lett, and P. S. Julienne, 2006, Reviews of Modern Physics **78**(2), 483, ISSN 00346861, URL <http://link.aps.org/doi/10.1103/RevModPhys.78.483><http://journals.aps.org/rmp/abstract/10.1103/RevModPhys.78.483>.
- [43] Julienne, P. S., 2009, in *Cold molecules : theory, experiment, applications*, edited by R. V. Krems, B. Friedrich, and W. C. Stwalley (CRC Press, Boca Raton, Fla.), chapter Chapter 6, 1st edition, ISBN 9781420059038 1420059033, pp. 221–244, [0902.1727](http://arxiv.org/abs/0902.1727), URL <http://arxiv.org/abs/0902.1727>.
- [44] Julienne, P. S., 2009, Faraday Discussions **142**(0), 361, ISSN 13596640, URL <http://dx.doi.org/10.1039/B820917K>.
- [45] Julienne, P. S., 2009, Understanding cold atomic and molecular collisions, [0902.1727](http://arxiv.org/abs/0902.1727), URL <http://arxiv.org/abs/0902.1727>.
- [46] Julienne, P. S., and B. Gao, 2006, AIP Conference Proceedings **869**(1), 261, ISSN 0094243X, URL <https://aip.scitation.org/doi/abs/10.1063/1.2400656>.
- [47] Katori, H., T. Ido, Y. Isoya, and M. Kuwata-Gonokami, 1999, Physical Review Letters **82**(6), 1116, ISSN 10797114, URL <http://link.aps.org/doi/10.1103/PhysRevLett.82.1116>.

- [48] Ketterle, W., D. S. Durfee, and D. M. Stamper-Kurn, 1999, Proc. Int. School of Physics-Enrico Fermi , 679904034, URL <https://arxiv.org/abs/cond-mat/9904034>.
- [49] Köhler, T., T. Gasenzer, and K. Burnett, 2003, Physical Review A **67**(1), 13601, ISSN 1050-2947, URL <http://link.aps.org/doi/10.1103/PhysRevA.67.013601>.
- [50] Köhler, T., K. Góral, and P. S. Julienne, 2006, Reviews of Modern Physics **78**(4), 1311, ISSN 00346861, URL <http://link.aps.org/doi/10.1103/RevModPhys.78.1311><http://link.aps.org/abstract/RMP/v78/p1311>.
- [51] Kon, W. Y., J. A. Aman, J. C. Hill, T. C. Killian, and K. R. A. Hazzard, 2018, 1812.11682, URL <http://arxiv.org/abs/1812.11682><https://arxiv.org/abs/1812.11682>.
- [52] Lang, F., K. Winkler, C. Strauss, R. Grimm, and J. H. Denschlag, 2008, Physical Review Letters **101**(13), 133005, ISSN 00319007, URL <http://link.aps.org/doi/10.1103/PhysRevLett.101.133005>.
- [53] Lin, Y. J., K. Jiménez-García, and I. B. Spielman, 2011, Nature **471**(7336), 83, ISSN 00280836, URL <http://www.nature.com/doifinder/10.1038/nature09887>.
- [54] Loftus, T. H., T. Ido, M. M. Boyd, A. D. Ludlow, and J. Ye, 2004, Physical Review A - Atomic, Molecular, and Optical Physics **70**(6), 063413, ISSN 10502947, URL <http://link.aps.org/doi/10.1103/PhysRevA.70.063413>.
- [55] Luo, F., G. C. Mcbane, G. Kim, C. F. Giese, and W. R. Gentry, 1993, The Journal of Chemical Physics The Journal of Chemical Physics The Journal of

- Chemical Physics **981**(10), URL <http://dx.doi.org/10.1063/1.464079><http://aip.scitation.org/toc/jcp/98/4>.
- [56] Makotyn, P., C. E. Klauss, D. L. Goldberger, E. A. Cornell, and D. S. Jin, 2014, Nature Physics **10**(2), 116, ISSN 17452473, URL <http://www.nature.com/doifinder/10.1038/nphys2850>.
  - [57] Martinez de Escobar, Y., P. Mickelson, M. Yan, B. DeSalvo, S. Nagel, and T. C. Killian, 2009, Physical Review Letters **103**, 200402, ISSN 0031-9007, URL <http://link.aps.org/doi/10.1103/PhysRevLett.103.200402>.
  - [58] Martinez de Escobar, Y. N., 2010, *Bose-Einstein Condensation of  $^{84}\text{Sr}$* , Ph.D. thesis, Rice University, URL <https://hdl.handle.net/1911/62163>.
  - [59] Martinez de Escobar, Y. N., P. G. Mickelson, P. Pellegrini, S. B. Nagel, A. Traverso, M. Yan, R. Côté, and T. C. Killian, 2008, Physical Review A **78**(6), 062708, ISSN 1050-2947, URL <https://link.aps.org/doi/10.1103/PhysRevA.78.062708>.
  - [60] Mazurenko, A., 2010, *Molecular Beam Nozzle Optimization*, Undergraduate, MIT, URL <http://ultracold.rice.edu/publications/2010mazurenkooven.pdf>.
  - [61] Méndez-Visag, C., 2014, Revista Peruana de Medicina Experimental y Salud Pública **31**(4), 725, ISSN 17264642, URL <http://www.ncbi.nlm.nih.gov/pubmed/10481000>.
  - [62] Mestrom, P. M. A., J. Wang, C. H. Greene, and J. P. D'Incao, 2017, Physical Review A **95**, 32707, ISSN 24699934.

- [63] Michael Viray, 2014, *Zeeman Tunable Saturated Absorption Spectroscopy Cell for Locking Laser Frequency to the Strontium 1S0-1P1 Transition*, Undergraduate, Rice University, URL <http://ultracold.rice.edu/publications/MichaelVirayREUReport>.
- [64] Mickelson, P. G., 2010, *Trapping and Evaporation of Mixtures Sr*, Ph.D. thesis, Rice University, URL <https://hdl.handle.net/1911/62095>.
- [65] Mickelson, P. G., Y. N. Martinez de Escobar, M. Yan, B. J. DeSalvo, and T. C. Killian, 2010, Physical Review A **81**(5), 051601, ISSN 1050-2947, URL <https://link.aps.org/doi/10.1103/PhysRevA.81.051601>.
- [66] Moritz, H., T. Stoferle, K. Gunter, M. Kohl, and T. Esslinger, 2005, Physical Review Letters **94**, 210401.
- [67] Mukaiyama, T., H. Katori, T. Ido, Y. Li, and M. Kuwata-Gonokami, 2003, Physical Review Letters **90**(11), 113002, ISSN 0031-9007, URL <https://link.aps.org/doi/10.1103/PhysRevLett.90.113002>.
- [68] Naidon, P., and S. Endo, 2017, Reports on Progress in Physics **80**, 056001, ISSN 00344885.
- [69] Nicholson, T. L., S. Blatt, B. J. Bloom, J. R. Williams, J. W. Thomsen, J. Ye, and P. S. Julienne, 2015, Physical Review A - Atomic, Molecular, and Optical Physics **92**(2), 022709, ISSN 10941622, URL <http://journals.aps.org/prap/abstract/10.1103/PhysRevA.92.022709>.
- [70] Pachomov, E., 2017, *One and two-color photoassociation spectroscopy of ultracold  $^{40}Ca$* , Ph.D. thesis, Leibniz Universitat Hannover, URL <http://opac.tib.eu/DB=1.12/SET=1/TTL=1/SHW?FRST=1>.

- [71] Pachomow, E., V. P. Dahlke, E. Tiemann, F. Riehle, and U. Sterr, 2017, Physical Review A **95**(4), 043422, ISSN 24699934, URL <http://arxiv.org/abs/1702.00710><http://link.aps.org/doi/10.1103/PhysRevA.95.043422>.
- [72] Pethick, C. J., and H. Smith, 2008, *Bose-Einstein Condensation in Dilute Gases* (Cambridge University Press, Cambridge), ISBN 9780511802850, URL <http://ebooks.cambridge.org/ref/id/CB09780511802850>.
- [73] Regal, C. A., C. Ticknor, J. L. Bohn, and D. S. Jin, 2003, Nature **424**, 47.
- [74] Sakurai, J. J., 1994, *Modern Quantum Mechanics, Supplement I* (Pearson), ISBN 978, URL [http://www.amazon.com/gp/product/0805382917/ref=pd\\_lpo\\_sbs\\_dp\\_ss\\_1?pf\\_rd\\_p=1535523722&pf\\_rd\\_s=lpo-top-stripe-1&pf\\_rd\\_t=201&pf\\_rd\\_i=0201539292&pf\\_rd\\_m=ATVPDKIKX0DER&pf\\_rd\\_r=0F9ZVFXMSJ1718HT9VN2](http://www.amazon.com/gp/product/0805382917/ref=pd_lpo_sbs_dp_ss_1?pf_rd_p=1535523722&pf_rd_s=lpo-top-stripe-1&pf_rd_t=201&pf_rd_i=0201539292&pf_rd_m=ATVPDKIKX0DER&pf_rd_r=0F9ZVFXMSJ1718HT9VN2).
- [75] Schöllkopf, W., and J. P. Toennies, 1994, American Association fot the Advancement of Science **266**(5189), 1345, URL <http://science.sciencemag.org/content/sci/266/5189/1345.full.pdf>.
- [76] Segal, S. R., Q. Diot, E. A. Cornell, A. A. Zozulya, and D. Z. Anderson, 2009, 0905.1979, URL <http://arxiv.org/abs/0905.1979><http://dx.doi.org/10.1103/PhysRevA.81.053601>.
- [77] Stellmer, S., 2013, *Thesis: Degenerate quantum gases of strontium*, Ph.D. thesis, University of Innsbruck, URL <http://www.ultracold.at/theses/2013-stellmer.pdf>.

- [78] Stellmer, S., F. Schreck, and T. C. Killian, 2013, *Degenerate quantum gases of strontium*, Ph.D. thesis, University of Innsbruck, Singapore, 1307.0601, URL <http://arxiv.org/abs/1307.0601> [http://dx.doi.org/10.1142/9789814590174\\_0001](http://dx.doi.org/10.1142/9789814590174_0001) [https://doi.org/10.1142/9789814590174\\_0001](https://doi.org/10.1142/9789814590174_0001) <http://www.ultracold.at/theses/2013-stellmer.pdf>.
- [79] Stellmer, S., M. Tey, R. Grimm, and F. Schreck, 2010, Physical Review A **82**, 41602, ISSN 1050-2947, URL <http://link.aps.org/doi/10.1103/PhysRevA.82.041602>.
- [80] Stenholm, S., 1988, *Laser cooling and trapping*, volume 9 of *Graduate Texts in Contemporary Physics* (Springer New York, New York, NY), ISBN 978-0-387-98728-6, NIHMS150003, URL <http://link.springer.com/10.1007/978-1-4612-1470-0>.
- [81] Syassen, N., D. M. Bauer, M. Lettner, T. Volz, D. Dietze, J. J. García-Ripoll, J. I. Cirac, G. Rempe, and S. Dürr, 2008, Science **320**(5881), 1329, ISSN 00368075, URL <http://www.ncbi.nlm.nih.gov/pubmed/18535241>.
- [82] Taie, S., S. Watanabe, T. Ichinose, and Y. Takahashi, 2016, Physical Review Letters **116**(4), 043202, ISSN 10797114, URL <http://link.aps.org/doi/10.1103/PhysRevLett.116.043202>.
- [83] Takahashi, Y., Y. Kikuchi, A. A. Buchachenko, K. Takahashi, P. S. Julienne, H. Yamada, M. Borkowski, Y. Takasu, and R. Ciuryło, 2017, Physical Review A **96**(6), 63405, ISSN 2469-9926, URL <https://link.aps.org/doi/10.1103/PhysRevA.96.063405>.

- [84] Tey, M. K., S. Stellmer, R. Grimm, and F. Schreck, 2010, Physical Review A - Atomic, Molecular, and Optical Physics **82**(1), 011608, ISSN 10502947, URL <http://journals.aps.org/prl/abstract/10.1103/PhysRevA.82.011608>.
- [85] Theis, M., G. Thalhammer, K. Winkler, M. Hellwig, G. Ruff, R. Grimm, and J. H. Denschlag, 2004, Physical Review Letters **93**(12), 123001, ISSN 0031-9007, URL <http://link.aps.org/doi/10.1103/PhysRevLett.93.123001>.
- [86] Wang, J., J. P. D’Incao, B. D. Esry, and C. H. Greene, 2012, Phys. Rev. Lett. **108**, 263001.
- [87] Wikner, A., 2017, *A MATLAB Script for Calibrating an Optical Lattice using Kapitza-Dirac Diffraction*, Ph.D. thesis, Rice University, URL <http://ultracold.rice.edu/publications/2017aWiknerKaptizaDirac.pdf>.
- [88] Wong, L. S., B. W. N. Voon, S. C. Teo, and A. Balakrishnan, 2016, Ecology, Environment and Conservation **22**(3), 1107, ISSN 0971765X, URL <http://link.aps.org/doi/10.1103/PhysRevLett.102.040402>.
- [89] Wynar, R., R. S. Freeland, D. J. Han, C. Ryu, and D. J. Heinzen, 2000, Science **287**, 1016.
- [90] Yamazaki, R., S. Taie, S. Sugawa, and Y. Takahashi, 2010, Physical Review Letters **105**(5), 050405, ISSN 00319007, URL <https://link.aps.org/doi/10.1103/PhysRevLett.105.050405>.
- [91] Yan, M., 2013, *Thesis: Optical Feshbach Resonances and Coherent Photoassociation in a BEC*, Ph.D. thesis, Rice University, URL <https://hdl.handle.net/1911/77594>.

- [92] Yan, M., B. J. Desalvo, B. Ramachandhran, H. Pu, and T. C. Killian, 2013, Physical Review Letters **110**(12), 123201, ISSN 00319007, URL <http://link.aps.org/doi/10.1103/PhysRevLett.110.123201><https://arxiv.org/abs/0906.1837>.
- [93] Zhang, X., M. Bishof, S. L. Bromley, C. V. Kraus, M. S. Safronova, P. Zoller, A. M. Rey, and J. Ye, 2014, Science **345**(6203), 1467, ISSN 10959203, URL <http://www.sciencemag.org/cgi/doi/10.1126/science.1254978><http://arxiv.org/abs/1403.2964>.
- [94] Zhang, X. L., R. S. Fletcher, S. L. Rolston, P. N. Guzdar, and M. Swisdak, 2008, Physical Review Letters **100**(23), 235002.
- [95] Zhu, B., B. Gadway, M. Foss-Feig, J. Schachenmayer, M. L. Wall, K. R. Hazzard, B. Yan, S. A. Moses, J. P. Covey, D. S. Jin, J. Ye, M. Holland, *et al.*, 2014, Physical Review Letters **112**(7), 070404, ISSN 00319007, URL <http://link.aps.org/doi/10.1103/PhysRevLett.112.070404>.

## Appendices

## Appendix A

### Two-particle momentum probability distribution

#### A.1 Standard form

Derivation of two particle relative momentum probability distribution function. Starting with the single particle Maxwell-Boltzmann momentum probability distribution function

$$f^1(\mathbf{p}) = \left( \frac{1}{2\pi k_B T} \right)^{3/2} e^{\left( \frac{-p^2}{2mk_B T} \right)} \quad (\text{A.1})$$

Extension of this simple Boltzmann equation into the two-particle regime can be complicated if there is a dependence of each particle on the others. If however, we make the assumption that particle collisions are rapid, we can approximate the two particle momentum distribution as the product of two single particle functions. The two particle distribution for a homogeneous system is then

$$\begin{aligned} f^2(\mathbf{p}_1, \mathbf{p}_2) &= f^1(\mathbf{p}_1)f^1(\mathbf{p}_2) \\ &= \left( \frac{1}{2\pi m k_B T} \right)^3 \exp \left( \frac{-(p_1^2 + p_2^2)}{2m k_B T} \right) \end{aligned} \quad (\text{A.2})$$

Next, we'd like to consider a center-of-mass frame for the distribution. So we'll define

$$\begin{aligned} \mathbf{P}_c &= \mathbf{p}_1 + \mathbf{p}_2 & M &= m_1 + m_2 = 2m \\ \mathbf{p}_r &= \frac{\mathbf{p}_1 - \mathbf{p}_2}{2} & \mu &= \frac{m_1 m_2}{m_1 + m_2} = \frac{m}{2} \end{aligned}$$

From these equations we can use conservation of energy to determine the quadrature sum of the two momenta

$$\begin{aligned}\frac{p_1^2}{2m} + \frac{p_2^2}{2m} &= \frac{P_c^2}{2M} + \frac{p_r^2}{2\mu} \\ p_1^2 + p_2^2 &= \frac{P_c^2}{2} + 2p_r^2\end{aligned}$$

Thus the momentum probability distribution take the form

$$f^2(\mathbf{P}_c, \mathbf{p}_r) = \left( \frac{1}{2\pi M k_B T} \right)^{3/2} \left( \frac{1}{2\pi \mu k_B T} \right)^{3/2} \exp \left( \frac{-P_c^2}{2M k_B T} \right) \exp \left( \frac{-p_r^2}{2\mu k_B T} \right) \quad (\text{A.3})$$

## A.2 Truncated form

Here we'll look at the effects of truncation of the Maxwell-Boltzmann. Such a system is not in thermal equilibrium and is limited to its truncation value.

Two particle momentum distribution [for correcting notation, use C and R when denoting CoM and Rel]

$$\begin{aligned}f_{\mathbf{r},trunc}^2(\mathbf{p}_1, \mathbf{p}_2) &= A^2 \left( \frac{1}{2\pi m k_B T} \right)^3 \exp \left( \frac{-(p_1^2 + p_2^2)}{2m k_B T} \right) \\ &\times \Theta \left( \epsilon_{max} - U(\mathbf{r}) - \frac{p_1^2}{2m} \right) \Theta \left( \epsilon_{max} - U(\mathbf{r}) - \frac{p_2^2}{2m} \right)\end{aligned} \quad (\text{A.4})$$

We have introduced a normalization constant  $A$  here to ensure the that integration over the truncated probability distribution remains equal to one. The meaning of  $r$  is such that f should be evaluated at each point in space. Furthermore since the atoms are held in a trapping potential, each point in space has a local trap depth relative to the lip at the top of the trap as shown in Fig. 5.2

We want the distribution of relative momenta so integrate out the center of mass.

Going to drop the two and trunc for now

$$\begin{aligned}
\tilde{f}_r(\mathbf{p}_{rel}) &= \int d^3\mathbf{P}_c f_r(\mathbf{p}_1, \mathbf{p}_2) \\
&= \left( \frac{1}{2\pi Mk_B T} \right)^{3/2} \left( \frac{1}{2\pi\mu k_B T} \right)^{3/2} A^2 \int d^3\mathbf{P}_c e^{\left( \frac{-P_c^2}{2Mk_B T} \right)} e^{\left( \frac{-p_r^2}{2\mu k_B T} \right)} \\
&\times \Theta \left( \epsilon_{max} - U(\mathbf{r}) - \frac{P_c^2}{8m} - \frac{p^2}{2m} - \frac{\mathbf{P}_c \cdot \mathbf{p}}{2m} \right) \Theta \left( \epsilon_{max} - U(\mathbf{r}) - \frac{P_c^2}{8m} - \frac{p^2}{2m} + \frac{\mathbf{P}_c \cdot \mathbf{p}}{2m} \right)
\end{aligned} \tag{A.5}$$

Spherically symmetric collisions so can integrate by transforming into spherical coordinates with the radius aligned along the interatomic axis

$$\begin{aligned}
\tilde{f}_r(\mathbf{p}) &= \left( \frac{1}{2\pi Mk_B T} \right)^{3/2} \left( \frac{1}{2\pi\mu k_B T} \right)^{3/2} e^{\left( \frac{-p_r^2}{2\mu k_B T} \right)} A^2 \int_0^\pi \sin \theta d\theta \int_0^{2\pi} d\phi \int_0^\infty dP_c P_c^2 e^{\left( \frac{-P_c^2}{2Mk_B T} \right)} \\
&\times \Theta \left( \epsilon_{max} - U(\mathbf{r}) - \frac{P_c^2}{8m} - \frac{p^2}{2m} - \frac{P_c p \cos \theta}{2m} \right) \Theta \left( \epsilon_{max} - U(\mathbf{r}) - \frac{P_c^2}{8m} - \frac{p^2}{2m} + \frac{P_c p \cos \theta}{2m} \right)
\end{aligned} \tag{A.6}$$

Making a change of variables

$$X = \cos \theta$$

$$dX = -\sin \theta d\theta$$

Substitute and integrate over  $\phi$

$$\begin{aligned}
\tilde{f}_r(\mathbf{p}) &= \left( \frac{1}{2\pi Mk_B T} \right)^{3/2} \left( \frac{1}{2\pi\mu k_B T} \right)^{3/2} e^{\left( \frac{-p_r^2}{2\mu k_B T} \right)} 2\pi A^2 \int_{-1}^1 dX \int_0^\infty dP_c P_c^2 e^{\left( \frac{-P_c^2}{2Mk_B T} \right)} \\
&\times \Theta \left( \epsilon_{max} - U(\mathbf{r}) - \frac{P_c^2}{8m} - \frac{p^2}{2m} - \frac{P_c p X}{2m} \right) \Theta \left( \epsilon_{max} - U(\mathbf{r}) - \frac{P_c^2}{8m} - \frac{p^2}{2m} + \frac{P_c p X}{2m} \right)
\end{aligned} \tag{A.7}$$

Recognize that the Heaviside functions cancel each other out on either side of zero, so can eliminate one of them and multiply by 2

$$\begin{aligned}
\tilde{f}_r(\mathbf{p}) &= \left( \frac{1}{2\pi Mk_B T} \right)^{3/2} \left( \frac{1}{2\pi\mu k_B T} \right)^{3/2} e^{\left( \frac{-p_r^2}{2\mu k_B T} \right)} 4\pi A^2 \int_0^1 dX \int_0^\infty dP_c P_c^2 e^{\left( \frac{-P_c^2}{2Mk_B T} \right)} \\
&\times \Theta \left( \epsilon_{max} - U(\mathbf{r}) - \frac{P_c^2}{8m} - \frac{p^2}{2m} - \frac{P_c p X}{2m} \right)
\end{aligned} \tag{A.8}$$

Rewrite using the infinite relative momentum probability distribution  $f_{\mathbf{r},\infty}(\mathbf{p})$  from Eq. A.3

$$\begin{aligned}\tilde{f}_{\mathbf{r}}(\mathbf{p}) &= \left( \frac{1}{2\pi\mu k_B T} \right)^{3/2} e^{\left( \frac{-p_r^2}{2\mu k_B T} \right)} \mathcal{G}(T, \epsilon_{max}, p_{rel}) \\ &= f_{\mathbf{r},\infty}(\mathbf{p}) \mathcal{G}(T, \epsilon_{max}, p_{rel})\end{aligned}\quad (\text{A.9})$$

where  $\mathcal{G}(T, \epsilon_{max}, p_{rel})$  is given by

$$\begin{aligned}\mathcal{G}(T, \epsilon_{max}, p_{rel}) &= A^2 \left( \frac{4\pi}{2\pi M k_B T} \right)^{3/2} \int_0^1 dX \int_0^\infty dP_c P_c^2 e^{\left( \frac{-P_c^2}{2M k_B T} \right)} \\ &\times \Theta \left( \epsilon_{max} - U(\mathbf{r}) - \frac{P_c^2}{8m} - \frac{p^2}{2m} - \frac{P_c p X}{2m} \right)\end{aligned}\quad (\text{A.10})$$

Now define two dimensionless variables  $\tilde{\epsilon}$  and  $\tilde{E}$  which will be used to change variables once more

$$\begin{aligned}\tilde{\epsilon} &= \frac{p_{rel}^2}{2\mu k_B T} & \tilde{E} &= \frac{P_c^2}{2M k_B T} \\ p &= \sqrt{2\mu k_B T \tilde{\epsilon}} & P_c &= \sqrt{2M k_B T \tilde{E}} \\ dpp^2 &= \frac{\sqrt{\tilde{\epsilon}}}{2} (2\mu k_B T)^{3/2} d\tilde{\epsilon} & dP_c P_c^2 &= \frac{\sqrt{\tilde{E}}}{2} (2M k_B T)^{3/2} d\tilde{E}\end{aligned}$$

Plugging these expressions into Eq.A.10 and rearranging

$$\begin{aligned}\tilde{f}_{\mathbf{r}}(\mathbf{p}) &= A^2 \frac{e^{-\tilde{\epsilon}}}{(2\pi\mu k_B T)^{3/2}} \int_0^1 dX \frac{2}{\sqrt{\pi}} \int_0^\infty d\tilde{E} e^{-\tilde{E}} \sqrt{\tilde{E}} \\ &\times \Theta \left( \eta(\mathbf{r}) - \frac{\tilde{E}}{2} - \frac{\tilde{\epsilon}}{2} - X \sqrt{\tilde{E}} \tilde{\epsilon} \right)\end{aligned}\quad (\text{A.11})$$

would like to turn this distribution into a relative energy distribution. Collisions are isotropic so we can use the relation

$$\begin{aligned}\int dpp^2 \int d\Omega_p \tilde{f}_{\mathbf{r}}(\mathbf{p}) &= \int d\tilde{\epsilon} \hat{f}_{\mathbf{r}}(\tilde{\epsilon}) = 1 \\ \Rightarrow 4\pi p^2 \tilde{f}_{\mathbf{r}}(\mathbf{p}) dp &= \hat{f}_{\mathbf{r}}(\tilde{\epsilon}) d\tilde{\epsilon}\end{aligned}\quad (\text{A.12})$$

using  $dpp^2$  given above we then write

$$\hat{f}_{\mathbf{r}}(\tilde{\epsilon}) = A^2 \sqrt{\tilde{\epsilon}} e^{-\tilde{\epsilon}} \frac{2}{\sqrt{\pi}} \int_0^1 dX \frac{2}{\sqrt{\pi}} \int_0^\infty d\tilde{E} e^{-\tilde{E}} \sqrt{\tilde{E}} \Theta \left( \eta(\mathbf{r}) - \frac{\tilde{E}}{2} - \frac{\tilde{\epsilon}}{2} - X \sqrt{\tilde{E}\tilde{\epsilon}} \right) \quad (\text{A.13})$$

We can now choose the normalization constant  $A^2$  using

$$\int_0^{2\eta(\mathbf{r})} d\tilde{\epsilon} \hat{f}_{\mathbf{r}}(\tilde{\epsilon}) = 1$$

where we have used an energy cutoff of  $2\eta(\mathbf{r})$  since either particle may have an energy in the range  $[0 \rightarrow \eta(\mathbf{r})]$ . With the normalization, the complete expression for  $\hat{f}_{\mathbf{r}}(\tilde{\epsilon})$  is then

$$\hat{f}_{\mathbf{r}}(\tilde{\epsilon}) = \frac{2}{\sqrt{\pi}} \sqrt{\tilde{\epsilon}} e^{-\tilde{\epsilon}} \hat{\mathcal{G}}(\eta_{\mathbf{r}}, \tilde{\epsilon}) \quad (\text{A.14})$$

where all the effects of the truncation have been moved to  $\hat{\mathcal{G}}$ , given by

$$\hat{\mathcal{G}}(\eta_{\mathbf{r}}, \tilde{\epsilon}) = \frac{\int_0^1 dX \frac{2}{\sqrt{\pi}} \int_0^\infty d\tilde{E} e^{-\tilde{E}} \sqrt{\tilde{E}} \Theta \left( \eta(\mathbf{r}) - \frac{\tilde{E}}{2} - \frac{\tilde{\epsilon}}{2} - X \sqrt{\tilde{E}\tilde{\epsilon}} \right)}{\int_0^{2\eta(\mathbf{r})} d\tilde{\epsilon} \frac{2}{\sqrt{\pi}} \sqrt{\tilde{\epsilon}} e^{-\tilde{\epsilon}} \int_0^1 dX \frac{2}{\sqrt{\pi}} \int_0^\infty d\tilde{E} e^{-\tilde{E}} \sqrt{\tilde{E}} \Theta \left( \eta(\mathbf{r}) - \frac{\tilde{E}}{2} - \frac{\tilde{\epsilon}}{2} - X \sqrt{\tilde{E}\tilde{\epsilon}} \right)}$$

we can check the limiting behavior of this equation since we expect when

$$\lim_{\eta \rightarrow \infty} \hat{\mathcal{G}}(\eta_{\mathbf{r}}, \tilde{\epsilon}) = 1$$

. Using

$$\int_0^\infty dx \sqrt{x} e^{-x} = \frac{\sqrt{\pi}}{2}$$

then this requirement is fulfilled.

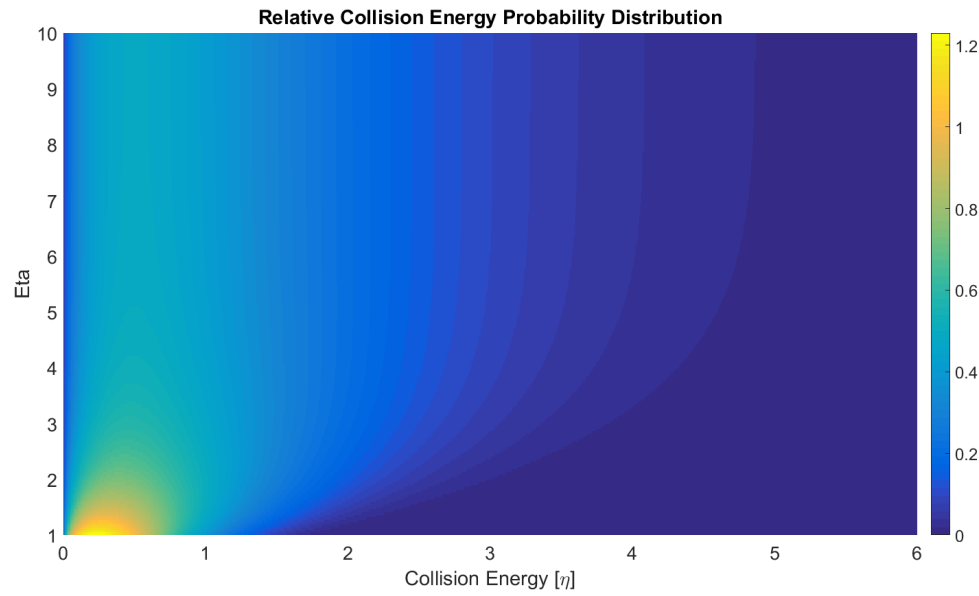


Figure A.1 : 2D Surface plot of the relative collision likelihood

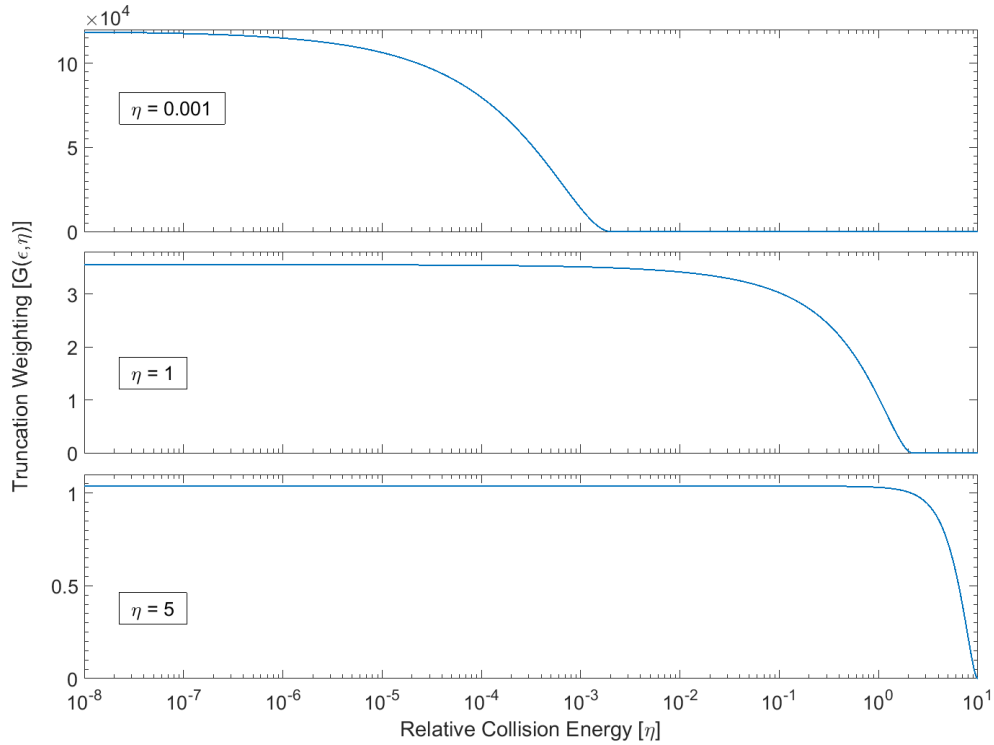


Figure A.2 : Behavior of  $G(\epsilon, \eta)$  vs. collision energy

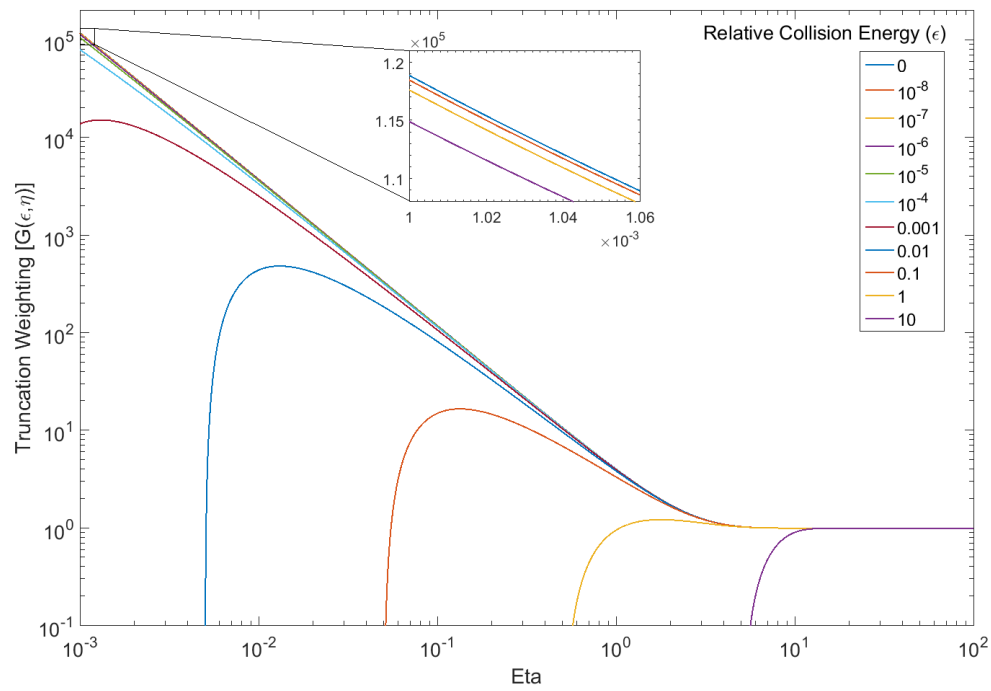


Figure A.3 : Behavior of  $G(\epsilon, \eta)$  vs.  $\eta$